

# Magazine of Civil Engineering

117(1), 2023

ISSN  
2712-8172



**Magazine of Civil Engineering**

ISSN 2712-8172

Online peer-reviewed open-access scientific journal in the field of Civil and Construction Engineering

**Founder and Publisher:** Peter the Great St. Petersburg Polytechnic University

This journal is registered by the Federal Service for Supervision of Communications, Information Technology, and Mass Media (ROSKOMNADZOR) in 2020. Certificate EI No. FS77-77906 issued February 19, 2020.

**Periodicity:** 8 issues per year

Publication in the journal is open and free for all authors and readers.

**Indexing:** Scopus, Web of Science (ESCI, RSCI), DOAJ, Compendex, EBSCO, Google Academia, Index Copernicus, ProQuest, Ulrich's Serials Analysis System, CNKI

**Corresponding address:** 29 Polytechnicheskaya st., Saint Petersburg, 195251, Russia

**Chief science editor:** associate member of RAS, D.S. in Engineering, Vitaly V. Sergeev

**Deputy chief science editors:**

D.S. in Engineering, Galina L. Kozinetc

D.S. in Engineering, Sergey V. Korniyenko

**Executive editor:** Ekaterina A. Linnik

**Translator, editor:** Darya Yu. Alekseeva

**DT publishing specialist:**

Anastasiya A. Kononova

**Contacts:**

E-mail: [mce@spbstu.ru](mailto:mce@spbstu.ru)

Web: <http://www.engstroy.spbstu.ru>

---

Date of issue: 13.02.2023

© Peter the Great St. Petersburg Polytechnic University. All rights reserved.

© Coverpicture – Ilya Smagin

**Editorial board:**

T. Awwad, PhD, professor, Damascus University, Syrian Arab Republic

M.I. Balzannikov, D.Sc., professor, Samara State University of Economics, Russia

A.I. Belostotsky, D.Sc., professor, StaDyO Research & Engineering Centre, Russia

A.I. Borovkov, PhD, professor, Peter the Great St. Petersburg Polytechnic University, Russia

A. Borodinecs, Dr.Sc.Ing., professor, Riga Technical University, Latvia

M. Veljkovic, PhD, professor, Delft University of Technology, The Netherlands

R.D. Garg, PhD, professor, Indian Institute of Technology Roorkee (IIT Roorkee), India

M. Garifullin, PhD, postdoctoral researcher, Tampere University, Finland

T. Gries, Dr.-Ing., professor, RWTH Aachen University, Germany

T.A. Datsyuk, D.Sc., professor, Saint-Petersburg State University of Architecture and Civil Engineering, Russia

V.V. Elistratov, D.Sc., professor, Peter the Great St. Petersburg Polytechnic University, Russia

T. Kärki, Dr.-Ing., professor, Lappeenranta University of Technology, Russia

G.L. Kozinetc, D.Sc., professor, Peter the Great St. Petersburg Polytechnic University, Russia

D.V. Kozlov, D.Sc., professor, National Research Moscow State Civil Engineering University, Russia

S.V. Korniyenko, D.Sc., professor, Volgograd State Technical University, Russia

Yu.G. Lazarev, D.Sc., professor, Peter the Great St. Petersburg Polytechnic University, Russia

M.M. Muhammadiev, D.Sc., professor, Tashkent State Technical University, Republic of Uzbekistan

H. Pasternak, Dr.-Ing.habil., professor, Brandenburgische Technische Universität, Germany

F. Rögner, Dr.-Ing., professor, Technology Arts Science TH Köln, Germany

V.V. Sergeev, D.Sc., professor, Peter the Great St. Petersburg Polytechnic University, Russia

T.Z. Sultanov, D.Sc., professor, Tashkent Institute of Irrigation and Agricultural Mechanization Engineers, Republic of Uzbekistan

M.G. Tyagunov, D.Sc., professor, National Research University "Moscow Power Engineering Institute", Russia

M.P. Fedorov, D.Sc., professor, Peter the Great St. Petersburg Polytechnic University, Russia

D. Heck, Dr.-Ing., professor, Graz University of Technology, Austria

A.G. Shashkin, D.Sc., "PI Georekonstruktsiya", LLC, Russia

V.B. Shtilman, D.Sc., JSC "B.E. Vedeneev VNIIG", Russia

**Contents**

Maddahi, M., Gerami, M., Naderpour, H. Effect of uncertainties of shear wall on reliability of rehabilitated structure	11701
Bulgakov, B.I., Nguyen, V.Q.D., Aleksandrova, A.V., Larsen, O.A., Galtseva, N.A. High-performance concrete produced with locally available materials	11702
Alekseytsev, A.V., Sazonova, S.A. Numerical analysis of the buried fiber concrete slabs dynamics under blast loads	11703
Sreekumar, M.G., Nair, D.G., Jagadish, K.S. Effects of gradation and clay minerals on stabilized lateritic soil blocks	11704
Ishchenko, A.A., Butsukin, V.V., Artiukh, V.G., Chernysheva, N.V. Diagnostics and reconstruction of bearing units	11705
Skripnikova, N.K., Semenovkykh, M.A., Shekhovtsov, V.V. Anorthite-based building ceramics	11706
Loganina, V.I., Akzhigitova, E.R. Mineral additive for lime dry building mixtures	11707
Aldungarova, A.K., Mkilima, T.M, Utepov, Ye.B., Tulebekova, A.S., Zharassov, Sh.Zh. Heterogeneous embankment dam under rapid drawdown	11708
Boiprav, O.V., Belousova, E.S., Ahmetdinova, E.S., Bogush, N.V. Charcoal-containing building materials for electromagnetic radiation shielding	11709
Stetjukha, V.A. Energy efficiency of underground structures in harsh climatic conditions	11710
Popov, A.L., Yadrikhinsky, V.A., Mestnikov, A.E. Peculiarities of hydration and frost resistance of cement with natural zeolite additive	11711
Fomin, A.Yu., Hafizov, E.R., Vdovin, E.A., Fafanov, F.R. Stone mastic asphalt modified with stabilizing additives of multifunctional action	11712
Tyukalov, Yu.Ya. Elliptical underground concrete block bridge with minimal weight	11713



Research article

UDC 624.046

DOI: 10.34910/MCE.117.1



## Effect of uncertainties of shear wall on reliability of rehabilitated structure

M. Maddahi , M. Gerami , H. Naderpour 

Semnan University, Semnan, Iran

 [m.maddah93@semnan.ac.ir](mailto:m.maddah93@semnan.ac.ir)

**Keywords:** special steel moment frame, steel shear wall, uncertainty, seismic rehabilitation, probabilistic seismic performance, fragility curve

**Abstract.** Uncertainties in seismic demand and structural capacity create conservatism in acceptance criteria for structural performance levels. In case of such conservations, rehabilitation costs can increase, and seismic evaluation results of the structures may be incorrect. In design and rehabilitation of structures, considering uncertainties and reducing them can decrease existing conservations and result in optimal design. Seismic rehabilitation guidelines use reliability index coefficients to consider the uncertainties of the existing structure. In seismic rehabilitation of structures, the existence of uncertainties in the secondary system, which are added to seismic rehabilitation of the existing structure, can lead to an increase in the existing uncertainties. Therefore, in this paper, on the example of rehabilitation of a 3-story steel frame structure of the SAC project by a steel shear wall, quantifying of uncertainties of steel shear walls was considered, and a parametric study of the reliability index of the structure was done. The studied structure was modeled in OpenSees software and was analyzed in the presence of uncertainties of the steel shear wall before and after rehabilitation. Based on the performed analysis and considered uncertainties, values of the reliability index of the rehabilitated structure by the steel shear wall were calculated. According to results, rehabilitation of structure reduced the maximum inter-story drift ratio and the probability of failure, while consideration of uncertainties of rehabilitated structure increased the maximum inter-story drift ratio and the probability of failure, and therefore existing conservatism dropped.

**Citation:** Maddahi, M., Gerami, M., Naderpour, H. Effect of uncertainties of shear wall on reliability of rehabilitated structure. Magazine of Civil Engineering. 2023. 117(1). Article no. 11701. DOI: 10.34910/MCE.117.1

### 1. Introduction

In recent decades, the performance-based seismic evaluation method has been continuously updated. ATC [1] began work on next-generation performance-based seismic design criteria under the ATC-58 project for new and existing structures. In addition, the FEMA 445 [2] released a report under the title "Guidelines for Next-Generation Methods". The main purpose of the next-generation methods was to examine conservatism of acceptance criteria and to modify the structural performance evaluation. In developing seismic evaluation methods based on performance, the existence of conservatism in the acceptance criteria of structural performance levels has increased the cost of retrofitting and reconstruction. Also, the results of the evaluation of the seismic performance of the structures are incorrect due to the existing conservatism. Hence, researchers analyzed the seismic evaluation of designed structures according to the old regulations in an analytical and laboratory manner. The results of the studies indicated a significant conservatism in the acceptance criteria of the old regulations. Therefore, this issue expressed the need for considering uncertainties in the estimation of structural engineering issues [3–6].

When the structural response is simulated, active loading on the system and resistance of the member cannot be definitively expressed in the presence of uncertainties. However, the possible range of

demand and resistance can be predicted and idealized. Consequently, a probabilistic design philosophy can provide a level of safety for engineered structures with the prediction of the failure probability. Therefore, definitive methods of structural design have been replaced by the reliability and risk-based methods, which have been spread around the world. Probabilistic methods of analysis of structures considered system properties and external forces as uncertain random variables [7]. The uncertainties in the probabilistic methods were categorized as aleatory and epistemic [8]. Aleatory uncertainty is also called random uncertainty or Type-A uncertainty, which is due to random changes of phenomena. As a result, these types of uncertainties cannot be reduced. In contrast, epistemic uncertainty is also called reducibility uncertainty or Type-B uncertainty, which is due to the limitation of knowledge or data. These types of uncertainties can be reduced by improving the mathematical models or increasing data collection.

Zareian and Krawinkler [9] proposed a probabilistic approach to minimize the failure potential of the structural systems based on various sources of uncertainty. Helmerich [10] investigated the reliability of steel structures and showed that structural resistance can be predicted by using appropriate models of material properties and geometric parameters. These studies have shown that a better description of the model uncertainties is necessary. Currently, the used probabilistic models for model uncertainties are largely based on visual judgment and limited information. Shafei et al. [11] presented a simple method for predicting the mean and dispersion of variables in the moment frame systems subject to seismic stimulation. Based on studies, the researchers considered probabilistic models for uncertainties and analyzed the structures. Torabian and Taghikhany [12] used the single-degree of freedom system to investigate the uncertainties of steel moment frames. They investigated the aleatory and epistemic uncertainties of structures using incremental dynamic analysis and the Latin Hypercube Sampling method.

Holicky et al. [13] tried to improve the model uncertainty definitions and proposed a general methodology to determine their quality by comparing the model and empirical results. They studied the implications of the model uncertainty for existing and new structures and provided examples based on recent studies on the flexural and shear strength of reinforced concrete beams. Asgarian and Ordoubadi [14] considered the parameters of the model and examined the effect of uncertainty of equivalent damping, effective seismic mass, yield strength, and ultimate strength of the steel structure. Hajirasouliha et al. [15] studied the effect of uncertainty in structural properties and ground motion on the performance of braced frames. In addition, Zhang et al. [16] studied uncertainties in steel structures such as uncertainty in cross-section and structural loading.

Dyanati et al. [17] considered the demand and capacity uncertainties of the braced frame system and examined the seismic performance of structures. Jiang and Ye [18–19] considered different sources of aleatory and epistemic uncertainties for seismic risk assessment of the structures. They modeled random variables by using the Latin Hypercube Sampling method. They showed that the uncertainties have a significant impact on seismic risk assessment of the structures, which cannot be neglected. Piluso et al. [20] developed the seismic design method of moment resisting frames with considering the uncertainties of the material properties and the theory based on the failure mechanism. Norouzi and Gerami [21] studied the effect of uncertainty in characteristics of the ground motion on the performance of steel moment frames. Astroza et al. [22] proposed a new approach to reduce the modeling uncertainty. They considered three-story steel frame structure with modeling uncertainty such as geometry, inertia properties, gravity loads, and damping properties. Wijaya et al. [23] considered the steel structures with the hysteretic dampers, and investigated uncertainties using the Latin hypercube Sampling method.

These researches were done in the seismic design of structures considering uncertainties in the designed structures. In seismic regulations such as FEMA P695 [24], the aleatory and epistemic uncertainties are considered separately. In these regulations, uncertainties are considered based on qualitative data in existing structures. In seismic rehabilitation of structures, the secondary system, which is added to the existing structure also has uncertainties. These uncertainties may increase the uncertainties of the rehabilitated structure.

In this study, a steel shear wall was used for rehabilitation of the moment frame. Then, uncertainties of the steel shear wall and quantification of them were investigated to evaluate the uncertainties in seismic rehabilitation. The design and evaluation of the seismic performance of structures should be performed using reliability-based methods. In this study, the effect of uncertainties on the seismic performance of the rehabilitated steel moment frame was studied using the reliability methods.

## 2. Methods

### 2.1. Specifications of the selected structural model

In this paper, a 3-story steel moment frame was selected [25]. This structure, designed in accordance with the UBC94 regulation, met the requirements of gravity and seismic design. The structure was designed as a special moment frame and an office building located on stiff soil in Los Angeles. In this structure, the

perimeter moment frames were considered as a structural system. The plan and height of the desired structure are indicated in Fig. 1. As shown in Fig. 1, the structure is three-dimensional. Because three-dimensional modeling of the structure increases the volume of the problem, the structure was modeled two-dimensionally. In a two-dimensional model, an equivalent gravity column was used to reduce the uncertainties caused by simplification.

There were rigid connections in the lowest floor of this structure. The damping of the structure was 2 %, and the yield strength and modulus of elasticity of the beams and columns were 50 kip and 29000 ksi, respectively. The sections assigned to members of the structure are presented in Table 1. The regulations, published after the Northridge earthquake, proposed design recommendations for the creation of a plastic hinge in the beam and away from the column surface. Here, the displacement of the plastic hinge away from the surface of the column was done by increasing the beam capacity in the column surface via adding the cover plates on the flange of the beam. The bilinear moment-rotation relationship with strain hardening of 3 % was used to define the plastic behavior of beams and columns. Rigid elements with rotational spring were used to model the panel zone in the OpenSees software [26]. In this model, the trilinear shear force-shear strain relationship was used to describe the shear behavior of the panel zone. Details of the panel zone are indicated in Fig. 2.

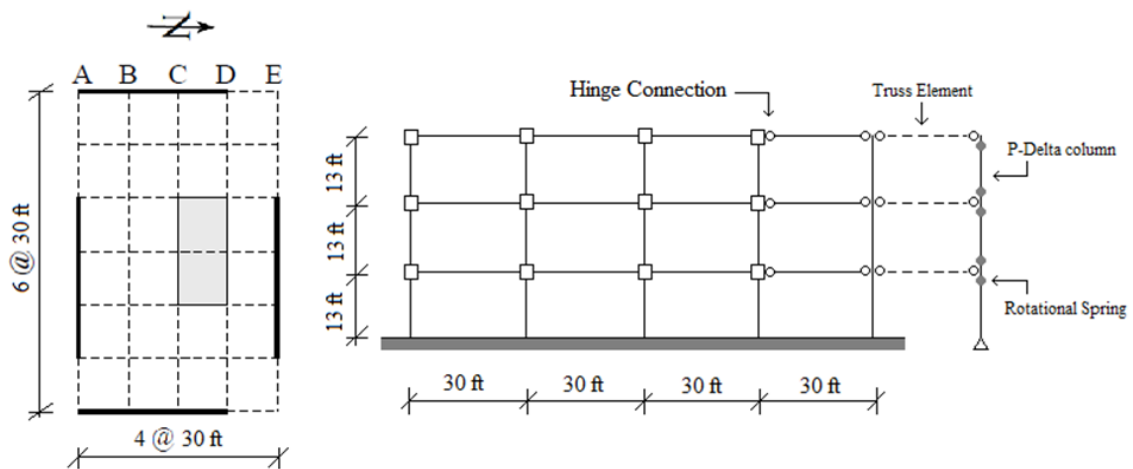


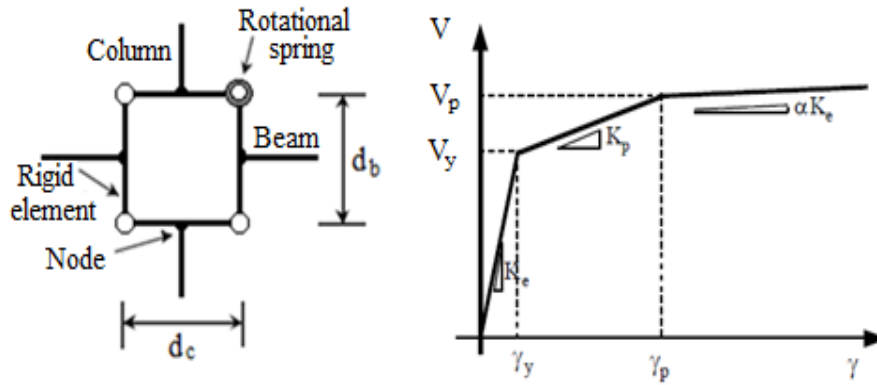
Figure 1. Plan and height of the 3-story structure [25].

Table 1. Sections assigned for the studied structure.

Story	Moment Resisting Frame (MRF)			Gravity Frame (GF)	
	Columns		Beam	Column	Beam
	Exterior	Interior			
1	W14x257	W14x311	W30x116	W14x68	W16x26
2	W14x257	W14x311	W30x116	W14x68	W16x26
3	W14x257	W14x311	W24x62	W14x68	W14x22

## 2.2. Rehabilitation of the selected structure

Based on the performed evaluations on the structure, its weaknesses were determined. The use of appropriate methods is essential for correcting the weaknesses and performing the rehabilitation. For rehabilitation, according to requirements of the structure, the proper strategy should be selected. In this paper, the steel shear wall was considered for rehabilitation of the existing structure. Different methods are available to design and analyse steel shear walls, and the strip model method is one of the most popular ones. This method includes a set of stretching strips and it was first suggested by Thorburn et al. [27]. Fig. 3 shows an example of stretching strips that is equivalent to a steel shear wall in the strip model.



**Figure 2. Analytical model and the trilinear shear force–shear strain relationship for panel zone [25].**

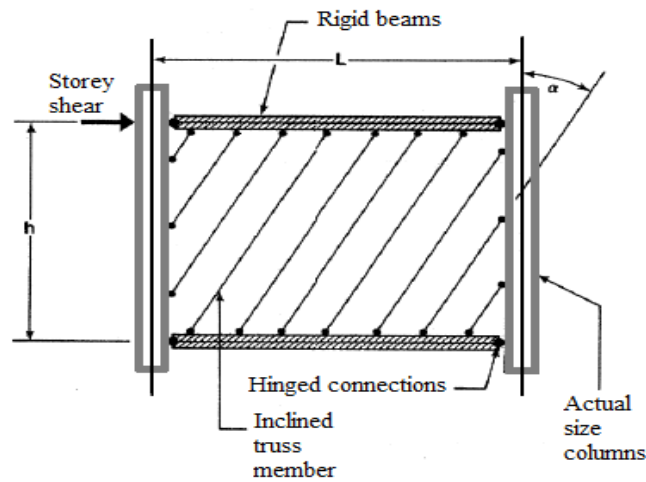


**Figure 3. An example of the strip model of the steel shear wall [27].**

In the strip model method, the shear wall is equivalent to a brace. Then the thickness of the steel shear wall is calculated according to Eq. (1):

$$t_w = \frac{2A_g \Omega \sin \theta}{L \sin 2\alpha} \tag{1}$$

Here, the parameters of  $\theta$ ,  $A_g$  and  $\alpha$  are the angle between the equivalent brace and the vertical line, the cross-section of the equivalent brace, and the tensile field angle, respectively;  $\Omega$  is the over strength coefficient of the steel shear wall that is equal to 1.2.

Timler and Kulak [28] presented Eq. (2) for the estimation of the tensile field angle ( $\alpha$ ), which includes geometric properties of the steel shear walls and boundary elements.

$$\tan^4 \alpha = \frac{1 + \frac{t_w L}{2A_c}}{1 + t_w h \left( \frac{1}{A_b} + \frac{h^3}{360I_c L} \right)} \tag{2}$$

Here, parameters of  $L$ ,  $h$  and  $t_w$  are the width of the frame span, the height of the floor, the thickness of the steel shear wall, respectively;  $A_b$  and  $A_c$  are the cross-sections of the beam and the column;  $I_c$  is the moment of inertia of the column. This equation is used to design steel shear walls by American and Canadian regulations [29–30]. After determining the thickness of the steel shear wall and by considering the appropriate number of tensile strips, the cross-section of these strips in each floor is calculated using Eq. (3):

$$A_s = \frac{L \cos \alpha + h \sin \alpha}{n} t_w \tag{3}$$

In this equation, the parameter of  $n$  is the number of strips per span. To describe the behavior of steel shear walls, at least ten tensile strips were placed in each span. After the design of the shear walls Eqs. (4)–(5) must be controlled to prevent the buckling of the columns along the shear wall in each floor:

$$I_c \geq \frac{0.00307th^4}{L} \tag{4}$$

$$M_{fpc} \geq \frac{\sigma_{ty}th^2}{4} \cos^2 \alpha, \tag{5}$$

where  $M_{fpc}$  and  $\sigma_{ty}$  are the plastic moment of the column and the tensile field stress, respectively. In addition, Eq. (6) must be controlled to prevent bending of the beam in each floor:

$$M_{fbb} \geq \frac{\sigma_{ty}tL^2}{8} \sin^2 \alpha, \tag{6}$$

where  $M_{fbb}$  is the plastic moment of the beam.

In this paper, steel plates with low yield strength ( $F_y = 35$  kip) and 29000 ksi elastic modulus were used for the steel shear wall. The rehabilitated structure with the steel shear wall was modeled with a strip model. For the strip model, the trilinear force-deformation relationship with 2 % strain hardening was used, which was derived from the work of Purba and Bruneau [31]. Fig. 4–5 show the rehabilitated structure with the steel shear wall and the used force-deformation relationship, respectively.

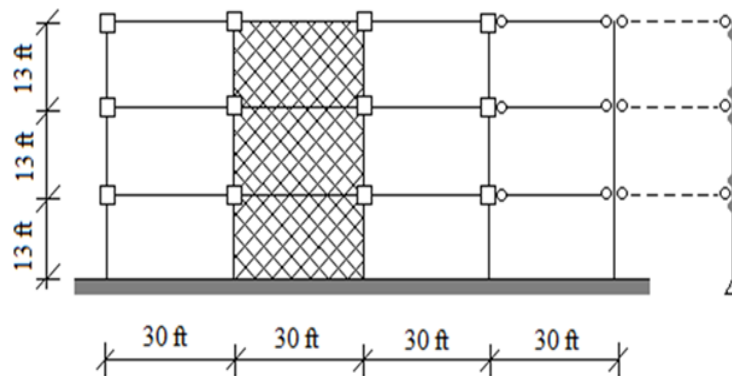


Figure 4. Rehabilitated structure with steel shear wall.

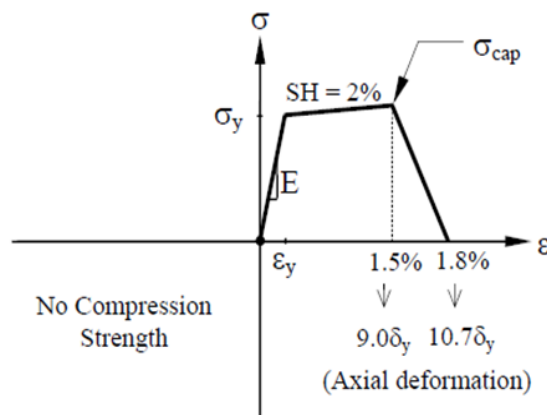


Figure 5. Trilinear force-deformation relationship of steel shear wall [31].

### 2.3. Selected records to evaluate the seismic performance

The incremental dynamic analysis method describes the behavior of the structure in a wide range of different intensities of the earthquake. In the incremental dynamic analysis method, the influence of different records is considered with a deterministic model of the structure; hence, this method involves only the aleatory uncertainty. A developed dynamic analysis method is proposed to consider epistemic uncertainties. In this method, aleatory and epistemic uncertainties are considered by using the probabilistic distribution of the structural model. Records were selected and scaled according to the location of the structure to perform incremental dynamic analysis. Selected records include far-field and near-field records. So far, extensive studies have been done to define the near-field record and to distinguish it from a far-field record. In the classification of records, the distance from the site to the earthquake center is the distinctive feature between far-field and near-field records. Usually, in near-field records, distances between 20 and 60 km are defined as near faults. However, there is no global definition of which site may be classified as a near or far fault. In this paper, 15 km distance from the fault was considered as a criterion for the classification of far-field and near-field records [32]. All selected records are located on D soil [33]. Tables 2–3 show far-field and near-field records.

**Table 2. Details of the far-field records.**

No.	Earthquake	Year	Station	$M_W$	$R_{fb}$ (km)	$R_{rup}$ (km)
1	San Fernando	1971	2516 Via Tejon PV	6.61	55.2	55.2
2	Tabas, Iran	1978	Ferdows	7.35	89.76	91.14
3	Imperial Valley06	1979	Coachella Canal #4	6.53	49.1	50.1
4	Victoria, Mexico	1980	SAHOP Casa Flores	6.33	39.1	39.3
5	Coalinga-01	1983	Parkfield–Cholame	6.36	55.05	55.77
6	N. Palm Springs	1986	Hesperia	6.06	71.7	72.97
7	Whittier Narrows-01	1987	Canyon Country-W Lost	6	44.88	48.18
8	Loma Prieta	1989	Richmond City Hall	6.93	87.78	87.87
9	Landers	1992	Baker Fire Station	7.28	87.94	87.94
10	Northridge-01	1994	Huntington Bch-Waikiki	6.69	66.43	69.5

**Table 3. Details of the near-field records.**

No.	Earthquake	Year	Station	$M_W$	$R_{fb}$ (km)	$R_{rup}$ (km)
1	Parkfield	1966	Cholame–Shandon	6.19	12.9	12.9
2	Gazli	1976	Karakyr	6.80	3.92	5.46
3	Coalinga	1983	Pleasant Valley P.P. bldg	6.36	7.69	8.41
4	N. Palm Springs	1986	North Palm Springs	6.06	0	4.04
5	Whittier Narrows-01	1987	Santa Fe Springs E. Joslin	6	11.47	14.49
6	Superstition Hills-02	1987	Parachute Test Site	6.54	0.95	0.95
7	Loma Prieta	1989	Gilroy Araay #2	6.93	10.38	11.07
8	Erzican, Turkey	1992	Erzican	6.69	0	4.38
9	Kobe	1995	KJMA	6.9	0.94	0.96
10	Chi-Chi	1999	TCU065	7.62	0.57	0.57

The selected records were scaled according to NIST GCR 11-917-15 publication [34]. In two-dimensional analyses, the selected records should be scaled so that the mean value of the response spectrum for the set of records is not lower than the site design response spectrum within the periodic range of  $0.2T$  to  $1.5T$ . In Fig. 6, the site design response spectrum, the scaled spectrum of the selected records, and the mean spectrum of these records are indicated.

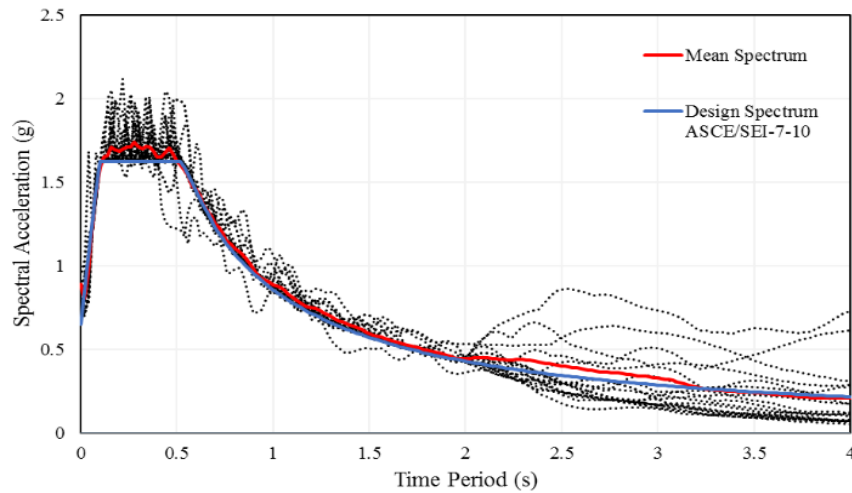


**Figure 6. The design spectrum and the scaled spectrum of selected records along with the average range of these records.**

#### 2.4. Evaluation of probabilistic seismic performance

Despite large uncertainties in the seismic demand and capacity, the results of the design and evaluation of the seismic performance of structures is valid only if these uncertainties are considered with a realistic approach. In other words, designing and evaluating the seismic performance of structures should be done using reliability methods. Reliability was first used by researchers who were working in the field of structural safety. The purpose of reliability is to express the completeness of probability of failure [35]. Each reliability issue has two components: random variables and state functions. Random variables express uncertainty in the problem while the state functions define the failure event. In general, the limit state function is defined as Eq. (7):

$$g(R,S) = R - S, \quad (7)$$

where  $g$  is a limit state function, and a boundary limit state occurs in the state of  $g = 0$ . In this equation,  $g > 0$  indicates a safe structure, and  $g < 0$  denotes the failure of the structure.  $R$  and  $S$  express the capacity and demand, respectively, which include a set of random variables. The probability of failure ( $P_f$ ) is expressed in Eq. (8) as the multiple integrals:

$$P_f = P(g \leq 0) = \int_{g \leq 0} f(x) dx, \quad (8)$$

where  $f(x)$  is the probability density function (PDF) for random variables. Variations of statistical distribution for the randomized model and number of random variables can complicate the evaluation of Eq. (8) using the integration method. Different methods of reliability are used to solve this problem. In this paper, the Latin Hypercube Sampling (LHS) method was used to consider demand and capacity uncertainties of the structural system, which is a common example of reliability methods.

Initially, the structure with basic parameters was analyzed with selected seismic records. The results of this stage were associated with uncertainty caused by various seismic records. In the next step, different realities of the structural model were formed considering force-deformation relationship parameters of the steel shear wall as probabilistic variables. Epistemic uncertainty was determined by conducting incremental dynamic analysis on each of these structural realities. Table 4 shows the statistical characteristics of the selected probabilistic variables. 160 structural realizations were used based on the considered probabilistic variables for the rehabilitated structure with the steel shear wall [36].

**Table 4. Statistical characteristics of random input variables.**

Name	Symbol	Mean	C.O.V	Distribution	Reference
Steel yield strength	$F_y$	35 kip	0.07	Lognormal	Melchers [37], JCSS [38]
Elastic stiffness	$E$	29000 ksi	0.03	Lognormal	Schmidt and Bartlett [39], Dexter et al. [40]
Strain hardening	$a_h$	0.02	0.4	Normal	Sadowski et al. [41–42]
Post-capping stiffness	$a_c$	-0.68	0.4	Normal	Lignos and Krawinkler [43]

According to FEMA 356 [44], the inter-story drift ratio is considered an index to measure of structural damage. Values of 0.7 %, 2.5 %, and 5 % were proposed by FEMA 356 as the permissible inter-story drift ratio for three structural performance levels of Immediate Occupancy (IO), Life Safety (LS) and Collapse Prevention (CP), respectively. In this paper, the spatial acceleration in the main period of structure ( $S_a$ ) was used to measure the seismic intensity. The fragility function  $F_r(x)$  was also used to express the probability of exceedance of different damage states, which is expressed by Eq. (9) [45]:

$$F_r(x) = \Phi \left[ \frac{(\ln x - \ln \hat{S}_a)}{\beta_R} \right], \quad (9)$$

where  $\hat{S}_a$  expresses the median value of the structural fragility in unit  $S_a$ ,  $\beta_R$  is the standard deviation of lognormal of the system fragility, and  $\Phi$  denotes the standard normalized cumulative distribution function. The uncertainties associated with seismic demand and the structural capacity are expressed by the  $\beta_R$  parameter that is calculated using Eq. (10):

$$\beta_R = \sqrt{\beta_{D|S_a}^2 + \beta_c^2}. \quad (10)$$

$\beta_{D|S_a}$  and  $\beta_c$  parameters represent the uncertainty in seismic demand and the uncertainty in the structural capacity, respectively. In limit states of IO and LS, the value of  $\beta_c$  is 0.25, and in the limit state of CP is 0.15 [45–46]. The annual exceedance probability of the limit state is defined in Eq. (11):

$$P_{LS} = k_0 \hat{S}_a^{-k} \exp \left[ \frac{(k\beta_R)^2}{2} \right], \quad (11)$$

where  $k_0 \hat{S}_a^{-k}$  expresses the seismic hazard, and the exponential expression is the correction factor that applies to the variability of seismic demand and structural capacity;  $k_0$  and  $k$  indicate the risk scale and the slope of the seismic hazard curve, respectively.

### 3. Results and Discussion

#### 3.1. Sensitivity analysis

In this paper, the sensitivity of the rehabilitated structure response with the steel shear wall was evaluated to assume yield strength, elastic stiffness, strain hardening, and post-capping stiffness of the trilinear force-deformation relationship of the steel shear wall as the probabilistic parameters. For each of these parameters, base value and an appropriate range of changes were considered. In Fig. 7, the IDA curves show the sensitivity of the rehabilitated structure response with the steel shear wall to the probabilistic parameters.

The values of 30, 35 and 40 ksi were considered for the yield strength parameter to investigate the effect of the sensitivity of the structure response to this parameter. The value of 35 ksi was considered as the base value, and the values of 30 and 40 ksi were considered as the lower and upper bounds of the selected range for this parameter, respectively. In Fig. 7a, the IDA curves show the sensitivity of the rehabilitated structure response with the steel shear wall to the yield strength parameter. The values of 25000, 29000, and 33000 kip were considered for the elastic stiffness parameter with 29000 kip considered as the base value. The IDA curves in Fig. 7b show the sensitivity of the response of the rehabilitated structure with the steel shear wall to this parameter. As can be seen in Fig. 7a-b, the effect of the two probabilistic parameters of yield strength and elastic stiffness of trilinear force-deformation relationship is more on the response of the rehabilitated structure with steel shear wall (17.5 % and 19 %).

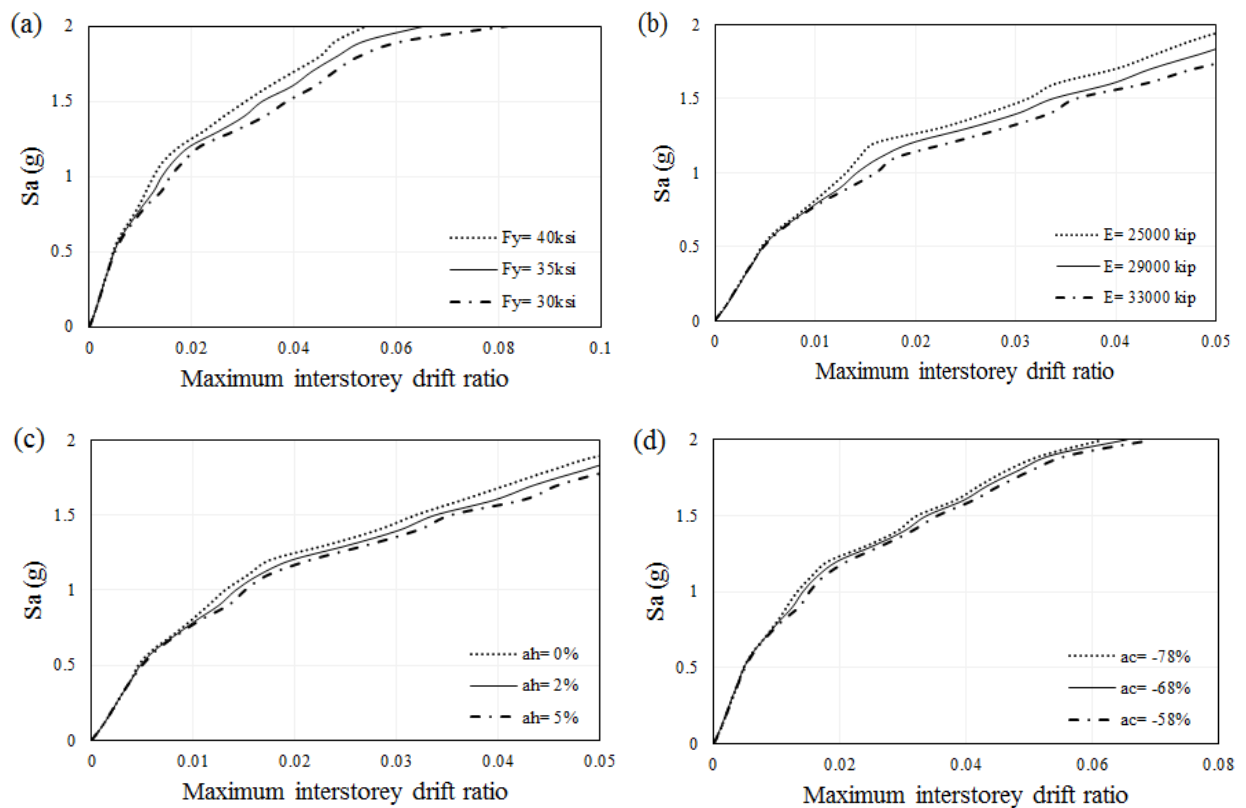


**Figure 7. The sensitivity of median IDA curve to probabilistic parameters of steel shear wall: (a) The effect of steel strength parameter, (b) The effect of elastic stiffness parameter, (c) The effect of strain hardening parameter, (d) The effect of post-capping stiffness parameter.**

The strain hardening is defined as a ratio of the plastic stiffness to the elastic stiffness in the force-deformation relationship of the steel shear wall. The value of 2 % was considered as the base value, and the values of 0 % and 5 % were considered as the lower and upper bounds of the selected range for this parameter, respectively. Fig. 7c shows the IDA curves of rehabilitated structure with the steel shear wall for base value and values of the considered range. Based on the results, the effect of this parameter on the response of the rehabilitated structure with steel shear wall is 7.6 %.

The post-capping stiffness, called negative strain hardening, was considered as probabilistic parameter with a base value of  $-68\%$  and a range of  $-78\%$  to  $-58\%$ . The sensitivity of the rehabilitated structure response to this parameter was indicated in Fig. 7d. As can be seen, the effect of the post-capping stiffness parameter of the trilinear force-deformation relationship of steel shear wall in the rehabilitated structure with the steel shear wall is 6.1 % that is less than the three considered probabilistic parameters.

### 3.2. Quantifying the considered uncertainties

Structural fragility curves indicate the exceedance probability of the defined damage states for records with specific intensity. Here, the maximum inter-story drift ratio was used to define the damage states, and values of 0.7 %, 2.5 %, and 5 % were used for Immediate Occupancy (IO), Life Safety (LS), and Collapse Prevention (CP) as performance levels of FEMA. In Fig. 8–11, structural fragility curves and IDA curves are shown for the structure before and after the rehabilitation and with considering uncertainties.

In Tables 5–6, values of uncertainties of seismic demand and total uncertainties of the structure, which are shown by parameters  $\beta_{D|S_a}$  and  $\beta_R$ , were included for the structure before and after of rehabilitation. In these tables, the median values of fragility were calculated according to Eq. (9) for the structure before and after rehabilitation and with considering uncertainties.

According the results in the Tables 5–6, the dispersion of the aleatory uncertainty of the steel moment frame structure was 0.32 and 0.38 for far-field and near-field records, respectively. This value was close to the dispersion value of steel moment frame structure [47]. The dispersion of the aleatory and epistemic uncertainties of the rehabilitated structure with steel shear wall was 0.27–0.34. This value was lower than the dispersion value of moment frame equipped with brace [47], and it was more than the dispersion value of moment frame structure [14].

As can be seen in Tables 5–6, the median value of fragility increased due to rehabilitation of the structure in the limit state of LS under far-field records from  $0.47 g$  to  $1.27 g$  and under near-field records from  $0.57 g$  to  $1.49 g$ . Also, it can be seen, median values of fragility increased due to rehabilitation of the structure in other limit states. The results of fragility curves of the rehabilitated structure with and without considering uncertainties showed that median values of fragility were reduced by considering uncertainties in all limit states.

The results of the IDA curves showed that rehabilitation of the structure reduced the maximum inter-story drift of the structure in the limit states of IO, LS, and CP. Comparison of the IDA curves of the rehabilitated structure with and without considering the uncertainties demonstrated that the maximum inter-story drift of the structure increased by 28.8–52 % under far-field records and by 24.1–39.3 % under near-field records by means of considering the uncertainties. This shows that conservatism was reduced by considering the uncertainties.

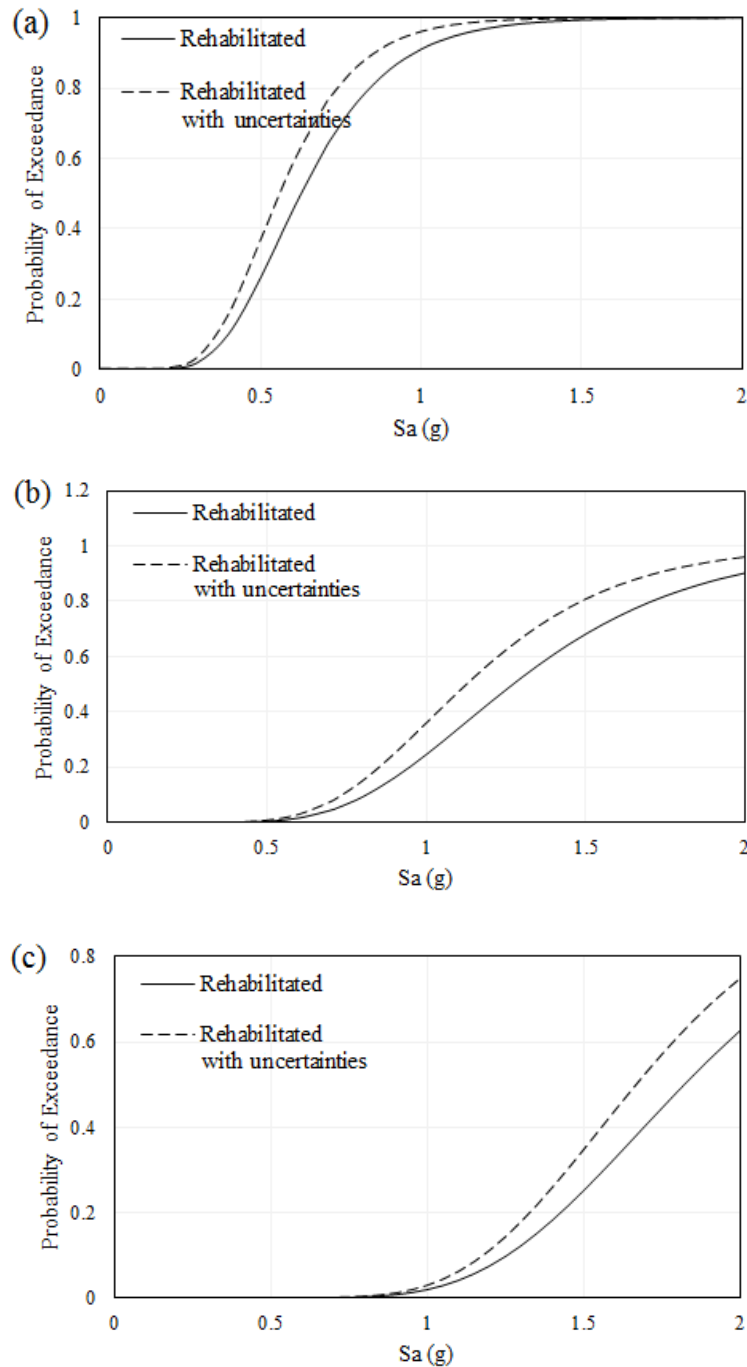


Figure 8. Fragility curve for the limit states under far-field records: (a) the limit state of IO, (b) the limit state of LS, (c) the limit state of the CP.

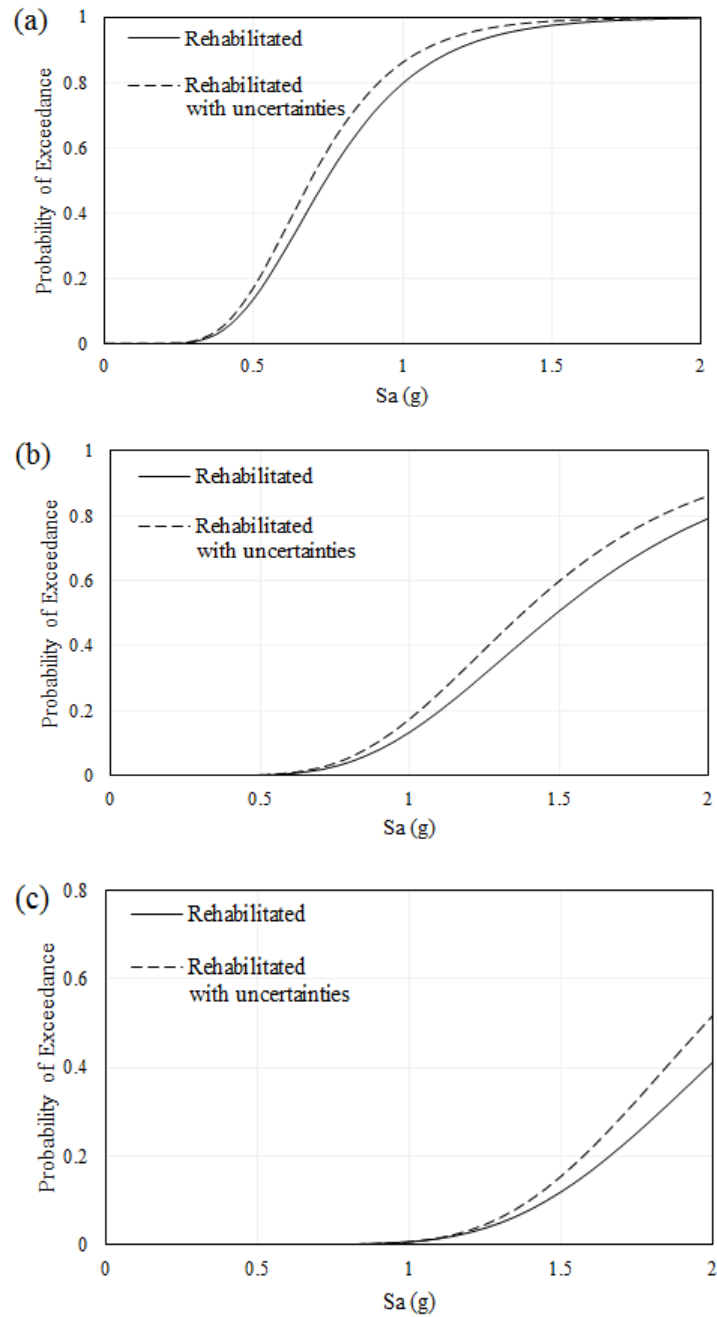


Figure 9. Fragility curve for the limit states under near -field records: (a) the limit state of IO, (b) the limit state of LS, (c) the limit state of the CP.

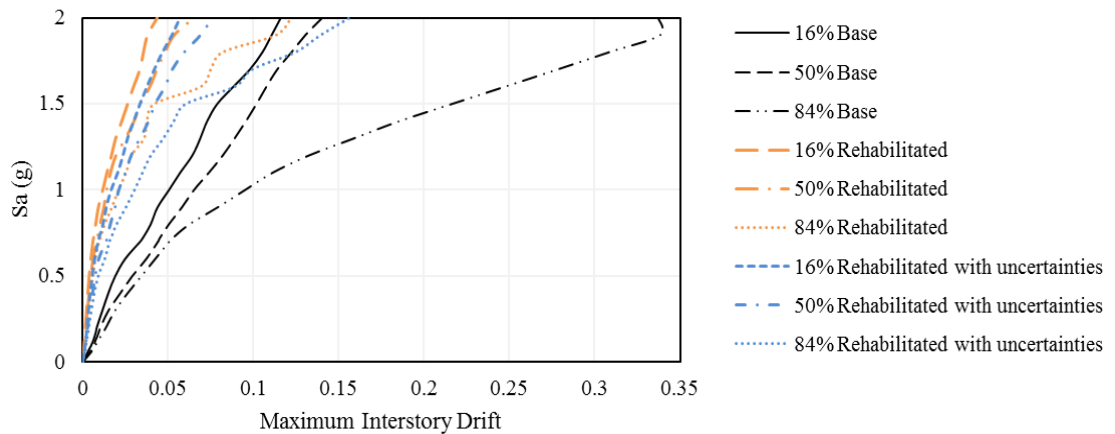


Figure 10. IDA curve of the structure under far-field records.

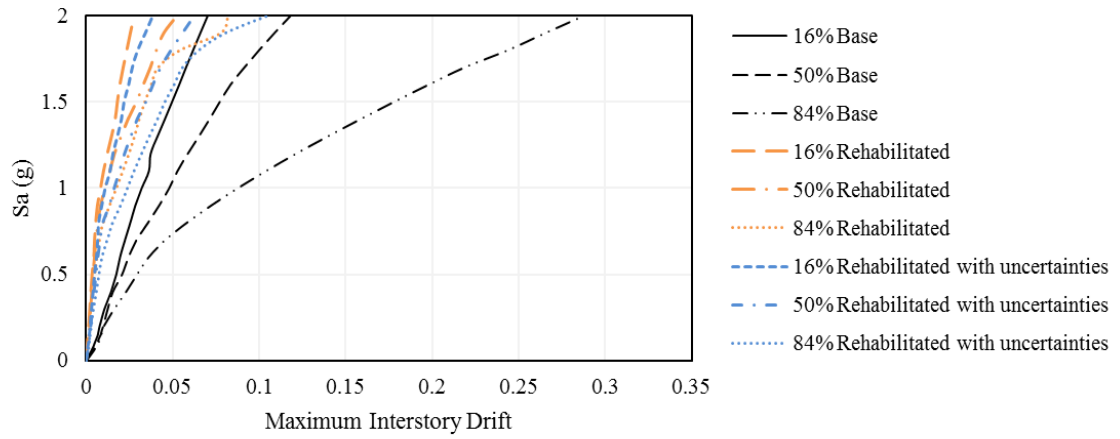


Figure 11. IDA curve of the structure under near-field records.

Table 5. Seismic demand statistics and median fragility values of structures under far-field records.

Case	$\beta_{D S_a}$	$\beta_R$			$\hat{S}_a(g)$		
		IO	LS	CP	IO	LS	CP
Base building	0.32	0.41	0.41	0.36	0.11	0.47	0.79
Rehabilitated building	0.25	0.35	0.35	0.29	0.63	1.27	1.82
Rehabilitated building with uncertainties	0.22	0.33	0.33	0.27	0.56	1.13	1.67

Table 6. Seismic demand statistics and median fragility values of structures under near-field records.

Case	$\beta_{D S_a}$	$\beta_R$			$\hat{S}_a(g)$		
		IO	LS	CP	IO	LS	CP
Base building	0.38	0.45	0.45	0.41	0.13	0.57	1
Rehabilitated building	0.26	0.36	0.36	0.30	0.74	1.49	2.14
Rehabilitated building with uncertainties	0.23	0.34	0.34	0.27	0.69	1.38	1.97

### 3.3. Annual exceedance probability of the limit states

The annual exceedance probability of three limit states of IO, LS, and CP was calculated for the structure before and after the rehabilitation and considering the uncertainties based on Eq. (11). In this equation,  $k_0$  and  $k$  are the seismic hazard parameters, which are considered  $3.03e-4$  and  $2.69$  for the Los Angeles region [47]. The results of the calculated annual exceedance probability are presented in Tables 7–8. The annual exceedance probability value was  $0.000064$ – $0.0021$  for rehabilitated structure with considered uncertainties, and it was lower than the value of moment frame equipped with brace [47].

Table 7. Annual exceedance probability of selected limit states under far-field records.

Case	Annual exceedance probability ( $P_{LS}$ )		
	IO	LS	CP
Base building	0.2109	0.00424	0.000913
Rehabilitated building	0.0016	0.00025	0.000082
Rehabilitated building with uncertainties	0.0021	0.00032	0.000099

**Table 8. Annual exceedance probability of selected limit states under near-field records.**

Case	Annual exceedance probability ( $P_{LS}$ )		
	IO	LS	CP
Base building	0.1524	0.00286	0.000557
Rehabilitated building	0.0011	0.00017	0.000048
Rehabilitated building with uncertainties	0.0013	0.00020	0.000064

As the Tables 7–8 show, the annual exceedance probability of three limit states was reduced with the rehabilitation of the structure. This shows that rehabilitation of the structure improved the seismic performance of the structure. In addition, the results of the Tables 7–8 show that the annual exceedance probability of the limit states of IO, LS, and CP increased by 31.2, 28 and 20.7 % under far-field records, and also this parameter increased by 18.2, 17.6 and 33.3 % under near-field records by considering the uncertainties in the rehabilitated structure. Comparing the results of the Tables 7–8 showed that reduction or growth in annual exceedance probability under far-field records was greater than near-field records. Based on the response spectrum of selected far-field records, this may be due to the greater impact of these records in the main period of the rehabilitated structure.

#### 4. Conclusions

In this paper, a 3-story structure of the SAC project was selected, verified in OpenSees software, and rehabilitated with a steel shear wall. The structure was analyzed with a base model and with selected records. The results of this case captured the uncertainty caused by various seismic records. In this paper, the trilinear force-deformation relationship was considered for the steel shear wall. Based on this relationship, four parameters of yield strength, elastic stiffness, strain hardening, and post-capping stiffness were considered as probabilistic variables, and probabilistic models of the structure were created. Both aleatory and epistemic uncertainties were considered taking into account probabilistic models of the structure and with performing incremental dynamic analysis.

1. Sensitivity analysis was done in order to investigate the effect of each considered probabilistic variable on the structural response. The results of the sensitivity analysis showed that the effect of the two parameters of the yield strength and elastic stiffness of the force-deformation relationship of the steel shear wall on the response of the rehabilitated structure with steel shear wall are greater (17.5 % and 19 % respectively), while the effect of the post-capping stiffness parameter is the lowest (6.1 %).

2. The results of the analysis showed that rehabilitation of the structure reduced the maximum inter-story drift of the structure in three limit states of Immediate Occupancy, Life Safety, and Collapse Prevention. Comparison of the IDA curves of the rehabilitated structure with and without considering the uncertainties demonstrated that the maximum inter-story drift of the structure increased by 24.1–52 % by means of considering the uncertainties. This shows that considering the uncertainties reduced conservatism.

3. The annual exceedance probability of three limit states of Immediate Occupancy, Life Safety, and Collapse Prevention was reduced by the rehabilitation of the structure. This showed that rehabilitation of the structure improved the seismic performance of the structure. In addition, the results showed that the annual exceedance probability of three considered limit states by considering uncertainties in the rehabilitated structure increased by 20.7–31.2 % under far-field and 17.6–33.3 % near-field records, respectively. The analysis results indicated that far-field records have more influence on the results due to the greater impact of far-field records in the main period of the rehabilitated structure.

#### References

- Hamburger, R.O. Development of next-generation performance-based earthquake engineering design criteria for buildings (ATC-58 project). In Structures Congress 2006: Structural Engineering and Public Safety, 2006. Pp. 1–8. DOI: 10.1061/40889(201)31
- FEMA445. Next-generation performance-based seismic design guidelines program plan for new and existing buildings. Redwood City, 2006.
- Siahos, G., Dritsos, S. Procedural assumption comparison for old buildings via pushover analysis including the ASCE 41 update. Earthquake Spectra. 2010. 26 (1). Pp. 187–208. DOI: 10.1193/1.3272266
- Acun, B., Sucuoglu, H. Performance of reinforced concrete columns designed for flexure under severe displacement cycles. ACI Structural. 2010. 107(3). P. 364.
- Acun, B., Sucuoglu, H. Evaluation of the performance limit states of reinforced concrete columns in view of experimental observations. Teknik Dergitechnical. 2011. 22(3). Pp. 5523–5541.
- Ricci, P., Verderame, G. M., Manfredi, G. ASCE/SEI 41 provisions on deformation capacity of older-type reinforced concrete columns with plain bars. Structural Engineering. 2012. 139 (12). P. 04013014. DOI: 10.1061/(ASCE)ST.1943-541X.0000701

7. Ditlevsen, O., Madsen, H.O. Structural reliability methods. New York: Wiley, 1996.
8. Hacking, I. The emergence of probability: A philosophical study of early ideas about probability, induction and statistical inference. Cambridge University Press, 2006.
9. Zareian, F., Krawinkler, H. Assessment of probability of collapse and design for collapse safety. *Earthquake Engineering and Structural Dynamics*. 2007. 36 (13). Pp. 1901–1914. DOI: 10.1002/eqe.702
10. Helmerich, R., Kühn, B., Nussbaumer, A. Assessment of existing steel structures, a guideline for estimation of the remaining fatigue life. *Structure and Infrastructure Engineering*. 2007. 3 (3). Pp. 245–255. DOI: 10.1080/15732470500365562
11. Shafei, B., Zareian, F., Lignos, D.G. A simplified method for collapse capacity assessment of moment-resisting frame and shear wall structural systems. *Engineering Structures*. 2011. 33 (4). Pp. 1107–1116. DOI: 10.1016/j.engstruct.2010.12.028
12. Torabian, S., Taghikhany, T. Assessment of seismic collapse uncertainties of steel moment resisting frames by means of single degree of freedom systems. *Proceedings of the Institution of Mechanical Engineers, Part O: Risk and Reliability*. 2014. 228(5). Pp. 504–517. DOI: 10.1177/1748006x14535760
13. Holicky, M., Retief, J.V., Sykora, M. Assessment of model uncertainties for structural resistance. *Probabilistic Engineering Mechanics*. 2016. 45. Pp. 188–197. DOI: 10.1016/j.probengmech.2015.09.008
14. Asgarian, B., Ordoubadi, B. Effects of structural uncertainties on seismic performance of steel moment resisting frames. *Constructional Steel Research*. 2016. 120. Pp. 132–142. DOI: 10.1016/j.jcsr.2015.12.031
15. Hajirasouliha, I., Pilakoutas, K., Mohammadi, R.K. Effects of uncertainties on seismic behavior of optimum designed braced steel frames. *Steel and Composite Structures*. 2016. 20 (2). Pp. 317–335. <http://dx.doi.org/10.12989/scs.2016.20.2.317>
16. Zhang, H., Shayan, S., Rasmussen, K.J., Ellingwood, B.R. System-based design of planar steel frames, I: Reliability framework. *Constructional Steel Research*. 2016. 123. Pp. 135–143. DOI: 10.1016/j.jcsr.2016.05.004
17. Dyanati, M., Huang, Q., Roke, D. Cost-benefit evaluation of self-centering concentrically braced frames considering uncertainties. *Structure and Infrastructure Engineering*. 2017. 13 (5). Pp. 537–553. DOI: 10.1080/15732479.2016.1173070
18. Jiang, L., Ye, J. Seismic risk assessment of a 2-storey steel-sheathed CFS building considering different sources of uncertainty. *Structures*. 2018. 16. Pp. 347–357. DOI: 10.1016/j.istruc.2018.10.010
19. Jiang, L., Ye, J. Quantifying the effects of various uncertainties on seismic risk assessment of CFS structures. *Bulletin of Earthquake Engineering*. 2020. 18. Pp. 241–272. DOI: 10.1007/s10518-019-00726-w
20. Piluso, V., Pisapia, A., Castaldo, P., Nistri, E. Probabilistic theory of plastic mechanism control for steel moment resisting frames. *Structural Safety*. 2019. 76. Pp. 95–107. DOI: 10.1016/j.strusafe.2018.08.003
21. Norouzi, A.H., Gerami, M. Quantifying response variability of steel moment frames due to seismic uncertainties. *Asian Journal of Civil Engineering*. 2019. 20 (4). Pp. 503–514. DOI: 10.1007/s42107-019-00115-3
22. Astroza, R., Alessandri, A., Conte, J.P. A dual adaptive filtering approach for nonlinear finite element model updating accounting for modeling uncertainty. *Mechanical Systems and Signal Processing*. 2019. 115. Pp. 782–800. DOI: 10.1016/j.ymssp.2018.06.014
23. Wijaya, H., Rajeev, P., Gad, E., Amirsardari, A. Effect of hysteretic steel damper uncertainty on seismic performance of steel buildings. *Journal of Constructional Steel Research*. 2019. 157. Pp. 46–58. DOI: 10.1016/j.jcsr.2019.02.016
24. FEMA P695. Quantification of building seismic performance factors. US Department of Homeland Security, Washington, 2009.
25. Gupta, A., Krawinkler, H. Seismic demands for the performance evaluation of steel moment resisting frame structures. Doctoral Dissertation. Stanford University, 1998.
26. McKenna, F. OpenSees: Open system for earthquake engineering simulation. Berkeley University of California, 2003. [www.opensees.berkeley.edu](http://www.opensees.berkeley.edu).
27. Thorburn, L.J., Montgomery, C.J., Kulak, G.L. Analysis of steel plate shear walls. Structural Engineering Report No. 107. Department of Civil Engineering, University of Alberta, Edmonton, Canada, 1983.
28. Timler, P.A., Kulak, G.L. Experimental study of steel plate shear walls. Structural Engineering Report No. 114. Department of Civil Engineering, University of Alberta, Edmonton, Canada, 1983.
29. CAN/CSA S16-09. Design of steel structures. Willowdale, Ontario, Canada, 2009.
30. ANSI/AISC 341. Seismic provisions for structural steel buildings. Chicago, Illinois, 2010.
31. Purba, R., Bruneau, M. Seismic performance of steel plate shear walls considering various design approaches. Technical Report MCEER-14-0005, 2014.
32. Structural Engineers Association of California. SEAOC blue book: Recommended lateral force requirements and commentary. Structural Engineers Association of California, Sacramento, 1999.
33. Davoodi, M., Sadjadi, M. Assessment of near-field and far-field strong ground motion effects on soil-structure SDOF system. *Civil Engineering*. 2015. 13 (3). Pp. 153–166. DOI: 10.22068/IJCE.13.3.153
34. Whittaker, A., Atkinson, G., Baker, J., Bray, J., Grant, D., Hamburger, R., Somerville, P. Selecting and scaling earthquake ground motions for performing response-history analyses (Grant/Contract Reports (NISTGCR)-11-917-15). US Department of Commerce, 2011.
35. Thoft-Christensen, P., Baker, M.J. Reliability of structural systems. *Structural Reliability Theory and Its Applications*. Springer, Berlin, Heidelberg, 1982. Pp. 113–127. DOI: 10.1007/978-3-642-68697-9
36. Rajeev, P., Tesfamariam, S. Seismic fragilities of non-ductile reinforced concrete frames with consideration of soil structure interaction. *Soil Dynamics and Earthquake Engineering*. 2012. 40. Pp. 78–86. DOI: 10.1016/j.soildyn.2012.04.008
37. Melchers, R.E. Structural reliability analysis and prediction. Wiley, New York, 1999.
38. JCSS, J. Probabilistic model code. Joint Committee on Structural Safety, 2001.
39. Schmidt, B.J., Bartlett, F.M. Review of resistance factor for steel: data collection. *Canadian Journal of Civil Engineering*. 2002. 29 (1). Pp. 98–108. DOI: 10.1139/I01-081
40. Dexter, R.J., Graeser, M., Saari, W.K., Pascoe, C., Gardner, C.A., Galambos, T.V. Structural shape material property survey. Final Report to Structural Shape Producer's Council. University of Minnesota, Minneapolis, USA, 2000.
41. Sadowski, A.J., Rotter, J.M. Solid or shell finite elements to model thick cylindrical tubes and shells under global bending. *Mechanical Sciences*. 2013. 74. Pp. 143–153. DOI: 10.1016/j.jimecsci.2013.05.008

42. Sadowski, A.J., Rotter, J.M., Reinke, T., Ummenhofer, T. Statistical analysis of the material properties of selected structural carbon steels. *Structural Safety*. 2015. Pp. 26–35. DOI: 10.1016/j.strusafe.2014.12.002.
43. Lignos, D. G., Krawinkler, H. Deterioration modeling of steel components in support of collapse prediction of steel moment frames under earthquake loading. *Structural Engineering (ASCE)*. 2011. 137. Pp. 1291–302. DOI: 10.1061/(ASCE)ST.1943-541X.0000376
44. FEMA 356. *Prestandard and commentary for the seismic rehabilitation of buildings*. US Department of Homeland Security, Washington, 2000.
45. Ellingwood, B.R., Kinali, K. Quantifying and communicating uncertainty in seismic risk assessment. *Structural Safety*. 2009. 31 (2). Pp. 179–187. DOI: 10.1016/j.strusafe.2008.06.001
46. Kinali, K., Ellingwood, B.R. Seismic fragility assessment of steel frames for consequence-based engineering: A case study for Memphis, TN. *Engineering Structures*. 2007. 29 (6). Pp. 1115–1127. DOI: 10.1016/j.engstruct.2006.08.017
47. Hossain, M.R., Ashraf, M., Padgett, J.E. Risk-based seismic performance assessment of yielding shear panel device. *Engineering Structures*. 2013. 56. Pp. 1570–1579. DOI: 10.1016/j.engstruct.2013.07.032

**Information about authors:**

**Mahdiye Maddahi, PhD**

E-mail: [m.maddah93@semnan.ac.ir](mailto:m.maddah93@semnan.ac.ir)

**Mohsen Gerami, PhD**

ORCID: <https://orcid.org/0000-0002-4113-932X>

E-mail: [mgerami@semnan.ac.ir](mailto:mgerami@semnan.ac.ir)

**Hosein Naderpour, PhD**

ORCID: <https://orcid.org/0000-0002-4179-7816>

E-mail: [naderpour@semnan.ac.ir](mailto:naderpour@semnan.ac.ir)

Received 04.03.2020. Approved after reviewing 28.09.2022. Accepted 21.11.2022.



Research article

UDC 666.97

DOI: 10.34910/MCE.117.2



## High-performance concrete produced with locally available materials

**B.I. Bulgakov** , **V.Q.D. Nguyen** , **A.V. Aleksandrova** , **O.A. Larsen** , **N.A. Galtseva** 

*Moscow State University of Civil Engineering (National Research University), Moscow, Russia*

 [fakultetst@mail.ru](mailto:fakultetst@mail.ru)

**Keywords:** superplasticizer, silica fume, sulfate-resisting Portland cement, silica flour, fly ash, high-performance concrete, strength and durability

**Abstract.** Vietnam is one of the countries most severely affected by climate change and sea level rise, especially in the south. High-performance concrete appears to be a better choice for strong and durable structures. The primary objective of this research was to use locally available materials to produce HPC reaching compression strength of over 100 MPa and suitable for Vietnamese climatic conditions and environment. The materials locally available in Vietnam used in the study included: sulfate-resisting Portland cement (PCSR40), crushed granite as coarse aggregate (size 9.5÷19 mm), river sand with fineness modulus of 3.0, Sika®Viscocrete®-151 type superplasticizer, mineral materials (class F fly ash and silica fume), and potable water. All concrete mixtures were designed according to TCVN 10306-2014 standard. For compressive strength, concrete samples were tested after 3, 7, 28, 56, and 450 days, while the tests for splitting tensile and flexural strengths, water absorption and permeability were conducted after 28 days. In this experimental research, the greatest compressive strength values obtained at 450 days of age were 95.426 MPa in a mix containing 10 %SF + 20 %FA + 20 %Qp and 101.597 MPa in a mix containing 12.5 %SF + 20 %FA + 20 %Qp. The results showed that the optimum high-performance concrete mixes used for construction in aggressive corrosive environment of Southern Vietnam contain 7.5 %SF + 30 %FA, 10 %SF + 20 %FA, 10 %SF + 30 %FA, 12.5 %SF + 20 %FA, respectively. This study showed that the HPC produced with locally available materials in Vietnam can have compressive strength exceeding 110 MPa as well as other excellent mechanical properties. All of this can be achieved simply by using materials available at the local markets, provided they are carefully selected and properly mixed to optimize grain size distribution.

**Citation:** Bulgakov, B.I., Nguyen, V.Q.D., Aleksandrova, A.V., Larsen, O.A., Galtseva, N.A. High-performance concrete produced with locally available materials. Magazine of Civil Engineering. 2023. Magazine of Civil Engineering. 117(1). Article no. 11702. DOI: 10.34910/MCE.117.2

### 1. Introduction

In the late 1980s, a number of countries launched major specific research programs on high-performance concrete (HPC), among which are the USA [1], Norway [2], Canada [3], France [4], Switzerland [5], Australia [6], Germany [7], Japan [8], Korea [9], China [10], Taiwan [11] etc. European and UK standards for HPC define HPC as “High workability concrete; Self-consolidating concrete (SCC); Foamed concrete; High strength concrete; Lightweight concrete; No-fines concrete; Pumped concrete; Sprayed concrete; Waterproof concrete; Autoclaved aerated concrete; Roller-compacted concrete” following ACI [12]. Russian documents do not provide such a classification. However, Professor Yu.M. Bazhenov considers the concrete to be high-quality if it meets the requirements high strength, durability, workability, and stability of the volume [13–15]. In recent years, HPC was used in the manufacture of elements of the tunnel under Bolshaya Dmitrovka street, tubes of the Lefortovskiy tunnel in Moscow, and

in the construction of multi-story centers "Moscow City", cooling towers working under the threat of acid, and even in the construction of load-bearing walls of a house [16–17] as well as a number of other transport and industrial construction projects. In Vietnam, HPC is a relatively new research topic, not much research has been published yet. Vietnam has begun to apply high-strength concrete with aggregate and conventional cement using superplasticizer, with water to cement ratio of about 0.35–0.40, with slump reaching 15–20 cm, kept at least 60 minutes, with compression strength of 50–70 MPa and early strength  $R_7 = 0.85R_{28}$ . This is the type of concrete used mainly in houses, bridges, roads, and irrigation structures in Vietnam. However, Vietnam is located in the wet-hot dry tropics with high chloride ion content. Long seacoast of more than 3200 km is immediately affected by climate change, rising sea water, sea water intrusion + chemical wastewater from industrial areas, which is one of the basic causes of the deterioration of the construction. The impact of the "sour" and "salty" environments leads to corrosion and destruction of the construction due to the quality of concrete that does not meet the requirements of corrosion resistance in aggressive corrosive environment as well. In order to solve this problem, HPC was designed with properties far superior to conventional concrete both on strength and durability, which helps extend the service life of concrete structures. For this reason, it is a perfect choice for constructions in harsh climatic and environmental conditions [18–20].

Ahmet Benli [21] studied the mechanical and durability properties of self-compacting mortars (SCM) by addition of fly ash (FA) and silica fume (SF) in concrete mixtures partially replacing cement at varying levels from 5 to 25 % by weight of FA and 5 %, 10 %, and 14 % by weight of SF. Results show that binary mixes of FA reduce strength when the content of FA increases. The binary mix with 10 % by weight of silica fume reaches the highest tensile strength of 10.5 MPa and compressive strengths of 81.5 MPa after 180-day curing. In that time, the mixture containing 5 % FA reached compressive strength of 84.3 and flexural strength of 10.21 MPa. On the other hand, the ternary mixes with 10 % by weight of FA and SF got 84.4 MPa for compressive strength and 10.09 MPa for tensile strengths.

Karthikeyan [22] researched strength and durability characteristics of HPC by changing metakaolin (MK) and silica fume content for the purpose of improving concrete mix and the life span of structures. The main parameter investigated in this study is designed concrete mix of the following composition: 0.63 t/m<sup>3</sup> cement + 1.15 t/m<sup>3</sup> coarse aggregate + 0.51 T/m<sup>3</sup> manufactured sand. The water/binder ratio adopted was 0.28 and superplasticizer "ViscoCrete 20 HE" dosage was fixed at 1 % of the binder mass, by which SF and MK were used individually to partially replace cement in the range of 0–15 %. The authors concluded that the optimum content of MK or SF used to partially replace cement stood at 15 %: at this level, the highest compressive strength attained was 85 MPa and 80.34 MPa for HPC(MK) and HPC(SF) specimens, respectively, which was higher compared to the other replacements.

Bilek et al. [23] conducted studies aimed at producing high-performance concrete with compressive strengths ranging from 120 to 170 MPa by using a ternary binder. Water/binder ratio was kept at a constant level of 0.225 for all mixes. The authors found an optimum composition of concrete mixture containing: 650 g Portland cement CEM I 42.5 R + 75 g metakaolin + 40 g fly ash + 35 g ground limestone + 20 g superplasticizer + 165 g water + 960 g sand + 40 g steel fibers with length of 13 mm & diameter of 0.20 mm. They achieved compressive strength of 140 MPa at the age of 28 days.

Ali Alsaman et al. [24], by using locally available materials like Portland cement (type I), steel fibers (0.02×12.7 mm), class F fly ash, chemical admixtures of polycarboxylate-based types, silica fume and river sand presented 3 different grain sizes as fine aggregate to study strength development of UHPC mixes. Their results proved that the mix containing total cementitious materials dosage at 1009 kg/m<sup>3</sup> had compressive strength at 155.2 MPa after 90-day curing without heat curing. When increasing the fly ash content to 20 %, compressive strength of the concrete achieved 152.1 MPa at the age of 90 days.

Ahmet Benli et al. [25] studied the influence of replacing cement with different dosages of FA type F and SF on rheological and mechanical properties, the freeze-thaw resistance in self-compacting mortars (SCM). The weight binder was kept at 640 kg/cm<sup>3</sup> for all mortar mixtures including replacement levels of fly ash at 25–40 % and of silica fume at 5–20 % by weight of cement, respectively, and water/binder ratio was between 0.43 and 0.50. The results proved that with SF or FA content increasing elastic modulus reduced, while the decrease in the elastic modulus of SCM containing SF was more dramatic than in SCM incorporating FA because of the deleterious effects of SF on freeze-thaw cycles. In addition, the SCM incorporating SF had compressive and flexural tensile strength higher than the control mixture and the SCM with FA at the curing age of 28 and 91 days.

Harpreet Singh et al. [26] studied concrete mix design using industrial by-products, for example, SF, FA to partially replace cement and fine aggregate at levels of 10, 15 and 20 %. Their research results showed that the optimal content of both admixtures in concrete mix was at 15 % and compressive/flexure/split tensile strength values were higher than those for ordinary concrete at the age of 28 days.

Hajek and Fiala [27, 28] studied the influence of HPC. Through the process of analysis and assessment, the authors observed that HPC is a construction material that has technology character necessary to concrete structures that need sustainability and high resilience under the impact of harsh environments, thereby extending the life of construction works and consequent social and economic improvements.

Mohamed and Najm [29] studied properties of self-consolidating concrete (SCC) by using industrial by-products, namely, ground granulated blast furnace slag (GGBS), SF, and FA to replace cement content up to 80 %, by weight of cement. The water-binder ratio adopted was 0.36 and cementitious materials content was approximately 480 kg/m<sup>3</sup>. Glenium Sky 504 superplasticizer was used and kept constant at 1.5 % of the total weight of cementitious materials, crushed granite was used as coarse aggregate of 14 mm size with a total amount of 800 kg/m<sup>3</sup>, fine aggregates consisted of 313.6 kg/m<sup>3</sup> dune sand and 582.4 kg/m<sup>3</sup> black sand for all 19 mixes; fly ash content was from 10 to 40 %, silica fume from 5 to 20 % or GGBS (10–80 %). The results showed that the SCC mix containing 20% fly ash had compression strength values of 67.9 MPa at 28 days, compared to 61.3, 56.5, and 55.8 MPa for 10 %, 30 %, and 40 % replacements, respectively. The mixture containing SF at 15 %, and FA at 20 %, had compressive strength higher by 44 % than control concrete at the age of 28 days. Furthermore, replacing cement with up to 40 % fly ash produced a competitive compressive strength high enough for many practical structural design applications. And 35 % is the optimum GGBS replacement ratio producing a high 28-day compressive strength of 81 MPa.

Chena et al. [30] attempted to produce HPC by using fly ash microspheres (FAM) and condensed silica fume (CSF). In their study, HPC was manufactured from the binary mixes of FAM and CSF by replacing ordinary Portland cement (OPC) with 20 %, and 40 % by weight of FAM and 10 %, 20 % by weight of CSF. The water to cementitious materials (w/cm) ratio ranged from 0.14 to 0.3. The results proved that the mix containing CSF = 20 %, when the w/cm ratio was 0.16, had the highest compressive strength of 159 MPa at the age of 28 days with flow spread = 80 mm. When the w/cm ratio was 0.3, then the compression strength was 105 MPa at the age of 28 days, with flow spread = 180 mm. The mix with FAM = 20 %, CSF = 10 %, when the w/cm ratio was 0.16, the compressive strength reached 135 MPa at the age of 28 days, flow spread = 113 mm. When the w/cm ratio was 0.3, then the compression strength reached 95 MPa at the age of 28 days, flow spread = 300 mm. From the results study we can conclude that the addition of CSF and FAM can significantly increase the packing density, consequently enhancing flowability and strength performance.

S.W. Yoo et al. [31] appraised autogenous shrinkage (AGS) in HPC with water-binder ratio of 0.3 with mineral admixtures of the following content: fly ash (0–30 %), silica fume (0–15 %), chemical admixture shrinkage reducing agent (0.5–1.0 %), and expansion agent (5–10 %). The autogenous shrinkage in HPC with FA was decreasing continuously with larger FA replacement. The AGS in HPC with SF was higher compared to that in ordinary Portland cement concrete. Use of both admixtures in adequate amount can lower autogenous shrinkage as well as improve the strength.

Elahi et al. [32] evaluated the mechanical and durability properties of HPC containing supplementary cementitious materials (SCM) such as SF, FA, and GGBFS, water to binder ratio constant was fixed at 0.3 in binary and ternary systems. In the experimental study, cement content was replaced with 70 % GGBFS, SF reached 15 %, and FA was up to 40 %. The ternary mixes containing FA or GGBFS with 50% replacement level and 7.5 % SF performed the best amongst all the mixes to resist the chloride diffusion. The replacement of 7.5 % SF performed better than other SCM for strength development. There was a benefit in the case of absorptivity with the addition of 50 % GGBS and 20 % FA compared to the control mix.

P.H Hanh et al. [33] used an experimental plan method to find the optimum proportion of the concrete mix based on preliminary proportioning according to ACI. The experiment results indicated that it is possible to make M100 grade HPC that suits marine environment by using available materials in Vietnam. It showed high impermeability (stable current of circuit 2.7–3.5 mA, destroyed time 41 days), high elastic modulus (6.5 MPa), high ability to steel adhesion (steel adhesion factor = 33.37), high strength development (60 MPa) at 3 days. Five categories of HPC namely Normal Strength Concrete (35 MPa), Medium Strength Concrete (56 MPa), High Strength Concrete (62 MPa), Very High Strength Concrete (98 MPa), Ultra High Strength Concrete (120 MPa) with slump value ranged from (100–200 mm) were designed by El Shikh [34].

Arunachalam et al. [35] performed experiments to make a comparative study on the properties of HPC with water to binder ratio of 0.28, fly ash (25 % and 50 % replacement) and without fly ash (control concrete) in the normal and aggressive environment (Al<sub>2</sub>SO<sub>4</sub> and NaCl). After time curing 28-day, concrete samples continue cured in an aggressive environment until the 60<sup>th</sup> day, compressive strength has been gone down about 25 % compared to strength at age 28-day. Meanwhile, test results indicate that HPC mixtures containing FA content at levels 25 %, and 50 % by weight of the cement, have a significant increase in compressive strength for both curing environments from 7 to 60 days. HPC utilizing fly ash and micro silica as cement replacing materials were investigated [36] to study permeation related properties

like permeability, porosity, and absorptivity with different curing conditions namely moist and air curing, at temperature 5 °C. Results proved above values reduced to mix containing low w/cm ratio, plus 10 % SF and FA replacement between range 15–20 %. Same permeability values were not achieved for specimens cured at 5 °C in comparison with moist and air curing.

Mohd Zain et al. [37] studied mechanical properties of HPC with four different type concrete mixtures with GGBS, SF and FA at 25 % water to binder ratios. Mineral admixtures partially replaced cement at levels of 10–50 %. The authors concluded that the mix consist of 10 % SF achieved compressive strength values of 130 MPa and  $5.28 \times 10^4$  MPa of modulus of elasticity, at age 91-day when specimens cured in water at a temperature of 20 °C or wrapped by wet burlaps at temperature of 35 °C. These values were higher than compared to other mixes in the same curing conditions. This showed that the SF can influence concrete's performance, it as a filler leads to porosity reducer in concrete's microstructures.

Tamimi, A.K. [38] studied the influence of HPC mix in HCl and H<sub>2</sub>SO<sub>4</sub> environments. Control mix contained 400 kg of ordinary Portland cement, aggregates with max size 15 mm, melamine superplasticizer and had the water/binder ratio at 0.35 and 0.4. The author used 10 % silica fume and various percentages (40, 60, and 80 %) of pulverized FA to partially replace cement content. The results indicate that the mix containing 10 % SF combined with 60 % pulverized fly ash and 30 % OPC would produce optimum protection against acid attacks, which was proven through experiments in the acidic environment (with 1 % HCl and H<sub>2</sub>SO<sub>4</sub> content), at 20 °C temperature.

Vietnam is one of the countries most severely affected by climate change and sea level rise, especially in the southern part [39–43]. To solve this problem, high-performance concrete appears to be a better choice for a strong and durable structure. Therefore, the primary objective of this research is to produce HPC with compression strength of over 100 MPa suiting Vietnam climatic conditions and environment by means of using locally available materials.

## 2. Methods and Materials

In this study, the physico-mechanical properties of concrete are determined through the change in compressive strength and loss of weight of the concrete samples immersed in three environments after a period of 450 days. (1) The saline-alkaline medium was chosen to soak experimental samples in Hung Thanh of Dong Thap province: it characterizes the environment in the Mekong River Delta region (Southern Vietnam); (2) Seawater environment used to cure the concrete samples is from Chan May Port in Thua Thien – Hue Province (South Central Coast – Central Vietnam); (3) and potable water used to cure control concrete is the control environment. The chemical composition of the sample immersion environments is shown in Table 1 and 2.

**Table 1. The composition of the main ions in source of water used for concrete sample curing.**

Source of water	pH	SO <sub>4</sub> <sup>2-</sup> (mg/l)	Cl <sup>-</sup> (mg/l)	Mg <sup>2+</sup> (mg/l)	Ca <sup>2+</sup> (mg/l)
Potable water	6.53	103	182		
Saline-alkaline environment	4.43	490	97.2	696	560
Seawater	7.8 – 8.4	(1.4÷2.5)×10 <sup>3</sup>	(6.5÷18.0)×10 <sup>3</sup>	(0.2÷1.2)×10 <sup>3</sup>	

**Table 2. The pH value and the salt content (g/l) of saline-alkaline medium experimental samples were soaked in.**

Months	1	2	3	4	5	6	7	8	9	10	11	12	Aver. value
pH	5.08	5.02	4.56	4.10	3.52	3.12	3.13	3.46	3.96	5.22	6.2	6.05	4.43
Salt content	25.9	25.5	24.3	23.3	22.3	22.0	22.2	23.7	25.2	25.6	26.1	27.0	24.43

The material types like cement, aggregates, mineral materials etc., used in the mix before, underwent preliminarily physical and chemical analyses to determine whether they are in compliance with the standard used. A total of 15 different mixes with concrete grades higher or equal to M80 were designed, in compliance with Vietnamese Standard TCVN 10306-2014 “High strength concrete-proportional design with cylinder sample”, and their properties, such as workability, as well as strength and durability, were tested. The total dosage of cementitious materials was fixed at 550 kg/m<sup>3</sup>. Similarly, the dose of aggregates, chemical admixture, and w/cm ratio were fixed in all the mixes. Substituted mineral materials like silica fume with content selected as (0 %, 5 %, 7.5 %, 10 %, 12.5 %) were combined with class F fly ash at content levels (0 %, 20 %, 30 %, 40 %) to partially replace sulfate-resistant cement by weight in the mixes. Compressive strength was tested using 15 cm<sup>3</sup> cube samples; tensile strength as well as modulus of elasticity, were tested using cylindrical samples (d×h=15×30 cm); 15×15 cm cylinders and 10×10×40 cm prisms were utilized to test permeability/water absorption and flexural strength, respectively.

Here is the list of other materials used to design the HPC mixtures:

1. Cement PC<sub>SR</sub>40 (type 5) of Luks Cement (Vietnam) Limited is sulfate-resistant Portland cement with the following parameters: compressive strength at 3 days 25.7 MPa and 28 days 46.5 MPa; time of initial setting 130 min, and final setting 175 min; C<sub>3</sub>A content 2.49 % and C<sub>4</sub>AF+2C<sub>3</sub>A content 21.23 %; specific gravity 3.15 g/cm<sup>3</sup>; sulfate resistance at 14 days expansion 0.0156 %. Other components are presented in Table 3. The type of the cement used complied Vietnamese Standard TCVN 7711-2013 "Sulfate resistant blended Portland cements".

2. Crushed aggregate with maximum size of 19 mm (60 %) and 9.5 mm (40 %) from a local source (Ga Loi stone-pit in Central region of Vietnam) was used as coarse aggregate with the following parameters: specific gravity 2.68 g/cm<sup>3</sup>, volume of coarse aggregates 2.63 g/cm<sup>3</sup>, water absorption 0.5 %, fineness modulus about 6.5÷6.8, and average strength 105.593 MPa.

3. Natural sand exploited from Huong river, Vietnam, with fineness modulus of 3.0, specific gravity of (2.6–2.65) g/cm<sup>3</sup>, moisture of 1 %, was used as fine aggregate in compliance with Vietnamese Standard TCVN 7570-2006 "Aggregates for concrete and mortar – Specifications".

4. Water used to mix and cure the concrete complied Vietnamese Standard TCVN 4506-2012 "Water for concrete and mortar - Technical specification".

5. The chemical plasticizing admixture used was Poly-Carboxylic Ether Sika®ViscoCrete®-151, which is brown in color with specific gravity of 1.075–1.095 kg/l. Its recommended dosage for 1 kg of cement is 0.018 l, which is used for effective workability in accordance with Vietnamese Standard TCVN 8826-2011/2 "Chemical admixtures for concrete" (ASTM C494 Type G).

6. Fly ash, available as a byproduct of the thermal power plants Pha Lai (Vietnam), was used in dry powder form. Class F fly ash was supplied and rounded to angular shape. It had low CaO content and exhibited Pozzolonic properties in accordance with Vietnamese Standard TCVN 10302-2014 "Activity admixture - Fly ash for concrete, mortar and cement".

7. Silica Fume is being used increasingly as a supplementary cementing material for concrete. Admixture in dry densified form obtained from Sikacrete® PP1 – Sika limited Vietnam has particle size < 0.1 μm and specific gravity approximately 2.15 g/cm<sup>3</sup> in accordance with Vietnamese Standard TCVN 8827-2011 "Highly activity puzzolanic admixtures for concrete and mortar - Silicafume and rice husk ash".

8. Quartz sand powder used in this study has specific gravity 2.56 g/cm<sup>3</sup>, has a form of white powder with particles size ranging from 5 to 10 μm partially replacing fine aggregate. Quartz powder is milled from local silica white sand in the Central region of Vietnam.

Table 3 gives the physicochemical composition of material types used in the mix.

**Table 3. The physicochemical composition of material types used in the mix.**

Compositions	Cement PC <sub>SR</sub> 40	Fly ash	Silica Fume	Quartz powder
<i>Chemical constituent (%)</i>				
CaO	62.10	0.70	0.31	0.051
SiO <sub>2</sub>	20.59	57.42	92.49	99.72
Al <sub>2</sub> O <sub>3</sub>	3.82	24.07	0.868	0.0429
Fe <sub>2</sub> O <sub>3</sub>	5.10	6.10	1.90	0.039
SO <sub>3</sub>	2.05	0.30	0.3	–
BaO	1.89	–	–	–
MgO	1.701	0.951	0.841	0.0369
MnO	1.249	2.622	0.141	–
K <sub>2</sub> O	0.630	3.612	1.231	0.0059
Na <sub>2</sub> O	0.135	0.27	0.38	0.020
TiO <sub>2</sub>	0.12	0.70	–	0.044
Loss of ignition	1.07	5.74	1.68	0.042
<i>Physical properties</i>				
Specific gravity	3.15	2.34	2.15	–
Blaine's fineness, cm <sup>2</sup> /g	3350	3728	16028	–
Fineness (90-μm sieve)	0.7	–	–	–
Bulk density (kg/l)	–	2.19-2.56	0.50-0.70	–

The HPC was produced by mixing the designed mix proportions of cement, FA, SF, Qp, SP, and water together following the existing mix design methods with a standard mixer complying with Vietnamese Standard TCVN 10306:2014 "High strength concrete-proportional design with cylinder sample" and

conforming to ACI 211.1-91 “Standard Practice for Selecting Proportions for Normal Heavyweight, and Mass Concrete”, Russian Code Design SP 28.13330.2017 “Protection against corrosion of construction”, Interstate Standard GOST 26633-2015. To start with the experiments, a control mix with target strength of 80 MPa and slump of 50±100 mm was obtained without addition of any mineral admixtures and also with no Qp content. Mix proportions for 1 m<sup>3</sup> HPC mix consisted of total dosage binder 550 kg/m<sup>3</sup> + 1088 kg/m<sup>3</sup> coarse aggregate + 621.7 kg/m<sup>3</sup> fine aggregate + 156 l/m<sup>3</sup> water + 9.9 l/m<sup>3</sup> superplasticizer (similar to 1.8 % by mass of binder), entrapped air is 2 %, and w/b ratio is fixed at 0.3, while sand was partially replaced by 20 % quartz sand flour: these parameters remained fixed for different 15 mixes. The total dose of mineral substitutes for cement is represented by the (SF)<sub>α</sub>(FA)<sub>β</sub> formula, where α and β are the percentages of SF and FA, respectively, to replace cement in the mixture. The authors proposed mix combinations categorized into four SF replacement levels (5 %, 7.5 %, 10.5 %, and 12.5 %) and three FA replacement levels (20 %, 30 %, and 40 %). In each of the SF series, the FA content was set at 20 %, 30 % and 40 %, as shown in Table 4.

First, the dry materials (cement, SF, FA, fine and coarse aggregates, quartz sand powder) were blended for 2–3 min inside a plastic bag in dry form. Secondly, water containing the plasticizer was added and blended for another 4–5 min. After 6–8 min in the mixer or until concrete mix achieved the homogeneous and uniform consistency, during mixing, temperature varied following ambient temperature from 28–39 °C. The slump of the fresh concrete mixes was determined by Abrams cone (d×D×H = 100×200×300 mm) according to Vietnamese Standard TCVN 3016-1993 “Heavyweight concrete compounds – Slump test” and Interstate Standard GOST 10181-2014 “Concrete mixtures. Methods of testing”. After that, the concrete mixes were put into different casting molds of cubes/cylinders/prisms specimens and preserved at room temperatures around 30±2 °C until 24 hours. Then the specimens were stripped from molds and transferred to a fresh-water tank for curing until the time of testing. The specimens strength was tested after 3d, 7d, 28d, and 56-day curing. Vietnamese Standard TCVN 10303-2014 “Concrete - Control and assessment of compressive strength” was used to test compressive strength, while Vietnamese Standard TCVN 3119-1993 “Concrete-Method for determination of flex. Tensile strength” was used for flexural/tensile strength tests according to Interstate Standard GOST 18105-2018 “Concretes. Rules for control and assessment of strength”. Concrete strength testing machines (Matest model C089-17N (3000 kN) and TYPE-2000) were used for strength tests. The loading rates applied in the compressive and tensile splitting strength tests were 10 kN/s and 1.6 kN/s, respectively. All experiments on mechanical properties and durability characteristics of concrete were performed in laboratory LAS-XD 578, which is a synthetic laboratory for testing building materials and construction quality in central Vietnam directly under Vietnam Institute for building science and technology (IBST Vietnam). Table 5 shows the number of specimens cast and the testing arrangement.

### 3. Results and Discussion

There are numerous benefits in incorporating SCM into HPC mix design, including an improvement in workability of fresh concrete, reducing/eliminating free lime content, decreasing the C/S ratio of C-S-H in hardened cement pastes, mitigating alkali-aggregate reactions, etc. The products resulting from the reactions between lime and SCM refine the pore structure and reduce the permeability of hardened pastes.

Table 5 represents the required range of slump values within 105–270 mm. In theory, the addition of mineral admixtures (MA) finer than cement to fill into the voids between the cement grains and the addition of another even finer MA to fill into the voids between the larger particles should be able to reduce the voids to a greater extent than it is possible with the addition of just one MA. It is caused by the fact that the added fillers which are more finely-powdered than cement particles may be inert. It means that on the one hand they do not have chemical reactivity and in this case act as an additive that seals the structure of concrete hardened cement paste, on the other hand they may be active and participate in pozzolanic reactions, producing more C-S-H gel to form the structure of hardened concrete [43]. As usual FA particles which are spherical in shape and more finely-powdered than the particles of used Portland cement can fill the voids between its grains, while more dispersed SF particles < 0.1 μm in size can fill the voids between the particles of FA and cement. Such subsequent filling of voids will boost the hardened cement paste density by optimizing of density packaging of finely-powdered particles in its structure. In addition, finely-powdered mineral additives, in particular fly ash, may have a plasticizing effect, increasing the workability of the concrete mixture [44]. Due to the spherical shape of the fly ash particles, they have the effect of ball bearings. As a result, good conditions for increasing the mobility of neighboring particles in the concrete mixture are formed. Portland cement in the binder composition can be partially replaced by fly ash, which is cost-effective [45-47]. The quartz sand powder particles will fill the voids between the grains of aggregates. It will create the most optimal density packaging for the microstructure of the Portland cement - SF - FA - quartz powder filler matrix.

**Table 4. Mix proportions of 1 m<sup>3</sup> concrete.**

Mix No.	Supplementary cementitious materials, kg/m <sup>3</sup>					Aggregates, kg/m <sup>3</sup>						Water liter	Super plasticizer		(W+SP)/B W/B	Slump mm	Material cost USD
	Cement PC <sub>CR40</sub>	Silica fume		Fly ash		Coarse aggregate		Fine aggregate		Quartz sand powder			%	liter			
	kg	%	kg	%	kg	kg	C/F	kg	%	5µm	10µm						
M1	550	-	-	-	-	11088	1.75	621.7	-	-	-	156	1.8	9.9	0.3	105	75.26
M2	550	-	-	-	-	1088	1.75	497.4	20	62.2	62.2	156	1.8	9.9	0.3	185	77.21
M3	412.5	5.0	27.5	20	110	1088	1.75	621.7	0	0	0	156	1.8	9.9	0.3	245	82.91
M4	412.5	5.0	27.5	20	110	1088	1.75	497.4	20	62.2	62.2	152	1.8	9.9	0.3	220	83.96
M5	357.5	5.0	27.5	30	165	1088	1.75	497.4	20	62.2	62.2	156	1.8	9.9	0.3	260	81.21
M6	302.5	5.0	27.5	40	220	1088	1.75	497.4	20	62.2	62.2	156	1.8	9.9	0.3	265	78.46
M7	398.8	7.5	41.3	20	110	1088	1.75	497.4	20	62.2	62.2	156	1.8	9.9	0.3	260	90.08
M8	343.8	7.5	41.3	30	165	1088	1.75	497.4	20	62.2	62.2	156	1.8	9.9	0.3	260	87.33
M9	288.8	7.5	41.3	40	220	1088	1.75	497.4	20	62.2	62.2	156	1.8	9.9	0.3	265	84.58
M10	385	10	55	20	110	1088	1.75	497.4	20	62.2	62.2	156	1.8	9.9	0.3	245	96.20
M11	330	10	55	30	165	1088	1.75	497.4	20	62.2	62.2	156	1.8	9.9	0.3	265	93.45
M12	275	10	55	40	220	1088	1.75	497.4	20	62.2	62.2	156	1.8	9.9	0.3	270	90.71
M13	371.3	12.5	68.8	20	110	1088	1.75	497.4	10	62.2	62.2	156	1.8	9.9	0.3	240	102.32
M14	316.3	12.5	68.8	30	165	1088	1.75	497.4	10	62.2	62.2	156	1.8	9.9	0.3	230	99.57
M15	261.3	12.5	68.8	40	220	1088	1.75	497.4	10	62.2	62.2	156	1.8	9.9	0.3	265	96.823

**Table 5. Test results of mechanical properties for varying mineral admixtures replacement levels in high-performance concrete.**

Mix No.	Compressive strength and weight of concrete cured in corrosive medium, MPa											Splitting tensile strength, MPa	Flexural strength, MPa
	Compressive strength of concrete cured in freshwater environment, MPa				Seawater environment								
	3 days	7 days	28 days	450 days	450 days	Str. loss (%)	450 days	Str. loss (%)	$M_1^{28}$ (g)	$M_2^{450}$ (g)	Mass loss (%)		
M1	67.6	71.1	83.6	86.4	86.4	0.4	82.6	8.1	8320	8145	2.1	5.70	7.85
M2	72.6	82.6	89.3	95.1	94.3	0.8	93.8	1.3	8310	8299	0.1	5.99	9.16
M3	41.3	62.2	65.3	67.3	65.7	2.4	61.0	9.4	8330	8159	2.1	4.86	7.84
M4	52.4	76.0	81.8	92.8	92.1	0.8	91.3	1.6	8100	8085	0.2	5.70	8.77
M5	67.3	73.0	80.2	86.5	85.8	0.8	84.4	2.4	8238	8225	0.2	5.60	8.32
M6	56.7	61.0	70.8	78.1	75.9	2.8	74.4	4.7	8120	8096	0.3	5.13	8.16
M7	60.0	81.0	89.5	94.2	93.0	1.2	92.4	1.9	8125	8115	0.1	6.0	9.17
M8	69.3	75.0	84.0	88.4	88.1	0.4	88.0	0.5	8105	8096	0.1	5.66	8.85
M9	59.1	66.7	74.8	84.2	83.3	1.0	82.5	1.9	8050	8028	0.3	5.32	8.39
M10	62.2	81.9	87.9	95.4	94.9	0.5	94.0	1.5	8150	8125	0.3	5.93	9.10
M11	63.9	67.5	88.8	92.6	91.6	1.1	91.4	1.3	8105	8078	0.3	6.06	9.34
M12	65.3	72.4	85.9	91.6	82.9	2.6	79.7	6.4	8090	8046	0.5	6.08	9.26
M13	59.0	83.8	91.2	101.6	101.1	0.5	101.0	0.6	8143	8112	0.4	6.18	9.37
M14	72.2	76.1	84.2	92.6	87.5	0.9	86.1	2.4	8075	8059	0.2	5.76	8.90
M15	56.4	57.3	76.1	88.0	84.9	0.1	83.1	2.3	8030	7990	0.5	5.39	8.46

Note:  $M_1^{28}$  (g) is weight of sample concrete at 28 days of age, 24 h after removing from the mold and cured in freshwater tank at temperatures varying in the ambient range of 28–39 °C; and  $M_2^{450}$  (g) is weight of sample concrete at 450 days of age after the sample was removed from the freshwater tank and soaked in saline-alkaline medium at temperatures varying in the ambient range of 28–39 °C.

Then, we compared the properties of the prepared HPC samples with various cement content replaced by FA and SF as in Table 5. It can be noticed that, regarding mechanical strength, the samples completely satisfied quality requirements, except for M1 mixes only. Mutual differences in mechanical strength and permeability coefficient of HPC mixtures probably originate from the physical and chemical properties of the applied fillers, since the other components were the same in all samples.

Table 5 gives information on the properties of concrete mixtures containing 20 % quartz powder and binder content of 550 kg/m<sup>3</sup> including triple blending cement with two supplementary cementitious materials of SF and FA in different proportions. Table 5 shows mechanical properties gradually increasing according to curing time: the lowest value was achieved in the test at 3-day age, followed by slow augmentation from 7<sup>th</sup> to 28<sup>th</sup> day, a sharp increase starting from the 28<sup>th</sup> day in all samples, and then resulting in a gradual increase at later ages. The impact of quartz sand powder dosage on the mechanical properties of different HPC mixtures is illustrated in Fig. 1 and Fig. 3.

The average values of compressive strength for HPC mixtures obtained from 3 test samples of the same curing age are provided in Table 5. A comparison of the specimens from M2 to M13 and control mix specimen M0 under different curing periods and conditions is presented in Fig. 1. The compressive strength results at the age of 28 days range between 70.8–91.2 MPa and the 450-days strength of all mixes was in the range of 78.1–101.6 MPa.

At the age of 3 days, the specimen M2 had the lowest value of 52.44 MPa, while sample M5 reached the highest strength at 101.6 MPa after 450 days of curing, increasing it by 48.4 % since day 3. This indicates that the strength improved gradually with the time of curing, which is due to C-H-S gel being continuously supplemented through pozzolanic reactions. At the age of 28 days, the HPC mixtures M3, M4, M7, M9, and M5 obtained the highest values of compressive strengths among the remaining samples. The bar chart in Fig. 1 illustrates that the compressive strength of almost all samples beside control mix M0 (containing no additional materials) was low at the age of 3 days. It is interesting to see that the compressive strength of HPC with higher replacement of cement (about 40–42.5 %), such as in specimens M7 and M12, was higher than that of the control mix M0. The results displayed in Fig. 1 indicate that almost all specimens were developing compressive strength slower than the control mix. The reason is that the pozzolan reaction in concrete mixtures occurs slowly, fly-ash concrete achieves significant improvement in its mechanical properties at later ages, the samples react to makes a denser form of C-S-H gel:  $m\text{Ca}(\text{OH})_2 + n\text{SiO}_2 + p\text{H}_2\text{O} \rightarrow m\text{CaO} \cdot n\text{SiO}_2 \cdot (m+p)\text{H}_2\text{O}$ . After 7 days of curing, the compressive strength for the samples M5, M4, M3, M2, M12, M7, M6, and M10, with replacement levels at 20–30 % for fly ash and 5–2.5 % for SF, achieved strength values superior (by 2.5–18 %) to those of control mix M0 (71.101 MPa). On the other hand, samples M11, M7, M9, and M13 with 40 % fly ash and SF in the range between 5 and 12.5 % obtained compressive strength similar to the previous findings [48–49]. As seen in Fig. 1, there is a slight increase in the compressive strength of concrete mortars kept in water after 28 days of curing concretes when using 20 % fly ash incorporated with different replacement levels of SF from 5 to 12.5 % corresponding to samples M2, M3, M4, M5. Increasing fly ash content in the mixture up to 30 % in combination with SF replacement rates of 5–12.5 %, which corresponds to mixtures M10, M6, M7, and M12, showed compressive strength higher than or similar to control mix M0. On the contrary, however, the addition of up to 40 % FA to the mixture containing SF with different replacement rates (5–12.5 %), indicated a downward trend for strength in samples M11, M8, M9, and M13. Notice that there's only one mix (sample M9) that obtained strength higher than the control mix without any additional materials (M0). This demonstrates that the action of micro fillers as well as an increase in the pozzolans reaction of SF and FA particles still do not offset the dilution effect in adhesive cement at the age of 28 days.

The diagram in Fig. 3 shows the average flexural strength of different HPC mixes after 28-day curing. The control mix had a flexural strength of 8.8 MPa, while the group of samples M3, M4, M7, M9, and M5 modified by the industrial by-product waste materials had flexural strength values higher than that of the control mixture by up to 3.4–5.2 %. Besides, the remaining specimens also had the flexural strength value approximately equal to the control mix. The addition of same materials improved the interface characteristics between the bonding layer and aggregate, leading to increased interface adhesion, and hence ameliorating the bending resistance of the concrete. On the other hand, Fig. 3 shows that the splitting tensile strength values obtained were up to 7.4 % greater than the control mix in the mixtures using a combination of 10 % SF plus 30–40 % FA or 20 % FA plus 7.5/12.5 % SF. Conversely, some mixtures showed a drop in tensile strength (about 6.1 %) at the age of 28 days compared with the control mix, as for example, in mixtures with silica fume at levels of 5–12.5 % combined with 40 % content of fly ash partially replacing cement in the mixture.

The results of mass loss and compressive strength for concrete samples during the immersion period of 14 months in marine and saline-alkaline media are summarized in Table 5, as well as in Fig. 2. Based on the data obtained, simultaneous examination of the surface of the experimental samples as shown in

Fig. 4 indicated that the surface of the samples began to show signs of corrosion, e. g., fine aggregate emerging, discoloration, salt agglomeration; marine creatures sticking, etc.

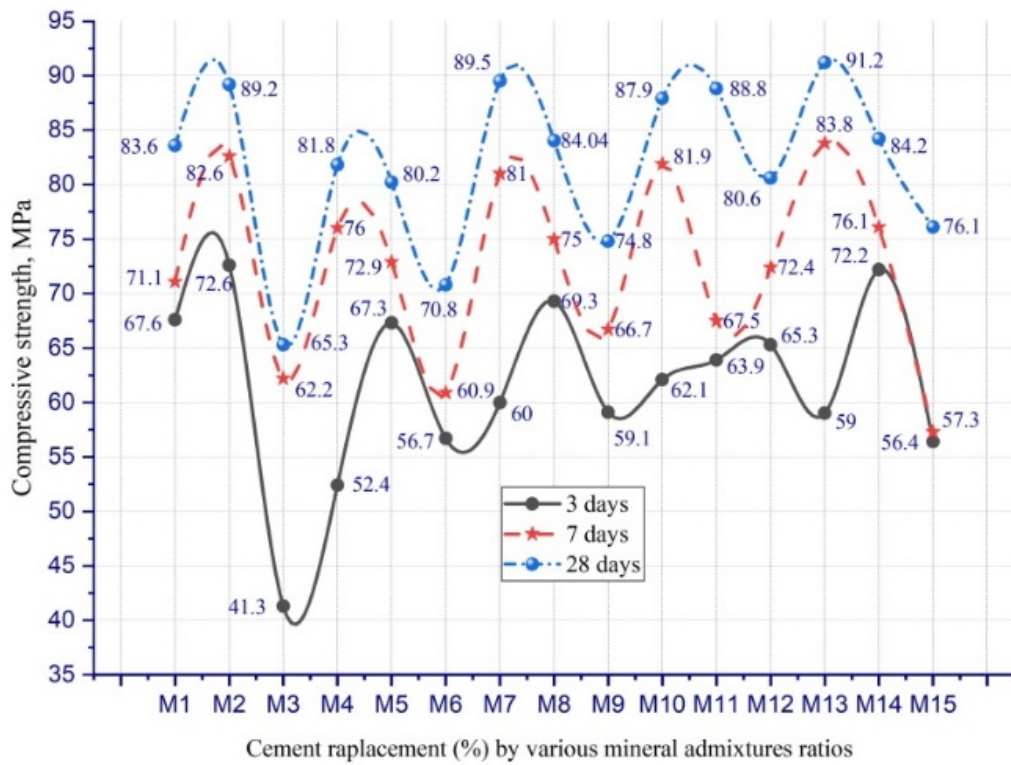


Figure 1. Compressive strength of HPC mixtures at different ages.

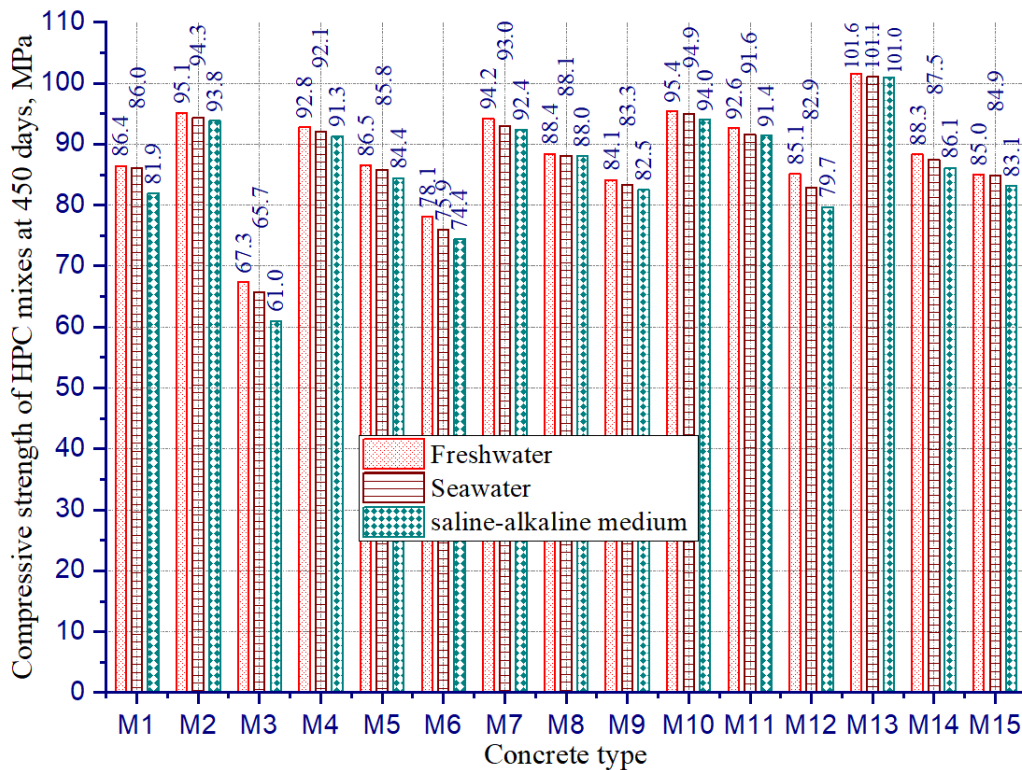
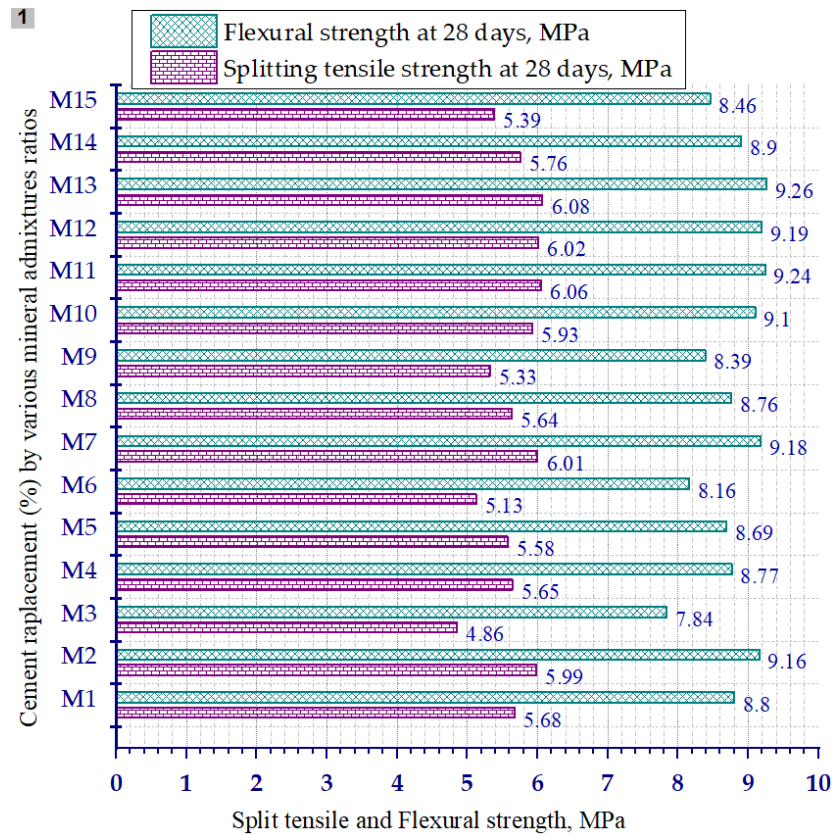


Figure 2. Compressive strength of HPC mixtures at 450 days in different environments.



**Figure 3. Flexural, splitting tensile strength of HPC mix at 28 days.**

The PC<sub>SR40</sub> sample (M0) in the saline-alkaline medium after 450 days exhibited strong damage followed by high mass loss of about 2.1 % and compressive strength loss at 5.1 %, which was higher than in seawater environment (strength loss 0.4 %). Sample M1 showed similar compressive strength loss at 9.4 % and degradation of physical-mechanical properties, so further investigation was stopped. Cement content of 45–52.5 % replaced by 40 % fly ash and from 5 to 12.5 % SF in samples M11, M7, M9, and M13 showed compressive strength loss at 1.9–6.4 % and mass loss of about 0.3–0.5 %. In contrast, cement content of 25–32.5 % replaced by 20 % fly ash and from 5 to 12.5 % SF in samples M2, M3, M4, and M5 showed compressive strength loss at 0.6–1.9 % and mass loss of about 0.1–0.4 %. At the same time, cement content of 35–42.5 % replaced by 30 % fly ash and from 5 to 12.5 % SF in samples M10, M6, M7, and M12 showed compressive strength loss at 0.5–2.4 % and mass loss of about 0.1–0.3 %. All these mixtures demonstrated that weight loss, as well as strength, are much higher than in the seawater environment. We could conclude that during this period, different corrosion resistance in seawater and saline-alkaline media is obviously the consequence of the applied FA, SF, and Qp fillers. The samples corroded in varying degrees depending on different percentages of active mineral admixture ratios used to replace the cement content in concrete.

Based on the results of the analysis of environmental composition, the results of the evaluation of the corrosive process products, the authors found that concrete in saline-alkaline medium was corroded by acid corrosion mechanism in the most basic corrosion form.

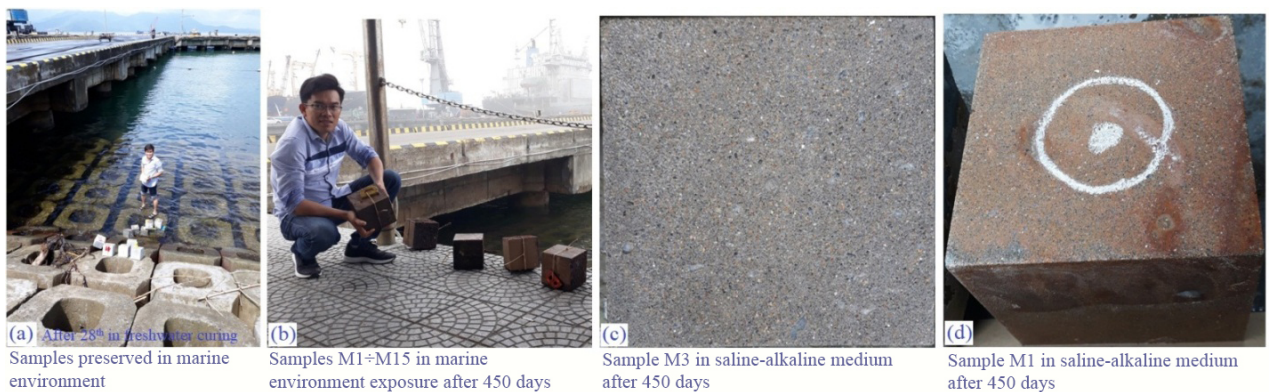


**Figure 4. Effect of curing methods: (a, b) seawater curing and (c, d) saline-alkaline curing.**

Permeability is a measure of the ease with which the substances are transported due to a pressure differential, while absorptivity and absorption-to-porosity are measures of the absorption characteristics of concrete. The permeability of concrete is a function of the w/b ratios, aggregates particles size, pore size, and its distribution in the mix. The permeability of hardened cement paste greatly affects the durability of concrete and in turn, is strongly affected by the pore structure. The pore structure is formed during the hydration process. The void spaces between the cement particles start to fill up with hydration products. The w/b ratio and the degree of hydration determine the total capillary porosity. In general, the capillary porosity rises or drops as the w/b ratio rises or reduces. In addition, adding a supplementary cementitious material finer than cement such as FA and SF (incorporated with a reasonable dosage of superplasticizer) to fill into the voids can significantly increase the packing density of the cementitious materials leading to low permeability of the concrete. Therefore, blending Portland cement with pozzolanic materials has become an increasingly accepted practice in the construction of structures exposed to harsh environments such as offshore structures, highway bridges, tunnels, sewage pipes, and structures for wastes containing toxic chemicals and radioactive elements. According to TCVN 3116- 2007<sup>[14]</sup>, cylindrical samples are used to check the water permeability, correspondent to GOST 12730.5-2018<sup>[15]</sup>. As expected, water permeability values decreased (i.e., the concrete became more impervious) with increasing age due to the improvement on concrete microstructure, resulting from the increased amount of the C-S-H phase.

**Table 6. Water permeability and water absorption of concrete at the 28<sup>th</sup> day**

Mix N <sup>o</sup>	M1	M2	M3	M4	M5	M6	M7	M8	M9	M10	M11	M12	M13	M14	M15
Water permeability, $K_t \cdot 10^{-11}$ cm/sec	1.60	1.18	3.16	1.21	1.33	2.6	1.13	1.21	1.98	1.1	1.03	1.09	1.01	1.08	1.63
Concrete grades for watertightness	W16 – W20														
Water absorption in 24 hours, %	2.50	2.39	3.23	2.52	2.57	3.01	2.38	2.53	2.86	2.43	2.19	2.33	2.03	2.54	2.82

An economic analysis was carried out for all the mixes. The unit price includes the costs of all ingredients necessary for producing the HPC mixtures, excluding the transportation costs. For this, the material prices used were as follows: Cement PC<sub>SR</sub>40 – 1.66 vnd/kg ; Silica Fume Sikacrete<sup>®</sup> PP1 – 12.00 vnd/kg, 86 % higher unit price than the cement; class F fly ash – 500.00 vnd/ton, 69 % lower unit price than the cement; coarse aggregate – 320.00 vnd/m<sup>3</sup>; fine aggregate – 400.00 vnd/m<sup>3</sup>; quartz powder – 600.00 vnd/ton; potable water – 16.72 vnd/m<sup>3</sup>; and Sika<sup>®</sup>ViscoCrete<sup>®</sup>151 – 44.00 vnd/l. The exchange rate was 1USD = 23.23 VND. The material cost of the concrete per cubic meter for each mix are presented in Table 4. These costs apply to locally available materials in Thua Thien Hue province, Vietnam, in 2019. It can be noted from the figures in Table 4 that the control mix has the lowest price, but as the SF content added was gradually rising, so were the prices of the concrete. Among the samples that have the compression strength greater than or equal to the control mixture (86.5 MPa after 450 days), sample M5 (12.5 % SF + 20 % FA) mix had the maximum strength attained (101.6 MPa), while also having the highest material price (103.04 \$/m<sup>3</sup>). The average cost per strength was 0.87 \$/m<sup>3</sup>/MPa for the control mixture; 0.91 \$/m<sup>3</sup>/MPa corresponds to M1 mixture; 0.96 \$/m<sup>3</sup>/MPa to M10, M3, and M6 mixtures; 1.0 \$/m<sup>3</sup>/MPa for the designed M8, M4, M7, M5 mixtures, respectively; and 1.13\$/m<sup>3</sup>/MPa corresponds to M12 mixture.

## 4. Conclusion

Based on the observations and the experimental studies through the results achieved in this study, the following conclusions may be drawn.

The research results are consistent with the results previously obtained by other authors.

The authors developed a method of HPC mix proportioning for a target strength range of approximately 80 MPa to suit Vietnamese climatic conditions by using locally available materials. Moreover, part of cement content in mixes was replaced by industrial by-product waste materials such as FA and SF with dosages ranging within 25–55 %, but still assuring the total binder fixed constant of 550 kg/m<sup>3</sup>. The results confirmed that at the age of 56 days, almost all concrete mixes designed in the above research attained strength ranging from 85 to 105 MPa, and their physical properties continued to grow at older ages.

It was established that high-performance concrete with respect to strength and durability can be produced from mixtures with a water-binder ratio at 0.35 and cementitious material content of at least 550 kg/m<sup>3</sup>, including 20 to 40 % fly ash and 5 to 12.5 % silica fume. The results of the experiment showed that almost all the mixes containing SF content at 10 % reached the highest physical properties at all ages.

Therefore, 10 % is the optimum replacement content of SF in concrete mixtures when combined with 20–40 % FA content.

## References

- Hoff, G.C. Utilization of high-strength concrete in North America. Proceeding of the Third International on Utilization of High-Strength Concrete in Lillehammer. Oslo, 1993. Pp. 28–36.
- Holand, I. High-strength concrete in Norway – Utilization and Research. Proceeding of the Third International on Utilization of High-Strength Concrete. Oslo, 1993, Pp. 68–79.
- Pierre-Claude Aitcin and Moussa Baalbaki. Canadian Experience in Producing and testing HPC, ACI SP-159, 1996. Pp. 295–308.
- De Larrard. A survey of recent research performed in French “LPC” Network on High-Performance Concrete. The Third International on Utilization of High-Strength Concrete. Norwegian Concrete Association, Oslo, 1993, Pp. 57–67.
- Sicard, V., Pons, G. Bétons à hautes performances: quelques phénomènes différés liés à leur desiccation [High-performance concretes: some phenomena in relation to desiccation]. *Materials and Structures*. 1992. 25(10). Pp. 591–597. DOI: 10.1007/bf02472227
- Potter, R.J., Guirguis, S. High-strength concrete in Australia. The Third International on Utilization of High strength Concrete in Lillehammer, Norway. Oslo, 1993, Pp. 581–589.
- König, G. Utilization of High-strength concrete in Germany. Proceeding of The Third International on Utilization of High strength Concrete in Lillehammer, Norway. Oslo, 1993. Pp. 45–56.
- Aoyama, H., Murato, T., Hiraishi, H., Bessho, S. Outline of the Japanese National Project on Advanced Reinforced Concrete Buildings with High-Strength and High-Quality Materials. ACI SP-121. 1990. Pp. 21–31.
- Shin, S.-W. High-strength concrete in Korea. *Engineered Concrete Structures*, Portland Cement Association, Skokie, IL. 1990. 3(2). Pp. 3–4.
- Jinquan, Z., Qingchang, H. High strength concrete in China. *Engineered Concrete Structures*. Portland Cement Association. 1993. 6(2). Pp. 1–3.
- Chern, J.C., Hwang, C.L., Tsai, T.H. Research and development of High-performance Concrete in Taiwan. *Concrete International*. 1995. 17(10). Pp. 71–77.
- Russell, H.G. What is High Performance Concrete? *Concrete Products Magazine*. 1999. Pp. 121–22.
- Bazhenov Y.M., Aleksandrova O.V., Nguyen D.V.Q., Bulgakov B.I. High-performance concrete produced with locally available materials in Vietnam. *Stroitel'nye Materialy [Construction Materials]*. 2020. 3. Pp. 32–38. (rus) DOI: 10.31659/0585-430X-2020-779-3-32-38
- Bazhenov, Y.M., Demyanova, V.S., Kalashnikov, V.I. *Modifitsirovannyye vysokokachestvennyye betony [Modified high-quality concrete]*. Publishing House of Association of construction universities (book). Moscow, 2006. 368 p. (rus)
- Bazhenov Y.M., Nguyen, V.Q., Aleksandrova O.V. Effect of quartz powder and mineral admixtures on the properties of high-performance concrete. *Vestnik MGSU*. 2019. 14(1). Pp. 102–117. DOI: 10.22227/1997-0935.2019.1.102-117
- Pulyaev, S., Pulyaev, I., Korovyakov, V., Sitkin, A. Research of hydration heat of Portland cement used in bridge construction of Kerch Strait. *MATEC Web Conf. Building Materials*. 2018. 251. 01036. DOI: 10.1051/mateconf/201825101036.
- Pulyaev, I., Pulyaev, S. Effects of heat exchange features hardening concrete with environment on its heat physical properties. *Mater. Today Proc.* 2019. 19. Pp.1937–1940. DOI: 10.1016/j.matpr.2019.07.045
- Shah, S.P., Ahmad, S.H. *High Performance Concrete: Properties and Applications* (book), Mc-Graw-Hill Inc. Pub., New York, 1994, 395 p.
- Kumbhar, P.D., Pranesh Murnal. "Effect of Humidity and Temperature on Properties of High Performance Concrete", *New Building Materials and Construction World*. 2011. 16(11). Pp. 204–10.
- Drzymała, T., Jackiewicz-Rek, W., Tomaszewski, M., Kuś, A., Gałaj, J., Śukys, R. Effects of high temperature on the properties of High-performance concrete (HPC). *Procedia Engineering*. 2017. 172. Pp. 256–263. DOI: 10.1016/j.proeng.2017.02.108
- Benli, A. Mechanical and durability properties of self-compacting mortars containing binary and ternary mixes of fly ash and silica fume. *Structural Concrete*. International Federation for Structural Concrete. 2019. Pp. 1–13. DOI: 10.1002/suco.201800302
- Karthikeyan, G., Balaji, M., Adarsh R. Pai, Muthu Krishnan, A. High-Performance Concrete (HPC)—An Innovative Cement Concrete Mix Design to Increase the Life Span of Structures. *Sustainable Construction and Building Materials*. 2018. Pp. 189–199. DOI: 10.1007/978-981-13-3317-0\_17
- Bilek, V., Pytlík D., Bambuchova, M. High Performance Concrete with Ternary Binders. *Key Engineering Materials*. 2018. 761. Pp. 120–123. DOI: 10.4028/www.scientific.net/KEM.761.120
- Alsalmán, A., Dang, C.N., Hale, M.W. Development of Ultra-High Performance Concrete With Locally Available Materials. *Journal of Construction and Building Materials*. 2017. 133. Pp. 135–145. DOI: 10.1016/j.conbuildmat.2016.12.040
- Benli, A., Turk, K., Ceren, K. Influence of Silica Fume and Class F Fly Ash on Mechanical and Rheological Properties and Freeze-Thaw Durability of Self-Compacting Mortars. *Journal of Cold Regions Engineering*. 2018. 32(3). DOI: 10.1061/(asce)cr.1943-5495.0000167
- Singh, H., Thakur, S. Research on effect of silica fume and fly ash with partial replacement of cement and fine aggregate. *International Journal of Civil Engineering and Technology (IJCIET)*. 2018. 9(8). Pp. 113–119.
- Hajek, P. Advanced high-performance concrete structures – challenge for sustainable and resilient future. The 4<sup>th</sup> International Conference on Rehabilitation and Maintenance in Civil Engineering (ICRMCE 2018). *MATEC Web of Conferences*. 2018. 195. DOI: 10.1051/mateconf/201819501001
- Hajek, P., Fiala, C. *Advanced Concrete Structures for the Sustainable- and Resilient-Built Environment*. ACI, Moscow, 2018. Pp. 69.1–69.8.
- Osama, A.M., Omar, F.N. Compressive strength and stability of sustainable self-consolidating concrete containing fly ash, silica fume, and GGBS. *Frontiers of Structural and Civil Engineering*. 2017. 11(4). Pp. 406–411. DOI: 10.1007/s11709-016-0350-1
- Chena, J.J., Ng, P.L., Li, L.G., Kwan, A.K.H. Production of High-performance Concrete by Addition of Fly Ash Microsphere and Condensed Silica Fume. *Procedia Engineering*. 2017. 172. Pp.165–171. DOI: 10.1016/j.proeng.2017.02.045

31. Sung, W. Y., Kwon, S.J., Jung, S.H. Analysis Technique for Autogenous Shrinkage in High Performance Concrete with Mineral and Chemical Admixtures. *Construction and Building Materials*. 2012. 34. Pp. 1–10. DOI: 10.1016/j.conbuildmat.2012.02.005
32. Elahi, A., Basheer, P.A.M., Nanukuttan, S.V., Khan, Q.U.Z. Mechanical and Durability Properties of High-performance Concretes Containing Supplementary Cementitious Materials. *Construction and Building Materials*. 2010. 24(3). Pp. 292–299. DOI: 10.1016/j.conbuildmat.2009.08.045
33. Pham, H.H., Nguyen, V.T. High performance concrete used for marine gravity concrete works. The 3<sup>rd</sup> ACF International Conference, Vietnam, 2008. Pp. 598–606.
34. El Shikh, M.M.Y. Economy of Using High Performance Concrete in Columns. 33rd Conference on Our World in Concrete & Structures. Singapore, 2008 Pp. 1–8.
35. Arunachalam, K., Gopalakrishnan, R. "Experimental Investigation on High Performance Fly Ash Concrete in Normal and Aggressive Environment," 29th Conference on Our World in Concrete & Structures. Singapore, 2004. Pp. 181–188.
36. Khan, M.I. Permeation of High performance concrete. *Journal of Materials in Civil Engineering*. 2003. 15(1). Pp. 84–92. DOI: 10.1061/(ASCE)0899-1561(2003)15:1(84)
37. Zain, M., Radin, S. Physical properties of High-performance concrete with admixtures exposed to a medium temperature range 20°C to 50°C. *Cement and Concrete Research*. 2000. 30(8). Pp. 1283–1287. DOI: 10.1016/S0008-8846(00)00294-5
38. Tamimi, A.K. High-performance concrete mix for an optimum protection in acidic conditions. *Materials and Structures*. 1997. 30(3). Pp. 188–191. DOI: 10.1007/BF02486392
39. Kwan, A.K.H., Chen, J.J. Adding fly ash microsphere to improve packing density, flowability and strength of cement paste. *Powder Technology*. 2013. 234. Pp. 19–25. DOI: 10.1016/j.powtec.2012.09.016
40. Ministry of Natural Resources and Environment (Vietnam). Climate change and Sea level rise scenarios for Viet Nam – Ha Noi. 2016. 188 p.
41. Scott, A., Kulp, H. Strauss Benjamin. New elevation data triple estimates of global vulnerability to sea-level rise and coastal flooding. *NATURE COMMUNICATIONS*. 2019. 12 p. DOI: 10.1038/s41467-019-12808-z
42. Khuong, V.H., Le M. Acid acid water causes corrosion of reinforced concrete for irrigation works in the Mekong Delta. *Journal of Science. Technology. Water Resources and Environment*. 2009. 26.
43. Khuong, V.H. Evaluation of concrete strength on irrigation works in the Mekong Delta. *Journal of Construction Science and Technology*. Hanoi. 2019. 9.
44. Jae, H.K., Nagy, N., Surendra, P.S. Effect of powder materials on the rheology and formwork pressure of self-consolidating concrete. *Cement and Concrete Composites*. 2012. 34 (6). Pp. 746–753. DOI: 10.1016/j.cemconcomp.2012.02.016
45. Alireza Kashani, R.S., Nicolas, G.G., Qiao, J.S.V. Deventer, John L.Provis, Modelling the yield stress of ternary cement-slag-fly ash pastes based on particle size distribution. *Powder Technology*. 2014. 266. Pp. 203–209. DOI: 10.1016/j.powtec.2014.06.041
46. Dale, P. B., Ferraris, C.F., Galler, M.A., Hansen, A.S., Guynn, J.M. Influence of particle size distributions on yield stress and viscosity of cement fly ash pastes. *Cement and Concrete Research*. 2012. 42(2). Pp. 404–409. DOI: 10.1016/j.cemconres.2011.11.006
47. Lee, C.Y., Lee, H.K., Lee, K.M. Strength and microstructural characteristics of chemically activated fly ash-cement systems. *Cement and Concrete Research*. 2003. Vol. 33 (3). Pp. 425–431. DOI: 10.1016/S0008-8846(02)00973-0
48. Shaikh, F., Supit, S. Compressive strength and durability properties of high volume fly ash concretes containing ultrafine fly ash. *Construction and Building Materials*. 2015. 82. Pp. 192-205. DOI: 10.1016/j.conbuildmat.2015.02.068
49. Saha, A.K., Sarker, P.K. Sustainable use of ferronickel slag fine aggregate and fly ash in structural concrete: Mechanical properties and leaching study. *Journal of Cleaner Production*. 2017. 162. Pp. 438–448. DOI: 10.1016/j.jclepro.2017.06.035

#### **Information about authors:**

**Boris Bulgakov**, PhD in Technical Science

ORCID: <https://orcid.org/0000-0002-4737-8524>

E-mail: [fakultetst@mail.ru](mailto:fakultetst@mail.ru)

**Vinh Quang Nguyen**,

ORCID: <https://orcid.org/0000-0001-5840-5279>

E-mail: [ndvquang@hueic.edu.vn](mailto:ndvquang@hueic.edu.vn)

**Olga Aleksandrova**, PhD in Technical Science

ORCID: <https://orcid.org/0000-0003-1791-8515>

E-mail: [aleks\\_olvl@mail.ru](mailto:aleks_olvl@mail.ru)

**Oksana Larsen**, PhD in Technical Science

ORCID: <https://orcid.org/0000-0002-9612-7190>

E-mail: [larsen.oksana@mail.ru](mailto:larsen.oksana@mail.ru)

**Nadezhda Galtseva**, PhD in Technical Science

ORCID: <https://orcid.org/0000-0003-2014-6739>

E-mail: [gsicevanadezda@mail.ru](mailto:gsicevanadezda@mail.ru)



Research article

UDC 624.03

DOI: 10.34910/MCE.117.3



## Numerical analysis of the buried fiber concrete slabs dynamics under blast loads

A.V. Alekseytsev , S.A. Sazonova 

Moscow State University of Civil Engineering (National Research University), Moscow, Russia

✉ [aalexw@mail.ru](mailto:aalexw@mail.ru)

**Keywords:** FRC, blast load, mechanical safety, numerical analysis, deformable supports, implicit dynamic simulation, strength, progressive collapse, damping

**Abstract.** The approach to numerical modeling of fiber reinforced concrete slab (FRCS) under blast load is considered. The slab is used for coverings of buried protective structures. The stress-strain state of this structure is investigated in the dynamic setting. The loads in this case change in time in terms of both intensity and area. The calculation makes provision for the consideration of rigid and deformable structure of support units. The damping properties of the structure are evaluated for its resistance to progressive collapse. Concrete dilatation and softening are factored in the numerical simulation. The bond between the fiber concrete and the reinforcement was modeled by introducing interpolation elements that simulate the absence of deformation in the area of their contact. The interaction of FRCS with the deformed support was modeled using the linear contact. The transition from the elastic-plastic deformation stage to the rigid stage was performed by introducing gap elements. The geometric nonlinearity, as well as the physical nonlinearity for fiber-reinforced concrete and reinforcement, was taken into account in estimating the ultimate loading. The load absorbed by the structure through the thickness of the ground during detonation explosion of a charge on its surface was considered. To realize numerical integration of the system motion equations, an implicit scheme was used. It is based on a modification of the Newmark step method in which effective matrices of fiber concrete and reinforcement stiffness are constructed at each step considering the loading history of the structure for its deformed state. The possibility of effective regulation of the stress-strain state of FRCS was established, which allows the design of effective and safe structures of this type.

**Citation:** Alekseytsev, A.V., Sazonova, S.A. Numerical analysis of the buried fiber concrete slabs dynamics under blast loads. Magazine of Civil Engineering. 2023. 117(1). Article no. 11703. DOI: 10.34910/MCE.117.3

### 1. Introduction

In connection with the need to ensure the mechanical safety of load-bearing structures under special influences, the topic of the article is relevant. External challenges require the design of new structures and reconstruction of existing buried protective structures. At the same time, the impacts from soil, transferred to the structure, most often have the highest intensity for the cover slabs. The results of deformation analysis and design of bearing systems under such impacts show that a significant increase in material intensity of bearing systems is required to ensure mechanical safety [1–5]. In addition, the choice of dynamic calculation methodology is of interest. A number of works [6–8] are aimed at the investigation of the dynamics of building structures with high loading rates. In this case, explicit solvers are most often used, and the criterion for material failure is often equivalent von Mises stresses. Such works are devoted to the resistance to explosive loads for reinforced concrete and steel frames [9–13], plates [14–18], for panels of steel plates with corrugated middle layers [4, 7, 19, 20], etc.

The study of the dynamics of structures with low impact velocities is characteristic when assessing the resistance to progressive collapse of structures at local mechanical damage [21–26], at combined

damage [27]. For such calculations with relatively long transient dynamic process time, implicit integration schemes can be effectively used [28–30].

Reducing the consumption of materials for supporting structures under dynamic loads can be achieved by regulating the values of the spectrum vibrations that can be excited by the dynamic action. Such regulation is possible by changing the configuration or supports stiffnesses, as well as by introducing additional devices [31, 32]. In analytical studies of this issue, there are certain difficulties with implementation for engineering calculations. Therefore, numerical simulation is currently the only way to solve this kind of problems in an approximate manner. The search for rational stiffnesses of supports in the dynamic formulation of calculation problems is very time consuming. The selection of optimum values by manual method seems to be ineffective, so to solve these problems it is preferable to use optimization methods. Among many of these methods, it is reasonable to use both gradient and probabilistic approaches [33–35].

Another equally important task is the modeling of dynamic loads on structures [36–40]. For low-velocity dynamics and for relatively simple structures, a simplified energy approach can be applied, according to which the dynamic force can be calculated as the difference between the doubled value of the static force in the calculation of a damaged structure and the static force for an undamaged structure. However, this approach can be applied when the basic form of oscillations excited by the dynamic action coincides with the deformed pattern from the action of the static load. In a number of cases, in particular, when the load changes in time and in the area of action on the structure, it is impossible to use a static equivalent.

Consideration of the transient dynamics of structures is closely related to the use of the damping model. Often the Rayleigh scheme is used, which allows taking into account the damping of vibrations in the medium (inertial damping) and the damping of vibrations as a result of internal friction in the material (structural damping). In this calculation accuracy depends on the values of coefficients  $\alpha$  and  $\beta$ . There are also other models, such as the Kelvin-Voigt, nonlocal in time model [41]. To determine the damping properties of structures, a number of experimental studies have been performed, for example [42], which found that the coefficient  $\beta$  varies within a fairly wide range of 0.01–0.2, depending on the design of nodes and the degree of structural damage. For the case we are considering, no values for the  $\alpha$  coefficient are given in the literature. This is due to the fact that the medium in which the vibrations occur includes two phases with significantly different properties. On the top of this medium is represented by the ground, and on the bottom – it is air.

This paper considers an approach to modeling fiber reinforced concrete slab (FRCS) under area-variable dynamic loads. The slab is considered to be buried in dense soil. An explosion at the ground surface is considered as the initial momentum. The symmetric and asymmetric effects of the blast load pulse are considered. The analysis of dynamic displacements of the structure and deformations of materials with changes in the stiffness of the support joints is performed.

## 2. Methods

### 2.1. Statement of the problem

Examine an explosion on the surface of the ground, which affects the structure buried in the ground by depth  $h$  (Fig. 1 a). In the general case of the detonation type of explosion, there are two phases: discharge and compression. The character of change in the initial pulse during the duration of these phases is shown in Fig. 1 b [43]. The influence of the duration of the discharge phase  $\tau_1$  on the load transmitted to the RFCS buried in the ground was not considered. Assume that the explosion energy is transmitted to the ground and then to the structure for a time of  $\tau_2$ . In this case, the blast wave front  $D$  can be transferred to the slab both symmetrically and asymmetrically (Fig. 1 d). The process of oscillations of the mechanical system "structure-soil" under explosive impacts is a complex little-studied problem. However, in [43] the results of numerical simulation of blast wave propagation in the ground with transmission to the structure as a function of the depth  $h_1 - h_3$  for dense three-phase soil (Fig. 1 c) are presented. Given this time distribution of pressure, it is assumed that the structure-soil system interacts on the basis of one-sided contact. The contact elements have compressive stiffness  $EA \gg 0$  and tensile stiffness  $EA \approx 0$ .

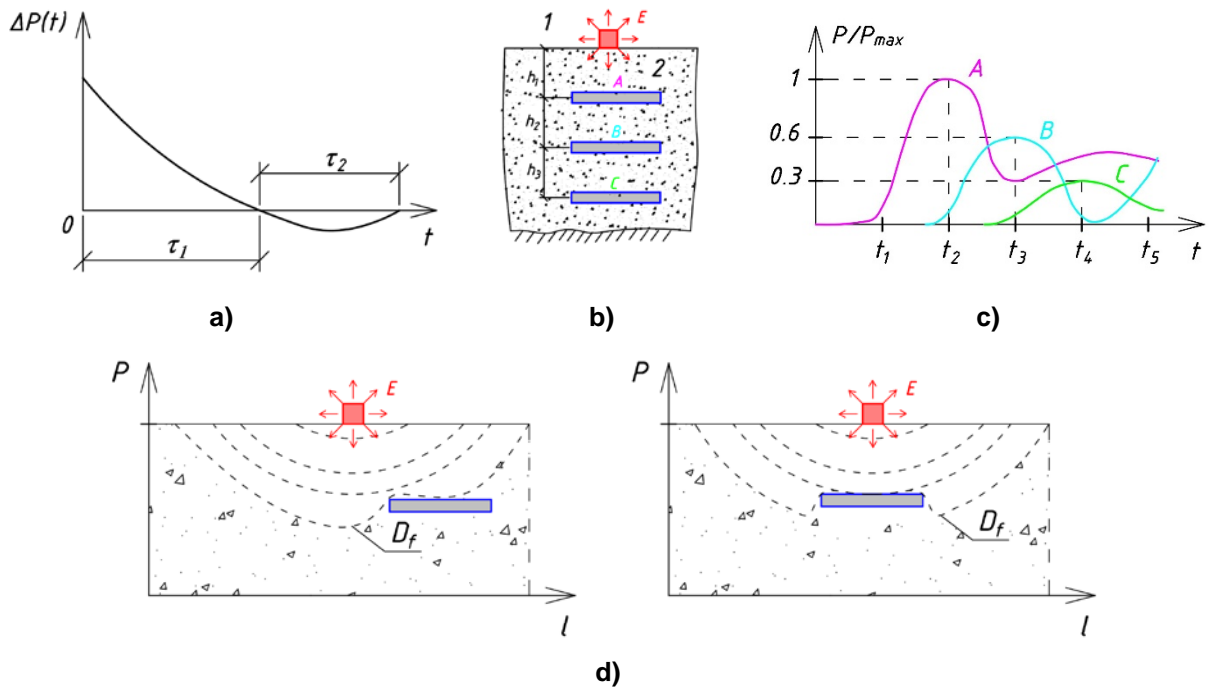


**Figure 1. Initial data for modeling the blast load.**

## 2.2. Modeling of blast loads

The initial explosion intensity is characterized by a pulse value (Fig. 1 a), which can be determined on the basis of the experimentally verified Johnes-Wilkins-Lee (JWL) model:

$$P = A \left( 1 - \frac{\omega}{R_1 V} \right) e^{-R_1 V} + B \left( 1 - \frac{\omega}{R_2 V} \right) e^{-R_2 V} + \frac{\omega E}{V}, \quad (1)$$

where the values  $A$ ,  $B$ ,  $R_1$ ,  $R_2$ ,  $\omega$ ,  $E$  are constants, which are determined on the basis of the methods of works [44, 45],  $V$  is the relative volume of explosive substance, determined by the method JWL. As an example of a reference explosion for TNT, values  $A = 3.712$  Mbar,  $B = 0.0323$  Mbar,  $R_1 = 4.15$ ,  $R_2 = 0.95$ ,  $\omega = 0.3$ ,  $E = 0.07$  Mbar are given in [46].

Based on the oscillation graph shown in Fig. 1 c, consider that the pulse impact  $\tilde{i}$  can be represented in the form of an equivalent load  $q_{eq}$ , acting for time  $t$ :

$$\tilde{i} = \mu P \tau_2 / 2 = q_{eq} t, \quad (2)$$

where  $\mu$  is the coefficient of maximum pulse reduction due to structural burial,  $t$  is the action time of the equivalent load  $q_{eq}$ .

Considering the duration  $\tau_2$  of the compression phase and assuming the magnitude  $t \approx 0.2T$ , it is possible to represent the load on the structure as a sum:

$$F(t) = q_{st} f_{st}(t) + \sum_{i=1}^S q_{i,eq} f_i(t), \quad (3)$$

where  $q_{st}$  is the intensity of constant loads,  $f_{st}(t)$  is the unit function of change in static load introduced to ensure the stability of the numerical integration procedure,  $q_{i,eq}$  is the maximum intensity of dynamic load of  $i$  type,  $S$  is the number of functions modeling the change in load in time by area and intensity,  $f_i(t)$  this is the unit function of change in time of dynamic load. The type of these functions is presented in section 3.1.

### 2.3. Modeling of FRCS deformations

The problem is solved in a dynamic formulation based on an implicit scheme for numerical integration of the equations:

$$M \ddot{\vec{y}} + C \dot{\vec{y}} + K_{\tau} \vec{y} = \vec{F} + \vec{G}\chi, \quad (4)$$

where  $M$  is the mass matrix,  $C$  is the damping matrix,  $K_{\tau}$  is the general tangent stiffness matrix for the finite element system,  $\vec{y}$  is the displacement vector,  $\dot{\vec{y}}$ ,  $\ddot{\vec{y}}$  are the vectors of first and second derivatives of displacements,  $\vec{F}$ ,  $\vec{G}$ , is the vectors of nodal forces from external dynamic loads and gravity forces respectively,  $\chi$  is the Heaviside function equal to one at  $t > 0$  else  $\chi = 0$ .

The matrix  $C$  is defined as follows:

$$C = \beta K_{\tau}; K_{\tau} = K_{bo} + K_{so} + K_{po} + K_{co} + K_{b\sigma} + K_{s\sigma} + K_{p\sigma}, \quad (5)$$

where  $K_{bo}$ ,  $K_{so}$ ,  $K_{po}$  are, respectively, the deformation matrices for fiber concrete, reinforcement, and supports (when considering non rigid supports),  $K_{co}$  is the stiffness matrix of the contact finite elements,  $K_{b\sigma}$ ,  $K_{s\sigma}$ ,  $K_{p\sigma}$  are the geometric matrices for fiber concrete, reinforcement, and supports.

Fibre concrete is modeled by hexahedral solid elements, for which the Drucker-Prager material model is implemented, determined by the concrete internal friction angle  $\tilde{\varphi}$  and cohesion stress  $\tilde{c}$ ; the presence of fibre in the concrete is modeled by increasing the design tensile strength  $R_{bt}$ . A polymeric fiber is considered, for which the design compressive resistance  $R_b$  of fiber concrete is taken equal to that of the concrete matrix. Consideration of dilatation is performed for the level of relative stresses  $\sigma/R_b \geq 0.3$ , with subsequent softening when stresses  $\sigma = R_b$  are reached. Rebars are modeled by means of spatial rod elements deforming in accordance with the Prandtl elastoplastic model. The yield criterion is the equivalent Mises stresses, the fracture criterion is the level of deformation exceeding the value 0.025. In the case of modeling of deformable support structures, shell elements deformed elastoplastically without hardening are used.

### 2.4. Modeling the contact interaction

There are two types of contact interaction in the problem under consideration (Fig. 2 a). The first one simulates a one-sided connection of the structure with the above ground. Simplified, this connection can be modeled by an element of GAP type working only in compression. The first node of the element is connected to the structure, the second node is connected to a point mass from the action of the ground. The ground is considered to be unbound particles as a result of the passage of the blast wave. The second type of contact determines the interaction of FRCS with the supporting structure (Fig. 2 b).

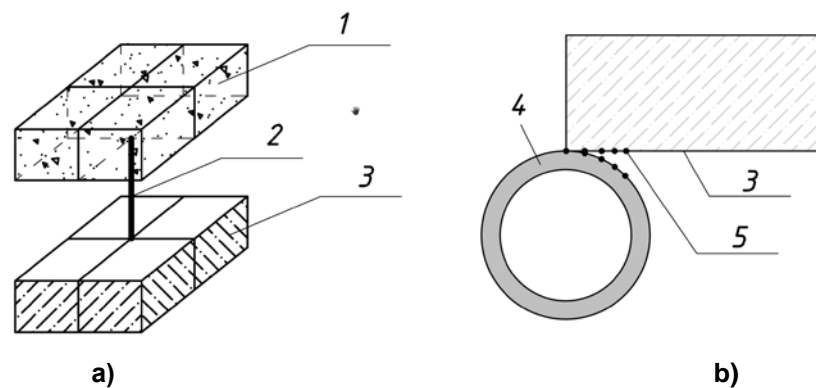


**Figure 2. Contact interaction types: 1 – ground, 2 – GAP element, 3 – FRCS, 4 – damping support, 5 – contact search nodes.**

This contact is of the "surface-surface" type and, taking into account the small variations in rotation angles during oscillations in the supports, is accepted as glue. The friction in this contact in the plane of the plate is not taken into account in the case of additional attachment of the support to the plate with anchors. The distance to find the nodes glued in the contact interaction is assumed to be 5 mm. If the elastoplastic

structure of the support has significant deformations, causing its transition to the rigid phase of deformation, GAP-type elements can also be used for this purpose.

### 3. Results and Discussion

#### 3.1. Input data and model description

Consider the FRCS structure, which is part of the covering of the structure. Lateral loads transferred from the explosion to the structure are not considered. The geometry of the slab is shown in Fig. 3 a, b. The dimensions are taken from the album U 01-01-/80 "Unified prefabricated monolithic structures of buried premises with beam type slabs". The reinforcement scheme was adopted as a typical one. Initially, a 3D-solid model for fiber concrete and a reinforcement cage model in the form of lines were made. This model was imported into the Femap 2021.2 preprocessor where the finite element model was created.

##### 3.1.1. Simulation of loads

Two types of loads were considered in accordance with Fig. 1 d. Modeling of dynamic loading by explosive load transmitted through the ground to the structure was performed as follows. To reproduce the distribution of the load over the area, divide the slab into 5 sections Fig. 4 b.

To describe the symmetrical momentum propagation scenario, and we will use the time functions (Fig. 4 a) for each of the loads  $q_1 - q_3$ . The load taken by the plate during normal operation is denoted by the variable  $q_4$ . It increases for 0.5 sec and remains constant over the entire integration time interval. The residual load intensity in  $0.3q$  for each of loads  $q_1(t)$ ,  $q_2(t)$ ,  $q_3(t)$  approximates the additional load from the structure-disturbed soil. The distribution of the load in time, taking into account the summation for each moment of time, is shown in Fig. 4 b.

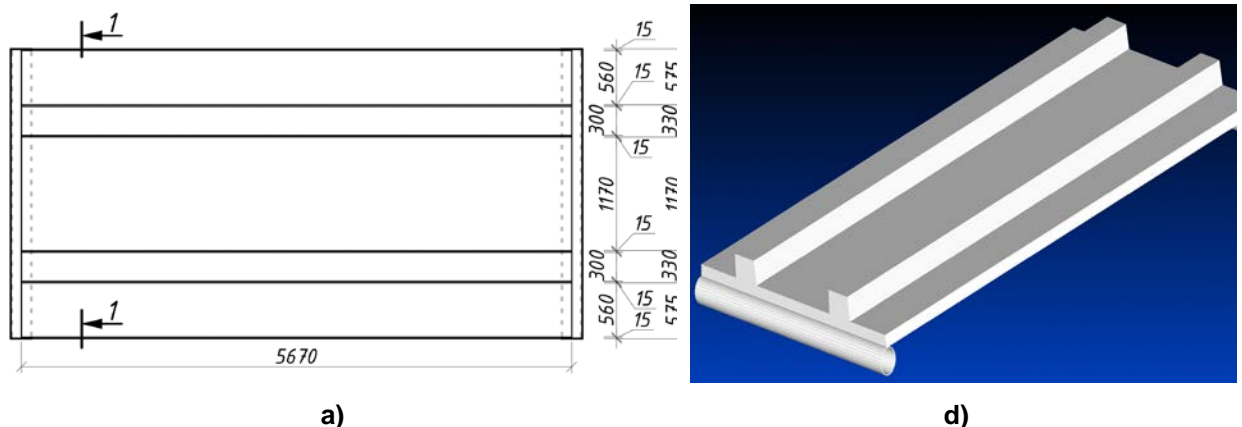
Five different time functions  $f_1 - f_5$  are used to describe the asymmetric loading scenario. Their formation is similar to Fig. 4 a, and the summation of the loads for each time moment gives the load distribution shown in Fig. 4 c.

##### 3.1.2. Material Models and Finite Elements

Fibre concrete with non-metallic fiber for FRCS was modeled based on the Drucker-Prager failure criterion described by the following equation:

$$\sqrt{\frac{1}{6}[(\sigma_1 - \sigma_2)^2 + (\sigma_2 - \sigma_3)^2 + (\sigma_1 - \sigma_3)^2]} = A + B(\sigma_1 + \sigma_2 + \sigma_3), \quad (6)$$

where  $\sigma_1$ ,  $\sigma_2$ ,  $\sigma_3$  are the principal stresses in the fiber concrete, and  $\sigma_1 > \sigma_2 > \sigma_3$ .



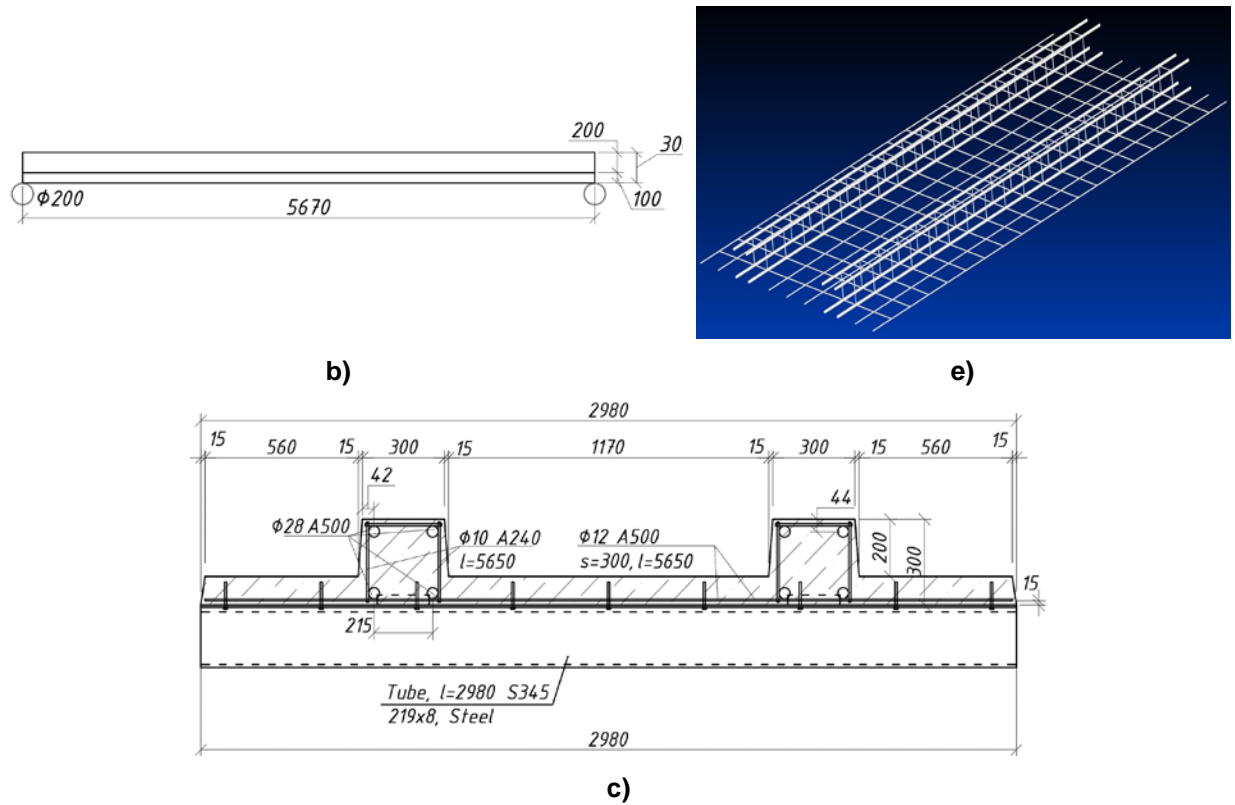


**Figure 3. Geometry and model of FRCS.**

Where the constants are:

$$A = \frac{2}{\sqrt{3}} \left( \frac{R_b R_{bt}}{R_b + R_{bt}} \right), \quad B = \frac{2}{\sqrt{3}} \left( \frac{R_{bt} - R_b}{R_b + R_{bt}} \right), \quad (7)$$

where  $R_{bt}$  is the limit design tensile stress in fiber concrete,  $R_b$  is the limit design compressive stress. The initial parameters of fiber concrete presented in Table 1 were used.

This criterion (6) was chosen from the considerations of modeling the plastic work of fiber concrete together with the reinforcement in estimating the ultimate loading of the structure. The Drucker-Prager model allows for dilatation under loading as well as softening of the material during the pre-fracture stage. At the same time, there are a number of strength models, such as Mohr-Coulomb, Willam-Warnke, geological CAP model and others, which allow modeling the deformations of concrete and reinforced concrete as a three-dimensional body.

**Table 1. Parameters of the fiber concrete deformation model**

Compressive strength $R_b$ , MPa	Tensile strength $R_{bt}$ , MPa	Angle of internal friction $\varphi$ , deg.	Cohesion $C$ , MPa	Angle of dilatation, deg.	Dilatation level $\sigma/R_b$
11.5	4.0	35	3.0	25	0.8

A bilinear model with a tangent modulus equal to zero is used to simulate the deformations of the reinforcement and steel pipe. For the reinforcement, equivalent von Mises stresses  $R_s = 420$  MPa are taken as yield stresses. For steel pipes the yield stresses is  $R_y = 325$  MPa.

The fiber concrete was represented by coordinated hexahedral solid elements, which were connected to the rod elements 1 of the rebars (Fig. 5 b). For such connections, interpolation elements 2 were used under the hypothesis of rigid coupling of fiber concrete and reinforcement. In this case, the connection node 3 of the interpolated rigid element 2 with the fiber concrete has a dependence on the linear displacements and angles of rotation from the connection node with the reinforcement. If it is assumed that during deformation the contact determining the bond between the concrete and the reinforcement is pliable, then BEAM or GAP elements can be used as connection elements 2 for which a shear stiffness function is specified.

The partitioning of the solid geometric object for fiber concrete was accepted with the maximum size of the finite elements not more than 0.05 m. The rod elements have a partitioning step of 0.01 m. The finite elements of the plates on the supports have a size of 0.05 m.

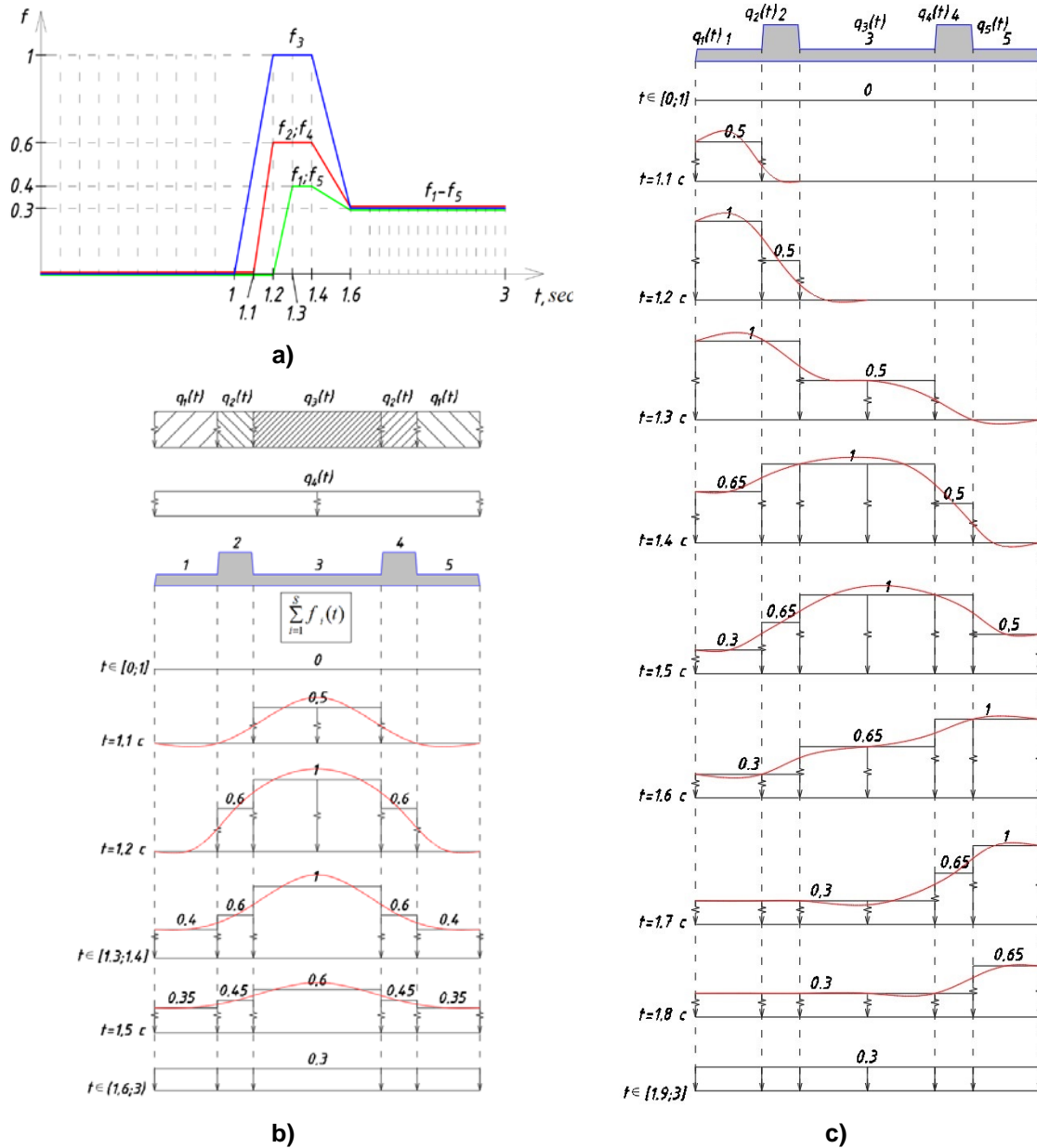


Figure 4. Distribution of dynamic load in time.

The softening function shown in Fig. 5, a is used, which simulates the fracture of fiber concrete when the level of ultimate strain reaches the value 0.0035.

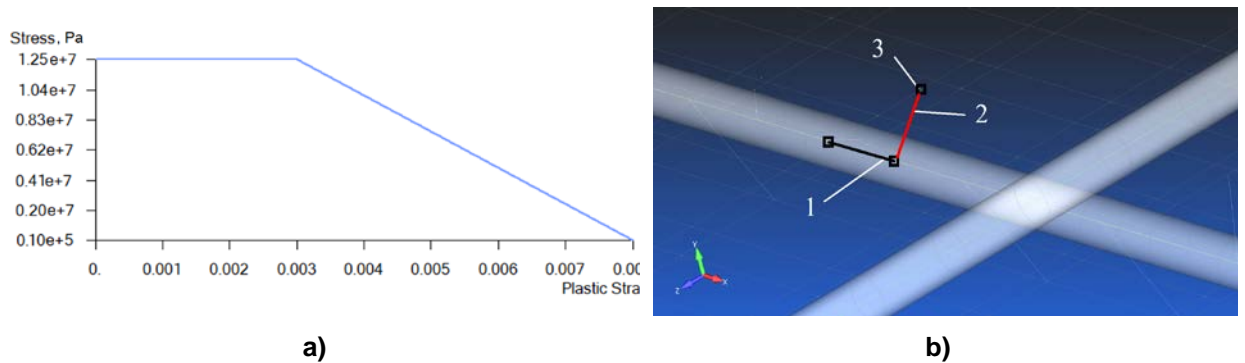


Figure 5. Function of fiber concrete softening and model of its adhesion with reinforcement: 1 – rebar; 2 – interpolation element; 3 – fiberconcrete element node.

### 3.1.3. Kinematic constraints

Two cases of support fixtures were considered:

- hinged fixed support at the right edge of FRCS and hinged moving support at the left edge (CS1);
- the same support conditions, but in the zone of pipe contact with the wall of a reinforced concrete buried structure (CS2).

When considering symmetric loading, the supports only support compressive forces. In asymmetric loading, pipe detachment from the FRCS can be observed. In this calculation, this detachment does not occur due to the anchors introduced connecting the FRCS to the pipe and spaced 350 mm apart. For vertical deformations of the pipe, the support assembly is assumed such that there are no restrictions on horizontal deformations. Otherwise, GAP elements can be used to simulate this constraint.

## 3.2. Model verification. Ultimate static loading

### 3.2.1. Compression model of fiber concrete prism

To determine the values of cohesion stresses and the angle of internal friction given in Table 1, a numerical calculation up to failure of a standard 30×30×90 mm fiber concrete prism was performed. The Drucker-Prager plasticity model was used. The condition for achieving failure is the value of compressive stresses  $\sigma_c = R_b$ , and for tensile stresses –  $\sigma_t = R_{bt}$ . The test results of the prism are shown in Fig. 6,  $C = 3.0$  MPa,  $\varphi = 35^\circ$ .

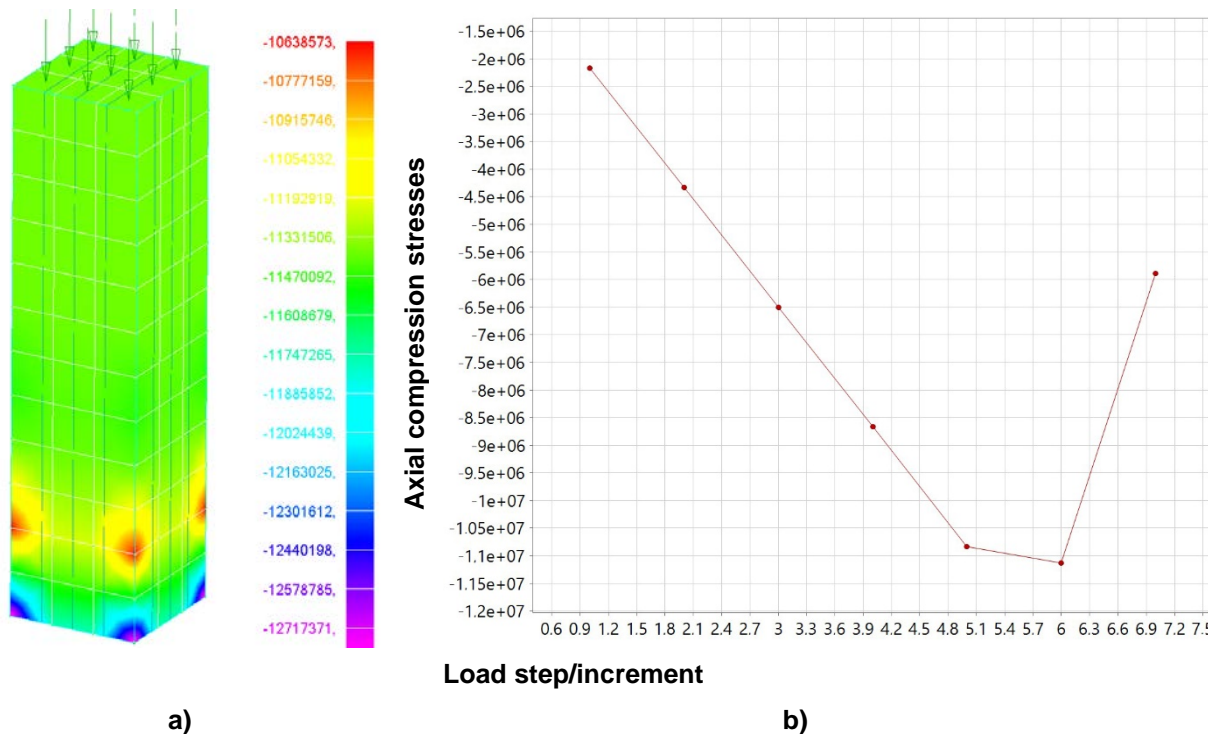
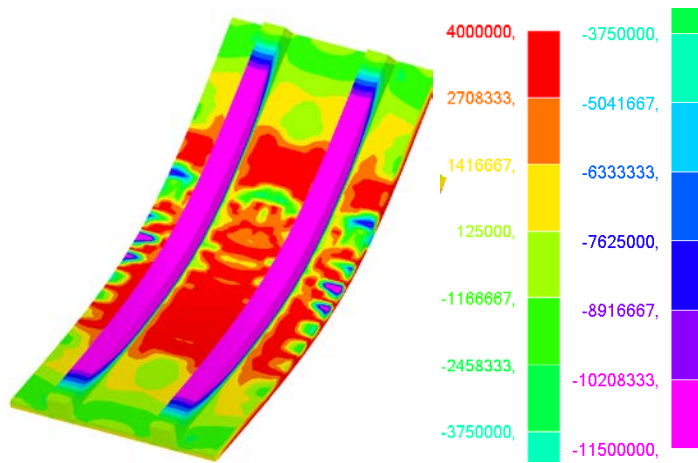


Figure 6. Results of the verification of the computational model.

### 3.2.2. Static calculation results

The calculation was performed for the action of a load uniformly distributed over the area of the structure. To account for physical nonlinearity, the Newton-Raphson method was used with a force unconstraint equal to 0.001. At each step, 25 iterations were considered. Reaching the limit load level was fixed in the state just before the formation of the mechanism. That is, when the stiffness matrix of the system became ill-conditioned or its determinant was equal to zero. The sequential additional loading assumed 50 steps of 2 kN/m<sup>2</sup> at each step. At 21 steps the calculation was interrupted. As a result, a maximum load of 40 kN/m<sup>2</sup> was determined. The maximum deflection of the slab was 8.5 cm. The distribution of axial longitudinal stresses in the fiber concrete is shown in Fig. 7.



**Figure 7. Results of static analysis for FRC, kN/m2.**

At the same time through cracks are formed in the slab part and the fiber concrete goes out of operation, transferring the load to the reinforcement mesh and beams. The stresses in the reinforcement reach the yield strength. At the level of load of 20 kN/m<sup>2</sup> the transition of the slab to the limit state starts, which indicates the correctness of the chosen model with its standard operational load of 18 kN/m<sup>2</sup>, including its own weight of 3 kN/m<sup>2</sup> and the weight of the overlying 1 m thick soil – 15 kN/m<sup>2</sup> (the value is taken from the album of typical solutions U 01-01-/80 "Unified precast-monolithic structures of underground premises with beam type slabs").

### 3.3. Dynamic loads

#### 3.3.1. Symmetrical influences

The stress change fields in the fiber concrete in time are shown in Fig. 8. When an explosive load is transmitted through the ground, the entire fiber concrete slab of the FRCS goes out of operation in 0.6 s, and the reinforcement works as a cable structural system. By the time of 2.0 sec the top layer of fiber concrete is destroyed. In this case, as can be seen in the graph (Fig. 9 a) of stresses change in the lower working rebars in time, the stresses in this reinforcement reach the yield strength.

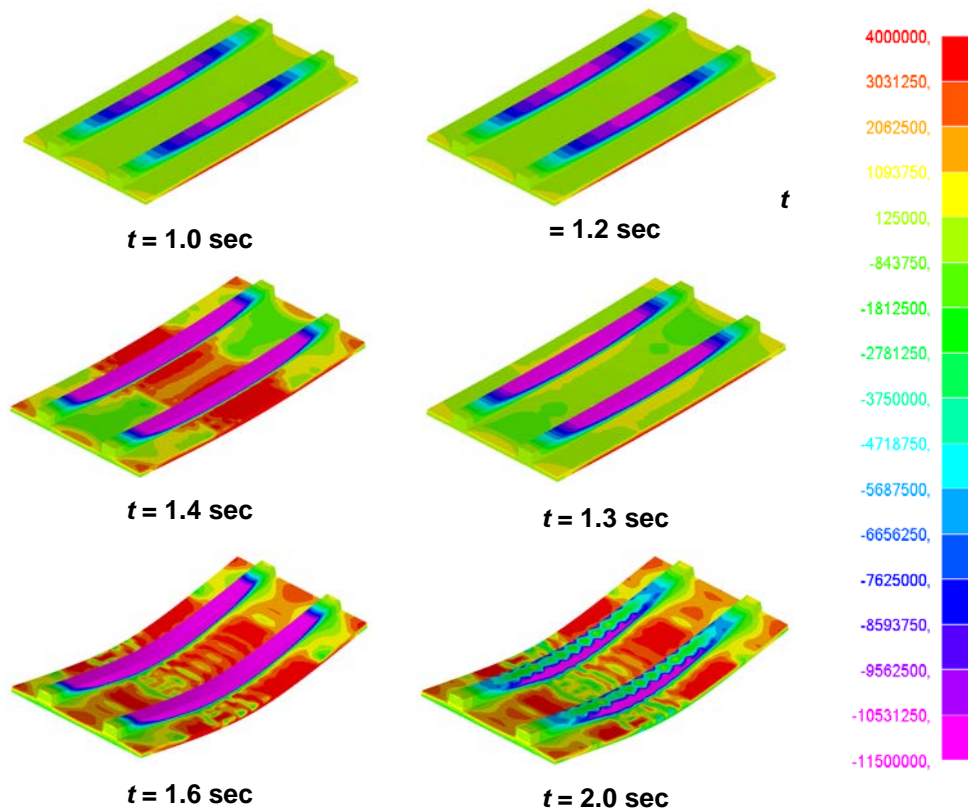


**Figure 8. Stress state of fiber concrete under dynamic impact from blast load transmitted through the ground.**

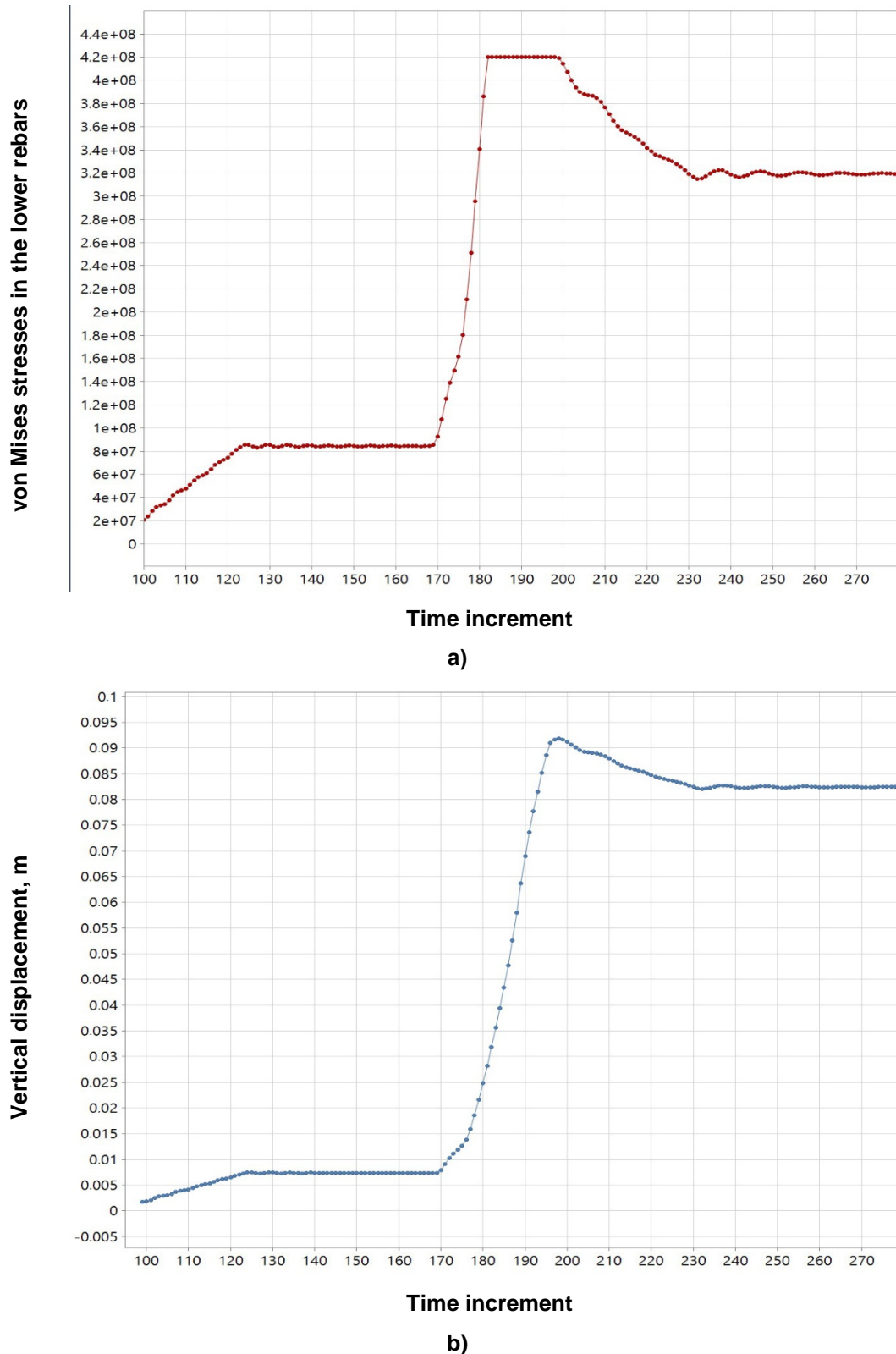


**Figure 9. Character of changes in the components of the stress-strain state in time: (a) – displacements; (b) – von Mises stresses in the lower rebars.**

The oscillations of the system are damped quite rapidly, the character of this damping is not harmonic due to the significant damping by the fractured soil. The graph of changes in the structure's displacements in time for the characteristic point in the middle of the span is shown in Fig. 9 b. When the anchoring variant (CS1) was used in the system, the system collapsed on the fiber concrete with a load exceeding 25 kPa. The introduction of a deformable tubular support (CS2) did not cause the structure to collapse up to a load of 38 kPa, which has a significant effect in improving the safety of such a structure. At the same time, the tubular support deformed in time as shown in Fig. 10.

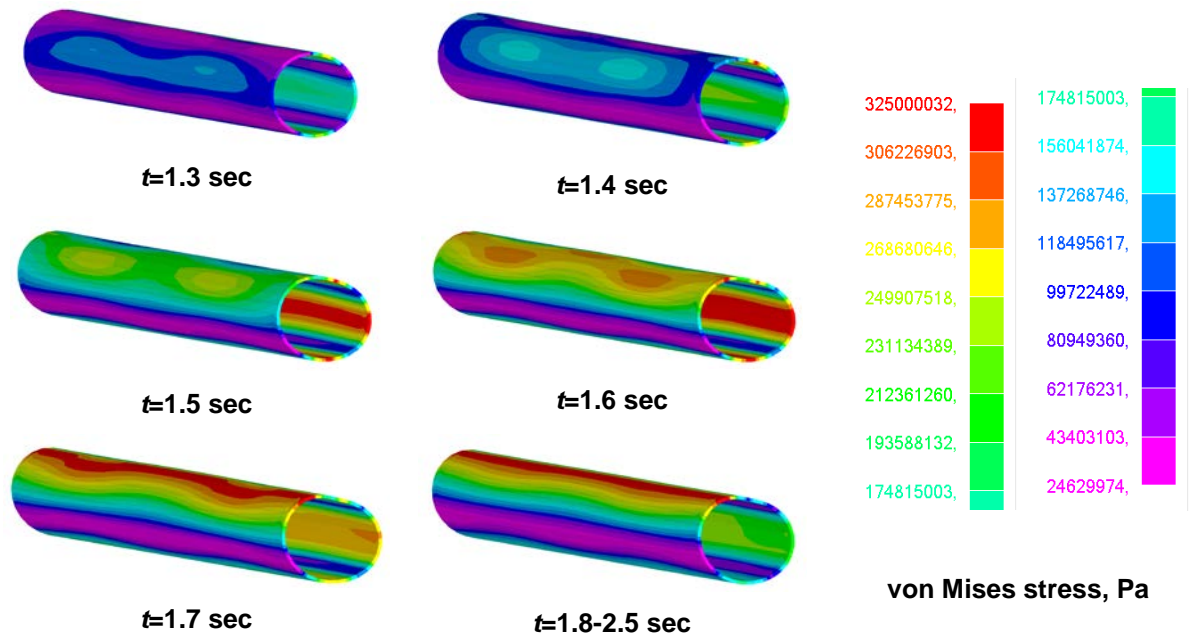


**Figure 10. Deformation of the left tubular support during FRCS blast loading.**

**3.3.2. Asymmetric loading**

Calculation of the asymmetric impact showed that with this form of impulse, the load limit value was 26 kPa. This shows an almost equivalent effect in the location of the structure in the immediate spot of the explosion. The nature of the stress redistribution shown in Fig. 11 suggests that the load-carrying capacity margin is higher under this action than under the symmetrical action. Deformation of tubular support is shown in Fig. 12, the limiting value of dynamic load applied to the plate is 39 kPa. It should be noted that the introduction of a damping support here led to a very significant effect, because the limiting load obtained under static loading is 40 kPa. The collapse of the fiber concrete of the structure under this influence begins from the time of 1.3 sec, and by the time of 1.4 sec through formation of cracks is observed, the same as under symmetrical loading.

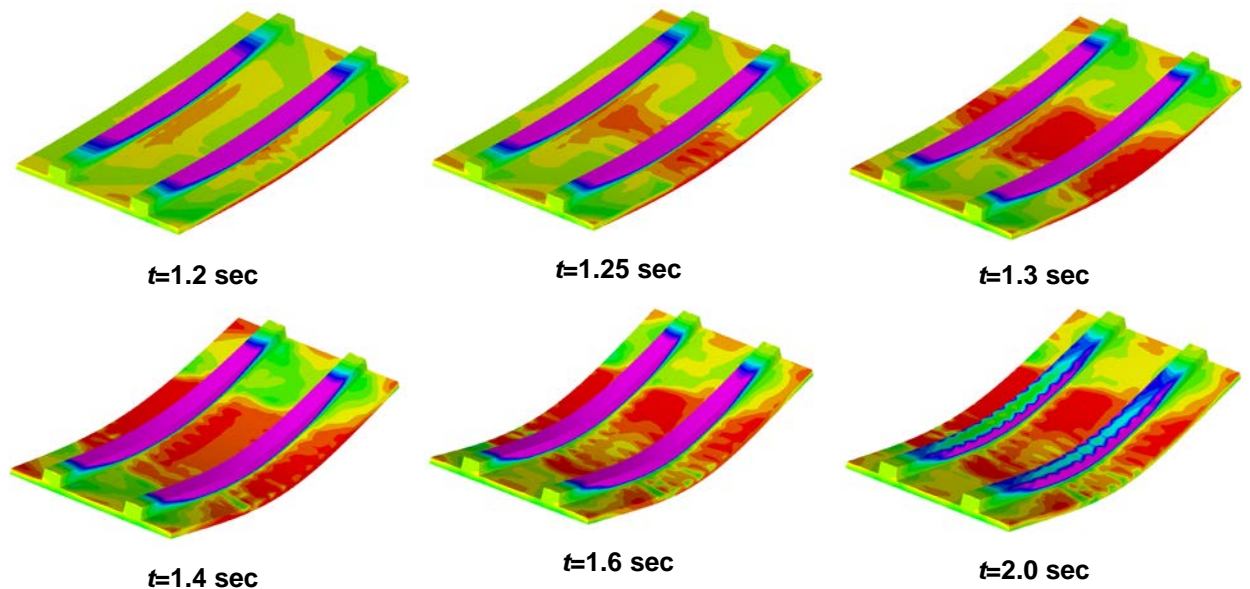


**Figure 11. Stress state of fiber concrete under asymmetric loading.**

The deformation of the right tubular support here has the character shown in Fig. 12. At a time of 1.4 sec the stress in the upper fiber at the right edge of the steel tube reaches the yield stress, then this stress state is redistributed to the left edge in 0.2 sec and subsequently stress relaxation occurs.

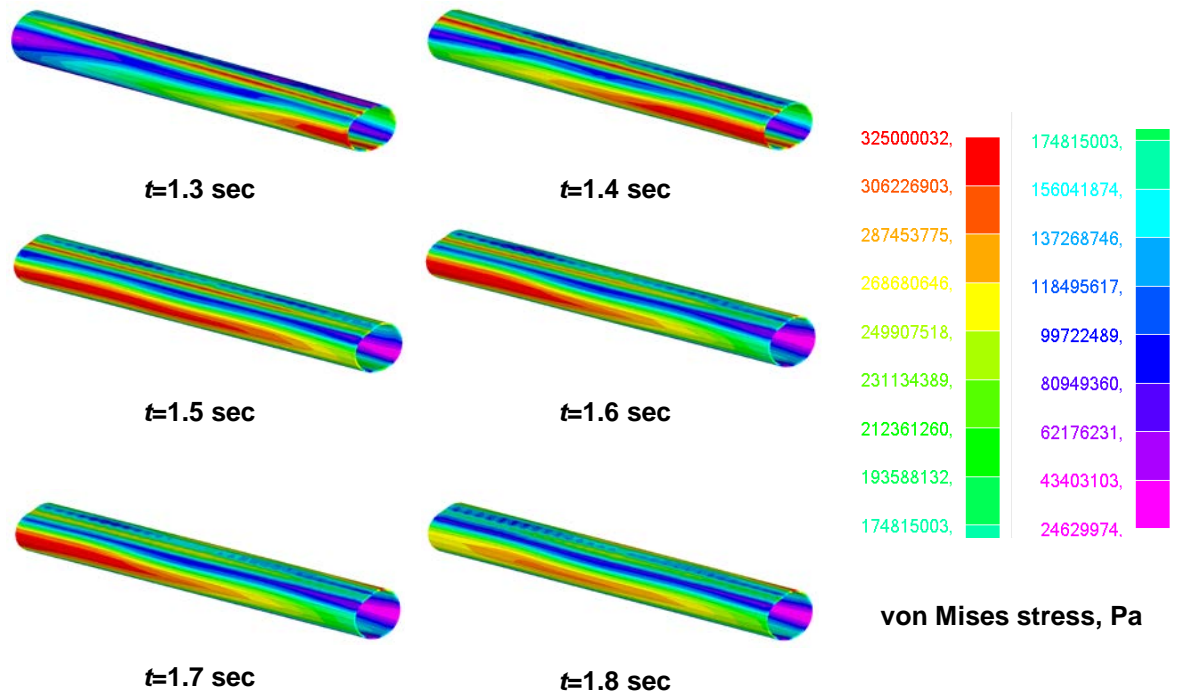


**Figure 12. Deformation of the right FRCS tubular support under asymmetric loading.**

It is notable that the presence of anchors, providing the connection of the pipe and FRCS, prevents the pipe from detachment and contributes to the dissipation of the blast energy, which is spent on the deformation of the pipe during its loading and unloading. The nature of the contact interaction with the pipe is shown in Figure 13. As can be seen in the figure the stiffness of the tube does not allow for its significant deflections and determines the elastic-plastic nature of the deformations without changing to the rigid body stage. In order to improve the damping properties of the support with the possibility of saving material, a compressible insert inside the pipe is allowed. Comparison of the ultimate load of the obtained calculation results is given in Table 2.

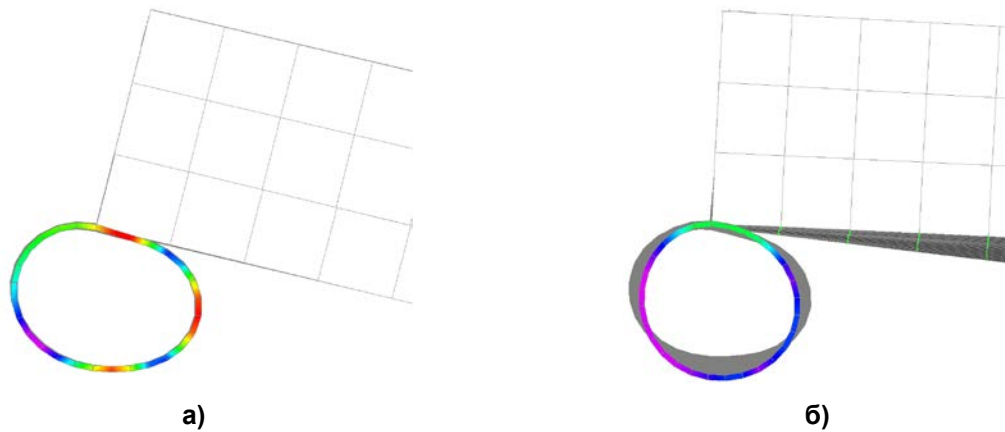


**Figure 13. Deformations of the tubular support considering its contact interaction with FRCS: a) – for symmetric loading; b) – for asymmetric loading.**

**Table 2. Calculation results of the dynamic load limit value.**

Maximum dynamic load				Symmetrical static load (CS2), kPa
symmetrical (CS1), kPa	symmetrical (CS2), kPa	asymmetric (CS1), kPa	asymmetric (CS2), kPa	
25	38	26	39	40
Increasing the intensity dynamic load, %				
–	100(38-25)/25= = 52	–	100(39-26)/26= = 50	–

### 3.4. Discussion

The model of vibration damping is very important in dynamic calculations. In this work, this model is presented on the basis of the combined use of the Rayleigh scheme, which takes into account only the structural damping at the lowest frequencies of the slab vibrations, and the contact finite elements. With the presence of support tubes, damping was considered in the range of 23.1–24.2 Hz, and for rigid supports this interval was 13.7–14.8 Hz. The damping coefficient was assumed to be 0.1, taking into account local structural damage, based on the recommendations of [42]. It is likely that quantitatively different results can be achieved using improved damping models, such as the nonlocal in time model from [41].

The conducted research has prospects both in terms of preparation and conducting of experiments on dynamic effects on buried structures and in terms of selection of rational parameters of reinforcement and stiffnesses of damping supports for structures of this type. The problem of designing rational parameters can be solved using heuristic methods, for example [31], that allow topological synthesis of objects. Thus, as an example, we can consider the possibility of intermittent pipe supports instead of a continuum support.

## 4. Conclusion

1. The approach to modeling FRCS under dynamic actions with variable in area and intensity loading, simulating blast, taking into account the possible burial of the structure in the ground, including:

- modeling the propagation of dynamic loads using time functions normalized to the value of the peak load;
- an approximate account of the damping of the medium, representing on the one hand the ground and on the other hand the air environment.

2. High efficiency of application of elastoplastic supports for damping vibrations of protective constructions has been revealed. It has been established that the cupping effect in the propagation of progressive destruction of an individual structure can increase the resistance to mechanical damage and the overall level of mechanical safety of structures.

## References

1. Quek, J., Chunlin, L., Musngi, J.V., Malalasekara, P.B. A comparison of finite element simulation and experimental results from reinforced concrete columns wrapped with fibre-reinforced polymer subjected to blast loading. 2020. International Journal of Computational Methods and Experimental Measurements. 8 (3). DOI: 10.2495/CMEM-V8-N3-233-242
2. Senthil, K., Gupta, I., Rupali, S., Pelecanos, L. A review on the performance of reinforced concrete structures under blast loading. 2020. Journal of Structural Engineering & Applied Mechanics. 3 (4). DOI: 10.31462/jseam.2020.04216228
3. Isaac, O.S., Jagadeesh, G. Impulse Loading of Plates using a Diverging Shock Tube. 2020. Experimental Mechanics. 60 (4). DOI: 10.1007/s11340-019-00573-5
4. Brekken, K.A., Reyes, A., Børvik, T., Berstad, T., Langseth, M. Sandwich panels with polymeric foam cores exposed to blast loading: An experimental and numerical investigation. 2020. Applied Sciences (Switzerland). 10 (24). DOI: 10.3390/app10249061
5. Li, Y., Chen, Z., Ren, X., Tao, R., Gao, R., Fang, D. Experimental and numerical study on damage mode of RC slabs under combined blast and fragment loading. 2020. International Journal of Impact Engineering. 142. DOI: 10.1016/j.ijimpeng.2020.103579
6. Xu, M., Yang, Y., Lei, H., Wang, P., Li, X., Zhang, Z., Fang, D. Dynamic response of fiber metal laminates subjected to localized high impulse blast loading. 2020. Composite Structures. 243. DOI: 10.1016/j.compstruct.2020.112216
7. Mai, V.C., Vu, N.Q., Nguyen, V.T., Pham, H. Ultra-high performance fiber reinforced concrete panel subjected to severe blast loading. 2020. Defence Science Journal. 70 (6). DOI: 10.14429/DSJ.70.15835
8. Nili, M., Ghorbankhani, A.H., Alavinia, A., Zolfaghari, M. Assessing the impact strength of steel fibre-reinforced concrete under quasi-static and high velocity dynamic impacts. 2016. Construction and Building Materials. 107. Pp. 264–271. DOI: 10.1016/j.conbuildmat.2015.12.161
9. Mishra, N., Netula, O. Behaviour of Reinforced Concrete Framed Structure Subjected to Blast Loading. 2021. International Journal of Advanced Research in Engineering and Technology (IJARET). 12 (1).
10. Mistri, A., Sarkar, P., Davis, R. Column-beam moment capacity ratio and seismic risk of reinforced concrete frame building. 2019. Proceedings of the Institution of Civil Engineers: Structures and Buildings. 172 (3). Pp. 189–196. DOI: 10.1680/jstbu.17.00100
11. Weng, J., Tan, K.H., Lee, C.K. Modeling progressive collapse of 2D reinforced concrete frames subject to column removal scenario. 2017. Engineering Structures. 141. Pp. 126–143. DOI: 10.1016/j.engstruct.2017.03.018
12. Kabantsev, O.V., Tamrazian, A.G. Allowing for changes in the calculated scheme during the analysis of structural behaviour. 2014. Magazine of Civil Engineering. 49 (5). Pp. 15–26 + 123–124. DOI: 10.5862/MCE.49.2
13. Yang, T., Han, Z., Deng, N., Chen, W. Collapse responses of concrete frames reinforced with BFRP bars in middle column removal scenario. 2019. Applied Sciences (Switzerland). 9 (20). DOI: 10.3390/app9204436
14. Kumar, V., Kartik, K.V., Iqbal, M.A. Experimental and numerical investigation of reinforced concrete slabs under blast loading. 2020. Engineering Structures. 206. DOI: 10.1016/j.engstruct.2019.110125
15. Almस्ताfa, M.K., Nehdi, M.L. Machine learning prediction of structural response for FRP retrofitted RC slabs subjected to blast loading. 2021. Engineering Structures. 244. DOI: 10.1016/j.engstruct.2021.112752
16. Chuzel-Marmot, Y., Ortiz, R., Combesure, A. Three dimensional SPH-FEM gluing for simulation of fast impacts on concrete slabs. 2011. Computers and Structures. 89 (23–24). Pp. 2484–2494. DOI: 10.1016/j.compstruc.2011.06.002

17. Del Linz, P., Fan, S.C., Lee, C.K. Modeling of combined impact and blast loading on reinforced concrete slabs. 2016. *Latin American Journal of Solids and Structures*. 13 (12). Pp. 2266–2282. DOI: 10.1590/1679-78252516
18. Mastali, M., Ghasemi Naghibdehi, M., Naghipour, M., Rabiee, S.M. Experimental assessment of functionally graded reinforced concrete (FGRC) slabs under drop weight and projectile impacts. 2015. *Construction and Building Materials*. 95. Pp. 296–311. DOI: 10.1016/j.conbuildmat.2015.07.153
19. Zhou, X., Jing, L. Deflection analysis of clamped square sandwich panels with layered-gradient foam cores under blast loading. 2020. *Thin-Walled Structures*. 157. DOI: 10.1016/j.tws.2020.107141
20. Yang, L., Sui, L., Li, X., Dong, Y., Zi, F., Wu, L. Sandwich plates with gradient lattice cores subjected to air blast loadings. 2021. *Mechanics of Advanced Materials and Structures*. 28 (13). DOI: 10.1080/15376494.2019.1669092
21. Terrenzi, M., Spacone, E., Camata, G. Collapse limit state definition for seismic assessment of code-conforming RC buildings. 2018. *International Journal of Advanced Structural Engineering*. 10 (3). Pp. 325–337. DOI: 10.1007/s40091-018-0200-6
22. Lazar Sinković, N., Dolšek, M. Fatality risk and its application to the seismic performance assessment of a building. 2020. *Engineering Structures*. 205. DOI: 10.1016/j.engstruct.2019.110108
23. Shokrabadi, M., Burton, H.V. Risk-based assessment of aftershock and mainshock-aftershock seismic performance of reinforced concrete frames. 2018. *Structural Safety*. 73. Pp. 64–74. DOI: 10.1016/j.strusafe.2018.03.003
24. Sinković, N.L., Brozović, M., Dolšek, M. Risk-based seismic design for collapse safety. 2016. *Earthquake Engineering and Structural Dynamics*. 45 (9). Pp. 1451–1471. DOI: 10.1002/eqe.2717
25. Thai, D.K., Pham, T.H., Nguyen, D.L. Damage assessment of reinforced concrete columns retrofitted by steel jacket under blast loading. 2020. *Structural Design of Tall and Special Buildings*. 29 (1). DOI: 10.1002/tal.1676
26. Alekseytsev, A.V. Mechanical safety of reinforced concrete frames under complex emergency actions. 2021. *Magazine of Civil Engineering*. 103 (3). DOI: 10.34910/MCE.103.6
27. Leppänen, J. Dynamic behaviour of concrete structures subjected to blast and fragment impacts. 2002. ... of *Structural Engineering, Concrete Structures*. .... pp. 96. [https://www.msb.se/siteassets/dokument/amnesomraden/krisberedskap-och-civilt-forsvar/befolkningsskydd/skyddsrum/akademiska-avhandlingar/dynamic-behaviour-of-concrete-structures-subjected-to-blast-and-fragment-impacts\\_lic.pdf](https://www.msb.se/siteassets/dokument/amnesomraden/krisberedskap-och-civilt-forsvar/befolkningsskydd/skyddsrum/akademiska-avhandlingar/dynamic-behaviour-of-concrete-structures-subjected-to-blast-and-fragment-impacts_lic.pdf)
28. Kristoffersen, M., Hauge, K.O., Minoretti, A., Børvik, T. Experimental and numerical studies of tubular concrete structures subjected to blast loading. 2021. *Engineering Structures*. 233. DOI: 10.1016/j.engstruct.2020.111543
29. Maazoun, A., Matthys, S., Belkassam, B., Atoui, O., Lecompte, D. Experimental study of the bond interaction between CFRP and concrete under blast loading. 2021. *Composite Structures*. 277. DOI: 10.1016/j.compstruct.2021.114608
30. Li, Z.X., Zhang, X., Shi, Y., Wu, C., Li, J. Finite element modeling of FRP retrofitted RC column against blast loading. 2021. *Composite Structures*. 263. DOI: 10.1016/j.compstruct.2021.113727
31. Alekseytsev, A.V., Gaile, L., Drukis, P. Optimization of steel beam structures for frame buildings subject to their safety requirements. 2019. *Magazine of Civil Engineering*. 91 (7). Pp. 3–15. DOI: 10.18720/MCE.91.1
32. Kumpyak, O.G., Galyautdinov, Z.R., Kokorin, D.N. Strength of concrete structures under dynamic loading. *AIP Conf. Proc.* 2016. 1698. 070006. DOI: 10.1063/1.4937876
33. Nguyen, W., Bandelt, M.J., Trono, W., Billington, S.L., Ostertag, C.P. Mechanics and failure characteristics of hybrid fiber-reinforced concrete (HyFRC) composites with longitudinal steel reinforcement. 2019. *Engineering Structures*. 183. Pp. 243–254. DOI: 10.1016/j.engstruct.2018.12.087
34. Kyriakides, N., Sohaib, A., Pilakoutas, K., Neocleous, K., Chrysostomou, C., Tantele, E., Votsis, R. Evaluation of Seismic Demand for Substandard Reinforced Concrete Structures. 2018. *The Open Construction and Building Technology Journal*. 12 (1). Pp. 9–33. DOI: 10.2174/1874836801812010009
35. An, H., Hou, S., Liu, L. Experimental and numerical study of the concrete stress and fracture propagation processes by blast. 2019. *Engineering Letters*. 27 (4). Pp. 1–7.
36. Chen, Y., May, I.M. Reinforced concrete members under drop-weight impacts. 2009. *Proceedings of the Institution of Civil Engineers: Structures and Buildings*. 162 (1). Pp. 45–56. DOI: 10.1680/stbu.2009.162.1.45
37. Qasrawi, Y., Heffernan, P.J., Fam, A. Dynamic behaviour of concrete filled FRP tubes subjected to impact loading. 2015. *Engineering Structures*. 100. Pp. 212–225. DOI: 10.1016/j.engstruct.2015.06.012
38. Ngo, T., Mendis, P. Modelling the dynamic response and failure modes of reinforced concrete structures subjected to blast and impact loading. 2009. *Structural Engineering and Mechanics*. 32 (2). Pp. 269–282. DOI: 10.12989/sem.2009.32.2.269
39. Niroomandi, A., Pampanin, S., Dhakal, R.P., Ashtiani, M.S., De La Torre, C. Rectangular RC walls under bi-directional loading: recent experimental and numerical findings. *Hamilton: 2018 New Zealand Concrete Industry Conference*. 11/10/2018-13/10/2018
40. Magnusson, J., Hallgren, M., Ansell, A. Shear in concrete structures subjected to dynamic loads. 2014. *Structural Concrete*. 15 (1). Pp. 55–65. DOI: 10.1002/suco.201300040
41. Sidorov, V., Badina, E., Detina, E. Nonlocal in time model of material damping in composite structural elements dynamic analysis. 2021. *International Journal for Computational Civil and Structural Engineering*. 17 (4). Pp. 14–21. DOI: 10.22337/2587-9618-2021-17-4-14-21
42. Russell, J.M., Owen, J.S., Hajirasouliha, I. Experimental investigation on the dynamic response of RC flat slabs after a sudden column loss. 2015. *Engineering Structures*. 99. DOI: 10.1016/j.engstruct.2015.04.040
43. Mkrtychev, O., Savenkov, A. Modeling of blast effects on underground structure. 2019. *International Journal for Computational Civil and Structural Engineering*. 15 (4). DOI: 10.22337/2587-9618-2019-15-4-111-122
44. Giam, A., Toh, W., Tan, V.B.C. Numerical review of Jones-Wilkins-Lee parameters for trinitrotoluene explosive in free-air blast. 2020. *Journal of Applied Mechanics, Transactions ASME*. 87 (5). DOI: 10.1115/1.4046243
45. Gamo, J., Ouellet, F., Bae, S., Jackson, T.L., Kim, N.H., Haftka, R., Hughes, K.T., Balachandar, S. Calibration of reactive burn and Jones-Wilkins-Lee parameters for simulations of a detonation-driven flow experiment with uncertainty quantification. 2020. *Physical Review Fluids*. 5 (12). DOI: 10.1103/PhysRevFluids.5.123201
46. Castedo, R., Natale, M., López, L.M., Sanchidrián, J.A., Santos, A.P., Navarro, J., Segarra, P. Estimation of Jones-Wilkins-Lee parameters of emulsion explosives using cylinder tests and their numerical validation. 2018. *International Journal of Rock Mechanics and Mining Sciences*. 112. DOI: 10.1016/j.ijrmms.2018.10.027

**Information about authors:**

**Anatoly Alekseytsev**, Doctor of Technical Science

ORCID: <https://orcid.org/0000-0002-4765-5819>

E-mail: [aalexw@mail.ru](mailto:aalexw@mail.ru)

**Svetlana Sazonova**,

ORCID: <https://orcid.org/0000-0003-4025-2053>

E-mail: [s.sazonovaa17@mail.ru](mailto:s.sazonovaa17@mail.ru)

*Received 06.05.2022. Approved after reviewing 28.09.2022. Accepted 06.10.2022.*



Research article

UDC 624.138

DOI: 10.34910/MCE.117.4



## Effects of gradation and clay minerals on stabilized lateritic soil blocks

M.G. Sreekumar<sup>1</sup>  , D.G. Nair<sup>1</sup>  , K.S Jagadish<sup>2</sup>

<sup>1</sup> Cochin University of Science and Technology, Kochi, Kerala, India

<sup>2</sup> Indian Institute of Science, Bengaluru, Karnataka, India

✉ [sreekuair@cusat.ac.in](mailto:sreekuair@cusat.ac.in)

**Keywords:** stabilized earthen block, clay mineral, soil gradation, lateritic soil, kaolinite, compressive strength

**Abstract.** Building blocks extracted from natural lateritic soil strata have wide popularity in masonry construction in the state of Kerala in India. However, extensive variations in strength and physical properties can be observed in these blocks even though they are collected from the same location. Stabilized soil blocks from this lateritic soil can be a sustainable solution for standardization. This research aims at optimizing the soil gradation and assessing the significance of clay minerals for the strength characteristics of stabilized earthen building blocks from lateritic soil. Lateritic soil samples from four different locations and depths were collected and tested for their characterization, as well as chemical and mineralogical investigations. The suitability of stabilizers such as cement, lime, and quarry waste was investigated and stabilized lateritic building blocks were manufactured in different particle combinations from each soil sample and tested to study the influences of gradation patterns on stabilization. The best combinations were further investigated for optimization studies. Combined effects of soil gradation, as well as the presence of chemical and mineral contents in the lateritic soil, were found to contribute toward strength gain. Results of the studies reveal the significance of silt content among the particles and the influence of kaolinite and hematite minerals in the soil samples on the strength gain of stabilized laterite blocks.

**Citation:** Sreekumar, M.G., Nair, D.G., Jagadish, K.S. Effects of gradation and clay minerals on stabilized lateritic soil blocks. Magazine of Civil Engineering. 2023. 117(1). Article no. 11704. DOI: 10.34910/MCE.117.4

### 1. Introduction

Tropical and sub-tropical countries are rich in lateritic soil deposits [1, 2]. The state of Kerala in India is covered with a laterite blanket of more than 60 % over various crystalline rocks [3, 4]. And the majority of this laterite deposit belongs to the category of moderate to weak laterization [5]. Building blocks extracted from this naturally available deposit are widely used in Kerala for masonry construction. But these laterite blocks are found highly varying in nature with respect to strength, durability, and physical characteristics [1, 4]. The availability of good quality cut laterite building blocks is further narrowed by the restriction imposed by Government on quarrying from greater depths. Stabilized building blocks made from abundantly available lateritic soil deposits can be suggested as a sustainable solution to overcome these issues of standardization and availability.

The lateritic soil is distinct from other soil types as it contains various chemicals and minerals. It is affluent in aluminium, iron, silica, and kaolinite clays and varies with mineral and chemical composition based on formation [6, 7]. Dense rainfall, warm temperature, and local topography influence the formation of a lateritic soil group. The existence of iron oxides influences the color of laterite soil and variation can be

observed from light red to brown shades [8]. Rock weathering in tropical areas is very rigorous as seen in the fast disintegration of feldspars as well as ferromagnesian raw materials. Displacement of bases including  $\text{Na}_2\text{O}$ ,  $\text{K}_2\text{O}$ , and  $\text{MgO}$ , silica, and the absorption of aluminium and iron oxides can also be noticed [9]. This procedure which includes leakage of silica and decomposition of iron and aluminium oxides is called laterization [10]. H.A. Narayanaswamy et al. observed a variation in the strength characteristics of lateritic rock with respect to location and strata along with a variation in dry and saturated environments. And they suggest climatic conditions in tropical countries and response to moisture owing to the porous nature of the material as the influential factors [11]. Similar observations were reported by Mc Farlane Mj and reported that the depth of induration of laterite profiles is due to water table fluctuations [12]. Mineralogy of the rocks and natural chemical stabilization (due to weathering) is responsible for the strength of these porous blocks. The induration of laterite is due to the development of constituent sesquioxides ( $\text{Fe}_2\text{O}_3$  and  $\text{Al}_2\text{O}_3$ ), precipitated, concentrated, and crystallized as a result of desiccation [13]. However, the significance of various chemicals and minerals present in the laterite soil towards strength gain of stabilized earthen blocks is yet to be studied.

As the characteristics of soil greatly vary according to particle sizes, a major challenge in the production of stabilized soil blocks is with respect to optimum soil grading limits influencing the strength and durability characteristics [14]. Hitherto, the documented research on compressed stabilized earth blocks indicates that all soils available in nature need improvements with respect to particle size proportions [15]. There are different recommendations for particle sizes that are suitable for earth construction. H. Danso conducted a review of different research on the suitability of particle size for adobe and reported desirable ranges for clay (0 % to 25 %), silt (0 % to 25 %), and sand (60 to 90 %) constituents [16]. Whereas the ranges suggested by L.P. Bengtsson and J.H. Whitaker are 20 % to 50 % for a combined proportion of clay-silt and 50 % to 80 % for sand particles [17]. But B.V. Venkatarama Reddy et al. restricted the upper range of clay as 14 % to 16 % suitable for stabilized mud blocks [18, 19]. C.A. Oyelami and J.L. Van Rooy [20] reviewed earlier findings and reported wide ranges for different constituents from various research. According to their review, clay content of about 23 % was reported by H. Houben and H. Guillaud [21], a range of 6 % to 30 % by V. Rigassi [22] and 5 % to 40 % clay content 10 % to 30 % silt, and 25 % to 80 % sand and fine gravel by M.C.J. Delgado and I.C. Guerrero [23]. It is clear from the above discussion that there is still no agreement between the different recommendations rather than suggesting a wide range for each constituent.

The main objective of this study is for finding out the optimum soil gradation for the production of stabilized building blocks from lateritic soil and also for investigating the significance of clay minerals and chemicals towards strength gain. Soil samples collected from different locations and depths are investigated for verifying the results.

## 2. Methods

Lateritic soils from four different locations of Cochin (Kerala, India), within a radius of 20 Km were collected and subjected to characterization studies. Stabilized lateritic blocks were made out of these samples with different mix proportions for finding out the suitability of stabilizers and gradation patterns. Optimization studies were conducted to identify the optimum gradation with respect to strength characteristics. Chemical and mineralogical characteristics of soil samples were also evaluated to investigate the influences. Details of experimental programs are illustrated in the following sections.

### 2.1. Materials

Lateritic soil (source material), river sand and quarry waste (as stabilizers with respect to the gradation of the source material), cement, and lime (stabilizers) were used. The properties of the materials are detailed below.

#### 2.1.1. Lateritic Soil

The soil samples used for this research are designated as S1, S2, S3, and S4 based on their locations. S1 sample was taken from Aluva (at an average depth of 3.50 m), S2 sample from Kakkanad (average depth of 1.50 m), S3, and S4 samples from different locations of Thrikkakkara from an average depth of 2.50 m and 4.50 m respectively. The samples were sieved through a 4.75 mm IS sieve and general properties were investigated (Table 1). The physical appearance of the soil samples is illustrated in Fig. 1.



**Figure 1. Pictures of the soil samples.**

**Table 1. Properties of lateritic soil samples.**

Properties	S1	S2	S3	S4
Colour	Blush red	Often red	Often red	Blush
Specific gravity	2.55	2.42	2.38	2.58
Liquid limit (%)	58	60	52	55
Plastic limit (%)	35	30	36	34
Shrinkage limit (%)	19.79	29	29	32
Plasticity Index (%)	23	30	17	21
pH value	4.73	4.49	4.55	4.22
Clay (%)	28	23	28	21
Silt (%)	18	15	16	20
Fine sand (%)	11	14	15	8
Medium sand (%)	23	32	24	34
Coarse sand (%)	20	16	17	17
Dry density (gm/cc)	1.64	1.64	1.64	1.67
Optimum moisture content	21	21	22	20

### 2.1.2. Sand & quarry waste

Sand and quarry waste passing through a 2 mm IS sieve and retaining on 425 microns IS sieve were used for modifying the gradation of soil samples as stabilizers. Properties of sand and quarry dust are tabulated in Table 2.

**Table 2. Properties of sand and quarry waste.**

Properties	River Sand	Quarry Dust
Specific gravity	2.61	2.8
Bulk density (g/cc)	1.47	1.18
% bulking	44	66
Porosity	0.37	0.42
Voids ratio	0.25	0.56
% Gravel	2.4	0
% Sand	98.8	86
% Silt	1.2	14
Fineness Modulus	3.23	2.38
Grading zone	Zone 1	Zone 2

### 2.1.3. Cement and lime

Commercially available 53 grade ordinary Portland cement and locally available shell lime were used as stabilizers.

## 2.2. Experimental Program

The experimental program was conducted through two stages. Initially, to investigate the suitability of the stabilizers and further for assessing the influence of soil gradation on strength gain. The significance of various chemicals and minerals present in the laterite soil towards strength gain was also assessed.

### 3. Results and Discussion

#### 3.1. Study on the suitability of stabilizers

The suitability of different stabilizers like sand, quarry waste, cement, and lime was investigated in this phase. Preliminary studies were conducted in S1 and S2 soil samples with cement and sand as stabilizers. Further, the studies were extended to S2, S3, and S4 samples with quarry dust and lime. Cement content was fixed as 8 % based on earlier studies [24–26]. Lime fixation studies were conducted based on previous researches and fixed the lime content [27, 28]. Mix designations and corresponding proportions of constituents with respect to different soil samples are shown in Table 3. Specified proportions of soil and stabilizers for each mix designation were taken and mixed thoroughly in a dry state to get a homogeneous mix. Optimum water content was determined and introduced to this mix, mixed well until a uniform consistency was obtained. The measured quantity of mix was then transferred to the mold of the manually operated block-making machine (ASTRAM) and compressed. The details of the block-making process are depicted in Fig. 2. The building blocks (190 mm × 110 mm × 100 mm) thus prepared were initially kept under a shade for 24 hours in a leveled platform and further subjected to 28 days of wet curing by covering with wet gunny bags. These building blocks after curing were subjected to different tests for density as per IS: 1725 -2013 [29], wet compressive strength as per IS: 3495 -Part I [30], and water absorption as IS: 3495 -Part II [31]. Results are presented in Table 4.



**Figure 2. Manufacturing process of Stabilized Lateritic soil block specimens.**

**Table 3. Mix designations and proportion.**

Sl No	Designation				Mix Proportion By Weight (%)				
	S1	S2	S3	S4	Soil	Sand	Quarry Dust	Cement	Lime
1	S <sub>10</sub> C <sub>8</sub>				90	10	–	8	–
2	S <sub>20</sub> C <sub>8</sub>				80	20	–	8	–
3	S <sub>25</sub> C <sub>8</sub>				75	25	–	8	–
4		A			100	–	–	8	
5		B	3X	4X	80	–	20	8	
6		RB			80	20		8	
7		C	3V	4V	75		25	8	
8		D	3Y	4Y	80		20	8	4
9		RD			80	20		8	4
10		E	3Z	4Z	75		25	8	4
11		RE			75	25		8	4

Preliminary studies conducted on the S1 sample gave satisfactory results for the stabilized lateritic block (S<sub>25</sub>C<sub>8</sub>, 3.60 N/mm<sup>2</sup>) using cement and sand as stabilizers. Whereas, in the S2 soil sample, quarry dust is additionally required for better results (B, 2.14 N/mm<sup>2</sup>). Improvement was further noticed on S2 blocks on lime stabilization (D, 3.16 N/mm<sup>2</sup>). Results of S1 and S2 samples indicate the influence of gradation on the suitability of stabilizers. Studies were extended to S3 and S4 soil samples to verify this.

Fig. 3 shows the variation in compressive strength of stabilized lateritic blocks made from the selected soil samples with their mix combinations giving maximum strength. On comparing the suitability of cement to cement- lime combination for stabilization, blocks made from S2, S3, and S4 showed better results for the latter in line with the low pH value of the soil samples. The strength characteristics of blocks from all the soil combinations except S4 samples showed significant variations in introducing quarry dust/sand as stabilizers but did not show a unique behavior regarding the quantity of stabilizer (sand/ quarry dust). This further justifies the significance of soil gradation in block making. Studies were extended to evaluate this influence and for identifying the optimization of gradation.

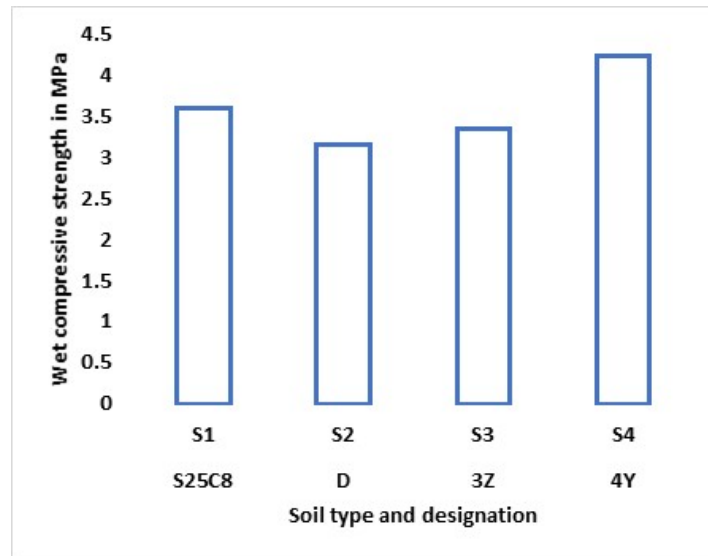


Figure 3. Selected mixes and Compressive strength of soil samples.

Table 4. Strength and durability properties of the stabilized lateritic blocks.

Sl No	Type of Soil	Designation	Test Results			
			Fresh Density (g/cc)	Dry Density (g/cc)	Wet Compressive Strength (MPa)	Water Absorption (%)
1	S1	S <sub>10</sub> C <sub>8</sub>	2.05	1.73	2.99	14.16
2	S1	S <sub>20</sub> C <sub>8</sub>	2.08	1.76	3.39	14.14
3	S1	S <sub>25</sub> C <sub>8</sub>	2.06	1.75	3.60	14.12
4	S2	A	1.94	1.67	1.72	14.72
5	S2	B	1.99	1.70	2.14	14.58
6	S2	RB	1.98	1.69	1.83	14.16
7	S2	C	1.98	1.69	1.94	14.63
8	S2	D	1.98	1.69	3.16	14.16
9	S2	RD	1.98	1.69	2.72	14.18
10	S2	E	1.98	1.69	2.98	14.16
11	S2	RE	1.98	1.69	2.57	14.15
12	S3	3X	2.01	1.70	2.16	14.18
13	S3	3Y	2.01	1.70	2.67	14.13
14	S3	3V	2.02	1.71	2.55	14.20
15	S3	3Z	2.03	1.72	3.35	14.14
16	S4	4X	2.00	1.70	4.10	14.12
17	S4	4Y	2.00	1.70	4.24	14.12
18	S4	4V	2.01	1.70	4.17	14.13
19	S4	4Z	2.00	1.70	4.22	14.12

### 3.2. Influence of soil gradation on strength gain

In this phase, quarry dust, cement (8 %), and lime (4 %) were selected as stabilizers based on the preliminary studies discussed above. Best mix combinations identified from each soil sample were selected and blocks were made and tested to confirm the results. In addition to this, one more combination was also tested in all samples by modifying the mix to restrict the clay content to the desired value of 15 % as reported by researchers [18, 19]. Since there were no considerable variations in the results of S4 samples, an additional mix was tested without adding quarry dust. The details of mix designations and gradation of soil samples before and after modification are tabulated in Table 5, and the results are presented in Table 6.

**Table 5. Mix designation and gradation of soil samples for optimization study.**

SI No:	Soil Type	Soil gradation before modification			Designation	Mix Proportion By Weight (%)		Soil gradation after modification		
		Sand	Silt	clay		Soil	Quarry dust	Sand	Silt	clay
1	S1	54	18	28	S1A	75	25	62	17	21
2	S1	54	18	28	S2B	54	46	69	16	15
3	S2	61	16	23	S2A	80	20	66	16	18
4	S2	61	16	23	S2B	66	34	70	15	15
5	S3	56	16	28	S3A	75	25	64	15	21
6	S3	56	16	28	S3B	54	46	70	15	15
7	S4	59	20	21	S4A	80	20	64	19	17
8	S4	59	20	21	S4B	72	28	67	18	15
9	S4	59	20	21	S4V	100	0	59	20	21

Results of all the soil samples were reconfirming the results of the preliminary studies. Also, S1, S3, and S4 samples were found to comply with the basic strength requirements as per IS 1725-2013. Whereas S2 showed slightly low values compared to the standards. Water absorption of the blocks was found lower and complies with Indian standards. The suitability of quarry dust over river sand was verified in the S1 sample. Whereas, the S4 sample confirmed the appropriateness of virgin soil over stabilized soil with respect to gradation. At the same time, modified mixes stabilized by restricting the clay content proved inferior among the selected combination.

**Table 6. Average measured strength and durability properties of soil samples.**

SI No:	Soil Type	Designation	Wet compressive strength (MPa)	Wet density	Dry density	Water absorption (%)
1	S1	S1A	3.98	2.02	1.72	14.12
2	S1	S1B	3.68	2.02	1.72	14.12
3	S2	S2A	3.13	2.02	1.72	14.14
4	S2	S2B	2.91	2.02	1.72	14.14
5	S3	S3A	3.50	2.02	1.72	14.15
6	S3	S3B	3.30	2.02	1.72	14.14
7	S4	S4A	4.47	2.01	1.72	14.14
8	S4	S4B	4.30	2.01	1.72	14.14
9	S4	S4V	4.68	1.99	1.70	14.18

**Table 7. Gradation of maximum strength gained lateritic soil sample after optimization.**

Serial No	Soil Sample	Designation	Before modification				After modification			
			Sand	Silt	Sand + Silt	Clay	Sand	Silt	Sand + Silt	Clay
1	S1	S1A	54	18	72	28	62	17	79	21
2	S2	S2A	61	16	77	23	66	16	82	18
3	S3	S3A	56	16	72	28	64	15	79	21
4	S4	S4V	59	20	79	21	59	20	79	21

Table 7 shows the gradation of selected mix combinations before and after modifications based on the above results. On examining the gradation of the optimized soil samples before and after modification, a uniqueness in the pattern in line with the strength gain can be noticed. Optimized mixes of S1, S3, and S4 showed a clay content of 21 % and a combined sand-silt content of 79 % in their modified gradation. The presence of high silt content observed in the S4 sample (20 %) justifies the significance of silt in strength characteristics. Variations in the results of S3 confirm this observation.

### 3.2.1. Statistical Analysis

Results obtained from the studies were statistically analyzed by linear correlation to establish the relationships between various variables and to determine their rate of dependence on each other. Fig. 4 illustrates the correlation of particles with strength.

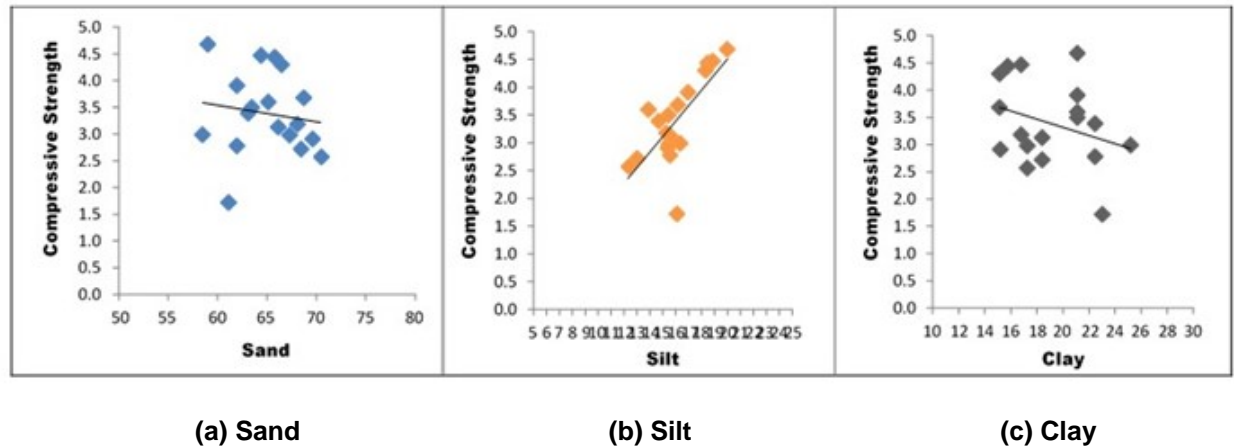


**Figure 4. Scatter plot showing the relationship between variables and Compressive Strength.**

Fig. 4 (a) showed only a negligible influence of sand content in the compressive strength of the blocks by representing it almost as a horizontal line with minimal slope. Whereas 4(b) showed a positive influence and 4(c) negative influence in terms of the presence of silt and clay respectively. Table 8 shows the correlation between different constituents and compressive strength. A high significance of silt was evident from the analysis with a p-value less than 0.05. However, the correlations of sand and clay particles were found insignificant with higher p-values.

This statistical analysis establishes a positive correlation and significance of silt content and a slight negative correlation with respect to clay content. On analyzing the results of experimental studies, it can be seen that maximum strength was reported for the sample with the highest silt content in concurrence with the results of statistical analysis. At the same time, soil samples with the lowest silt content did not give a result as projected by the statistical analysis. Sand being a mandatory component of soil like clay and silt, its elimination cannot be possible from the soil sample. This justifies the influence of sand + silt content as verified by experimental research (79 %). The silt content of the S4 sample (20 %) can be recommended as the optimized value for comparing the silt contents of other samples with respect to the strength of the blocks. Low values of the clay contents of the modified gradation compared to the original gradation justified the results of the statistical analysis. However, the S2 sample with the lowest clay content among the samples was behaving inferior. This indicated the significance of an optimum clay content (21 %) as verified by the experimental research.

**Table 8. Correlation analysis – influence of soil particles on compressive strength.**

Variable	Mean	Standard deviation	r - value	p - value
Sand	64.96	3.546	-0.140	0.581
Silt	15.98	1.995	0.722	0.001
Clay	19.06	3.118	-0.303	0.221
Compressive Strength	3.386	0.772		

### 3.3. Influence of chemical and mineralogical fraction of clay on strength gain

Even though the modified soil samples (S1, S3, and S4) showed similarity in gradation patterns, variations can be observed in the compressive strengths of corresponding building blockings. S4, the soil sample taken from the deepest source showed maximum strength compared to other soil samples. Strengths of S1, S2, and S3 were also found to vary in the same order corresponding to the source depths. Variations in clay mineralogy of collected soil samples from different depths can be considered as the reason. The strength of S2 also supports these observations and points towards the influence of clay

minerals along with gradation. As the presence of clay minerals varies in soil samples based on the depth of their source, the influence of clay minerals needs to be investigated.

Soil samples passing through a 75-micron sieve were subjected to energy dispersive X-ray spectrometry (EDAX) for identifying chemical composition and X-ray diffraction (XRD) for mineralogical analysis. Quantitative analyses were also carried out in both studies. The results of the EDAX analysis are presented in Table 9. Whereas Table 10 and Fig. 5–8 show the results of XRD analysis.

**Table 9. Chemical composition and oxides of lateritic soil samples.**

Soil Type	Al <sub>2</sub> O <sub>3</sub>	SiO <sub>2</sub>	Al <sub>2</sub> O <sub>3</sub> + SiO <sub>2</sub>	K <sub>2</sub> O	TiO <sub>2</sub>	Fe <sub>2</sub> O <sub>3</sub>	MgO
S1	41.34	46.41	87.75	0.86	1.42	9.38	0.61
S2	35.22	41.57	76.79	0.51	2.17	20.35	0.18
S3	37.82	46.79	84.61	0.49	2.36	11.79	0.75
S4	40.92	48.34	89.26	0.70	1.89	8.15	

Chemical analysis of soil samples showed a similar variation in the total content of Al<sub>2</sub>O<sub>3</sub> and SiO<sub>2</sub> as that of strength characteristics of the stabilized lateritic blocks made from the respective soil samples. At the same time, Fe<sub>2</sub>O<sub>3</sub> values were found to vary in the reverse order justifying its negative influence.

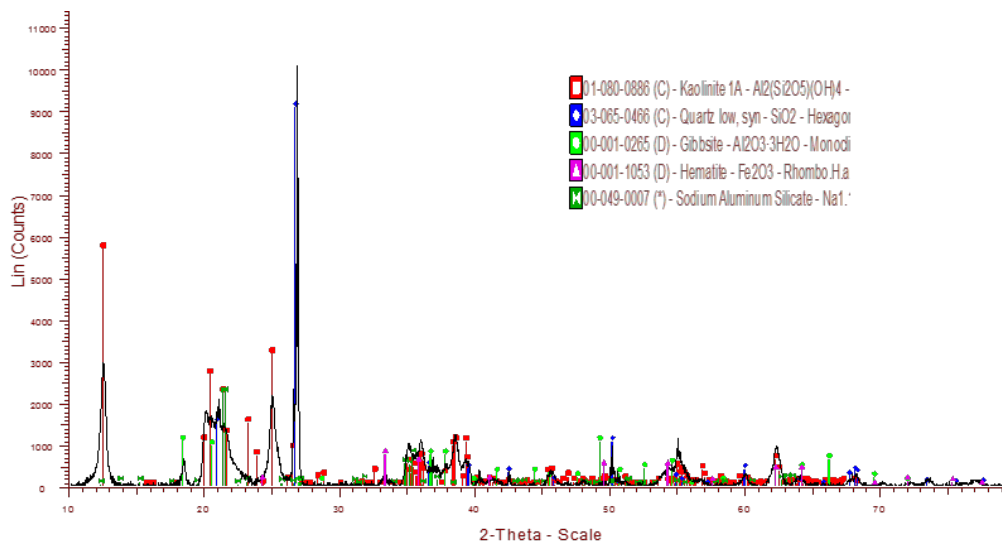


**Figure 5. X-ray diffraction pattern of soil sample S1.**

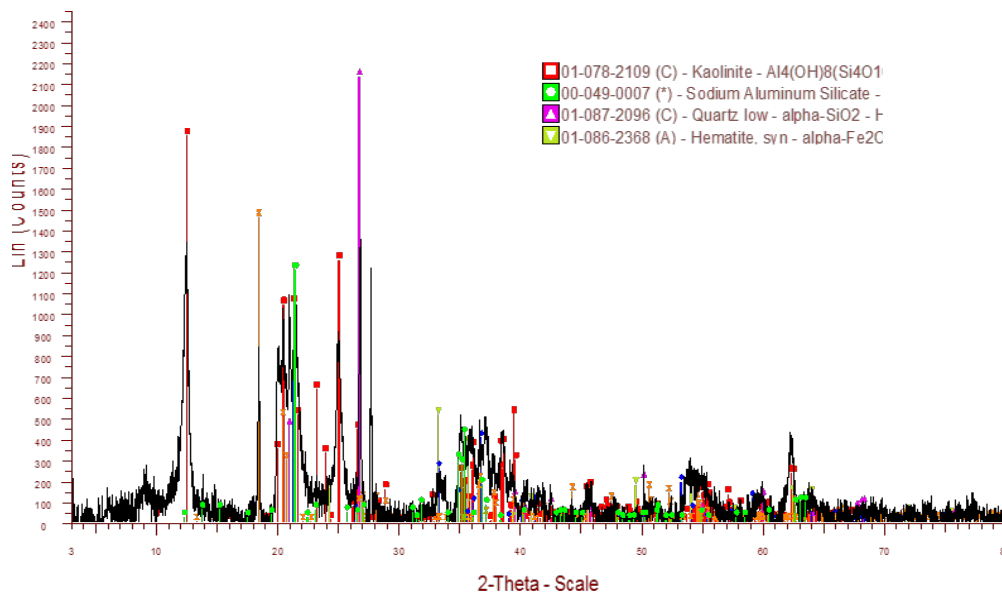


**Figure 6. X-ray diffraction pattern of soil sample S2.**

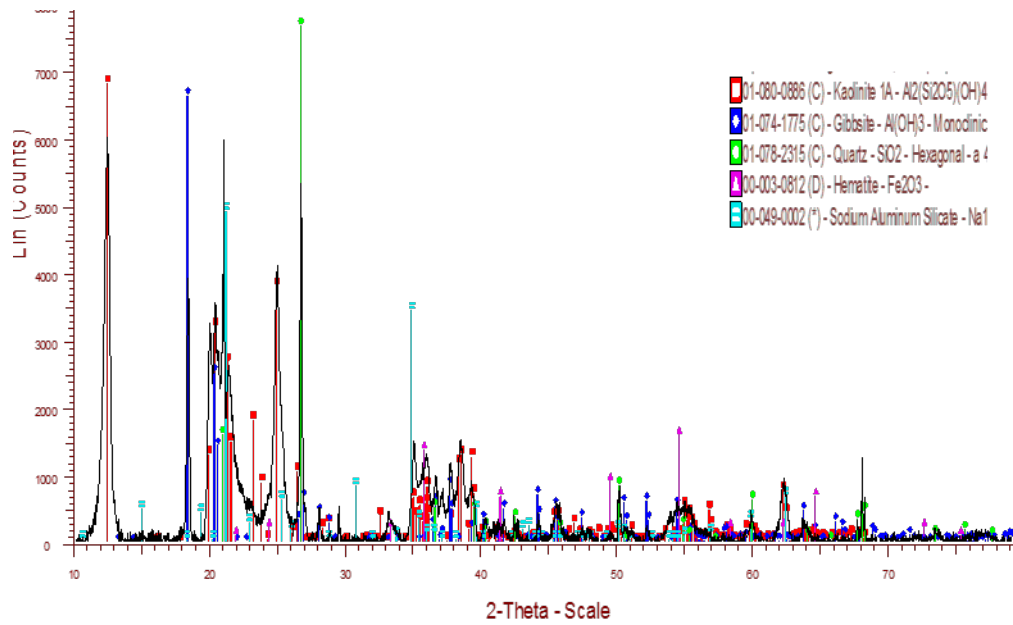


Figure 7. X-ray diffraction pattern of soil sample S3.

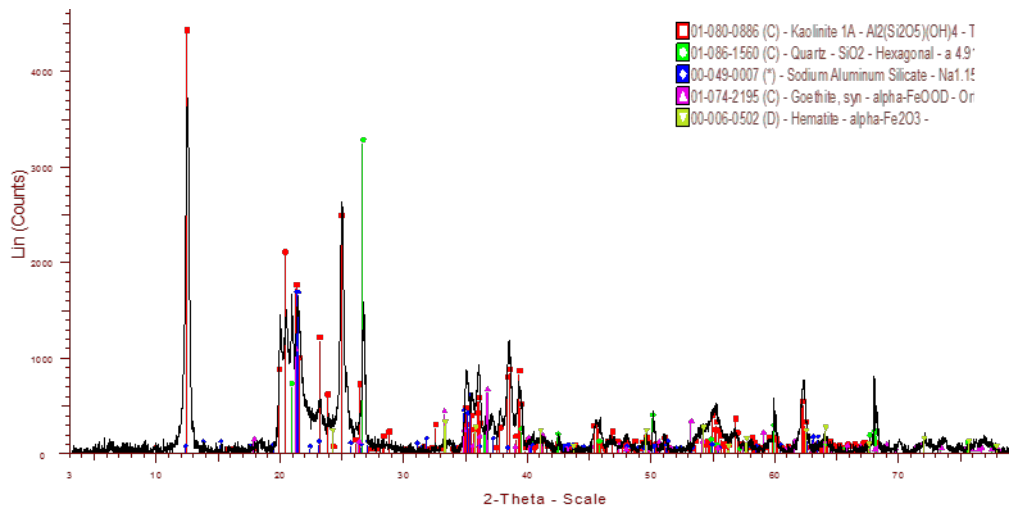


Figure 8. X-ray diffraction pattern of soil sample S4.

Table 10. Mineral composition of lateritic soil samples.

Soil Type	Kaolinite ( $Al_2Si_2O_5(OH)_4$ )	Quartz ( $SiO_2$ )	Hematite ( $Fe_2O_3$ )	Sodium aluminium silicon oxide ( $NaAlSi_3O_8$ )	Gibbsite ( $Al(OH)_3$ )
S1	82.85	4.43			12.72
S2	69.917	1.919	5.920	16.571	5.672
S3	72.22	3.74	2.06	11.84	10.14
S4	83.967	2.429	1.524	10.090	1.991

Table 10 and XRD patterns of the soil samples (Fig. 5–8) shows the presence of kaolinite ( $Al_2Si_2O_5(OH)_4$ ), gibbsite ( $Al(OH)_3$ ), sodium aluminium silicon oxide ( $NaAlSi_3O_8$ ), quartz ( $SiO_2$ ) and hematite ( $Fe_2O_3$ ) as the main minerals. Strength variation among the stabilized lateritic blocks was found to vary in the same order as that of kaolinite ( $Al_2Si_2O_5(OH)_4$ ) content in the respective soil samples similar to the observations on chemical composition. It is generally agreed that in a wetted soil-cement mixture, cement hydrates and cementitious products such as calcium-silicate hydrate (CSH) and calcium aluminate hydrate (CAH) are formed apart from the release of a small percentage of calcium hydroxide (lime) [19]. Alumina dissolves in the high pH environment created by the presence of lime. The major part of this dissolved alumina reacts and forms CAH and CASH phases [32]. The presence of the hydroxides of silica and alumina was evident in the identified minerals of soil samples in different compositions. This also contributes to strength characteristics.

The presence of hematite ( $\text{Fe}_2\text{O}_3$ ), as identified by XRD analysis was found to influence the strength in the reverse order. Soil samples collected from deep sources were having comparatively low iron content and showed more strength than that from lower depths with higher iron content. The colour of the soil samples were varying from bright red to pale red corresponding to the iron content.

Even though the presence of quartz is visible in all soil samples, the identified clay minerals contributed to the formation of cementitious phases, actively reacting with stabilizers (cement and lime) and thus resulting in strength gain.

#### 4. Conclusion

Source materials for lateritic soil blocks comprise different particle fractions such as sand, silt, and clay. Each of these components has its role in strength development. This study established a positive correlation and significance of silt content with an optimum value of 20 %. However, a combined influence of sand and silt was found more significant than individual influences. The optimum clay content of 21 % was also verified through experimental research. Thus the recommended gradation for locally available lateritic soil can be suggested as sand – 59 %, silt – 20 %, and clay – 21 %. These results are thus helpful in standardizing the production of stabilized lateritic soil masonry blocks.

This investigation also verified the influence of source depths on the strength characteristic of stabilized lateritic blocks. Based on the depth of extraction, chemical and mineralogical compositions of the soil samples vary. Soil samples from deeper sources showed higher strength compared to those from lower depths due to a higher concentration of oxides of alumina, silica, and kaolinite minerals. Experimental studies also verified the combined effects of  $\text{Al}_2\text{O}_3$  and  $\text{SiO}_2$  in the development of cementitious properties and strength gain. The presence of kaolinite minerals had a positive influence and hematite was found to have a negative influence on the strength gain.

These investigations could thus establish a clear guideline for gradation and combined effects of chemical-mineralogical compositions of the source material in the strength gain of masonry blocks made from lateritic soil.

#### References

- Maignien, R. Review of research on laterite. IV. France, Natural Resource Research, United Nation, 1966. 156 p.
- Gidigas, M.D. Laterite Soil Engineering: Pedogenesis and Engineering Principles. Amsterdam, Elsevier Scientific Publication Company, 1976. 554 p.
- Narayanaswamy, Ghosh, S.K. Lateritisation of gabbro-granophyre rock units of the Ezhimala Complex of north Kerala, India. Chemical Geology. 1987. DOI: 10.1016/0009-2541(87)90130-6
- Kasthurba, A.K., Santhanam, M., Mathews, M.S. Investigation of laterite stones for building purpose from Malabar region, Kerala state, SW India – Part 1 : Field studies and profile characterisation. 2007. 21. Pp. 73–82. DOI: 10.1016/j.conbuildmat.2005.07.006
- Kasthurba, A.K., Santhanam, M., Achyuthan, H. Investigation of laterite stones for building purpose from Malabar region, Kerala, SW India – Chemical analysis and microstructure studies. 2008. 22. Pp. 2400–2408. DOI: 10.1016/j.conbuildmat.2006.12.003
- Tardy, Y., Kobisek, B., Paquet, H. Mineralogical composition and geographical distribution of African and Brazilian peritropical laterites. The influence of continental drift and tropical paleoclimates during the past 150 million years and implications for India and Australia. Journal of African Earth Sciences. 1991. DOI: 10.1016/0899-5362(91)90077-C
- Frank C. Townsend, M. Geotechnical Characteristics of Residual Soils. Journal of Geotechnical Engineering. 1985. 111 (1). Pp. 77–94. URL: [https://doi.org/10.1061/\(ASCE\)0733-9410\(1985\)111:1\(77\)](https://doi.org/10.1061/(ASCE)0733-9410(1985)111:1(77))
- Syafalni, Lim, H.K., Ismail, N., Abustan, I., Mursheed, M.F., Ahmad, A. Treatment of landfill leachate by using lateritic soil as a natural coagulant. Journal of Environmental Management. 2012. DOI: 10.1016/j.jenvman.2012.08.001
- Mitchell, James Kenneth, K.S. Fundamentals of soil behavior. 3<sup>rd</sup> ed. New York, John Wiley and Sons, 2005. 577 p.
- Gidigas, M.D. Mode of formation and geotechnical characteristics of laterite materials of Ghana in relation to soil forming factors. Engineering Geology. 1972. DOI: 10.1016/0013-7952(72)90034-8
- Narayanaswamy, A.H., Mcgregor, F., Millogo, Y., Fabbri, A. Physical, Mechanical and Hygrothermal Properties of Lateritic Building Stones (LBS) from Burkina Faso. 2016. (November 2017). DOI: 10.1016/j.conbuildmat.2016.08.082
- McFarlane, M.J. Laterite and landscape. London, Academic Press, 1976.
- Varghes, T., Byju, G. Laterite soils – their distribution, characteristics and management. Technical Monograph No. 1. Thiruvananthapuram, India, 1993. 116 p.
- Venkatarama Reddy, B.V., Latha, M.S. Influence of soil grading on the characteristics of cement stabilised soil compacts. Materials and Structures/Materiaux et Constructions. 2014. 47 (10). Pp. 1633–1645. DOI: 10.1617/s11527-013-0142-1
- Nagaraj, H.B., Rajesh, A., Sravan, M.V. Influence of soil gradation, proportion and combination of admixtures on the properties and durability of CSEBs. Construction and Building Materials. 2016. 110. DOI: 10.1016/j.conbuildmat.2016.02.023
- Danso, H. Suitability of Soil for Earth Construction as Building Material. 2018. (December). DOI: 10.31031/ACET.2018.02.000540
- Bengtsson, L.P., Whitaker, J.H. Farm structures in tropical climates. Rome, Italy, FAO/SIDA COOPERATIVE PROGRAMME, 1988.
- Venkatarama Reddy, B.V. Stabilised soil blocks for structural masonry in earth construction. Modern Earth Buildings Materials, Engineering, Constructions and Applications. Woodhead Publishing, 2012. Pp. 324–363.
- Reddy, B.V.V., Latha, M.S. Applied Clay Science Retrieving clay minerals from stabilised soil compacts. Applied Clay Science. 2014. 101. Pp. 362–368. DOI: 10.1016/j.clay.2014.08.027. URL: <http://dx.doi.org/10.1016/j.clay.2014.08.027>

20. Oyelami, C.A., Van Rooy, J.L. Geotechnical characterisation of lateritic soils from south-western Nigeria as materials for cost-effective and energy-efficient building bricks. *Environmental Earth Sciences*. 2016. DOI: 10.1007/s12665-016-6274-1
21. Houben, H., Guillaud, H. *Earth construction: a comprehensive guide* 1994.
22. Rigassi, V. *Compressed earth blocks : Manual of production*. 1985. ISBN: 3528020792.
23. Delgado, M.C.J., Guerrero, I.C. Earth building in Spain. *Construction and Building Materials*. 2006. 20 (9). Pp. 679–690. DOI: 10.1016/j.conbuildmat.2005.02.006
24. Reddy, B.V.V., Gupta, A. Strength and elastic properties of stabilized mud block masonry using cement-soil mortars. *Journal of Materials in Civil Engineering*. 2006. 18 (3). Pp. 472–476. DOI: 10.1061/(ASCE)0899-1561(2006)18:3(472)
25. Sreekumar, M.G., Nair, D.G. Stabilized lateritic blocks reinforced with fibrous coir wastes *Methodology of Research*. *International Journal of Sustainable Construction Engineering & Technology*. 2013. 4 (2). Pp. 23–32.
26. Sreekumar, M G, D.G.N. Mechanical Properties of Stabilized Lateritic Soil Blocks with Fibrous Waste Additives. *International Journal of Sciences: Basic and Applied Research (IJSBAR)*. 2018. 8 (12). Pp. 336–350.
27. Eades, J.L., Grim, R.E. *A Quick Test to Determine Lime Requirements For Lime Stabilization* 1960.
28. Ciancio, D., Beckett, C.T.S., Carraro, J.A.H. Optimum lime content identification for lime-stabilised rammed earth. *Construction and Building Materials*. 2014. DOI: 10.1016/j.conbuildmat.2013.11.077
29. Bureau of Indian standards. IS 1725 : 2013 (Reaffirmed Year : 2019) *Stabilized Soil Blocks used in General Building Construction – Specification*. New Delhi, Bureau of Indian standards, 2013.
30. Bureau of Indian standards. Determination of compressive strength. IS: 3495 (Part 1): 2019 *Methods of test of burnt clay building bricks*. New Delhi, Bureau of Indian standards, 2019.
31. Bureau of Indian standards. Burnt Clay Building Bricks — Methods of Tests Part 2 Determination of Water Absorption (Fourth Revision). IS 3495 : Part 2 : 2019. New Delhi, Bureau of Indian standards, 2019.
32. Billong, N., Melo, U.C., Louvet, F., Njopwouo, D. Properties of compressed lateritic soil stabilized with a burnt clay-lime binder: Effect of mixture components. *Construction and Building Materials*. 2009. DOI: 10.1016/j.conbuildmat.2008.09.017

**Information about authors:**

**Moothattu Govindan Nair Sreekumar,**

ORCID: <https://orcid.org/0000-0002-0324-222X>

E-mail: [sreekuair@cusat.ac.in](mailto:sreekuair@cusat.ac.in)

**Deepa G. Nair, PhD**

ORCID: <https://orcid.org/0000-0003-1644-6317>

E-mail: [deepagnair@cusat.ac.in](mailto:deepagnair@cusat.ac.in)

**Kaup S. Jagadish, PhD**

E-mail: [ksjagadish@gmail.com](mailto:ksjagadish@gmail.com)

*Received 02.05.2021. Approved after reviewing 12.07.2022. Accepted 13.07.2022.*



Research article

UDC 669.04.004.58(075.8)

DOI: 10.34910/MCE.117.5



## Diagnostics and reconstruction of bearing units

A.A. Ishchenko<sup>1</sup> , V.V. Butsukin<sup>1</sup> , V.G. Artiukh<sup>2</sup> , N.V. Chernysheva<sup>2</sup>  

<sup>1</sup> Pryazovskyi State Technical University, Mariupol

<sup>2</sup> Peter the Great St. Petersburg Polytechnic University, St. Petersburg, Russia

 [chernat0000@mail.ru](mailto:chernat0000@mail.ru)

**Keywords:** diagnostics, foundation, bearing, vibration, constructing, repair, composite material, construction machine

**Abstract.** This paper presents new research results aimed at ensuring reliability and durability of equipment due to its diagnostics including monitoring and recording parameters changes of bearing units technical conditions determined before the moment of equipment shutdown, dismantling and fault detection of units as well as development of new methods for their restoration. As a method of operability recovery of unique bearing units a progressive approach is offered based on use of composite material 'Multimetal Stahl 1018'. A new field of application of composite material 'Multimetal Stahl 1018' to create temporary bearing sliding support instead of failed unique design construction with rolling bearings is described. Successful operation of majority of industrial equipment units restored using composite materials evidences broad prospects for solving various repair tasks mechanics of repair industries face including protection of foundations from destruction during vibration loads.

**Funding:** The research is partially funded by the Ministry of Science and Higher Education of the Russian Federation as part of the World-class Research Center program: Advanced Digital Technologies (contract No. 075-15-2022-311 dated 20.04.2022).

**Citation:** Ishchenko, A.A., Butsukin, V.V., Artiukh, V.G., Chernysheva, N.V. Diagnostics and reconstruction of bearing units. Magazine of Civil Engineering. 2023. 117(1). Article no. 11705. DOI: 10.34910/MCE.117.5

### 1. Introduction

Reliability and durability of equipment are determining factors for sustainability of any production based on use of continuous production cycles. Ensuring compliance of mechanical equipment with requirements of reliability and durability largely depends on maintaining operating condition of bearing assemblies [1]. Certain system of equipment maintenance has been developed at industrial enterprises that regulates procedure for carrying out work related to operation of bearing assemblies. Part of work is carried out by divisions of enterprises, extraordinary operations are usually carried out by specialized contractors. Diagnostics of mechanical equipment to ensure its trouble-free operation and, in particular, state of its bearing assemblies in combination with modern methods of restoring their performance has become increasingly widespread.

Large number of scientific works devoted to identification of damages of mechanical equipment bearing assemblies has been carried out [1–4]. Types of bearing assemblies damages are usually divided according to location of defects. Following main defects are distinguished: damages of rings, damages of cages, damages of rolling elements, etc. However, the same type of damage localized in different places can be caused by different reasons. Consequently, use of such classification for identifying causes of damage of machine elements, in particular rolling bearings, cannot guarantee acceptable accuracy. It is proposed to identify force effect on detail to determine cause of failure. Nature of wear of equipment detail

will depend on type of force and its direction. Appearance of failed detail surface is closely related to nature of its wear arising in damaged unit. It is possible to classify type of force action according to following types: circulating load (shaft imbalance); local load (gravity); axial load (axial forces arising in bevel gearing); load from misalignment of assembly details (misalignment of bearing and shaft) [5–8].

This classification allows localization of damage. Types of damage are proposed to be subdivided into:

1. mechanical ones are fatigue failure, abrasive wear, plastic deformation;
2. molecular mechanical ones are adhesive, selective transfer;
3. corrosion-mechanical ones are, in particular, oxidative wear.

Prevention of these and other types of destruction is the main task of diagnostics. To monitor technical condition of supporting elements of mechanical equipment, in general case, following diagnostic parameters are used [9]:

- visual inspection, including measurement of linear dimensions;
- control of machine noises;
- unit temperature control;
- lubricant analysis;
- analysis of drive current characteristics;
- measurement of vibration parameters.

Visual inspection usually allows identifying already developed damages, e.g. extrusion of end caps arising at the last stage of destruction of bearing assemblies. This method does not represent significant value from point of view of early diagnosis.

Mechanism noise control is based on subjective organoleptic sensations of specialists and allows getting high-quality picture of bearings conditions at 'good-bad' level. Under conditions of working equipment it is impossible to ensure effective listening to noise with help of stethoscope because according to labor protection rules it cannot be, e.g. on moving crane. In addition, experience of operating steel casting cranes has shown that the most likely damage is on internal (relative to the crane beams) bearings which are practically inaccessible for listening. One solution is to use ultrasonic stethoscopes manufactured by SKF.

Controlling temperature of bearing units can be effective if there is insufficient amount or inconsistency of grade of lubricant used at intensive stage of destruction of bearing unit elements during prolonged (more than 1 hour) operation of mechanism. Such solution is possible on practice but it is very difficult to provide:

- placing temperature sensors directly inside bearing assembly and ensuring reliable signal transmission to measuring device in existing production conditions;
- installation of sensors on equipment which has not place for installation of diagnostic devices.

It is preferable to use non-contact temperature measurement methods using pyrometer or thermal imager for temperature control. However, problem of control of hard-to-reach units (e.g. internal (relative to crane beams) bearings of running wheels of casting crane) is also not solved.

Lubrication analysis involves performing control operations of lubricant flow into friction zone and determining quality of lubricant. Problem of sampling lubricant from bearing housings during their operation is practically insoluble which makes this method inapplicable in real operation conditions.

Analysis of drive current characteristics on practice of support units diagnostics of equipment has not found wide application because it requires use of systems for recording electrical parameters of drive in production conditions which is difficult to implement on equipment. In addition, it needs involvement of qualified personnel to analyze obtained records in conjunction with technological processes and emerging loads in mechanical system.

Above analysis based on well-known publications showed that the most acceptable data sets in real operating conditions (allowing to assess condition of units with rolling bearings) are vibration parameters taking into account such factor as their negative impact on durability of foundations. Measurement of vibration parameters as effective method for detecting malfunctions of mechanical systems is widely used in practice of operating mechanical equipment [1–4, 6–10]. Well-developed algorithms and diagnostics standards including bearing assemblies are based on measurement of vibration parameters. However, experience of operating mechanical equipment has shown that this method also has limitations in terms of assessing state of bearing assemblies in specific operating conditions of construction industry. There are

cases when with favorable vibration parameters bearing units of critical equipment suddenly failed during absence of their obvious overload by external forces which could very likely be a consequence of deformation of foundation supports and, as a result, it resulted in uncontrolled misalignment of mechanism. As a rule such incidents remain in materials of factory investigations of accidents causes of operating equipment and are not subjected to thorough analysis and, accordingly, remain unknown to operational and design personnel involved in ensuring use and design of mechanical equipment. Familiarization with the results of investigations of such accidents will, from point of view of authors of this paper, improve work on ensuring reliable and durable use of mechanical equipment.

As it was mentioned above, condition for ensuring stable operation of construction industry is use of diagnostics of mechanical equipment and state of its bearing assemblies in combination with modern methods of restoring their performance. There is a problem associated with uniqueness and high cost of mechanical equipment bearing assemblies which makes it economically inexpedient to manufacture replaceable set of spare parts in advance or use reserve piece of equipment [1] during restoration of defective surfaces of mechanical equipment bearing assemblies. There is a danger of prolonged downtime of equipment which determines possibility of fulfilling production program of any enterprise in the event of premature or unpredictable failure of such units. This is due to need to wait for unique unit newly manufactured at machine-building enterprise (e.g. pins of support ring of oxygen converter) or with sufficiently long recovery cycle of expensive unit (e.g. custom-made gearbox housing). In the latter case, classical recovery technology is used including dismantling of defective assembly followed by transportation to mechanical workshop to remove defective fragments by machining, restoration of metal surface by cladding, heat treatment and finishing machining to achieve nominal size. At the same time, experience of solving problems of restoring various units using composite materials [1] or using composite elastomers [11, 12] is known. Use of composite materials to restore performance of unique and expensive bearing assemblies of mechanical equipment allows, in some cases, to solve problem arising from sudden failure of unique assembly with long production time and significantly reduce recovery time for single-piece products.

New results obtained during the performance of works to ensure the equipment reliability and durability can be shown. The complex of works comprise stages from diagnostics, that includes monitoring and recording of the parameters changes of bearing assemblies technical conditions, to determination of the equipment shutdown moment, disassembly and detection of assemblies, selection and assignment of a recovery method. Problem of assessing applicability of monitoring vibration parameters for determining performance of bearing assemblies is considered on example of wheel assemblies of steel casting crane. Problem of restoring unique and expensive bearing assemblies of mechanical equipment was solved in two versions, namely, temporary solution to restore operability of bearing support of support ring trunnion of the steelmaking converter and complete restoration of operability of worn surfaces being in contact with bearing of reducer of screw-down mechanism of hot thick strip rolling mill rolling stand. Progressive approach based on use of composite material 'Multimetal Stahl 1018' was used as method of restoring operability of bearing assemblies.

## 2. Methods

Steel casting crane is moved by four movement mechanisms where two ones are on each side of bridge. Each drive of the travel mechanism consists of an electric motor, a brake and a gearbox connected to driven wheel. The driven wheels of the crane are located in non-driven and driven balancing trolleys to main balancers. The main balancers are pivotally connected to the bridge. Wheels are installed in roll-out axle boxes connected to trolley frames. During operation of the crane there were sudden failures of the running wheel bearings with jamming of the mechanism and violation of technological sequence of steel smelting. During elimination of consequences by shop personnel reasons for sudden failures were not identified and therefore task was set to assess performance of units using vibration diagnostics methods.

To determine vibration parameters in the bearing assemblies of the driven wheels of the movement mechanism of the steel casting crane following instruments were used: 795 M vibration spectrum analyzer, vibrometer 107 B. Sensor is mounted using a magnet. The sensor installation place is on the driven wheel bearing assembly. The sensor orientation is in vertical direction.

Measurements were carried out in several frequency ranges: 2...400 Hz, 2...1000 Hz, 10...1000 Hz, 10...2000 Hz, 10...4000 Hz. Lower limit of ranges was determined being based on basic informative frequencies of bearing 3632 that has following data: rotation frequency (at nominal speed of the crane movement)  $f_{rot} = 3$  Hz; number of rolling bodies  $z = 15$ ; diameter of rolling elements  $d = 45$  mm; contact angle  $\alpha = 14^\circ$ ; diameter of circle passing through centers of rolling elements  $D = 250$  mm. Calculation based on known dependencies [10] showed that frequency associated with damage to:

- outer ring is 18.5 Hz;

- inner ring is 26.4 Hz;
- rolling elements is 16.1 Hz;
- separator is 1.2 Hz.

Repair of bearing assemblies was carried out according to:

- temporary option for destroyed roller spherical double-row bearing on trunnion of support ring of the 300 tons converter from drive side;
- full restoration option of operability for worn surfaces being in contact with bearings of screw-down mechanism reducer of hot thick strip rolling mill rolling stand.

Standard measuring tools such as calipers, micrometers, internal micrometers, locksmith rulers and sets of probes were used to assess size of defects in bearing assemblies as well as dimensions of technological equipment used for repairs and reconditioned surfaces.

### 3. Results and Discussion

In described case of studying vibration parameters of bearing assemblies of running wheels of steel casting crane choice of control points for measuring vibration was decided unambiguously due to design of bearing assembly. All wheel bearings are installed with transition fit and without bushes. Loading zone of external force and support reaction are located in the upper part of rings. Therefore, sensor for measuring vibration parameters must be located on top, in radial direction, vertically, in the middle of bearing.

Preliminary measurements of vibration parameters were carried out on operating equipment when the crane was moving without load to select frequency range and vibration parameters.

Spectral analysis of vibration parameters data obtained during experiment indicates quasi-polyharmonic composition of vibration signal with broadband components of shock processes. Spectrum contains components with frequencies: 6 Hz, 40 Hz, 50 Hz, 75 Hz, 86 Hz, 97...100 Hz, 120...123 Hz, 177...200 Hz, 256 Hz, 300...315 Hz, 400...444 Hz, 525 Hz, 1395 Hz, 1985 Hz, 2339 Hz, 2870 Hz, 3262 Hz, 4024 Hz. Signal is modulated by frequencies: 5...6 Hz, 24...27 Hz, 82 Hz.

Numerical results of eleven measurements of vibration parameters of the running wheel outer bearing using equipment described above are given in Tab. 1. The Tab. shows frequency ranges of measurements, root mean square values (RMS) of corresponding parameters and peak values of vibration acceleration recorded during the experiment.

Disassembly of failed bearing assembly of the running wheel during repair showed presence of traces of thickening and oxidation of lubricant (so-called 'lubricant coking'). General view of this unit is shown on Fig. 1. Traces of the bearing rotation in its housing were revealed on the outer surface of the outer ring of the bearing.

Below there is example of repairing a bearing assembly that has failed as a result of coking lubricant. As mentioned above, the repair of the bearing assembly according to the temporary option was carried out for surfaces being in contact with destroyed spherical double-row roller bearing on the trunnion (850 mm in diameter) of the bearing ring of the 300 tons converter from the drive side (refer to Fig. 2).

**Table 1. Vibration parameters measurement results.**

#	Frequency range, Hz	Vibration displacement, RMS, $\mu\text{m}$	Vibration speed, RMS, mm/s	Vibration acceleration, RMS, $\text{m/s}^2$	Vibration acceleration, peak, $\text{m/s}^2$
1	2...400	5.7	0.10	0.004	–
2	2...400	5.7	0.10	0.004	–
3	2...400	78.0	1.30	0.070	0.3
4	2...1000	263.0	43.40	0.800	–
5	2...1000	477.0	75.70	1.200	–
6	10...1000	603.0	44.70	1.800	2.1
7	10...1000	12.0	0.90	0.100	–
8	10...2000	14.0	1.30	0.200	–
9	10...4000	6.0	0.46	0.390	4.1
10	10...4000	10.0	1.00	0.400	–
11	10...4000	35.0	2.40	0.300	–



**Figure 1. Coking traces of lubricant on the running wheel bearing details.**



**Figure 2. Surface of the trunnion of the converter support ring after the destruction of the bearing.**

The unit is slow-moving (about 1 rpm) so its failure was not diagnosed in a timely manner. Due to its degree of damage done to the trunnion seating surface was very high. As it is seen on Fig. 2, the trunnion surface after contact with destroyed bearing elements and rollers is covered with dents and has noticeable wear of outer diameter surface. Such damage done to the bearing seat on the trunnion makes it impossible to further use the trunnion without dismantling and subsequent laborious restoration.

Considering that the trunnion is made as one piece with the converter support ring solution seems to be obvious. It is to order a new ring and a new bearing keeping in mind its unique characteristics both in size and design. But this rather long way did not exclude necessity of putting the converter into operation with some kind of temporary technical solution until moment of overhaul with installation of a new support ring and bearing.

It was decided on this support to switch temporarily to a sleeve bearing. To implement this idea it was necessary to restore the trunnion surface and install assembled cage on it which would subsequently be used as trunnion surface being in contact with inserts of sliding bearing. It was proposed using composite material 'Multimetall Stahl 1018' produced by company 'Diamant Metallplastik GmbH'. Technical characteristics of 'Multimetall Stahl 1018' are given in Tab. 2 [13, 14].

**Table 2. Technical characteristics of 'Multimetall Stahl 1018'.**

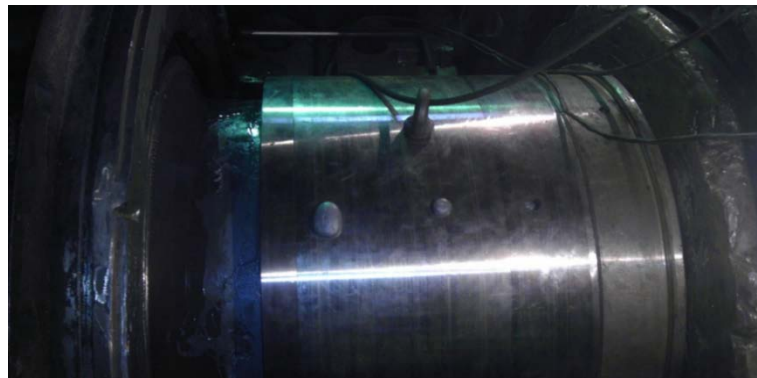
Compressive strength	N/mm <sup>2</sup>	max 160
Tensile strength	N/mm <sup>2</sup>	76
Shear strength	N/mm <sup>2</sup>	89
Bending strength	N/mm <sup>2</sup>	22
Elastic modulus	N/mm <sup>2</sup>	14.000
Linear elongation ratio		$32 \times 10^{-6} \text{ } ^\circ\text{K}$
Long-term temperature resistance	$^\circ\text{C}$	- 40 / + 90
Resistant to aging and weathering		very good
Processing time at +20 $^\circ\text{C}$	min	~ 45
Hardening at +5 $^\circ\text{C}$	hour	~ 72
Hardening at +20 $^\circ\text{C}$	hour	~ 24
Specific weight	gram/cm <sup>3</sup>	2.4

However, doubts arose whether the material could withstand part of weight of the converter with steel acting on the support. Theoretical calculations have confirmed possibility of using the composite when temperature of contact details does not exceed 80  $^\circ\text{C}$ . Preliminary temperature measurements showed that its values within area of the trunnion do not exceed 60  $^\circ\text{C}$ , hence restoration of the bearing surface of the trunnion was performed using the composite. Technology of using the composite and restoring the trunnion is illustrated on Fig. 3. The stages of this work included: degreasing the trunnion surface, preliminary installation of two parts of assembled cage 50 mm thick on base screws and centering it along axle of the trunnion, then dismantling the cage, applying the composite material (refer to Fig. 3a) and subsequent installation of the cage on the base screws with further connection of both parts with screws installed in

recesses relative to their working surface. Excess of the composite is visible, squeezed out through control holes which confirms complete filling with the composite of cavity between the old trunnion and inner surface of the cage (refer to Fig. 3b).



a)

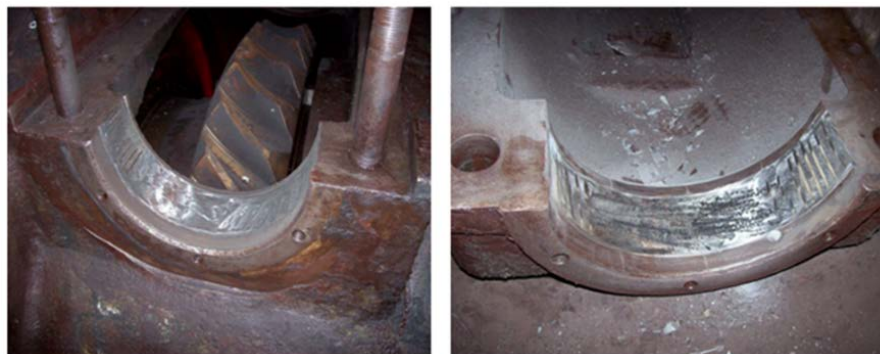


b)

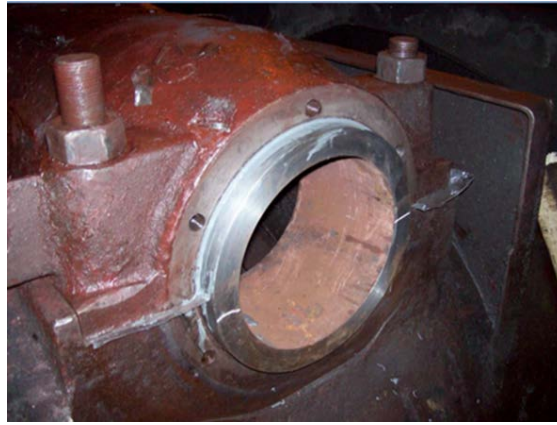
**Figure 3. Stages of the trunnion restoration: a) the composite application; b) installation of the assembled cage.**

Rebuilt according to this temporary scheme unit worked from March to June and was dismantled due to failure of the composite material because temperature in zone where the composite was located increased (when outside temperature increased) and during its destruction it was around 140 °C.

Complete restoration of operability of housings worn surfaces being in contact with rolling bearings is described using example of restoration of the screw-down mechanism reducer housings of the hot thick strip rolling mill rolling stand. The housings worn surfaces of the screw-down mechanism reducer are shown on Fig. 4. Standard technology for restoring those surfaces requires dismantling worm gear and transporting the reducer housings to machine shop for restoration. In this case, use of the composite material 'Multimetal Stahl 1018' made it possible to abandon operations performed in the mechanical shop. For this specially made polished template with diameter equal to diameter of outer ring of bearing was processed with special separator and after applying the composite to machined groove the template was installed on unworn surfaces being in contact with rolling bearing on both of the housings (refer to Fig. 4b).



a)



b)

**Figure 4. Restoration of housings worn surfaces being in contact with rolling bearing of the screw-down mechanism reducer housings of the hot thick strip rolling mill rolling stand: a) worn surfaces of the housings; b) formation of support surfaces using the specially made polished template.**

After 16 hours of complete polymerization of the composite the template was removed, excess of extruded and hardened composite was also removed. Restored housings worn surfaces are shown on Fig. 5. Restored unit was returned for another restoration after 3 years of operation.



a)



b)

**Fig. 5. Restored housings worn surfaces being in contact with rolling bearing: a) bottom housing; b) top housing.**

From data given in Table 1 it is clear that overall level of vibration parameters (except cases 4-6 in terms of vibration speed and vibration displacement) is low. Thus, RMS of vibration speed in most observations remain within limits corresponding to good technical condition of casting cranes that is less than 2.8 mm/s [9]. Cases 4-6 (where range of values is over 18 mm/s) correspond to unsatisfactory technical condition [9] and they can be apparently associated with insufficiently reliable fastening of the vibration sensor (using a magnet) which leads to jumps in readings when the casting crane passing joints of its rails.

In low-frequency region of spectrum which includes informative frequencies of bearings used in running wheel assemblies all recorded parameters have significant scatter of values, i.e. ratio of the highest value of RMS parameters to the lowest is around ten or more times. At the same time, in measurement range from 10 to 4000 Hz RMS vibration accelerations are quite stable, i.e. ratio of the highest RMS value to the smallest is approximately 1.3 with peak value exceeding RMS by about 10–13 times. For the first stage of further research it is advisable to use specified measurement range (from 10 to 4000 Hz) with vibration acceleration control as a parameter giving relatively stable readings. To assess effectiveness of proposed measures to improve monitoring system of technical condition of running wheels bearings it is necessary to carry them out for at least 6-12 months with statistical analysis of obtained results and subsequent refinement of monitoring method and frequency range of controlled parameters.

Failure of running wheel bearings at moderate vibration rates of the unit may be due to phenomenon of thickening and oxidation of lubricant ('lubricant coking') revealed during disassembly of defective unit shown on Fig. 1. On the investigated crane this phenomenon was noted: in bearings located on side of heat effect acting from moving ladle with hot steel leading to elevated temperature of the bearing assembly

details and in irrational lubricant supply device designed during development of the crane. Coking of the lubricant leads to increase of torque of resistance between rolling elements of bearing and their rolling path; the torque of resistance becomes greater than torque fixing fit of the bearing outer ring in the bearing housing which ultimately leads to wear of the bearing seat and appearance of additional shock loads due to appearance of gaps. Temporarily rebuilt converter trunnion assembly of the converter support ring worked, as indicated above, from March to June and it was dismantled due to destruction of the composite material. Temperature in zone where the composite was located was around 140 °C (before repair measurements on operating converter showed temperature of about 60 °C in this zone at permissible operating temperature of the applied composite material of 80 °C). Thus, it can be stated that the composite material can withstand significant loads in compliance with temperature limits that in this case made it possible to solve problem of starting the converter and using it in time interval necessary to prepare for replacement of the support ring and bearing.

The gearbox housing of the screw-down mechanism of the hot thick strip rolling mill rolling stand with full restoration of performance of worn surfaces being in contact with rolling bearings using the composite material has been successfully operated for three years that exceeds service life of such units restored using known technology including dismantling, moving to specialized section of mechanical workshop, machining in order to remove defective layer, followed by cladding and precise machining.

The restoration technology with formation of worn surfaces of the housings by the composite material using the polished template showed greater load-bearing capacity of restored assembly in comparison with traditional restoration method. This feature can be explained by fact that polished outer ring of bearing contacts restored by the composite material surface and formed, as shown above, using the polished template. At traditional technology of restoring support surface after its machining with milling cutter makes bearing outer ring to be sat on tops of microroughness of milled surface. Even with slight dynamic loads these tops of microroughness can be pressed down which is reason for subsequent wear of bearing seat [15–25].

Another factor providing increase of loading capacity is ability of the composite enclosed in a closed volume, according to developed technical proposals of the restored unit design, to partially damp shock and vibration loads without destruction which contributes to increase of service life of supporting surface of both mechanism itself and metal structures or foundations on which it is installed.

#### 4. Conclusion

The authors analyzed known methods for diagnostics of running wheels bearing assemblies on example of a casting crane in steelmaking shop. Analysis showed that vibration parameters give the most acceptable data in real operating conditions to evaluate technical state of rolling bearings. However, this method is not universal because its application must be combined with thorough analysis of design and loading of diagnosed bearing unit. For the considered crane, there were cases of failure of running wheel bearings with moderate vibration of the unit associated with lubricant coking under influence of elevated temperatures because of peculiarities of technological process structural elements were heated from the ladle with hot liquid steel and influence of irrational device for supplying lubricant material to bearing assembly.

At present, composite material 'Multimetal Stahl 1018' can have a new application of creating temporary sliding bearing support instead of failed unique design with rolling bearings. Usage of such support instead of spherical double-row ball bearing (diameter of trunnion is 850 mm) of damaged roller for support ring of the 300 tons converter allowed the converter to work for three months. This helped to reduce economic losses associated with long production and installation time of new trunnion unit and corresponding downtime of the converter. Longer service life of the temporary support can be provided by combining this method of bearing assembly temporary restoration with additional cooling system.

Restoration of machines housings with worn surfaces under outer rings of bearings using conventional technology requires significant time and money expenses for dismantling and cladding of worn surfaces and subsequent machining.

Usage of composite material 'Multimetal Stahl 1018' to restore support surfaces of bearing units of screw-down mechanism reducer of hot thick strip rolling mill rolling stand allowed to refuse operations carried out in machine shop and meeting deadline for current repair of equipment.

Successful operation of majority of industrial equipment assemblies restored with help of composite materials testifies to broad prospects for solving various repair problems facing mechanics of repair industries.

## References

1. Kravchenko, V.M., Ischenko, A.A., Sidorov, V.A., Butsukin, V.V. Ekspluatatsiya ta obsluhovuvannya mashyn [Operation and maintenance of machines]. Donetsk: Donbass, 2014. 543 p.
2. Bigus, G.A., Daniev, Y.F., Bystrova, N.A. Osnovy diagnostiki tekhnicheskikh ustroystv i sooruzheniy [Fundamentals of diagnostics of technical devices and structures]. Moscow: Bauman Moscow State Technical University, 2015. 445 p.
3. Smolin, A.A., Vorobiev, E.V. Sistema diagnosticheskogo sostoyaniya ob'ektov mobil'noy tekhniki [System for diagnostic state of mobile equipment]. Omsk scientific bulletin. 2015. 1. Pp. 67–68.
4. Plaksin, A.M., Gritsenko, A.V. Razrabotka sredstv i metodov testovogo diagnostirovaniya mashin [Development of tools and methods for test diagnostics of machines]. Krasnoyarsk State Agrarian University bulletin. 2013. 12. Pp. 185–193.
5. Kravchenko, V.M., Sidorov, V.A., Kikalov, V.S. Klassifikatsiya vidov povrezhdeniy podshipnikov kacheniya metallurgicheskoy mashin [Classification of damages types of metallurgical machines rolling bearings]. Dnipro University of Technology scientific bulletin. 2007. 2. Pp. 3–6.
6. Reshetnyak, S.E., Maximov, A.D. Analiz iznosa i prichin vykhoda iz stroya podshipnikov kacheniya vysokoskorostnykh uzlov [Analysis of wear and causes of failure of high-speed units rolling bearings]. Moscow Polytechnic University bulletin. 2014. 1(19). Pp. 152–157.
7. Savchenko, A.P., Minchenya, N.T. Issledovaniye iznosa radial'no-upornykh podshipnikov [Investigation of wear of angular bearings]. Belarusian National Technical University bulletin. 2006. 3. Pp. 60–64.
8. Shakhanov, N.I. Prognozirovaniye otkazov oborudovaniya v usloviyakh malogo kolichestva polomok [Predicting equipment failures in low-failure conditions]. Cherepovets State University. 2016. 6. Pp. 36–41.
9. Seroshtan, V.I., Ogar, Y.S., Golovin, A.I. Diagnostirovaniye gruzopod'yemnykh mashin [Diagnostics of lifting machines]. Moscow: Mechanical engineering, 1992. 192 p.
10. Shirman, A.R., Soloviev, A.D. Prakticheskaya vibrodiagnostika i monitoring sostoyaniya mekhanicheskogo oborudovaniya [Practical vibration diagnostics and condition monitoring of mechanical equipment]. Moscow, 1996. 276 p.
11. Artiukh, V.G., Karlushin, S.Yu., Sorochan, E.N. Peculiarities of Mechanical Characteristics of Contemporary Polyurethane Elastomers. Procedia Engineering. 2015. 117. Pp. 938–944. DOI: 10.1016/j.proeng.2015.08.180
12. Artiukh, V.G., Galikhanova, E.A., Mazur, V.M., Kargin, S.B. Energy intensity of parts made from polyurethane elastomers. Magazine of Civil Engineering. 2018. 81 (5). Pp. 102–115. DOI: 10.18720/MCE.81.11
13. Ishchenko, A., Rassokhin, D., Nosovskaya, E. Experimental study of cavitation destruction of a protective composite polyurethane-based material. Eastern-European Journal of Enterprise Technologies. 2019. 5/12 (101). Pp. 23–28.
14. Arustamian, A., Solek, K., Kalisz, D. Identification of yield point of polymer-based composite material in the conditions of increased temperatures. Arch. Metall. Mater. 2016. 61(3). Pp. 1561–1566.
15. Efremov, D.B., Gerasimova, A.A., Gorbatyuk, S.M., Chichenev, N.A. Study of kinematics of elastic-plastic deformation for hollow steel shapes used in energy absorption devices. CIS Iron and Steel Review. 2019. 18. Pp. 30–34. DOI: 10.17580/cisr.2019.02.06
16. Sotnikov, A.L., Rodionov, N.A., Ptukha, S.V. Analysis of Mechanical Loading of the Hinges and Supports of the Mold Vibration Mechanism on a Continuous Caster. Metallurgist. 2015. 58(9). Pp. 883–891.
17. Yakovlev, S.N., Mazurin, V.L. Vibroisolating properties of polyurethane elastomeric materials, used in construction. Magazine of Civil Engineering. 2017. 6. Pp. 53–60.
18. Solomonov, K.N. Application of CAD/CAM systems for computer simulation of metal forming processes. Materials Science Forum. 2012. V. 704–705. Pp. 434–439.
19. Pestryakov, I.I., Gumerova, E.I., Kupchin, A.N. Assessment of efficiency of the vibration damping material “Teroson WT 129”. Construction of Unique Buildings and Structures. 2016. 5(44). Pp. 46–57.
20. Ishchenko, A., Artiukh, V., Mazur, V., Poberezhskii, S., Aleksandrovskiy, M. Experimental study of repair mixtures as glues for connecting elastomers with metals. MATEC Web of Conferences. 2019. 265. Pp. 01016. DOI: 10.1051/mateconf/201926501016
21. Malinov, L.S., Malysheva, I.E., Klimov, E.S., Kukhar, V.V., Balalayeva, E.Yu. Effect of Particular Combinations of Quenching, Tempering and Carburization on Abrasive Wear of Low-Carbon Manganese Steels with Metastable Austenite. Materials Science Forum. 2019. Vol. 945. Pp. 574–578. DOI: 10.4028/www.scientific.net/MSF.945.574
22. Artiukh, V., Belyaev, M., Ignatovich, I., Miloradova, N. Depreciation of Bearing Blocks of Rollers of Roller Conveyers of Rolling Mills. IOP Conf. Series: Earth and Environmental Science. 2017. 90. Pp. 012228. DOI: 10.1088/1755-1315/90/1/012228
23. Maksarov, V.V., Keksin, A.I. Forming conditions of complex-geometry profiles in corrosion-resistant materials. IOP Conference Series: Earth and Environmental Science. 2018. 194 (6). Pp. 062016. DOI: 10.1088/1755-1315/194/6/062016
24. Snitko, S.A., Yakovchenko, A.V., Sotnikov, A.L. Influence of wheel billet stamping schemes on power modes of forming press operation and on wear of the deformation tool. Izvestiya Vysshikh Uchebnykh Zavedeniy. Chernaya Metallurgiya. 2018. 61(5). Pp. 385–392. DOI: 10.17073/0368-0797-2018-5-385-392
25. Gorbatyuk, S.M., Pashkov, A.N., Zarapin, A.Y., Bardovskii, A.D. Development of Hot-Pressing Technology for Production of Aluminum-Based Metal-Matrix Composite Materials. Metallurgist. 2019. 62(11-12). Pp. 1261–1266. DOI: 10.1007/s11015-019-00784-0

### Information about authors:

**Anatoliy Ishchenko**, Doctor of Technical Science

ORCID: <https://orcid.org/0000-0002-6189-7830>

E-mail: [kafedramz@gmail.com](mailto:kafedramz@gmail.com)

**Valerij Butsukin**, PhD in Technical Science

ORCID: <https://orcid.org/0000-0002-7935-2273>

E-mail: [butsukinne@ukr.net](mailto:butsukinne@ukr.net)

**Viktor Artiukh**, Doctor of Technical Science  
ORCID: <https://orcid.org/0000-0003-3620-3662>  
E-mail: [artiukh@mail.ru](mailto:artiukh@mail.ru)

**Natalia Chernysheva**, PhD in Technical Science  
ORCID: <https://orcid.org/0000-0002-2021-0860>  
E-mail: [chernat0000@mail.ru](mailto:chernat0000@mail.ru)

*Received 07.05.2021. Approved after reviewing 02.08.2022. Accepted 02.08.2022.*



Research article

UDC 666.3

DOI: 10.34910/MCE.117.6



## Anorthite-based building ceramics

N.K. Skripnikova , M.A. Semenovikh , V.V. Shekhovtsov 

Tomsk State University of Architecture and Building, Tomsk, Russia

✉ [semenovikhmark@gmail.com](mailto:semenovikhmark@gmail.com)

**Keywords:** ceramics, silicates, compressive strength, mechanical properties, X-Ray diffraction, differential thermal analysis, waste utilization, blast furnace sludge

**Abstract.** The paper presents the production technique of anorthite-based building ceramics using semidry pressing of the powder based on sintering of the raw mixture consisting of low-melting clay and blast furnace sludge (BFS) in different proportions. The fabricated ceramic specimens are sintered at 1050 °C. The raw mixture properties are studied to increase the anorthite phase content in ceramic specimens. Investigations of physical and mechanical properties of ceramic specimens show that the addition of BFS to the mixture composition provides the compressive strength of the obtained specimens up to 48.8 MPa, which is 25% higher than that of the reference specimen. The higher compressive strength is explained by the formation of the anorthite phase, which is proven by XRD investigation. According to the differential thermal analysis of the obtained specimens, exo-effect occurs at 1050 °C sintering, which is typical for the anorthite phase formation.

**Funding:** Grant N 20-79-10102 from the Russian Science Foundation.

**Citation:** Skripnikova, N.K., Semenovikh, M.A., Shekhovtsov, V.V. Anorthite-based building ceramics. Magazine of Civil Engineering. 2023. 117(1). Article no. 11706. DOI: 10.34910/MCE.117.6

### 1. Introduction

In construction industry, ceramic brick is currently one of the building materials that are often used. The ceramic brick performance and decorative properties allow it to remain a competitive building material. In this regard, many researchers are involved in studying the problem of the improvement of the ceramic brick performance and decorative properties. This work investigates the anorthite-based ceramics. Much attention is paid to the modification of building ceramic materials and products. Different approaches and methods are used to study these materials and their properties.

Brick with increased strength can be used in the construction of buildings with increased number of storeys and increased load. Also, such bricks can be used for construction in areas with a low average annual temperature due to their high heat resistance. Thus, the use of BFS and clay raw materials as raw materials will significantly improve the economics of enterprises for the production of ceramic products.

Sal [1] and Rat'kova et al. [2] optimized the aluminosilicate waste-based raw mixture with different chemical composition *via* varying the mixture composition. A comparative analysis of the obtained and reference specimens showed that the selection of the mixture composition provided a 5–7 % increase in the compressive strength, up to 3 % decrease in the ignition loss, and 6 % growth in the porosity of products.

Utilization of industrial by-products through their introduction in the ceramic mixture [3–17] has attracted much attention from research teams. For example, in [4], talcum powder is used as a by-product, which allows to reach the porosity up to 42 %. In works [5–9], the use of bottom ash waste provides the ceramics strength increase from 10 to 12 MPa. According to [10, 11], mining waste materials and tails are

used in the ceramic industry to improve the compressive strength from 18.5 to 22.8 MPa and minimize the water adsorption of the products down to 1.8 %. Several publications [12–14] have appeared for the past years documenting the use of ceramic waste, namely, porcelain and brick, that increase the compressive strength by two times and reduce the water absorption from 6.3 to 3.5 %. Therefore, the addition of non-standard materials to the ceramic mixture improves the ceramic brick performance by ~20 %.

As shown in [18–24], the physical and mechanical properties of ceramic brick directly depend on the rate of the crystal and amorphous phase formation and interaction. In varying the process conditions and chemical composition of the raw material in ceramic brick fabrication, it is possible to synthesize different energy-intensive phases such as anorthite, quartz, carbonates, montmorillonite, wollastonite, and others. The anorthite-based ceramics is rather promising material due to its high performance. Zong et al. [25] and Kamal et al. [26] report that the phase composition of the anorthite-based ceramics is rather high in anorthite due to the different chemical composition of the raw mixture components. In particular, the formation of the anorthite phase is conditioned by CaO content in the ceramic mixture. At the same time, the strength properties of the ceramic specimen increase by ~35 %, that can be explained by the anorthite phase morphology in the chemical composition of the raw mixture components. The anorthite phase crystals form a skeleton of the whole material due to their acicular shape and bound aluminosilicate compounds together, thereby forming conglomerates.

This paper proposes to utilize metallurgical raw materials. The aim of this work is to produce anorthite-based building ceramics incorporated with a raw mixture containing a carbonaceous raw material from the metallurgical production. The paper describes the ceramic brick fabrication with the different content of metallurgical raw materials in the laboratory conditions and presents the experimental results of the effect from the waste content in the ceramic mixture on the ceramic product performance and the anorthite phase concentration in the phase composition.

## 2. Methods

Clay from Verkhovoe deposit (Tomsk region, Russia) and carbonaceous raw material from the metallurgical production were used in our experiment. The carbonaceous raw material was a fine-grained substance formed during the blast furnace gas purification. Clay was dried to a constant humidity less than 1 % and grinded in a ball mill to obtain 50  $\mu\text{m}$  particles. Blast furnace sludge (BFS) was processed in the same manner. Ceramic specimens were produced using semidry pressing of the raw mixture. The raw mixture components were mixed and homogenized at various proportions. The mixture humidity was 10 %. The mixture was placed in pressurized vessels for 12 hours for the humidity to be uniformly distributed in it, and then subjected to mold pressing at 20–25 MPa. The obtained 50×50×25 mm specimens were dried at 90 °C for 6 hours to remove excess humidity. Afterwards, the specimens were baked in a laboratory furnace SNOL 12/16 at a maximum temperature of 1050 °C.

The XRF-1800 Sequential X-ray Fluorescence Spectrometer (Shimadzu, Japan) was used to analyze the chemical composition of the raw materials and the specimens obtained. The X-ray diffraction patterns of the specimens were recorded on a Shimadzu XRD-6000 Diffractometer (Japan). A differential thermal analysis (DTA) of specimens was carried out on a thermal analyzer Netzsch STA 449 F3 Jupiter (Germany).

## 3. Results and Discussion

The high physical and mechanical properties of ceramic specimens obtained in the laboratory conditions were provided by the prevailing concentration of silicon, aluminum, and calcium oxides in the chemical composition of the initial raw mixture. The concentration of these oxides was detected by analyzing the chemical composition of the raw mixture components given in Table 1.

**Table 1. Chemical composition of raw mixture components.**

Raw mixture components	Oxide content, wt.%						
	SiO <sub>2</sub>	Al <sub>2</sub> O <sub>3</sub>	CaO	MgO	FeO	Fe <sub>2</sub> O <sub>3</sub>	$\Delta m$
Clay	64.05	12.10	3.08	2.97	–	4.53	13.27
BFS	34.54	14.05	6.29	2.02	6.47	–	36.63

According to Table 1, the BFS chemical composition with 34.54 wt.% SiO<sub>2</sub>, 14.05 wt.% Al<sub>2</sub>O<sub>3</sub> and 6.29 wt.% CaO is sufficient for the building ceramics production. The larger loss on ignition of the blast furnace sludge is observed for carbon, whose concentration in the chemical composition is 30.5 wt.%. This fact indicates to a probable decrease in the sintering temperature due to the additional heat release caused

by carbon combustion during the specimen baking. Next, it is advisable to introduce the nondimensional coefficient  $C$  to describe the carbon concentration in the ceramic mixture:

$$C = \frac{m_C \cdot A_{BFS}}{m_{SiO_2} + m_{Al_2O_3} + m_{CaO} + \dots + m_i + (\Delta m - m_C \cdot A_{BFS})}, \quad (1)$$

where  $m_C$  is the carbon content in the blast furnace sludge, wt.%;  $m_i$  is the oxide content, wt.%;  $\Delta m$  is the ignition loss, wt.%;  $A_{BFS}$  is the BFS content in the mixture component, which varies between 0 and 1.0.

After studying the chemical composition of the raw mixture components, we selected mixtures with the different content of clay and BFS and CaO/Al<sub>2</sub>O<sub>3</sub> and CaO/SiO<sub>2</sub> ratios, as presented in Table 2. Kamal [22] suggested a high probability of the anorthite phase formation due to such contents.

**Table 2. Raw mixture components for ceramic specimens produced in laboratory conditions.**

Raw mixture components	Content, wt.%					
	Clay	100	90	80	70	60
BFS	0	10	20	30	40	50
	Oxide ratios, a.u.					
CaO/SiO <sub>2</sub>	-	0.122	0.131	0.141	0.153	0.166
CaO/Al <sub>2</sub> O <sub>3</sub>	-	0.491	0.493	0.495	0.497	0.499

Based on the analyzed compositions of the ceramic mixture, the ternary phase diagram is constructed for the SiO<sub>2</sub>-Al<sub>2</sub>O<sub>3</sub>-CaO system. Its chemical composition is reduced to three components in accordance with the molar ratio. In Fig. 1, points 1–6 correspond to the data given in Table 2 and characterize the BFS quantity from 0 to 50 wt.%, respectively. As can be seen from Fig. 1, the anorthite crystallization involves the compositions with ~25 wt.% BFS. For such specimens, there is a growing probability for the anorthite phase formation.

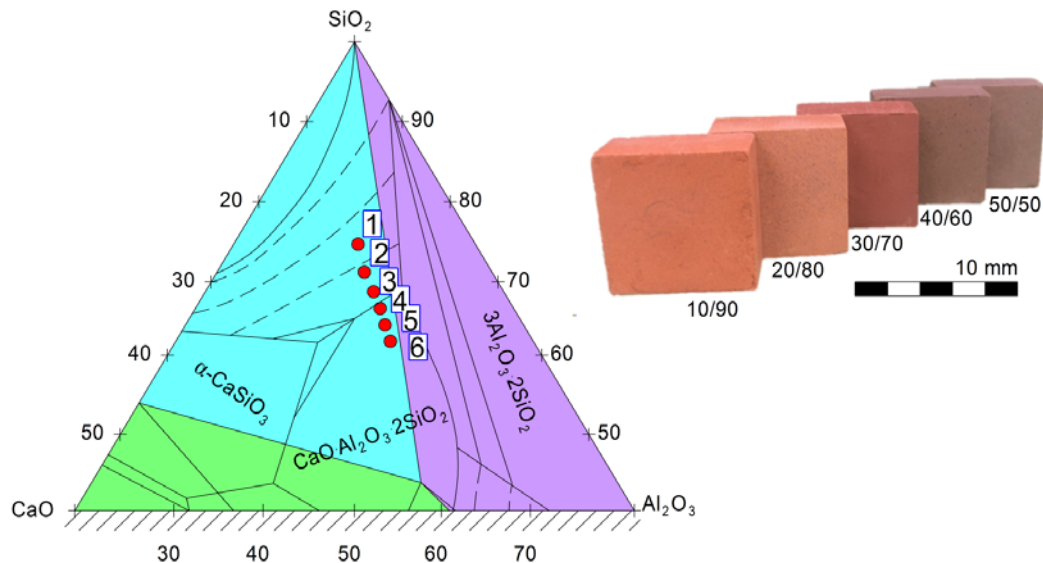


**Figure 1. Ternary phase diagram of SiO<sub>2</sub>-Al<sub>2</sub>O<sub>3</sub>-CaO system.**

The results of testing the physical and mechanical properties of the obtained specimens such as strength, density, water adsorption and frost resistance, are presented in Fig. 2.

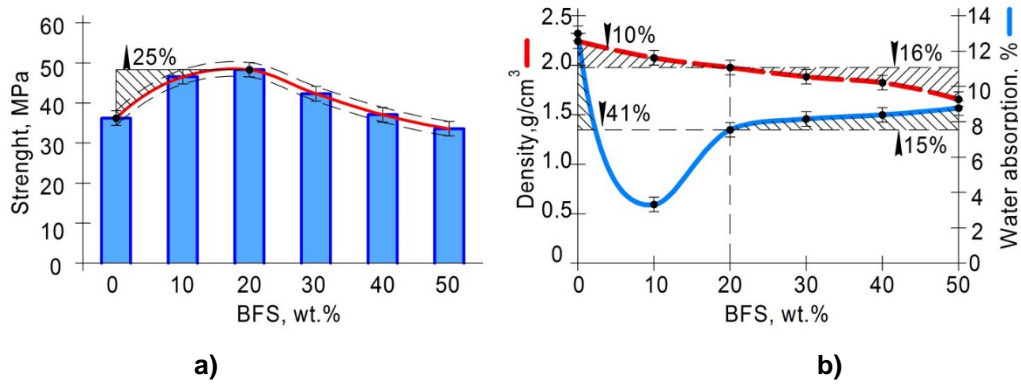


**Figure 2. Physical and mechanical properties of ceramic specimens depending on BFS content: a – strength dependence; b – density and water adsorption dependence.**

According to Fig. 2a, the compressive strength of the ceramic specimen with 20 wt.% BFS is 25 % higher (48.8 MPa) than that of the reference specimen, and this is the maximum value among other specimens tested. As can be seen from Fig. 2b, the density and water adsorption of this specimen is 1.95 g/cm<sup>3</sup> and 7.6 %, respectively. This is 5 and 40 % lower than those of the reference specimen, respectively. These results are achieved through the different carbon content  $C$  in the initial raw mixture. It is worth noting that at the carbon content of  $0.03 < C \leq 0.06$ , the strength properties of the ceramic specimen grow by  $\sim 25$  % of the reference specimen. At  $0.06 < C \leq 0.15$ , the strength properties lower down to 30 %, which is an 8 % loss of the reference specimen. The specimen density reduces linearly to 16 % at any carbon content.

Fig. 3 plots the DTA results of the raw mixtures that describe the phase transitions in ceramic specimens.

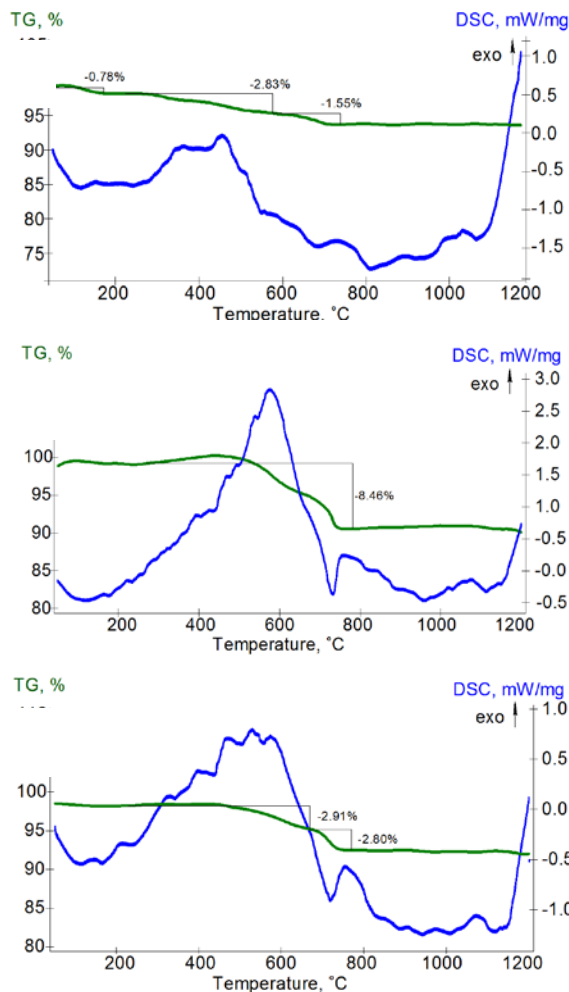


**Figure 3. DTA curves of raw mixture components: a – clay, b – BFS, c – clay/BFS mixture in 50:50 proportion.**

According to Fig. 3a, clay undergoes the following phase transitions. Endo-effect occurs at 140 °C sintering, which is characteristic to the humidity removal from the raw mixture. Exo-effect occurs at 470 °C sintering, and this is typical for burning-out of organic inclusions. The loss on ignition of clay is 2.83 % at a sintering temperature below 580 °C, which is typical for  $\text{Al}_4[\text{Si}_4\text{O}_{10}](\text{OH})_8$  dehydration, while in the temperature range of 580–750 °C, the loss on ignition is 1.55 %, which is accompanied by endo-effect. The latter indicates to the loss of hydroxyl groups of the  $(\text{Na}, \text{Ca})_{0.3}(\text{Al}, \text{Mg})_2\text{Si}_4\text{O}_{10}(\text{OH})_2 \cdot n\text{H}_2\text{O}$  crystal lattice and its destruction. A minor exo-effect is observed at 910 °C, which is conditioned by recrystallization of amorphous products of  $(\text{Na}, \text{Ca})_{0.3}(\text{Al}, \text{Mg})_2\text{Si}_4\text{O}_{10}(\text{OH})_2 \cdot n\text{H}_2\text{O}$  lattice degradation. Next, exo-effect is observed at 1050 °C sintering indicating to recrystallization of amorphous silicic acid. And then a large exo-effect occurs at 1200 °C, which is caused by the formation of the anorthite crystal phase.

As follows from Fig. 3b, the humidity removal occurs at 112 °C followed by exo-effect at 539 °C, when the formation of silicates occurs due to the reducing properties of carbon and its high heat capacity. In the temperature range of 539–749 °C, the loss on ignition of BFS is 8.46 %, exo-effect is observed at 575 °C, which is characteristic to the carbon removal. At 955 °C, we observed endo-effect that may indicate to the degradation of clay minerals, the loss of the hydrate group, and recrystallization of amorphous products of degradation. Recrystallization of the amorphous inclusions is observed at 1000 °C, and exo-effect occurs at 1100 °C indicating to the formation of a new aluminosilicate compound of the anorthite type.

The DTA curve for the clay/BFS mixture in 50:50 proportion given in Fig. 3c, has points typical for both pure clay and pure BFS. The largest exo-effects are observed at 550 and 1150 °C sintering. Due to the polymorphic modifications of  $\text{SiO}_2$  and  $\text{Al}_2\text{O}_3$ , the anorthite nuclei appear, which facilitate the formation of the main anorthite phase.

According to the DTA results, the BFS introduction in the ceramic mixture initiates the formation of the additional centers of thermal activity in the matrix volume due to the increase in the total thermal energy released after carbon combustion. Such a mechanism provides the additional thermal effect, which, in turn, provides a temperature shift of the anorthite nucleation toward an ~1050 °C region.

Based on the DTA, the dependence between the total thermal flux and the raw mixture composition is suggested in Fig. 4. One can see that the total thermal flux  $\Delta$  grows in the raw mixture composition with increasing BFS content  $k$ . The exponential curve described by the relation  $\Delta = 5 \cdot 10^{-7} k + 2 \cdot 10^{-5} k^2 + 0.0034k + 2.0986$ , indicates to the increase in the internal energy during the mixture heating, that results from the carbon burning-out from the blast furnace sludge. This phenomenon provides the additional energy source during the specimen heating.

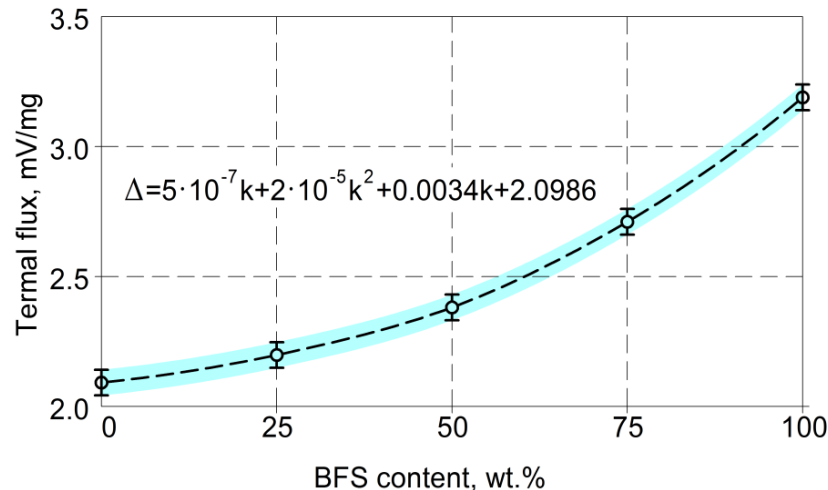


**Figure 4. Dependence between the total thermal flux and raw mixture composition.**

The phase identification in the obtained specimens is provided by the X-ray diffraction (XRD) analysis; the XRD patterns are given in Fig. 5. The initial materials (clay, BFS) are investigated as well as the reference specimen with the clay content of 100 wt.% and the specimen with 50 wt.% BFS.

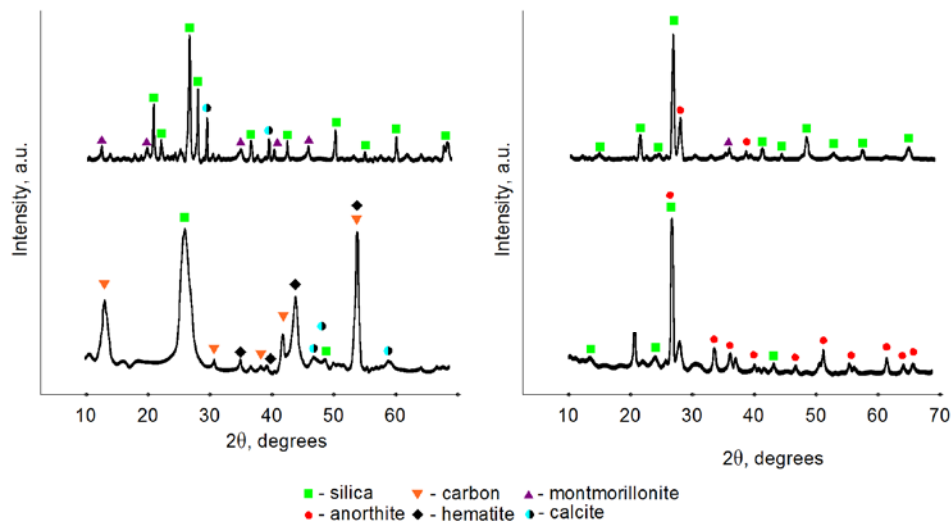


**Figure 5. XRD patterns of initial materials:**  
**a – clay, b – BFS, c – reference specimen, d – specimen with 50 wt.% BFS.**

As shown in Fig. 5, the initial clay is montmorillonite high in silica. The initial blast furnace sludge contains carbonaceous, ferrous and quartzous inclusions. The baked ceramic specimen made of 100 wt.% clay, contains silicate compounds and insignificant quantity of anorthite inclusions. The ceramic specimen with 50 wt.% BFS, contains silica and anorthite phases. Unlike the reference specimen, its XRD patterns have many diffraction peaks matching anorthite. Based on these XRD patterns, we show that the BFS addition to the raw mixture composition provides the increase in the anorthite phase content. This correlates with the experimental data on the physical and mechanical properties of the obtained specimens (see Fig. 2).

#### 4. Conclusion

The experimental data obtained in this work concerned the synthesis of the anorthite phase in the ceramic brick matrix with the addition of metallurgical raw materials. The physical and mechanical properties of ceramic brick and phase transformations during its sintering were investigated in the raw mixture components with the different BFS content by using the up-to-date techniques of materials science in construction. Summing up the results, it can be concluded that

- the BFS addition to the raw mixture allowed substituting up to 50 wt.% of the main component (clay) of the ceramic mixture by metallurgical raw materials. The obtained ceramic specimens were higher in the anorthite phase  $\text{CaO} \cdot \text{Al}_2\text{O}_3 \cdot 2\text{SiO}_2$  as compared to the reference specimen;
- the BFS addition to the raw mixture in the amount of 20 wt.% provided the formation of a ceramic skeleton possessing 48.8 MPa compressive strength and  $1.9 \text{ g/cm}^3$  density. Further increase in the BFS content reduced the compressive strength and the density down to 33.8 MPa and  $1.6 \text{ g/cm}^3$ , respectively;
- at  $0.03 < C \leq 0.06$  carbon concentration in the raw mixture, the strength properties of ceramic specimens increased by ~25 % as against the reference specimen. At  $0.06 < C \leq 0.15$ , the compressive strength reduced exponentially down to 30 %, which was an 8 % loss of the reference specimen. At the same time, the specimen density reduced linearly to 16 % at any carbon content;
- the BFS addition to the ceramic mixture initiated the formation of the additional centers of thermal activity in the matrix volume due to the increase in the total thermal energy released after the carbon combustion. Such a mechanism provided the additional thermal effect, which, in turn, shifted the temperature of the anorthite nucleation toward an ~1050 °C region.

Thus, the use of BFS in the composition of ceramic bricks can have a positive effect on the environmental situation and opens up new prospects for the use of ceramic materials in the construction industry.

#### References

1. Sal, J. Testing of brick clay modifications as a raw material for building ceramic products. MATEC Web of Conferences. 2019. 279. 02022.
2. Rat'kova, V.P., Yatsenko, N.D., Ivanyuta, G.N., Nechaev, P.B. Optimization of clay properties for selecting brick molding method. Glass and Ceramics. 2004. 61(11–12). Pp. 379–381.

3. Tuani, Z., Mariana, B., Naquiele, S., Ana, M.S., Robinson, C.D.C., Gihad, M., Erich, D.R. Potential re-use of sewage sludge as a raw material in the production of eco-friendly bricks. *Journal of Environment Management*. 2021. 297. 113238.
4. Zhigulina, A.Y., Montaev, S.A., Zharylgapov, S.M. Physical-mechanical properties and structure of wall ceramics with composite additives modifications. XXIV R-S-P Seminar on Theoretical Foundation of Civil Engineering. 2015. 111. Pp. 896–901.
5. Volokitin, G.G., Skripnikova, N.K., Volokitin, O.G., Lutsenko, A.V., Shekhovtsov, V.V., Litvinova, V.A., Semenovykh, M.A. Bottom ash waste used in different construction materials. *IOP Conference Series: Materials Science and Engineering*. 2017. 189. 012013.
6. Vasic, M.V., Goel, G., Vasic, M., Radojevic, Z. Recycling of waste coal dust for the energy-efficient fabrication of bricks: A laboratory to industrial-scale study. *Environmental Technology & Innovation*. 2021. 21. 101350.
7. Hui, T., Sun, H.J., Peng, T.J. Preparation and characterization of cordierite-based ceramic foams with permeable property from asbestos tailings and coal fly ash. *Journal of Alloys and Compounds*. 2021. 885. 160967.
8. Terrones-Saeta, J.M., Suarez-Macias, J., Iglesias-Godino, F.J., Corpas-Iglesias, F.A. Development of geopolymers as substitutes for traditional ceramics for bricks with chamotte and biomass bottom ash. *Materials*. 2021. 14(1). 199.
9. Yuan, Q., Mohajerani, A., Kurmus, H., Smith, J.V. Possible recycling options of waste materials in manufacturing ceramic tiles. *International Journal of GEOMATE*. 2021. 20(78). Pp. 73–80.
10. Simao, F.V., Chambart, H., Vandemeulebroeke, L., Cappuyns, V. Incorporation of sulphidic mining waste material in ceramic roof tiles and blocks. *Journal of geochemical exploration*. 2021. 225. 106741.
11. Yatsenko, N.D., Verevkin, K.A., Zubekhin, A.P. Mossbauer spectroscopy of phase and crystal-chemical states of iron oxides in ceramic brick. *Glass and Ceramics*. 2010. 67(5–6). Pp. 176–178.
12. De Silva, G.H.M.J.S., Hansamali, E. Eco-friendly fired clay bricks incorporated with porcelain ceramic sludge. *Construction and Building Materials*. 2019. 228. 116754.
13. Ismail, N., Salleh, N., Yusof, N.F.M., Jamellodin, Z. Strength, water absorption and thermal comfort of mortar bricks containing crushed ceramic waste. *Jurnal Teknologi*. 2017. 79(7). Pp. 167–173.
14. Coletti, C., Maritan, L., Cultrone, G., Mazzoli, C. Use of industrial ceramic sludge in brick production: Effect on aesthetic quality and physical properties. *Construction and Building Materials*. 2016. 24. Pp. 219–227.
15. Li, B., Guo, Y., Fang, J. Effect of MgO addition on crystallization, microstructure and properties of glass-ceramics prepared from solid wastes. *Journal of Alloys and Compounds*. 2021. 881. 159821.
16. Putrevu, M., Thiyagarajan, J.S., Pasla, D., Kabeer, K.I.S.A., Bisht, K. Valorization of red mud waste for cleaner production of construction materials. *Journal of Hazardous, Toxic, and Radioactive Waste*. 2021. 25 (4). 03121002.
17. Khattab, R.M., Abo-Almaged, H.H., Ajiba, N.A., Badr, H.A., Gaber, A.A., Taha, M.A., Sadek, H.E.H. Sintering, physicochemical, thermal expansion and microstructure properties of cordierite ceramics based on utilizing silica fume waste. *Materials Chemistry and Physics*. 2021. 270. 124829.
18. Skripnikova, N.K., Litvinova, V.A., Volokitin, G.G., Lutsenko, A.V., Volokitin, O.G., Semenovykh, M.A. Firing building materials based on aluminosilicate waste from the oil industry [in Russian]. *Bulletin of the Tomsk State University of Architecture and Civil Engineering*. 2017. 2(61). Pp. 141–147.
19. Lavrinenko, A.A., Svechnikova, N.Yu., Konovnitsyna, N.S., Igumensheva, E.A., Kuklina, O.V., Khasanzyanova, A.I. Utilization of bituminous coal flotation wastes in the manufacture of ceramic brick. *Solid Fuel Chemistry*. 2018. 52(6). Pp. 406–410.
20. Koleda, V.V., Mikhailyuta, E.S., Alekseev, E.V., Tsybul'ko, E.S. Technological particularities of clinker brick production. *Glass and Ceramics*. 2009. 66(3-4). Pp. 132–135.
21. Stryzewska, T. The change in selected properties of ceramic materials obtained from ceramic brick treated by the sulphate and chloride ions. *Construction and Building Materials*. 2014. 66. Pp. 268–274.
22. Kamal, T., Hanaa, H., Mohamed, W., Latifa, S. Effect of CaO/SiO<sub>2</sub> ratio on phase transformation and properties of anorthite-based ceramics from coal fly ash and steel slag. *Ceramics International*. 2020. 46(6). Pp. 7550–7558.
23. Erofeev, V.T., Rodin, A.I., Bochkina, V.S., Ermakov A.A. The formation mechanism of the porous structure of glass ceramics from siliceous rock. *Magazine of Civil Engineering*. 2020. 8(100). Pp. 10006.
24. Lu, J., Zhang, Zh., Li, Yi., Liu, Zh. Effect of alumina source on the densification, phase evolution, and strengthening of sintered mullite-based ceramics from milled coal fly ash. *Construction and Building Materials*. 2019. 229. 116851.
25. Zong, Y., Wan, Q., Cang, D. Preparation of anorthite-based porous ceramics using high-alumina fly ash microbeads and steel slag. *Ceramics International*. 2019. 45(17). Pp. 22445–22451.
26. Kamal, T., Hanaa, H., Mohamed, W., Latifa S. Effect of CaO/SiO<sub>2</sub> ratio on phase transformation and properties of anorthite-based ceramics from coal fly ash and steel slag. *Ceramics International*. 2020. 46(6). Pp. 7550–7558.

#### **Information about authors:**

**Nelli Skripnikova**, Doctor of Technical Science

ORCID: <https://orcid.org/0000-0003-3384-9564>

E-mail: [nks2003@mail.ru](mailto:nks2003@mail.ru)

**Mark Semenovykh**,

E-mail: [semenovykhmark@gmail.com](mailto:semenovykhmark@gmail.com)

**Valentin Shekhovtsov**, PhD in Technical Science

ORCID: <https://orcid.org/0000-0003-4068-3347>

E-mail: [shehovcov2010@yandex.ru](mailto:shehovcov2010@yandex.ru)

Received 02.09.2021. Approved after reviewing 09.09.2022. Accepted 14.09.2022.



Research article

UDC 691.5

DOI: 10.34910/MCE.117.7



## Mineral additive for lime dry building mixtures

V.I. Loganina  , E.R. Akzhigitova 

*Penza State University of Architecture and Construction, Penza, Russia*

✉ [loganin@mail.ru](mailto:loganin@mail.ru)

**Keywords:** hardening, compressive strength, mortar, lime, rheology, composite materials

**Abstract.** The article deals with lime dry building mixtures for the restoration of historical buildings. Considering the low strength and water resistance of coatings based on lime compositions, the possibility of using mixed clay fired at low temperatures (450–500 °C) as mineral additives in dry building mixtures was considered. The chemical and mineralogical composition of clays was established. The spectrum of the distribution of adsorption centers according to the acid-base type, as well as the nature of its change in the process of firing clay at different temperatures, was investigated. The regularities of the structure formation of lime finishing compositions with the use of mineral additives was established. It is shown that lime composites based on compositions with a mineral additive fired at a temperature of 450–500 °C are characterized by a high content of zeolites, a decrease in  $\text{Ca}(\text{OH})_2$ , and an increase in the amount of chemically bound lime by 31.8 %. It is shown that the introduction of clay fired at temperatures of 450–500 °C into the lime-sand composition contributes to a 2–2.6 times increase in compressive strength at the age of 28 days of air-dry hardening, depending on the firing temperature and the type of clay. The technological and operational properties of lime dry building mixtures and coatings based on them are given.

**Citation:** Loganina, V.I., Akzhigitova, E.R. Mineral additive for lime dry building mixtures. Magazine of Civil Engineering. 2023. 117(1). Article no. 11707. DOI: 10.34910/MCE.117.7

### 1. Introduction

Lime compositions are widely used for the restoration of historical buildings [1–7]. Finishing layers based on lime compositions have high vapor permeability and biostability, but low strength and water resistance. One of the ways to prevent premature destruction of lime finish coatings is to introduce modifying additives into the formulation [8–11].

One of the modifying additives used for the production of dry building mixtures (DBM) is metakaolinite. Metakaolinite chemically interacts with lime, which helps to increase the strength of the composition [12–16].

In lime plaster mixes, metakaolinite, being a clay material, provides excellent plasticity to the compositions and the absence of stickiness, which makes it possible to produce high-quality dry mixes. The light color of the additive also allows it to be used in decorative mixtures. The rate of reaction with lime in metakaolinite is higher than in pozzolanic additives, which ensures reliable binding of slow-hardening lime already in the first days of its hardening.

The work found that when mixing lime, water and metakaolinite, fired at a temperature of 730 °C, the strength of the composition is 10–15 MPa. Hydration products are mainly  $\text{C}_2\text{ASH}_8$  and CSH [17, 18]. In study [19], metakaolin was used to enhance the volume stability, mechanical properties and environmental erosion resistance of traditional plasters. Research results show that metakaolin reacts with  $\text{Ca}(\text{OH})_2$  via pozzolanic reactions. Additionally, the microstructure of mortars becomes more compact due to the formation of cross-linked microstructures.

Despite the numerous positive properties of the metakaolinite additive, one cannot fail to note, firstly, significant energy costs for the thermal processing of clay (up to 800 °C), since today, the issues of energy conservation are still relevant. Secondly, Russia has limited resources of kaolin clays. In connection with the above, the problem arises of developing a mineral additive that is not inferior in properties to metakaolinite, but can be obtained using a less energy-intensive technology based on local clays with a predominance of kaolinite.

The territory of the Volga region, including the Penza region, has significant reserves of mineral raw materials, in particular, clays, which can be used in the production of mineral additives for dry building mixtures.

It is known that the clay surface is a set of Lewis and Bronsted centers of both acidic and basic types [20, 21]. Most of the processes occurring on the surface of clay particles are local in nature and are largely determined by the energy parameters of specific active centers. In this regard, it is of particular importance to study the spectrum of the distribution of adsorption centers according to the acid-base type, as well as the nature of its change during the firing of clay at different temperatures [22].

The clays of the Volga region, including the Penza region, are mainly polymineral in terms of their mineralogical composition. It is proposed to obtain active mineral additives from polymineral clays by firing them at low temperatures. According to [23–25], when clay is fired in the temperature range of 450–650 °C, single-water kaolinite  $\text{Al}_2\text{O}_3 \cdot 2\text{SiO}_2 \cdot \text{H}_2\text{O}$  (hydroxoaluminium salt of metasilicic acid) is formed, which is more reactive with respect to lime than metakaolinite.

The aim of the work was to develop a scientifically grounded technological solution for obtaining a mineral additive based on mixed clays for lime dry building mixtures. To reach this goal, it is necessary to solve the following tasks:

- to evaluate the possibility of obtaining a mineral supplement during low-temperature firing of clays;
- to establish patterns of structure formation of lime mixtures with mineral additives;
- to develop a formulation of a lime dry building mixture and to determine the operational properties of a finishing layer based on it.

## 2. Methods

In the development of the mineral additive, the clays of the Vorobyevsky, Kameshkirsky, Belinsky, as well as the Issinsky deposits of the Penza region were used. The chemical composition of clays is presented in Table 1.

**Table 1. Chemical composition of clays.**

Chemical compound	The content of chemical compounds depending on from clay deposit, (%)			
	Belinsky	Kameshkirsky	Vorobyevsky	Issinsky
$\text{SiO}_2$	59.56	75.41	72.76	65.50
$\text{Al}_2\text{O}_3$	11.85	11.04	11.57	9.54
$\text{Fe}_2\text{O}_3$	4.54	6.61	7.39	7.72
Other	24.05	6.94	7.72	15.46

The indicator method of adsorption of indicators with different  $pK_a$  values was used to evaluate the acid–base sites on the surface of clay particles. The quantitative determination of the centers of adsorption was carried out photometrically. Optical density was measured on a KFK-3KM photocolormeter. The change in optical density as a result of the process of adsorption of the indicator ( $\Delta D$ ) on the sample surface was calculated by the formula

$$\Delta D = (D_0 - D_1) \pm (D_0 - D_2). \quad (1)$$

Number of active centers was calculated by the formula

$$q_{pKa} = \frac{N_{ind} V_{ind}}{D_0} \left( \left| \frac{D_0 - D_1}{a_1} \pm \frac{D_0 - D_2}{a_2} \right| \right), \quad (2)$$

where  $N_{ind}$  is concentration of the indicator solution, mg-mol/ml;  $V_{ind}$  is the volume of the indicator solution taken for analysis, ml;  $D_0$  is optical density of the indicator before sorption;  $D_1$  is optical density of the indicator after sorption;  $D_2$  is the optical density of the "blank" solution.

The “-” sign corresponds to a unidirectional change  $D_1$  and  $D_2$  relative  $D_0$ , i.e.  $D_1$  and  $D_2 < D_0$  or  $D_1$  and  $D_2 > D_0$ . The “+” sign corresponds to a multidirectional change  $D_1$  and  $D_2$  relative  $D_0$ , i.e.  $D_1 > D_0$ ,  $D_2 < D_0$  or  $D_1 < D_0$ ,  $D_2 > D_0$ .

Three series of solutions were prepared for photometry.

Series 1 (working solution). The required volumes of indicators with a certain  $pKa$  value were poured into centrifuge tubes with a capacity of 10 ml, diluted to the mark with water, mixed, and after 30 minutes weighed portions ( $a \approx 0.04$  g) of clay were poured out. After the adsorption equilibrium was established, the optical density value  $D_1$  was measured at a wavelength ( $\lambda_{max}$ ) corresponding to each indicator. Before measuring, the tubes with the material were centrifuged for 3-5 minutes.

Series 2 (“blank experience”). Weighed portions of the sample ( $a_2 \approx a_1$ ) were placed in dry centrifuge tubes and filled with 6 ml of water. After 1 hour, the solution was decanted into another tube with preliminary centrifugation. The required volumes of indicators were added to the solution, water was brought to the mark, the suspension was stirred, held for 30 minutes, and the value of optical density ( $D_2$ ) was measured, taking into account  $\pm \Delta D_2$  due to a change in the pH of the medium and dissolution of the sample.

Series 3 (indicator solution). The required volumes of indicators were poured into test tubes with a capacity of 10 ml, diluted to the mark with water, mixed, and after 30 minutes the optical density value ( $D_0$ ) was measured.

Based on the data obtained, a curve of the distribution of acid-base centers on the surface of diatomite in coordinates was constructed  $q_{pKa} = F(pKa)$ .

During the tests, the following indicators were used: brilliant green ( $pKa = + 1.5$ ), fuchsin ( $pKa = + 2.1$ ), methyl orange ( $pKa = + 3.46$ ), bromphenol blue ( $pKa = + 4.1$ ), bromocresol purple ( $pKa = + 6.4$ ), bromothymol blue ( $pKa = + 7.3$ ), thymol blue ( $pKa = + 8.8$ ), Nile blue ( $pKa = + 10.5$ ) and ethylene glycol ( $pKa = +14.2$ ). The determination of the cationic absorption capacity was carried out by the adsorption method based on the adsorption of an organic dye. Methylene blue solution was used as an organic dye. The research was carried out in the following sequence.

1. A 0.3 % solution of methylene blue was prepared and kept in a dark container and in a dark place for 3 days.
2. 10 g of clay was dried at a temperature of 105–110 °C and crushed until it completely passed through a sieve with 2500 holes/cm<sup>2</sup>.
3. In three volumetric flasks with a capacity of 100 cm<sup>3</sup> were placed 0.3 g of prepared clay.
4. Using a pipette, 50 cm<sup>3</sup> of a 0.3 % aqueous solution of organic dye were poured into the flasks.
5. The contents of the flasks were shaken for 20 min and quickly filtered through a Blue Ribbon filter.
6. Measurement of the concentration of the methylene blue solution after treatment with a sample of clay was carried out on a KFK-3KM spectrophotometer.
7. The calculation of the cationic absorption capacity of the material was carried out according to the formula:

$$A = abd 100/c \cdot 100 \cdot e, \quad (3)$$

where  $a$  is the difference in the percentage of methylene blue in the solution before and after clay treatment;  $b$  is the amount of methylene blue taken for analysis,  $b = 50$  ml;  $d$  is the percentage of the

dye,  $d = 0.3 \%$ ;  $c$  is sample of the test substance, taking into account hygroscopic water,  $c = 0.3 \text{ g}$ ;  $e$  is equivalent weight of methylene blue dye,  $e = 319.9$ .

The adsorption of the indicator under the conditions of analysis occurs both on the Bronsted centers and on the Lewis centers in accordance with its  $pK_a$  value. The quantitative determination as a result gives the total content of the Lewis and Bronsted centers of the corresponding force on the surface of the studied sample.

The studies were carried out in the field of Bronsted acid ( $pK_a$  from 0 to 7) and basic ( $pK_a$  from 7 to 13) centers, and Lewis acidic ( $pK_a > 13$ ) centers. Centers of neutral character correspond to  $pK_a = +7$ . An increase in  $pK_a$  values corresponds to an increase in the donor properties of metal atoms, and a decrease in acceptor properties.

To study structure formation, the kinetics of binding of calcium oxide CaO was determined. The content of active CaO in lime was determined by titrating a weighed portion of lime with hydrochloric acid. For this, a 1 g sample of lime was placed in a 250 ml conical flask, 150 ml of distilled water was added, covered with a watch glass and heated for 5–7 minutes. After cooling, 2–3 drops of a 1 % alcohol solution of phenolphthalein were added and titrated with 1 n hydrochloric acid until the contents were completely discolored. The amount of active calcium oxide was determined by the formula

$$\%CaO = \frac{V \cdot 2.804 \cdot K}{m}, \quad (4)$$

where  $\%CaO$  is the content of active CaO, %;  $V$  is the amount of 1 N hydrochloric acid solution consumed for titration, ml; 2.804 is the amount of CaO corresponding to 1 ml of 1 N hydrochloric acid solution, multiplied by 100;  $K$  is correction to the titer of 1 N hydrochloric acid solution;  $m$  is weight of lime, g.

The rheological properties of lime-sand compositions were assessed by the indicator of plastic strength, which was determined using a KP-3 conical plastometer.

### 3. Results and Discussion

Analysis of clays in terms of cationic absorption capacity allows us to assert that, in terms of mineralogical composition, the clay of the Vorobyevsky deposit belongs to the kaolinite type of clays, the Belinsky deposit – to the hydromica type, Kameshkirsky and Issinsky deposits – to the montmorillonite type (Table 2).

**Table 2. Cationic absorption capacity of the studied clays.**

Clay deposit	Cationic absorption capacity value, $E$ , mEq
Vorobyevsky	11.79
Belinsky	20.48
Kameshkirsky	42.50
Issinsky	39.73

In Fig. 1 shows the distribution curves of adsorption centers on the surface of clays.

The influence of the temperature factor led to a change in the energy state of the particles surface in the studied clays. Comparison of the distribution of adsorption centers on the surface of materials that have practically the same chemical, mineralogical, and granulometric compositions indicates that the number of Bronsted and Lewis acid centers on the surface of thermally treated clays exceeds the number of the same centers on the surface of unburnt clay.

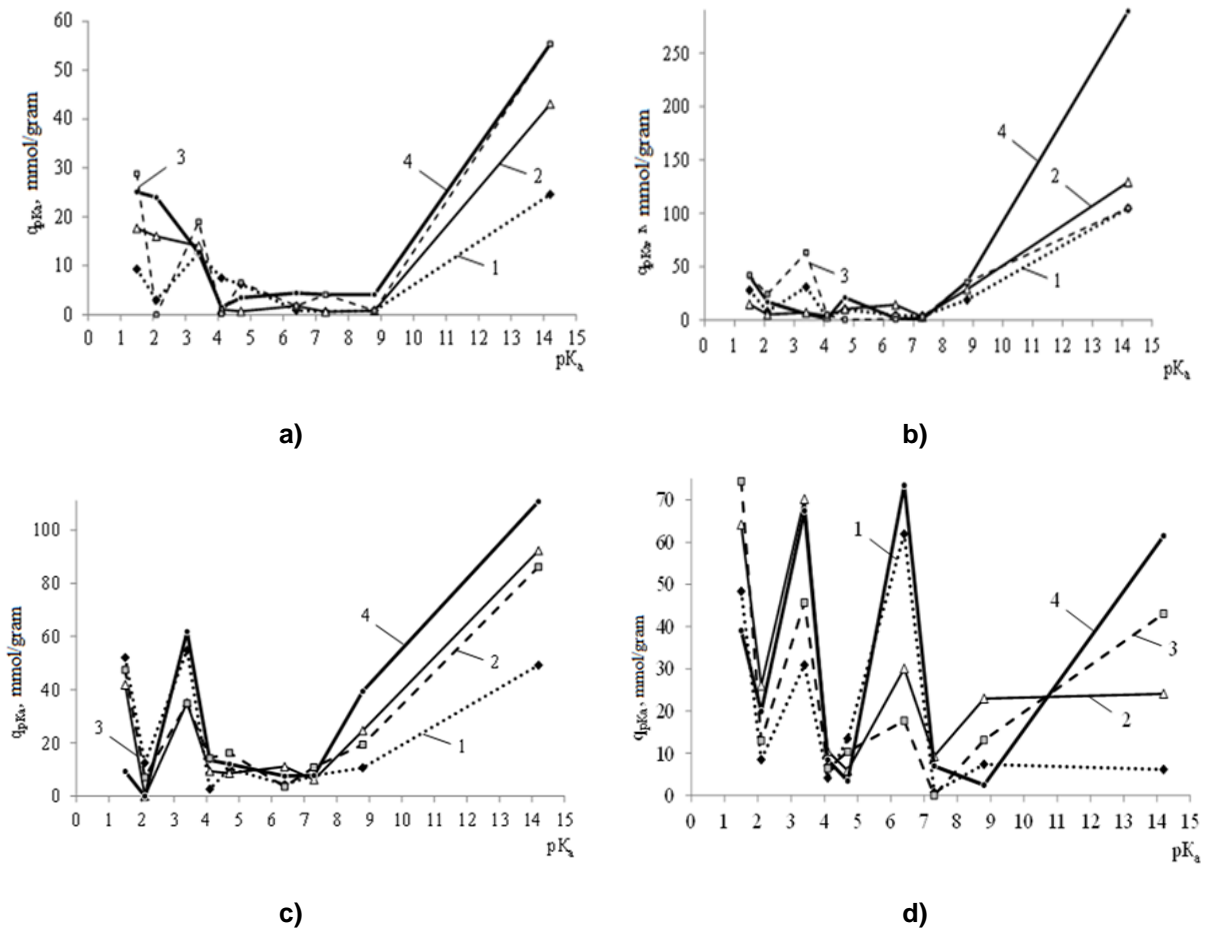


**Figure 1. Distribution of acid-base centers on the surface of mineral additives obtained at different burning temperatures of clay:**  
**a – from the Vorobievskoye deposit: 1 – without burning; 2 – at 500 °C; 3 – at 600 °C; 4 – at 450 °C; b- from the Kameshkirsky deposit:**  
**1 – without burning; 2 – at 450 °C; 3 – at 600 °C; 4 – at 400 °C;**  
**c – from the Belinsky deposit: 1 – without burning; 2 – at 600 °C; 3 – at 450 °C; 4 – at 500 °C; d – from the Issinsky deposit: 1 – without burning;**  
**2 – at 400 °C; 3 – at 600 °C; 4 – at 500 °C.**

Dehydration of the surface of layered aluminosilicates leads to the formation of a large number of Lewis centers. The number of active centers in the region  $pKa > 13$  on the surface of Kameshkir clay before firing was 104.57 mmol/g, after firing at a temperature of 400 °C – 413.65 mmol/g. It is the Lewis centers on the surface of the clay that give it a greater reactivity with the binder. Not only the quantity but also the total content of adsorption centers differs.

To study the process of dehydration of clay from the Vorobyovskoye deposit, its differential thermal analysis (DTA) was carried out (Fig. 2) [26–28]. When analyzing the obtained thermogram, it was found that 6.1 % of bound water is present in Vorobievskaya clay, which is gradually removed to a temperature of 1000 °C with the formation of new minerals. When burning clay at a temperature of 400 °C, 2.2 % of water is removed, at 500 °C – 3.4 %, at 550 °C – 3.7 %, at 600 °C – 4.0 %. It has been established that half of the bound water in the amount of 2.9 % in Vorobievskaya clay is removed at a temperature of 450 °C, at which monohydrate kaolinite is formed, which gives the mineral additive the greatest activity to lime.

The hardening process of lime compositions consists in carbonization, crystallization of lime, and additionally in the formation of calcium hydrosilicates, hydroaluminates and calcium hydroaluminosilicates. This helps to increase the strength of the finishing compositions. However, metakaolinite  $Al_2O_3 \cdot 2SiO_2$  can react with lime only with the dissolution of the initial substance, while monohydrate caolinite  $Al_2O_3 \cdot 2SiO_2 \cdot H_2O$  can interact with  $Ca(OH)_2$  topochemically [29, 30].

To determine the content of the mineral additive in the composition of the DBM, studies were carried out to select the optimal concentration of fired clay, at which the highest value of the ultimate strength in compression of the lime composite will be achieved. Clays of the Vorobyevsky, Kameshkirsky, Belinsky

and Issinsky deposits after burning at a temperature of 500 °C were used as a mineral additive, and Ukhtinsky sand was used as a fine aggregate.

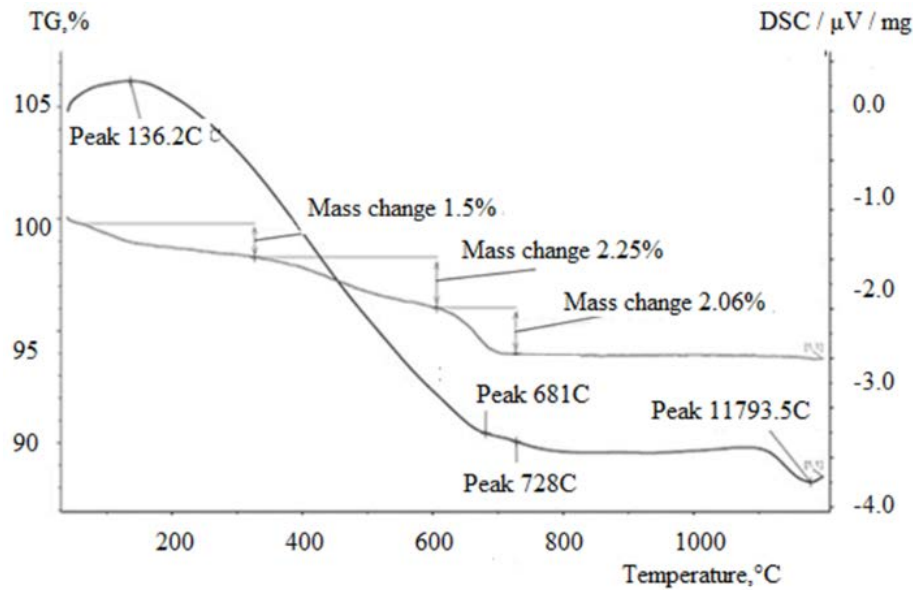


**Figure 2. Derivatogram of the Vorobyovskoe deposit clay.**

It was found that the highest compressive strength is achieved when a mineral additive is added to the composition of the DBM in an amount of 10 % of the lime mass. So, when Vorobyov's clay was added to the DBM formulation after burning at a temperature of 500 °C in an amount of 10 %, the compressive strength  $R_{cs}$  was 1.55 MPa, in an amount of 15 % – 1.38 MPa, in an amount of 20 % – 1.32 MPa. A similar pattern is also observed with the introduction of mineral additives based on Belinskaya, Issinskaya and Kameshkirskaya clays. This is probably due to the fact that with an increase in the amount of the mineral additive over 10 %, an excess of the finely dispersed fraction is obtained, which leads to a lack of mixing water.

Additionally, to assess the structure formation of lime-sand compositions with the addition of a mineral additive, the kinetics of lime binding was studied. Analysis of experimental data indicates that over time, there is a decrease in the amount of free lime. So, at the age of 7 days, the amount of free lime in the lime-sand composition is 84.5 %, and at the age of 28 days it is 78.6 %. A lower content of the amount of free lime in the compositions with the use of clay after firing at a temperature of 500 °C was established. So, in the samples with the addition of Belinskaya and Kameshkirskaya clays, fired at this temperature, the content of free lime on the 28<sup>th</sup> day of hardening decreased to 68.21 % and 70.83 %, respectively.

The introduction of fired clay into the lime-sand composition increases the compressive strength at the age of 28 days of air-dry hardening, depending on the firing temperature and the type of clay, by 2.0–2.6 times. With the introduction of Kameshkirsky clay, the highest value of the compressive strength at the age of 28 days of hardening is achieved with the introduction of an additive fired at a temperature of 400 °C into the composition, and is  $R_{cs} = 1.75$  MPa, while for the composition without the additive it is 0.84 MPa. With the introduction of Vorobyovskoy clay, fired at a temperature of 450 °C, the strength increases to 1.67 MPa. The introduction of Belinsky and Issinsky clays after firing at a temperature of 500 °C helps to increase the strength of the compositions to 2.2 and 1.68 MPa, respectively. The results of the conducted studies confirm that the addition of low-fired clay to the lime-sand composition contributes to an increase in the strength of lime composites by 6–26 % compared to metakaolinite due to the monohydrate kaolinite formed at a temperature of 400–500 °C, which decomposes in an aqueous alkaline medium to ions  $\text{Al}(\text{OH})_2^{2+}$  and  $\text{SiO}_3^{2-}$ . The infinite nanoradical  $[\text{SiO}_3]_{\infty}^{2-}$  has increased activity in an aqueous medium towards calcium oxide and hydrate, while infinite layers of the radical  $[\text{Si}_2\text{O}_5]_{\infty}^{2-}$  kaolinite and the final radical  $[\text{Si}_2\text{O}_7]^{6-}$  in metakaolinite have little activity towards lime.

In Fig. 3 shows the curves of the kinetics of the strength gain of lime compositions based on the results of the approximation of experimental data for determining the compressive strength of the test samples. The data were approximated using the CurveExpert 1.3 program. The dots in the figures indicate the experimental values of the ultimate compressive strength of lime samples. Based on the results of approximation and experimental studies (Fig. 3), it follows that clays after firing at temperatures of 400–500 °C (curve 2) contribute to a more intense structure formation of lime-sand samples than clays fired at a temperature of 600 °C (curve 1).

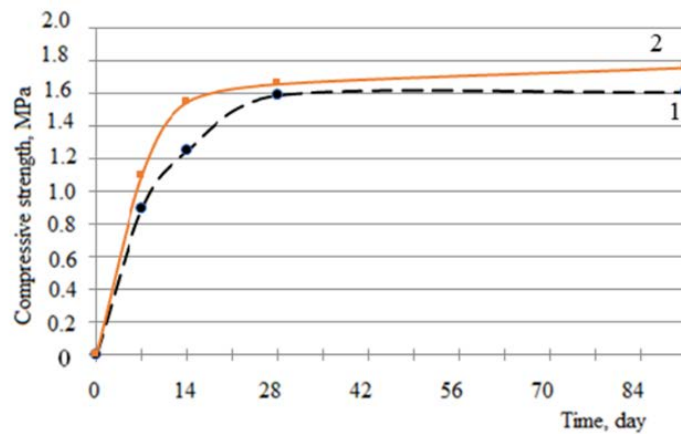


**Figure 3. Kinetics of strength gain of lime-sand compositions with the addition of clay from the Vorobievskoye deposit: 1 – after firing at  $t = 600\text{ }^{\circ}\text{C}$ ; 2 – after firing at  $t = 450\text{ }^{\circ}\text{C}$ .**

The curves shown in Fig. 3 are described by the exponential equation

$$y = a(1 - e^{-bx}), \quad (5)$$

where  $a$  is a constant that takes into account the maximum possible compressive strength;  $b$  is rate constant of structure formation;  $x$  is the hardening time.

The values of the rate constant of structure formation  $b$  are given in Table 3.

**Table 3. Values of constants for the kinetics of strength gain.**

Clay deposit	Clay firing temperature, $^{\circ}\text{C}$	$a$	$b$
Vorobievskoe	450	1.744	0.146
	600	1.611	0.123

The calculation results show that at low-temperature firing of clay, the value of the rate constant of structure formation is higher in comparison with firing clay at a temperature of  $600\text{ }^{\circ}\text{C}$ . Thus, the rate constant of structure formation  $b$  for lime compositions with the addition of Vorobiev's clay after firing at  $600\text{ }^{\circ}\text{C}$  was  $0.123\text{ MPa/day}$ , while for compositions with clay fired at  $450\text{ }^{\circ}\text{C}$  it was  $0.146\text{ MPa/day}$  (Table 3). A similar law is observed with the introduction of mineral additives based on Belinskaya, Kameshkirskaya and Issinskaya clays.

It was found that mineral additives increase the plastic strength in the early stages of hardening (Fig. 4). The fastest increase in plastic strength was observed for the composition with the addition of clay after firing at  $500\text{ }^{\circ}\text{C}$  (Fig. 4, curve 4), the plastic strength after 67 hours from the moment of mixing was  $0.064\text{ MPa}$ , while for the composition with the addition of clay fired at temperature of  $600\text{ }^{\circ}\text{C}$ , –  $0.054\text{ MPa}$ .

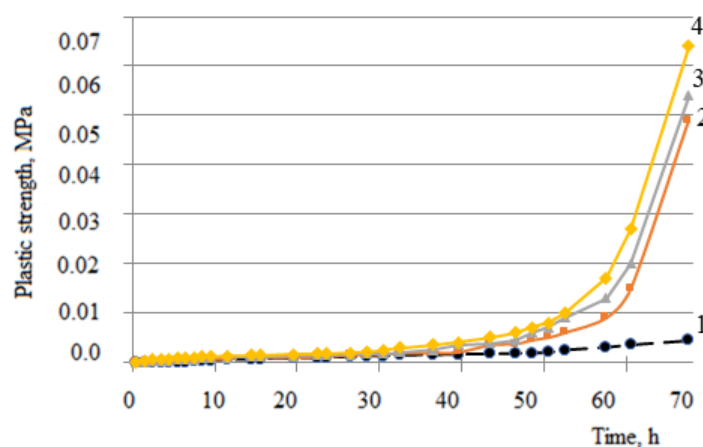


**Figure 4. The effect of the clay firing temperature on the kinetics of changes in the plastic strength of the mixture: 1 – control composition (without additive); 2 – clay content 10 % by weight of lime (without firing); 3 – clay content 10 % by weight of lime (clay fired at a temperature of  $600\text{ }^{\circ}\text{C}$ ); 4 – clay content 10 % by weight of lime (clay fired at a temperature of  $500\text{ }^{\circ}\text{C}$ ).**

The water-holding capacity of composites is 96.5–98 %. The results obtained agree with the data of the authors [31, 32]. The authors proposed, when developing a composition for restoration, to use a mixture of calcium hydroxide, pozzolan, volcanic ash and quartz sand as a filler. Using X-ray analysis and high-resolution SEM images of newly applied plaster, the transformation of portlandite to calcite and the pozzolanic effect of kaolinite are established.

We recommend using the proposed dry mortar for the restoration of historical buildings. The mortar mixture is well applied to the surface and is combined with previously finished surfaces.

Table 4 shows the compared indicators of technological and operational properties of finishing compositions based on developed dry mixes and a prototype composition. The technological and operational properties of the developed dry mixes were compared with the properties of the finishing classical Runit plaster based on air lime, produced by the company OOO "Azhioproekt" [33]. Plaster "Runit" is used for the restoration of buildings.

**Table 4. Technological and operational properties of finishing compositions.**

Name of indicator	Value of indicator of Finishing compositions	
	developed	prototype
Average density DBM, $\rho_a$ , kg/m <sup>3</sup>	1290–1304	1575
Viability at stored in open capacities, hour	8–10	$\geq 2$
Workability	good	good
Recommended thickness of one layer, mm	before 20	Before 20
Consumption of finishing composition at 1 layer is applied of thickness 10 mm, kg/m <sup>2</sup>	12–14	15–17
Water-holding capacity, %	98.0–98.3	95.0–97.0
Time of drying at 20 °C to degree "5", min	no more 55	no more 45
Adhesive durability $R_{ad}$ , MPa	0.60–0.76	0.40
Durability at compression, $R_c$ , MPa	2.52–3.71	0.40
Shrinkable deformations, $\varepsilon$ , %	0.027–0.034	0.030–0.040
Vapor coefficient $\mu$ , mg/m·h·Pa	0.055–0.058	0.047
Cracks due to shrinkage	no	no
Temperature of application, °C	5–35	5–35

It was found that the developed dry mix is not inferior to the prototype in terms of technological and operational properties. At the same time, the production of the proposed dry mixes is more economical due to the use of local raw materials and domestic additives.

## 4. Conclusions

1. The authors developed a technology and formulation of a mineral additive for lime dry building mixtures involving low-temperature firing of clays at a temperature of 400–500 °C. It was revealed that the effect of the temperature factor leads to a change in the energy state of the surface of clay particles, which consists in an increase in the number of Lewis centers (up to 4 times), as well as the total number of active centers (up to 2 times).

2. The study established regularities of the structure formation of lime finishing compositions with the addition of mineral additives. It was revealed by XRD and mechanical tests that samples based on compositions with a mineral additive fired at a temperature of 500 °C are characterized by a high content of zeolites, a decrease in portlandite, and an increase in the amount of chemically bound lime by 31.8 %. The optimal concentration of a mineral additive was selected, which is 10 % of lime mass. It is shown that the introduction of clay fired at temperatures of 450–500 °C into a lime-sand composition increases compressive strength at the age of 28 days of air-dry hardening, which, depending on the firing temperature and the type of clay, is 2–2.6 times.

3. The main technological and operational properties of the lime composition and coatings based on it were determined. The finishing layer based on the developed mixture is characterized by the following indicators: adhesion strength  $R_{adg} = 0.60–0.76$  MPa, cohesive strength  $R_{kog} = 0.35–0.36$  MPa, vapor permeability  $\mu = 0.055–0.058$  mg/mhPa, conditional coefficient crack resistance  $K_{tr} = 0.54–0.58$ , water

absorption by weight  $W_t = 12.29\text{--}13.62\%$ , softening coefficient  $K_p = 0.48\text{--}0.52$ , elastic modulus  $E_{el} = 40\text{--}50\text{ MPa}$ , deformation modulus  $E_{def} = 20.59\text{--}24.00\text{ MPa}$ , shrinkage deformations  $\varepsilon = 0.027\text{--}0.034\%$ .

## References

1. Shangina, N.N. Features of production and use of dry construction mixes for restoration of monuments of architecture. *Dry construction mixes*. 2011. 4. Pp.16–19.
2. Becerra, J., Ortiz, P., Martín, J.M., Zaderenko, A.P. Nanolimes doped with quantum dots for stone consolidation assessment. *Construction and Building Materials*. 2019. 199. Pp. 581–593. DOI: 10.1016/j.conbuildmat.2018.12.077
3. Frankeová, D., Koudelková, V. Influence of ageing conditions on the mineralogical micro-character of natural hydraulic lime mortars. *Construction and Building Materials*. 2020. 264.120205
4. Schueremans, L., Cizer, O., Janssens, E., Serré, G., Balen, K.V. Characterization of repair mortars for the assessment of the ir compatibility in restoration projects: Research and practice. *Construction and Building Materials*. 2011. 25(12). Pp. 4338–4350. DOI: 10.1016/j.conbuildmat.2011.01.008
5. Lindqvist, J.E., Sandström, M. Quantitative analysis of historical mortars using optical microscopy *Materials and Structures/Materiaux et Constructions*. 2000. 33(10). Pp. 612–617. DOI: 10.1007/bf02480600
6. Middendorf, B., Hughes, J.J., Callebaut, K., Baronio, G., Papayianni, I. Investigative methods for the characterisation of historic mortars – Part 1: Mineralogical characterisation. *Materials and Structures/Materiaux et Constructions*. 2005. 38(282). Pp. 761–769. DOI: 10.1617/14281
7. Middendorf, B., Hughes, J.J., Callebaut, K., Baronio, G., Papayianni, I. Investigative methods for the characterisation of historic mortars – Part 2: Chemical characterisation. *Materials and Structures/Materiaux et Constructions*. 2005. 38(282). Pp. 771–780. DOI: 10.1617/14282
8. Dabbaghi, F., Sadeghi-Nik, A., Ali Libre, N., Nasrollahpour, S. Characterizing fiber reinforced concrete incorporating zeolite and metakaolin as natural pozzolans. *Structures*. 2021. 34. Pp. 2617–2627.
9. Loganina, V., Fediuk, R. Improving the performance of lime-sand finishing mixes. *Construction and Building Materials*. 2020. 264. 120687.
10. Loganina, V.I., Makarova, L.V., Tarasov, R.V., Akzhigitova, E.R. Mineral additive based on the mixed-layer clays for dry construction mixes. *Contemporary Engineering Sciences*. 2014. 7(25-28). Pp. 1547–1554.
11. Loganina, V.I., Makarova, L.V., Tarasov, R.V., Sadovnikova, M.A. Composition limy binder with the use of the synthesized aluminosilicates for dry construction blends. *Advanced Materials Research*. 2014. 977. Pp. 34–37.
12. Rafat Siddique, Juvas Klaus. Influence of metakaolin on the properties of mortar and concrete: A review. *Applied Clay Science*. 2009. 43. Pp. 392–400.
13. Al-Akhras, N.M. Durability of metakaolin to sulfate attack. *Cement and Concrete Research*. 2006. 36(9). Pp. 1727–1734.
14. Ambroise, J., Maximilien, S., Pera, J. Properties of metakaolin blended cements. *Advanced Cement Based Materials*. 1994. 1. Pp. 161–168.
15. Badogiannis, E., Kakali, G., Dimopoulou, G., Chaniotakis, E., Tsvivilis, S. Metakaolin as a main cement constituent: exploitation of poor Greek kaolins. *Cement & Concrete Composites*. 2005. 27. Pp. 197–203.
16. Potgieter-Vermaak, S.S., Potgieter, J.H. Metakaolin as an extender in South African cement. *Journal of Materials in Civil Engineering*. 2006. 18(4). Pp. 619–623.
17. Murat, V. Hydration reaction and hardening of calcined clays and related minerals. I. Preliminary investigation on metakaolinite. *Cement and Concrete Research*. 1983.13(2). Pp. 259–266. DOI: 10.1016/0008-8846(83)90109-6
18. Weise, K., Ukrainczyk, N., Duncan, A., Koenders, E. Enhanced Metakaolin Reactivity in Blended Cement with Additional Calcium Hydroxide. *Materials*. 2022. 15 (1). e 367. DOI: 10.3390/ma15010367
19. Qiao, Z., Ding, Z., Wang, J., Wang, F., Xie, Z. Enhanced mechanical properties and environmental erosion resistance with metakaolin in a kind of Chinese traditional Lime-based mortar. *Construction and Building Materials*. 2022. 31724. e126110. DOI: 10.1016/j.conbuildmat.2021.126110
20. Morrison, S. *Chemical Physics of Solid Surface*. Moscow, World, 1980. 488 p.
21. Novikova, L.A., Belchinskaya, L.I., Resner, F. Determination of the type of active centers on the surface of clay minerals in the reaction of conversion of methylbutinol. *Sorption and chromatographic processes*. 2005. 5 (6). Pp. 806–815.
22. Ovcharenko, F.D., Zhukova, A.I., Vdovenko, N.V., Dyachenko, N.S., Vasilyev, N.G. Study of ion-exchange adsorption of butyl-monochloride on cation-substituted forms of montmorillonite. *Physicochemical mechanics and lyophilicity of dispersed systems*. 1971. 3. Pp. 8–13.
23. Válek, J., Van Halem, E., Viani, A., Pérez-Estébanez, M., Ševčík, R., Šašek, P. Determination of optimal burning temperature ranges for production of natural hydraulic limes. *Construction and Building Materials*. 2014. 66. Pp. 771–780. DOI: 10.1016/j.conbuildmat.2014.06.015
24. Frías, M., Cabrera, J. Influence of MK on the reaction kinetics in MK/lime and MK-blended cement systems at 20 °C. *Cement and Concrete Research*. 2001. 31(4). Pp. 519–527.
25. Poon, C.S., Kou, S.C., Lam, L. Compressive strength, chloride diffusivity and pore structure of high performance metakaolin and silica fume concrete. *Construction and Building Materials*. 2006. 20. Pp. 858–865.
26. Silva, B.A., Ferreira Pinto, A.P., Gomes, A. Influence of natural hydraulic lime content on the properties of aerial lime-based mortars. *Construction and Building Materials*. 2014. 72. Pp. 208–218. DOI: 10.1016/j.conbuildmat.2014.09.010
27. Fortes-Revilla, C., Martínez-Ramírez, S., Blanco-Varela, M. Modelling of slaked lime–metakaolin mortar engineering characteristics in terms of process variables. *Cement and Concrete Composites*. 2006. 28(5). Pp. 458–467.
28. Ventol, L., Vendrell, M., Giraldez, P., Merino, L. Traditional organic additives improve lime mortars: New old materials for restoration and building natural stone fabrics. *Construction and Building Materials*. 2011. 25(8). Pp. 3313–3318. DOI: 10.1016/j.conbuildmat.2011.03.020

29. Ševčík, R., Šašek, P., Viani, A. Physical and nanomechanical properties of the synthetic anhydrous crystalline CaCO<sub>3</sub> polymorphs: vaterite, aragonite and calcite. *Journal of Materials Science*. 2018. 53(6). Pp. 4022–4033. DOI: 10.1007/s10853-017-1884-x
30. Nunes, C., Slížková, Z. Freezing and thawing resistance of aerial lime mortar with metakaolin and a traditional water-repellent admixture. *Construction and Building Materials*. 2016. 114. Pp. 896–905. DOI: 10.1016/j.conbuildmat.2016.04.029
31. Paredes, M., Uc, J.M.C., Pacheco, E., C.R.R. Soberanis, C.R.R., Wakayama, S. Physicochemical and mechanical study of Mayan Archeological stony constructive materials. *Journal of Applied Research and Technology*. 2018. 16. e00875 DOI: 10.22201/icat.16656423.2018.16.4.727
32. Xu, L., Ma, X., Zhang, B., Zhang, Q., Zhao, P. Multi-analytical Studies of the Lime Mortars from the Yanxi Hall in the Yangxin Palace of the Palace Museum (Beijing). *Archaeometry*. 2019. 61 (2). Pp. 309–326. DOI: 10.1111/arcm.12421
33. Classic finishing plaster Runit [Electronic resource]: information on the products of LLC Agioproekt // Dry building mixtures Agio: [site]. Access mode: <http://www.agioprojekt.ru/products/243/>

**Information about authors:**

**Valentina Loganina**, Doctor of Technical Science

ORCID: <https://orcid.org/0000-0001-7532-0074>

E-mail: [loganin@mail.ru](mailto:loganin@mail.ru)

**Elvira Akzhigitova**, PhD in Technical Science

ORCID: <https://orcid.org/0000-0001-9536-8112>

E-mail: [il2018vira@mail.ru](mailto:il2018vira@mail.ru)

Received 19.10.2021. Approved after reviewing 28.09.2022. Accepted 29.09.2022.



Research article

UDC 627.824.31

DOI: 10.34910/MCE.117.8



## Heterogeneous embankment dam under rapid drawdown

A.K. Aldungarova<sup>1</sup> , T.M. Mkilima<sup>2</sup>  , Ye.B. Utepov<sup>2,3</sup> , A.S. Tulebekova<sup>2,3</sup> ,  
Sh.Zh. Zharassov<sup>2,3</sup> 

<sup>1</sup> D. Serikbayev East Kazakhstan Technical University, Ust-Kamenogorsk, Republic of Kazakhstan

<sup>2</sup> L.N. Gumilyov Eurasian National University, Astana, Republic of Kazakhstan

<sup>3</sup> CSI Research&Lab, LLP, Astana, Republic of Kazakhstan

✉ [tmkilima@gmail.com](mailto:tmkilima@gmail.com)

**Keywords:** slope stability, safety factor, embankment dam, numerical analysis, finite element

**Abstract.** Loading conditions are among the significant determinants of the stability of embankment dams: they need to be carefully investigated during the design phase of the dam construction. Unfortunately, it is almost impossible to investigate the combination of these parameters in-situ. In the current work, the influence of rapid drawdown loading conditions on the stability of the embankment dam was investigated with the help of numerical modeling for a case of the Aktobe dam in Kazakhstan. The seepage analyses were carried out concurrently with slope stability analyses. Mainly, five different drawdown cases were investigated, which are: steady-state, instantaneous drawdown, 5-days drawdown, 10-days drawdown, and 1m per day drawdown rate. In terms of flow type, both steady-state and transient flow conditions were investigated. In general, when the embankment was subjected to the 1 m per day drawdown rate a minimum factor of safety value of 1.486 was retrieved from computations. The factor of safety value is equivalent to a 3.7 % increase from the 10 days drawdown rate, 8.3 % from the 5 days drawdown rate and 48.6 % from the instantaneous drawdown.

**Funding:** This research was funded by the Science Committee of the Ministry of Education and Science of the Republic of Kazakhstan (Grant No. AP09258790).

**Citation:** Aldungarova, A.K., Mkilima, T.M., Utepov, Ye.B., Tulebekova, A.S., Zharassov, Sh.Zh. Heterogeneous embankment dam under rapid drawdown. Magazine of Civil Engineering. 2023. 117(1). Article no. 11708. DOI: 10.34910/MCE.117.8

### 1. Introduction

Embankment dams are artificial barriers constructed to retain or detain water for either permanent storage or release at a controlled rate, which have been in existence for millenia. It is believed that embankment dams date back to Ancient Egypt, India, and China [1]. Embankment dams are also famous in urban catchments, where they are used as flood control structures.

Embankment dams are considered to be the most economical type of dams, a phenomenon that is highly attributed to the fact that, the filling materials can be retrieved at the dam site with little or no processing before their application [2]. However, these dams are always challenged by the potential slope failure. The slope stability of an embankment dam is highly dependent on the material characteristics, slope steepness, and nature of loading [3].

The location and geometry of these dams are highly dependent on the results from feasibility studies that have to check geological issues, hydrological conditions, nature of the terrain as well as seismic factors; without forgetting the availability of the construction materials [4]. In most cases whether an embankment dam or concrete dam will be constructed is highly dependent on the size of the valley; whereby, concrete

dams are always preferable in narrow valleys while embankment or earth-fill dams are preferable in wider valleys with problematic foundation soil [5].

In terms of material characteristics; an embankment dam is normally created by the placement and compaction of a complex semi-plastic mound. This mound can have various compositions of earth-fill materials including: sand, clay, gravel, or rock. Gravels are among the materials used in the construction of embankment dams characterized by high hydraulic ( $k$ ) conductivities also known as permeability rates ranging from 1 to 100 cm/s. For instance, the Hazen equation has for long been used to estimate hydraulic conductivity in cm/s based on semi-empirical correlations with effective grain size ( $D_{10}$ ) as summarized in Equation 1 [6].

$$k = C \times D_{10}^2, \quad (1)$$

where,  $D_{10}$  represents the grain size in mm which is equivalent to 10 percent passing on the gradation curve for the soil, while the constant  $C$  varies from 0.4 to 1.2, with an average typical value being 1 [7]. Some other researchers have also tried to relate  $k$  to the  $D_{15}$  size for uniform filter sands as summarized in Equation 2 [8].

$$k = C \times D_{15}^2. \quad (2)$$

In terms of slope, it is always recommended to use shallow slopes such as 3 units horizontal to 1 unit vertical. For upstream slopes, the ratio is 4 units horizontal to 1 unit vertical, and for downstream slopes, 2.5 units horizontal to 1 unit vertical, especially for homogeneous or modified-homogeneous small dams constructed of fine-grained soils [9]. In terms of loading conditions several parameters have to be always taken into consideration when designing embankment, which are: end of construction, steady seepage, seismic forces, and most importantly rapid drawdown (from spillway elevation to the crest of the lowest gated or ungated outlet).

Despite the potential usefulness of these dams, slope failure has been always a significant concern [10]. A failure of such a dam likely leads to unmanageable catastrophic consequences. Loss of human lives, damage to domestic and wild life, loss of properties, and environmental degradation are among the potential results of the embankment dam slope failure. The slope failure process starts with seepage flow on the downstream slope of an embankment dam and is a primary indication of the migration of fine particles in the dam [11].

Unfortunately, another major issue of concern with embankment dams that has currently emerged is the potential of embankment failure under rapid drawdown scenarios [12]. Normally, an embankment dam is subjected to a fairly long-time constant elevation of water surface, which is also known as the long-term steady-state: the flow of water within the embankment (seepage) during the long-term reservoir level has likely reached a steady-state making the dam relatively stable. However, in some cases, the reservoir has to be drained rapidly either intentionally or due to the system failure upstream, including the impacts of land use/land cover change [13]. In such a case, the pore-water pressures developed within the embankment from the long-term steady-state conditions may remain relatively high, whereby the removal of water also removes the stabilizing effect of the reservoir's weight along the upstream side of the embankment and the embankment eventually fails [14–15]. However, the mode of failure due to the rapid drawdown conditions differs from one case to another. Therefore, the potential response of an embankment dam with a relatively low permeability material zone in the upstream face under rapid drawdown conditions is yet to be discovered.

There are already many cases of embankment dam failure, including the following examples. The Belci dam in Romania failed in 1991, and the embankment with a clay core was constructed in 1962 [16]. The Tous dam embankment dam in Valencia, Spain, failed due to overtopping in 1982 with an estimated damage of approximately 400 million USD [17]. The Upper Taum Sauk embankment dam failed on December, 14<sup>th</sup> 2005, in Missouri, the United States of America; the construction of the dam started in 1960 and ended in 1962, while it was put into operation in 1963 [18]. The Teton Dam located within the Teton River catchment in Madison County, southeast Idaho in the United States of America, faced a total failure in 1976 and is among the most famous case studies in terms of dam failure [19–22]. The Baldwin Hills 71 m high with a crest length of 198 m which was designed as a homogeneous embankment dam faced a failure in 1963 [23]. These are only some of the many cases of dam failures. With these cases, it is beyond reasonable doubt that the stability of embankment dams remains one of the most significant concerns for Civil and Geotechnical Engineers.

In this study, the influence of rapid drawdown loading conditions on the stability of the embankment dam is investigated with the help of numerical modeling for the case of the Aktobe dam in Kazakhstan.

## 2. Materials and Methods

### 2.1. Case study description

The Aktobe dam is located approximately 10 km from the Aktobe City center in Western Kazakhstan; latitude: 50°12'23.26"N and longitude: 57°18'36.18"E. The reservoir with a volume of approximately 245 million m<sup>3</sup> was put into operation in 1988. The Aktobe region is known to be among the largest regions in terms of area coverage in Kazakhstan with an approximate area of 300,629 km<sup>2</sup> occupying approximately 11 percent of the entire country.

Several rivers are decorating the Aktobe region including the Kargaly river which discharges its water into another river (Ilek River). One of the tributaries of the Ilek (left tributary) passes through the center of the Aktobe region. Sazdy River is another important river that passes within the city; whereby, large entertainment centers, shopping malls, and other social buildings are located along the river banks.

In terms of climatic conditions, the Aktobe region is characterized by a humid continental climate with significantly high seasonal variation levels in terms of temperature. The region is also characterized by harsh winters like many other parts of the country with temperatures dropping as low as -48 °C; whereas, the daily average minimum temperature is -16 °C. Also, the Aktobe region is characterized by hot summers with the temperature reaching 43 °C; whereas, the average maximum temperature is 30 °C. However, it is also worth pointing out that, the levels of weather changes are extremely high in the region in spring and autumn, especially during the windiest days of March. Moreover, the rainy seasons are generally during early spring and a bit of late autumn (the period when winter starts); characterized by heavy snows during the winter. On average, the annual precipitation in the Aktobe region is approximately 330 mm.

Like many other parts of Kazakhstan, the geological condition in the Aktobe region is characterized by significantly extensive basement rocks resulting from the Precambrian and relatively high widespread Paleozoic rocks. Based on some studies it has been observed that the groundwater of some parts of the region is characterized by high concentration levels of petroleum products [24].

### 2.2. Embankment geometry and modeling process

In this study, finite element method analyses were used to evaluate the potential influence of rapid drawdown loading conditions on slope stability of an earth-fill dam for the case of the Aktobe dam. The general modeling process is characterized by two main types of analyses, namely; seepage analysis and slope stability analysis. The seepage analysis was executed using the SEEP/W unit of the GeoStudio, while the slope stability was executed using the SLOPE/W of the GeoStudio 2018 R2 (version 9.1.1.14749). Mainly, five different drawdown cases were used, namely; steady-state, instantaneous drawdown, 5-day drawdown, 10-day drawdown, and 1 m per day drawdown rate. It is also worth noting that, the seepage analyses were carried out concurrently with slope stability analyses. The Aktobe dam embankment is characterized by a maximum water depth of 18.5 m, with an embankment height of 22.7 m (Fig. 1). The embankment is mainly divided into five different zones based on material properties (discussed in the materials properties section).

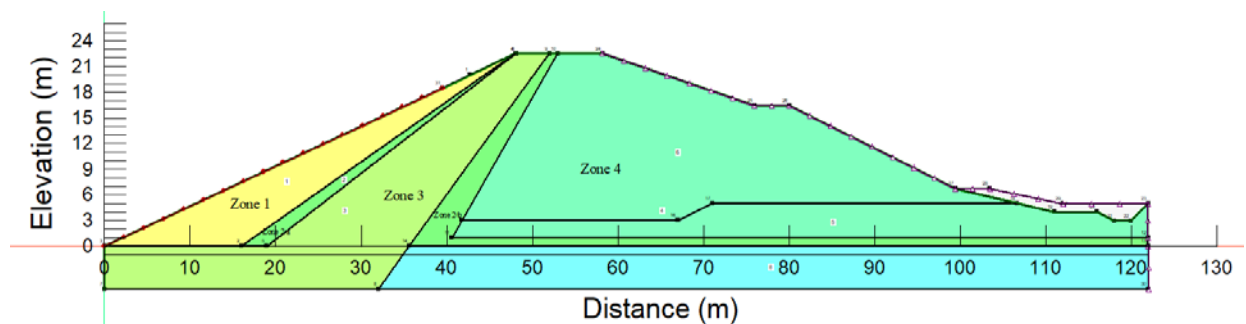


Figure 1. Embankment geometry.

### 2.3. Seepage analysis

In the seepage analysis, it was important to establish a long-term steady-state using the Steady-state type of analysis before subjecting the embankment to the transient analysis. In that matter, the developed long-term steady conditions were used to feed pore-water pressures to the transient seepage analyses through the "parent" approach. This was an important step or process because, from prolonged

develop a steady-state condition of seepage that has to be taken into consideration during the numerical modeling [25].

However, as previously mentioned, the numerical modeling process consisted of several drawdown rates (instantaneous, 5 days drawdown, 10 days drawdown, and 1 m per day drawdown rate) and isotropic hydraulic conductivity values. To model the transient flow through varying water levels as the reservoir was being drained, linear functions were specified as a boundary condition on the upstream face of the embankment. It is also worth highlighting that, the transient flow analyses received pore-water pressures from seepage analyses. Fig. 2 presents the summary of the drawdown boundary conditions for the 5 days drawdown, 10 days drawdown, and 1 m per day drawdown rates.

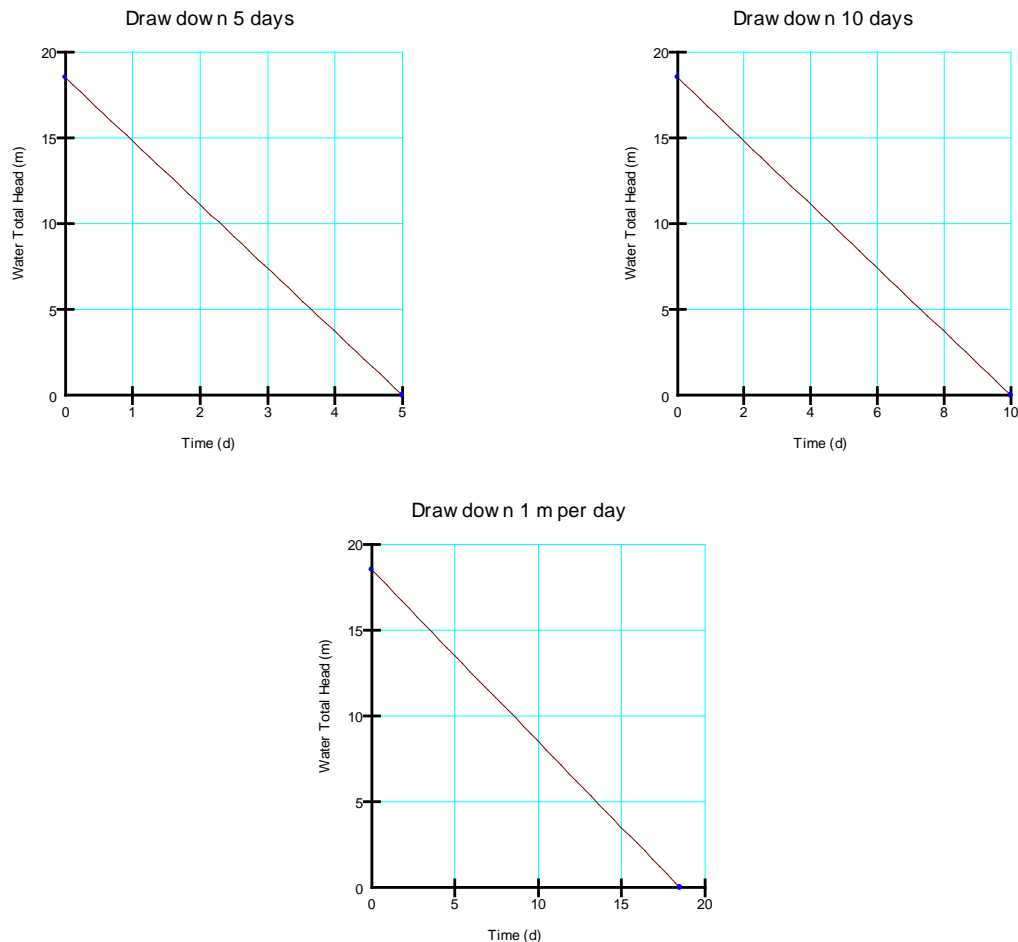


**Figure 2. Boundary conditions.**

#### 2.4. Slope stability analysis

As previously mentioned, the slope stability models received their pore-water pressures from the seepage analysis models. In general, the slope stability modeling is based on the Morgenstern–Price approach which is a general method of slices established based on the limit equilibrium. Its application requires the fulfillment of equilibrium of forces and moments acting on individual blocks. To generate the blocks, the soil above the slip surface has to be divided by dividing planes [26]. Generally, the method is a limit equilibrium approach used to assess the factor of safety value of the potential failure mass based on satisfaction of both force and moment equilibrium [27].

In this study, the Morgenstern–Price approach was selected due to the fact that it is capable of satisfying the equilibrium conditions and involves the least numerical difficulty [28]. Moreover, it has to be noted that the fundamental supposition governing the Morgenstern–Price method is that the ratio of normal to shear interslice forces through the sliding mass is characterized by an interslice force function resulting as a product of a specified function  $f(x)$  and an unknown scaling factor  $\lambda$ .

Several assumptions were incorporated in the formulation of the Morgenstern–Price method to compute the limit equilibrium of forces and moment on individual blocks [28]:

- The planes that divide one block and another are always vertical.

- The action line of the weight of the block passes through the center of the particular segment of slip surface represented by a point.
- The normal force is acting in the center of the particular segment of the slip surface at a point.
- The inclination of forces acting between blocks is different on each block at slip surface endpoints.

### 2.5. Material characteristics

The embankment was divided into different zones and each zone was assigned a specific type of material based on the heterogeneity of the Aktobe dam. Zone 1 was composed of more non-cohesive materials (coarse materials) mixed with some fine materials with fixed hydraulic conductivity based on the dam material characteristics. Zones 2 (a) and (b) were also characterized by non-cohesive soil (filter materials) with more sand and gravel. On the other hand, Zone 3 was mainly composed of relatively high cohesive soil material including fine-grained materials (clay). Moreover, Zone 4 was mainly composed of coarse material with relatively very little content of fines materials. In general, the liquid from all the zones ranged from 18 % to 52 %. From Table 1 it can be observed that some other parameters such as diameter at passing 10 %, diameter at passing 60 %, internal angle of friction (degree), as well as unit weight were specified in the model. Fig. 3 presents the summary of the volumetric water content and hydraulic conductivity functions assigned to the model from Zone 1 and 2.

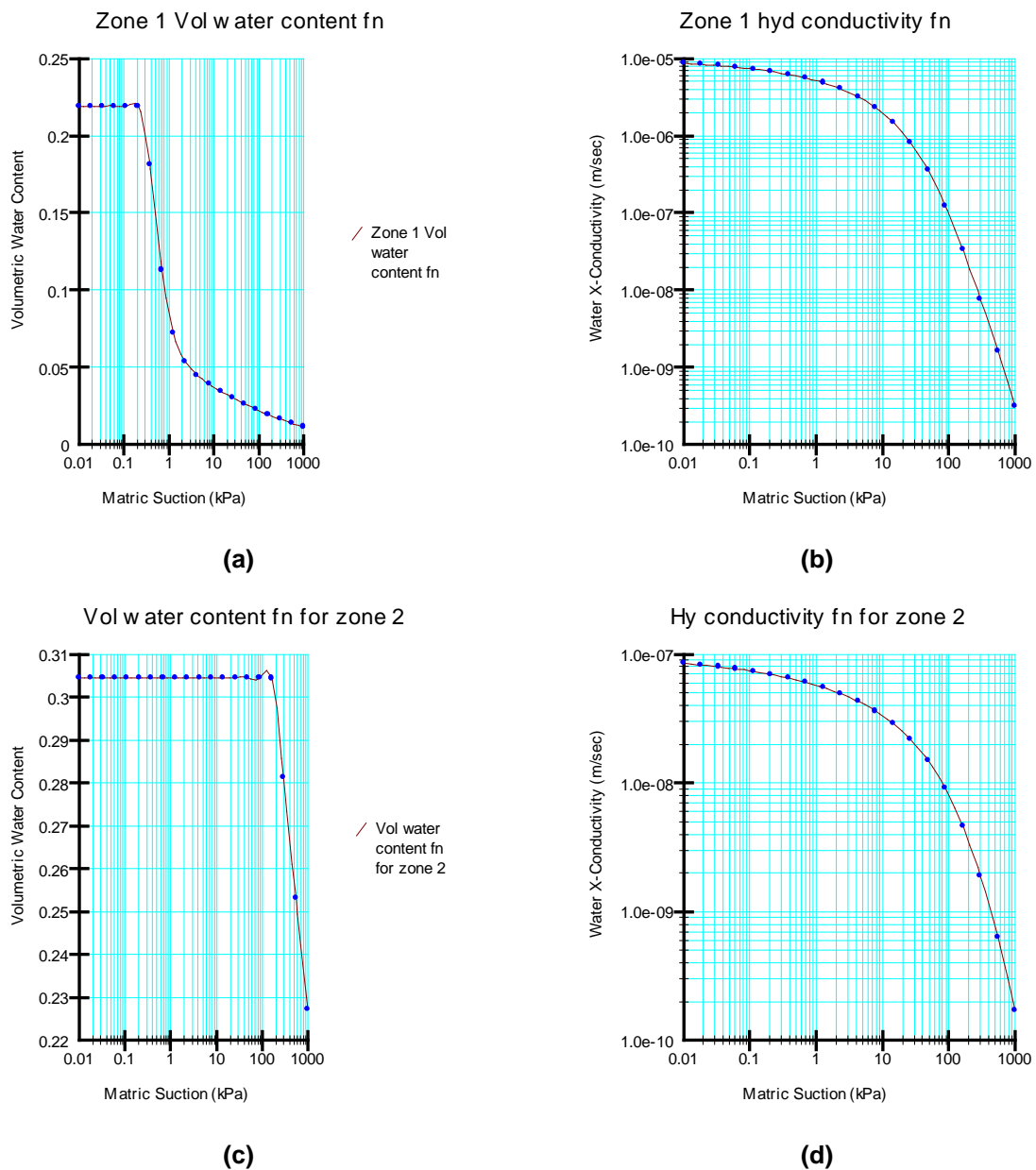


Figure 3. Volumetric water content and hydraulic conductivity functions for different zones.

**Table 1. Material properties.**

Parameter	Zone			
	Zone 1	Zone 2	Zone 3a,b	Zone 4
Saturated hydraulic conductivity (ksat), m/s	$1.2 \cdot 10^{-5}$	$1.42 \times 10^{-8}$	$1.1 \times 10^{-4}$	$5.2 \times 10^{-5}$
Diameter at passing 10 % (mm)	0.1	0.002	0.2	0.1
Diameter at passing 60 % (mm)	40	0.05	0.8	40
Liquid limit (%)	25 to 45	50		
Unit weight (kN/m <sup>3</sup> )	20.5	20	18.5	20.5
Saturated water content (%)	29.6	36.8	40.1	29.6
Internal angle of friction (degree)	40	28	38	40
Cohesion (kPa)	-	15	-	-

### 3. Results and Discussion

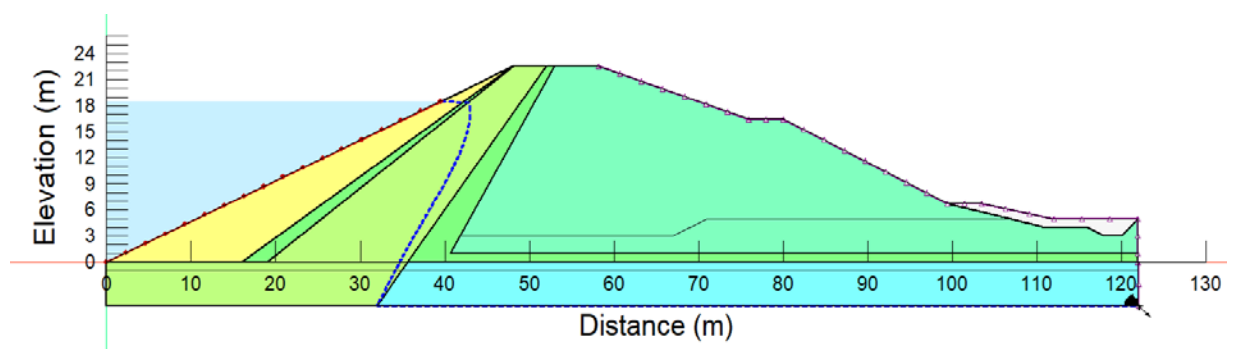
Both seepage and slope stability analyses were successfully executed. As previously mentioned, the investigation process is based on the different drawdown rates to investigate their influence on the stability of a heterogeneous embankment. Each investigated case started with seepage analysis followed by slope stability; whereby, the seepage model acted as a parent to the slope stability model. Also, both steady-state and transient flow conditions were taken into consideration.

#### 3.1. Seepage analysis

Generally, seepage flow within an embankment is the movement of water from the upstream side of the dam (where the reservoir is located) to the downstream side crossing the dam body preferably below the foundation. Due to the potential stability issues that can be associated, it is of significant importance to control seepage in earth-fill dams, especially during the design and construction phases of the dam.

From Fig. 4 it can be observed that, based on the material arrangements from the Aktobe dam, the modeling revealed that under long-term steady-state conditions the seepage within the embankment is safely carried without crossing the downstream face of the embankment. In the literature, it has been observed that seepage flow through earth-fill embankments is the principal cause that leads to failure due to some factors such as eroding, scouring, as well as piping [29].

Moreover, it is also important to investigate the long-term steady-state seepage because when the reservoir is filled, immediately water starts seeping through the body of the embankment. Whereby, after a certain time the seepages reach steady conditions, and a distinct phreatic line is generated; that means the embankment soil under the distinct phreatic line is relatively saturated and is under seepage pressure. Also, according to Perri et al., [30] an increase in embankment pore water pressures a phenomenon that is linked to the development of the long-term steady-state seepage condition can also result in an associated decrease in effective stress in the soil; whereby, the decrease in effective stresses leads to a reduction of the available effective strength of the soil.

**Figure 4. Steady-state seepage.**

From Fig. 5 it can be observed that the seepage line heights keep on decreasing with the decrease in water levels in the reservoir. It is also important to be noted that, the first seepage line indicates the initial water level in the reservoir. Then when the reservoir drawdown was simulated by instantaneously removing all the water, the water level was relatively sustained at the level of the toe of the slope making more of the seepage lines to be concentrated at the embankment toe [31].

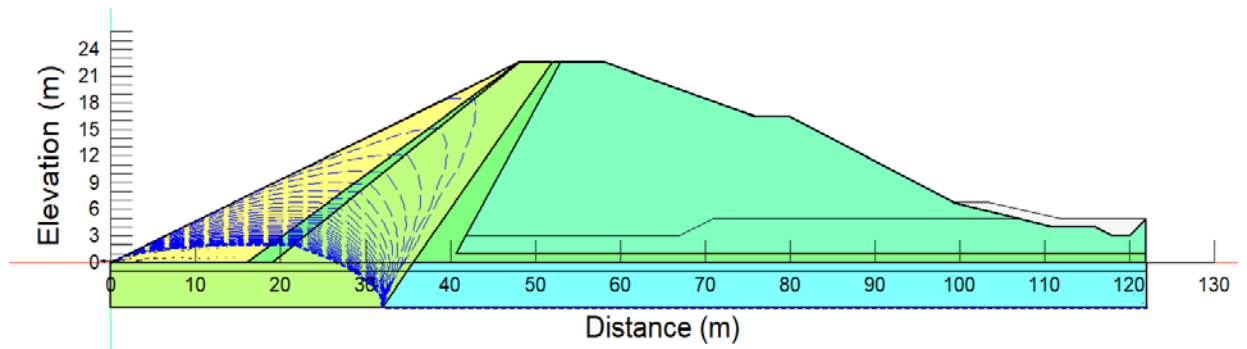


**Figure 5. Instantaneous seepage.**

### 3.2. Slope stability analysis

The evaluation of slope stability is mainly based on the factor of safety values. From Fig. 6 it can be seen that the long-term steady-state factor of safety value is 1.784 which is highly acceptable in terms of slope stability.

According to the Washington State Department of Transportation Geotechnical Design Manual [32], it is recommended that for slope stability analysis of permanent cuts, fills, and landslide repairs, 1.25 is adopted as the minimum safety factor value. Furthermore, it is recommended that larger safety factors must be adopted in a case when there is a potential uncertainty in the analysis input parameters. Also, according to Jiri H. et al., [33], some other authorities recommend a minimum factor of safety of 1.5 for slope stability analysis of embankments.

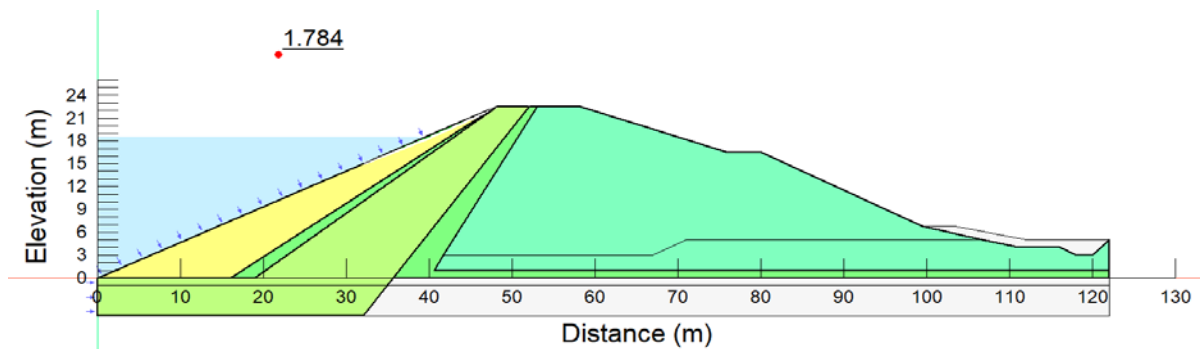
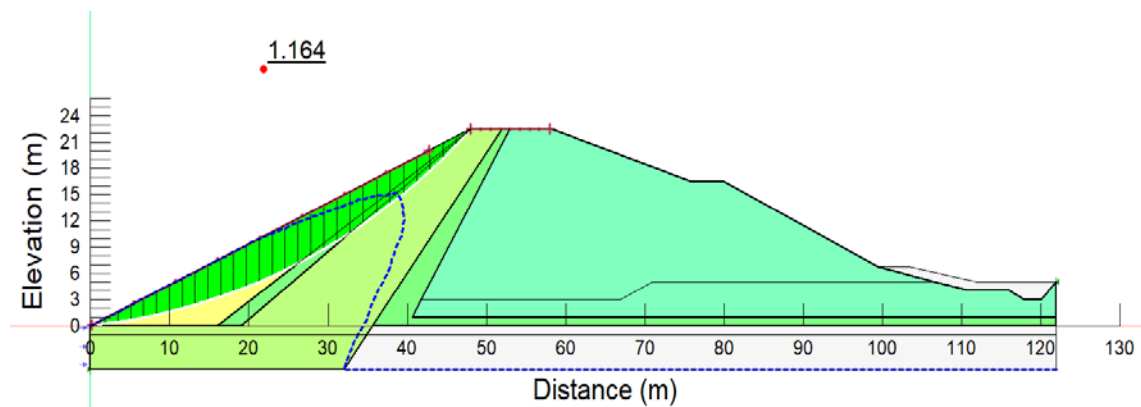
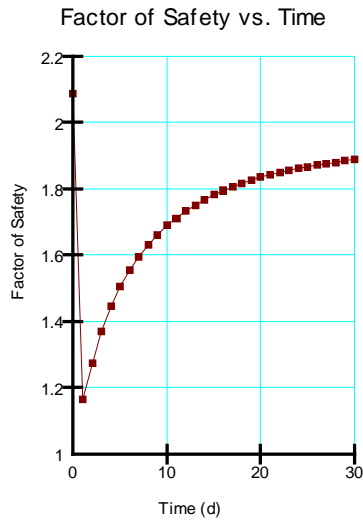


**Figure 6. Steady-state slope stability.**

When the embankment was subjected to the instantaneous a minimum factor of safety of 1.164 was retrieved; whereby, based on the recommendation of some authorities the obtained factor of safety is an indication of a potential failure. Also, from Fig. 7(b) it can be observed that the lowest factor of safety value was obtained within the first day of the instantaneous drawdown; that means, the potential failure is of immediate effect when the embankment is subjected to an instantaneous drawdown.



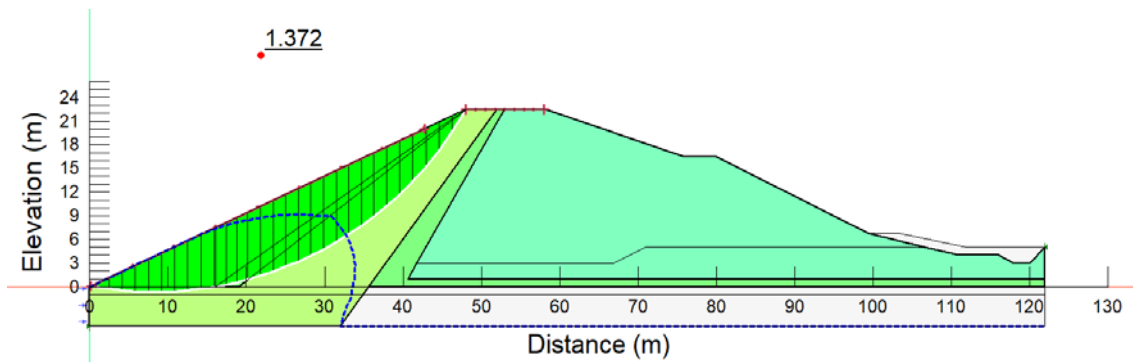
**(a)**



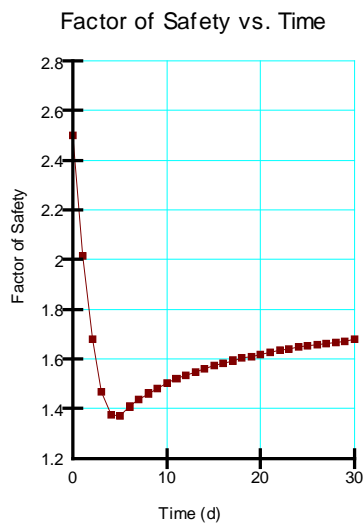
(b)

**Figure 7. Instantaneous slope stability.**

Also, when the embankment was subjected to 5 days drawdown rate a factor of safety of 1.372 was achieved which is a bit higher than the instantaneous drawdown (equivalent to a 17.9 % increase). However, with the fact that some other authorities recommend a minimum factor of safety of 1.5 to consider an embankment safe during loading, the 1.372 factor of safety value may also signify a potential failure. From Fig. 8 it can be observed that the minimum factor of safety value is obtained within the fourth and fifth day of the drawdown.



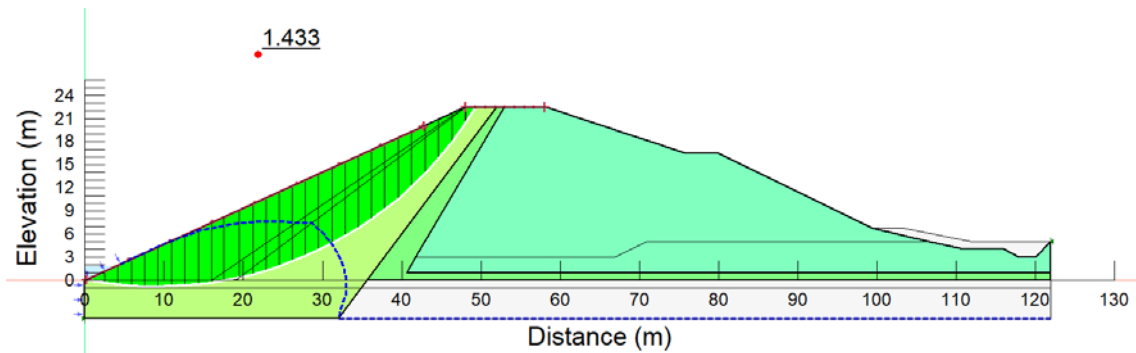
(a)



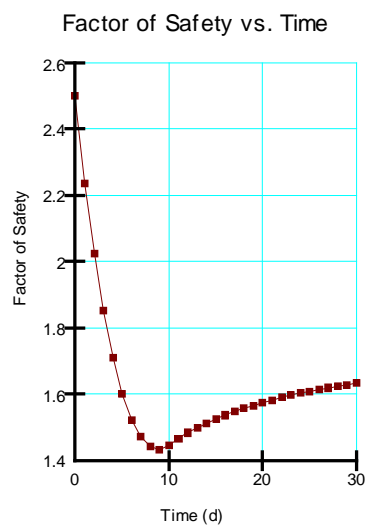
(b)

**Figure 8. Drawdown 5 days.**

Moreover, when the embankment body was subjected to 10 days drawdown rate, a minimum factor of safety of 1.433 was achieved; equivalent to a 4.4 % increase from the 5 days drawdown rate and 23.1 % from the instantaneous drawdown rate. From Fig. 9 it can be observed that the minimum factor of safety value is obtained within the 9<sup>th</sup> day of the reservoir draining.



(a)

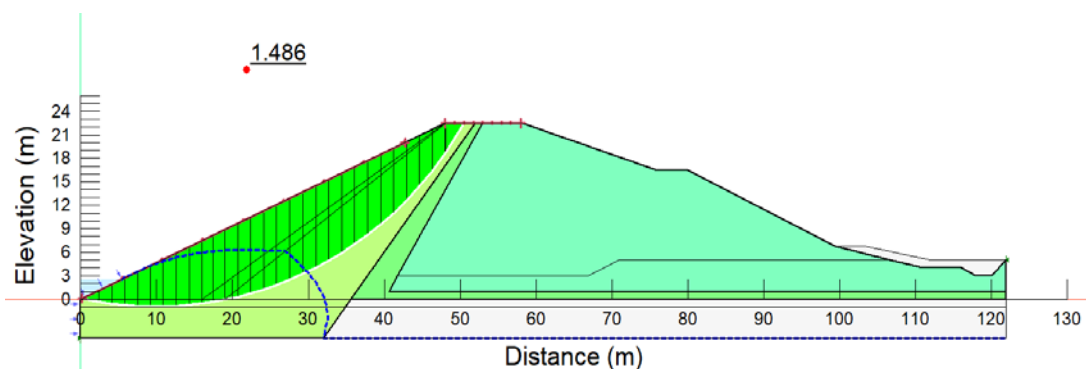


(b)

**Figure 9. Drawdown 10 days.**

Another case that was taken into account in this study is the 1 m per day drawdown rate (Fig. 10); whereby, when the embankment was subjected to the 1 m per day drawdown rate a minimum factor of safety value of 1.486 was retrieved from computations. The factor of safety value is equivalent to a 3.7 % increase from the 10 days drawdown rate and 8.3 % from the 5 days drawdown rate and 48.6 % from the instantaneous drawdown.

Furthermore, in the literature rapid reservoir draining has been noted to be among the critical factors in the stability of embankment slopes that were initially submerged from the upstream face. Therefore, the reduction process of water level leads to two main consequences; firstly, a decrease in terms of the external stabilizing hydrostatic pressure due to the unloading effect of removing water, and secondly, alteration of the internal pore water pressure [34].



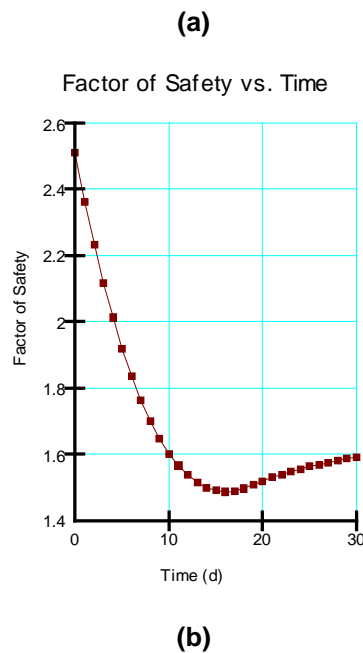


**Figure 10. Drawdown 1m per day.**

From Table 2 it can be observed that the minimum (min) factor of safety values were increasing with the decrease in drawdown rates. A similar phenomenon can be observed from the median, arithmetic mean (mean), and standard deviation. (STD). However, the maximum (max) factor of safety values remained constant as they are determined by the long-term steady state.

As previously mentioned, the minimum factor of safety when the embankment was subjected to the instantaneous drawdown case was 1.164, while the same embankment was subjected to the 1 m per day drawdown rate the minimum factor of safety was 1.49; which is equivalent to 48.6 % increase.

In most cases the minimum factor of safety is of interest because in geotechnical engineering, for instance, a factor of safety provides an overall picture of how much stronger a structure is than it needs to be for a specific type of loading; also expressed as the ratio of the capacity of the structure to the appropriate demand [35, 36]. Another key aspect to note is that these values are normally computed using detailed analysis due to the fact that comprehensive testing can be associated with feasibility issues on many engineering projects. However, the structure's ability to sustain potential loading conditions should be well checked in principle to resolute to a sensible accurateness. Moreover, well-designed with a sufficient value of factor of safety has the potential to increase the safety of people that in turn reducing the risk of failure of the particular structure [37–39].

**Table 2. Summary of the factor of safety values from the investigated drawdown rates.**

Drawdown type	Min	Max	median	Mean	STD
Instantaneous	1.164	2.512	1.556	1.552	0.201
Drawdown-5 days	1.372	2.512	1.562	1.583	0.202
Drawdown-10 days	1.433	2.512	1.567	1.624	0.231
Drawdown-1 m per day	1.486	2.512	1.569	1.692	0.271

On the other hand, Fig. 11 presents the summary of the factor of safety values distribution. It can be seen that, the data distribution from the instantaneous, 5 days, and 10 days drawdown rates is almost symmetrical; which means there was an equal data distribution with the list of factors of safety values. However, from the 11 m per day drawdown rate, the median is observed to be closer to the lower quartile of the boxplot meaning that the data distribution was positively skewed with higher values than the lower values.

In summary, the observed effects of the rapid drawdown loading conditions can be again linked to the fact that when the water in the reservoir is removed relatively fast the supporting water load from the upstream face of the embankment in combination with the changes in pore water pressure results in an undrained unloading condition in which total stresses decrease that in turn increases shear stresses within the embankment [40].

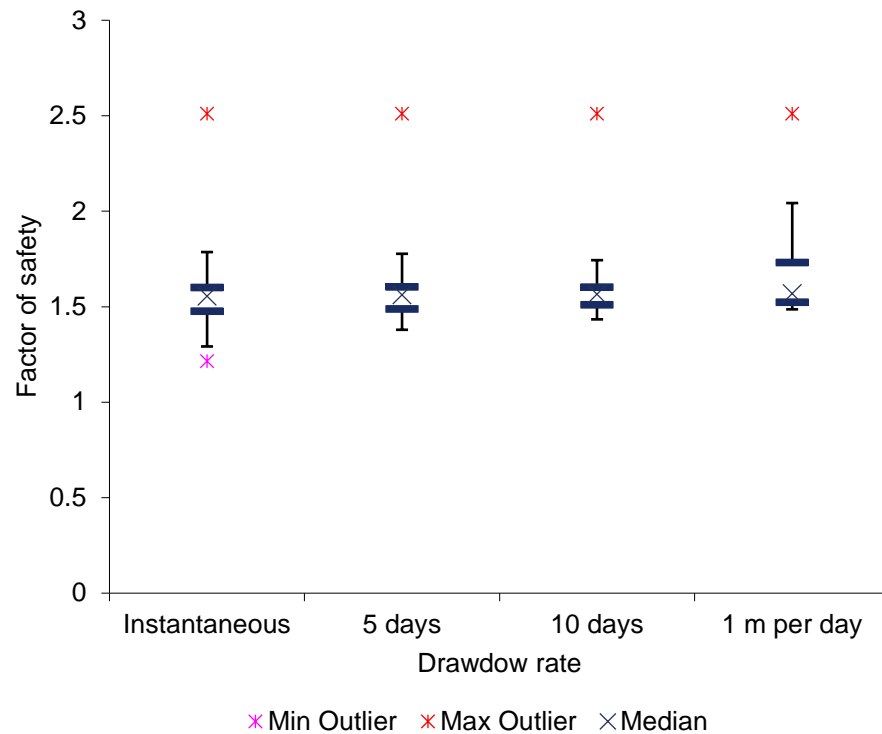


**Figure 11. Distribution of factor of safety values for the investigated drawdown rates.**

#### 4. Conclusions

1. The influence of rapid drawdown loading conditions on the stability of the embankment dam was investigated with the help of numerical modeling for the case of the Aktobe dam in Kazakhstan.
2. From the investigation results, it was observed that when the embankment was subjected to the 1 m per day drawdown rate, a minimum factor of safety value of 1.486 was retrieved from computations.
3. The factor of safety value is equivalent to a 3.7 % increase from the 10-days drawdown rate, 8.3 % from the 5-days drawdown rate, and 48.6 % from the instantaneous drawdown.
4. However, some authorities recommend a minimum factor of safety of 1.5 for an embankment to be regarded as safe enough in terms of slope stability.
5. Moreover, the results in this study further revealed that even a heterogeneous dam supplied with a core in the embankment can be highly susceptible to failure when subjected to rapid drawdown loading conditions.
6. Therefore, it is of significant importance to investigate the response of an embankment dam subjected to a rapid drawdown condition during the design phase of the embankment to avoid potential failure when the dam is already in operation.
7. The process ensures the stability of the structure as well as provides protection against health impacts and property damage.

#### 5. Conflict of Interests

The authors declare that there is no conflict of interest regarding the publication of this paper.

#### References

1. Yang, H., Haynes, M., Winzenread, S., Okada, K. The History of Dams. UC Davis. 1999.
2. de Rubertis, K. Embankment Dams. Monitoring Dam Performance. Reston, VA, American Society of Civil Engineers, 2018. Pp. 295–322.
3. Mkilima, T. Toe drain size and slope stability of homogeneous embankment dam under rapid drawdown. Technobius. 2021. 1(3). Pp. 0001. DOI: 10.54355/tbus/1.3.2021.0001
4. Yener Ozkan, M. A review of considerations on seismic safety of embankments and earth and rock-fill dams. Soil Dynamics and Earthquake Engineering. 1998. DOI: 10.1016/S0267-7261(98)00035-9
5. Slichter, F.B. Influences on Selection of the Type of Dam. Journal of the Soil Mechanics and Foundations Division. 1967. 93(3). Pp. 1–8. DOI: 10.1061/JSFEAQ.0000976

6. Wang, J.-P., François, B., Lambert, P. Equations for hydraulic conductivity estimation from particle size distribution: A dimensional analysis. *Water Resources Research*. 2017. 53(9). Pp. 8127–8134. DOI: 10.1002/2017WR020888
7. Fang, H.-Y., Daniels, J.L. Introduction to geotechnical engineering. *Introductory Geotechnical Engineering*. CRC Press, 2017. Pp. 1–26.
8. Fell, R., MacGregor, P., Stapledon, D., Bell, G. *Geotechnical Engineering of Dams*. CRC Press, 2005. ISBN: 9781000006681.
9. United States interior department of the interior; reclamation bureau. *Design of small dams*. California, United States bureau of reclamation, 1999. 904 p. ISBN: 0780352939.
10. Zhou, J., Li, E., Yang, S., Wang, M., Shi, X., Yao, S., Mitri, H.S. Slope stability prediction for circular mode failure using gradient boosting machine approach based on an updated database of case histories. *Safety Science*. 2019. 118. Pp. 505–518. DOI: 10.1016/j.ssci.2019.05.046
11. Jiang, X., Zhanyuan, Z., Chen, H., Deng, M., Niu, Z., Deng, H., Zuyin, Z. Natural dam failure in slope failure mode triggered by seepage. *Geomatics, Natural Hazards and Risk*. 2020. 11(1). Pp. 698–723. DOI: 10.1080/19475705.2020.1746697
12. Vandenberghe, D.R. Total stress rapid drawdown analysis of the Pilarcitos Dam failure using the finite element method. *Frontiers of Structural and Civil Engineering*. 2014. 8(2). Pp. 115–123. DOI: 10.1007/s11709-014-0249-7
13. Utepov, Y., Aniskin, A., Mkilima, T., Shakhmrov, Z., Kozina, G. Potential Impact of Land-Use Changes on River Basin Hydraulic Parameters Subjected to Rapid Urbanization. *Tehnicki vjesnik – Technical Gazette*. 2021. 28(5). Pp. 1519–1525. DOI: 10.17559/TV-20200808134641
14. Llanque Ayala, G.R., Chagas da Silva Filho, F., Ferreira Leme, R., Do Carmo Reis Cavalcanti, M., Fernando Mahler, C. Rapid drawdown in homogeneous earth dam considering transient flow and suction. *ingeniería e investigación*. 2020. 40(1). Pp. 17–26. DOI: 10.15446/ing.investig.v40n1.80002.
15. GEO-SLOPE International Ltd. *Rapid Drawdown with Multi-Stage*. (Fig. 1). 1200, 700 – 6<sup>th</sup> Ave SW, Calgary, AB, Canada, 2003.
16. Diacon, A., Sternatiu, D., Mircea, N. Analysis of the Belci dam failure. *International Water Power and Dam Construction*. 1992.
17. Alcrudo, F., Mulet, J. Description of the Tous Dam break case study (Spain). *Journal of Hydraulic Research*. 2007. 45(sup1). Pp. 45–57. DOI: 10.1080/00221686.2007.9521832
18. Rogers, J.D., Watkins, C.M., Chung, J.-W. The 2005 Upper Taum Sauk Dam Failure: A Case History. *Environmental and Engineering Geoscience*. 2010. 16(3). Pp. 257–289. DOI: 10.2113/gseegeosci.16.3.257
19. Bolton Seed, H., Duncan, J.M. The failure of Teton Dam. *Engineering Geology*. 1987. DOI: 10.1016/0013-7952(87)90060-3
20. Sherard, J.L. Teton Dam failure. *Engineering Geology*. 1987. 24(1–4). Pp. 283–293. DOI: 10.1016/0013-7952(87)90068-8
21. Penman, A.D.M. The Teton Dam failure. *Engineering Geology*. 1987. 24(1–4). Pp. 257–259. DOI: 10.1016/0013-7952(87)90065-2
22. Eikenberry, W.F., Arthur, H.G., Bogner, N.F., Lacy, F.P., Schuster, R.L., Willis, H.B. *Failure of Teton Dam: A Report of Findings*. US Department of the Interior Teton Dam Failure Review Group. 1977.
23. Sharma, R.P., Kumar, A. Case Histories of Earthen Dam Failures. *Seventh International Conference on Case Histories in Geotechnical Engineering*. 2013.
24. Idrissova, G.Z., Akhmedenov, K.M., Sergeeva, I.V., Ponomareva, A.L., Sergeeva, E.S. Monitoring studies of the ecological state of springs in the aktobe region in Western Kazakhstan. *Journal of Pharmaceutical Sciences and Research*. 2017. 9(7). Pp. 1122–1127.
25. Sarma, S.K. Stability analysis of embankments and slopes. *Géotechnique*. 1973. 23(3). Pp. 423–433. DOI: 10.1680/geot.1973.23.3.423
26. Atashband, S. Evaluate Reliability of Morgenstern–Price Method in Vertical Excavations. *Numerical Methods for Reliability and Safety Assessment 2015*.
27. Zhu, D.Y., Lee, C.F., Qian, Q.H., Chen, G.R. A concise algorithm for computing the factor of safety using the Morgenstern–Price method. *Canadian Geotechnical Journal*. 2005. 42(1). Pp. 272–278. DOI: 10.1139/t04-072
28. Price, V.E., Morgenstern, N.R. The Analysis of The Stability of General Slip Surfaces. *Géotechnique*. 1968. 18(3). Pp. 393–394. DOI: 10.1680/geot.1968.18.3.393
29. Salem, M.N., Eldeeb, H.M., Nofal, S.A. Analysis of seepage through earth dams with internal core. *International Journal of Engineering Research and Technology*. 2019. 8(08). DOI: 10.17577/IJERTV8IS080168
30. Perri, J.F., Shewbridge, S.E., Cobos-Roa, D.A., Green, R.K. Steady state seepage pore water pressures' influence in the slope stability analysis of Levees. *GeoCongress*. 2012. Pp. 604–613. DOI: 10.1061/9780784412121.063
31. Pinyol, N.M., Alonso, E.E., Olivella, S. Rapid drawdown in slopes and embankments. *Water Resources Research*. 2008. 44(5). DOI: 10.1029/2007WR006525.
32. Washington State Department of Transportation. *Geotechnical Design Manual M46-03.08*. 1996. (October). Pp. 103–110.
33. Herza, J., Ashley, M., Thorp, J. Factor of Safety? Do we use it correctly? *Proceedings Australian National Congress on Large Dams*, Hobart. 2018.
34. Alonso, E.E., Pinyol, N.M. Numerical analysis of rapid drawdown: Applications in real cases. *Water Science and Engineering*. 2016. 9(3). Pp. 175–182. DOI: 10.1016/j.wse.2016.11.003.
35. Sofianos, A.I., Nomikos, P.P., Papantonopoulos, G. Distribution of the factor of safety, in geotechnical engineering, for independent piecewise linear capacity and demand density functions. *Computers and Geotechnics*. 2014. 55. Pp. 440–447. DOI: 10.1016/j.compgeo.2013.09.024
36. Cherubini, C., Christian, J.T., Baecher, G.B., Failmezger, R.A., Focht, J.A., Focht, J.A., Koutsoftas, D.C., Ladd, C.C., Re, G. Da, Li, K.S., Lam, J., Moriwaki, Y., Barneich, J.A., Schmertmann, J.H., Duncan, J.M. Factor of safety and reliability in geotechnical engineering. *Journal of Geotechnical and Geoenvironmental Engineering*. 2001. 127(8). Pp. 700–721. DOI: 10.1061/(ASCE)1090-0241(2001)127:8(700)
37. Lu, R., Wei, W., Shang, K., Jing, X. Stability Analysis of Jointed Rock Slope by Strength Reduction Technique considering Ubiquitous Joint Model. *Advances in Civil Engineering*. 2020. Vol. 2020. Pp. 1–13. DOI: 10.1155/2020/8862243
38. Kassou, F., Ben Bouziyane, J., Ghafiri, A., Sabihi, A. Slope stability of embankments on soft soil improved with vertical drains. *Civil Engineering Journal*. 2020. 6(1). Pp. 164–173. DOI: 10.28991/cej-2020-03091461

39. Li, Y., Fan, W., Chen, X., Liu, Y., Chen, B. Safety criteria and standards for bearing capacity of foundation. *Mathematical Problems in Engineering*. 2017. Vol. 2017. Pp. 1–8. DOI: 10.1155/2017/3043571
40. Van Den Berge, D.R., Duncan, J.M., Brandon, T.L. Rapid drawdown analysis using strength reduction. 18<sup>th</sup> International Conference on Soil Mechanics and Geotechnical Engineering: Challenges and Innovations in Geotechnics, ICSMGE 2013. 2013.

**Information about authors:**

**Aliya Aldungarova, PhD**

ORCID: <https://orcid.org/0000-0002-9248-7180>

E-mail: [Liya\\_1479@mail.ru](mailto:Liya_1479@mail.ru)

**Timoth Mkilima,**

ORCID: <https://orcid.org/0000-0003-1170-0494>

E-mail: [tmkilima@gmail.com](mailto:tmkilima@gmail.com)

**Yelbek Utepov, PhD**

ORCID: <https://orcid.org/0000-0001-6723-175X>

E-mail: [utepov-elbek@mail.ru](mailto:utepov-elbek@mail.ru)

**Assel Tulebekova, PhD**

ORCID: <https://orcid.org/0000-0001-8553-3081>

E-mail: [krasavka5@mail.ru](mailto:krasavka5@mail.ru)

**Shyngys Zharassov,**

ORCID: <https://orcid.org/0000-0002-0002-8362>

E-mail: [zhshzh95@gmail.com](mailto:zhshzh95@gmail.com)

*Received 17.12.2021. Approved after reviewing 21.07.2022. Accepted 08.08.2022.*



Research article

UDC 691.3

DOI: 10.34910/MCE.117.9



## Charcoal-containing building materials for electromagnetic radiation shielding

O.V. Boprav , E.S. Belousova , E.S. Ahmetdinova , N.V. Bogush 

*Belarusian State University of Informatics and Radioelectronics, Minsk, Republic of Belarus*

✉ [smu@bsuir.by](mailto:smu@bsuir.by)

**Keywords:** activated charcoal, cost effective, EMI shielding, building gypsum

**Abstract.** The aim of the study presented in the current article was to experimentally substantiate the possibility of obtaining the cost effective building materials for electromagnetic radiation shielding by using powdered charcoal as a filler. Such charcoal properties as low cost and high carbon content (up to 90.0 wt.%) were the prerequisites for the study. To achieve the goal, a method for obtaining composite materials based on powdered charcoal and building gypsum was developed and experimentally substantiated by the authors. Further, the samples of charcoal-containing building materials were made according to the developed method and the electromagnetic radiation reflection and transmission coefficients values of the samples were measured in the frequency range of 0.7–17.0 GHz using scalar network analyzer. According to the measurements results, it was found that the average value of the electromagnetic radiation reflection coefficient in the specified frequency range of the materials produced in accordance with the presented method (when these materials thickness was equal to 1.0 cm) was –3.0 dB, and the average value of the electromagnetic radiation transmission coefficient was –25.0 dB. The studied materials are recommended for use in electromagnetic shielding of the rooms housing the electronic devices.

**Citation:** Boprav, O.V., Belousova, E.S., Ahmetdinova, E.S., Bogush, N.V. Charcoal-containing building materials for electromagnetic radiation shielding. *Magazine of Civil Engineering*. 2023. 117(1). Article no. 11709. DOI: 10.34910/MCE.117.9

### 1. Introduction

Nowadays the building materials for electromagnetic radiation shielding are one of the objects of scientific area dealing with the functional materials development and research. This is due to the combination of the following reasons:

1) expansion of the number of electronic devices used to solve industrial and household problems, and the increase in the level of the electromagnetic background associated with it (since in the course of their operation each of these devices forms and emits electromagnetic waves [1, 2] due to them containing antenna analogs);

2) the need for electromagnetic shielding of the rooms housing the electronic devices that are sensitive to interference (servers, medical equipment, measuring equipment, etc.) [2, 3].

Currently developed building materials suitable for electromagnetic radiation shielding are composites with the following combinations of components:

- 1) matrix and filler;
- 2) binder agent and filler.

The materials associated with the first combination, as a rule, are used as finishing panels for the walls of the rooms housing the electronic devices sensitive to interference. In such materials, porous substrates are their matrices, while iron, nickel, copper or carbon particles serve as their fillers. The technology obtaining such materials is based on deposition of these particles in the pores [4] or on the surface [5] of the matrices. Their main advantage is the possibility to produce finishing panels of complex shape on their basis (not flat and not associated with the regular geometric figures). For example, it's possible to obtain finishing panels, the surface of which contains a set of inhomogeneities interacting with and scattering the electromagnetic radiation. This is a very important property, especially when the shielded room should resemble an anechoic chamber. Moreover, such materials allow designing finishing panels of non-straight boundaries. This shape comes useful, when the room in need of shielding has uneven corners. In general, the shape of the panels, formed on the basis of the discussed materials, is defined by their matrices shape. However, the main disadvantage of such materials is technological complexity and high time consumption of their production. This disadvantage is critical, because the total square of the room might be comparable with the total square of the room walls, which should be covered by these panels, making it a challenge to cover everything.

The building materials suitable for electromagnetic radiation shielding and associated with the second of the presented combinations, are characterized by lower technological complexity compared with the materials of the first combination. This is due to the fact, that their production technology is based on the distribution of the particles or fibers, containing iron, nickel, copper or carbon, in the volume of binder agent, which is, as a rule, cement, building gypsum or polymer [6–11]. Such materials are used as building mixtures for covering the walls of the rooms housing interference-sensitive electronic devices with panels. These panels, compared with the matrix-and-filler panels, are characterized by regular (as a rule, rectangle or square) and flat shape.

It's necessary to stress, that carbon particles or fibers are a more promising source for the fillers in the composite panels. This is because metal powders (iron, nickel, copper etc.) give the composites high density and low mechanical strength [9]. This means, that such materials, when applied in the rooms housing interference-sensitive electronic devices, create a high load on the walls. In addition, such materials could be characterized by low adhesion to the walls.

Carbon particles and fibers, used as the fillers of the building materials, suitable for electromagnetic radiation shielding, are characterized by high cost, because the production of such fillers is based on the use of expensive components or equipment. This poses the scientific problem of searching or synthesis of low-cost carbon-containing fillers for obtaining cost effective building materials, suitable for electromagnetic radiation shielding. One of the variants of such fillers is presented in paper [12]. It is a mixture of tire waste and slag samples. To extend the results, achieved in the way of the indicated problem solving, the authors of the current paper set the following goal: experimentally substantiate the possibility of obtaining cost-effective building materials for electromagnetic radiation shielding by use powdered charcoal as a filler for such materials. To achieve the goal, the following tasks were solved:

1) the method for obtaining the materials based on powdered charcoal and building gypsum was developed and experimentally substantiated by the authors (the optimal volumetric ratio to mix powdered charcoal and building gypsum powder was established, and the equipment and accessories needed for the production were defined);

2) the samples of charcoal-containing building materials were made according to the developed method;

3) the electromagnetic radiation reflection ( $S_{11}$ ) and transmission coefficients ( $S_{21}$ ) values of the produced samples were measured and analyzed.

The prerequisites for the goal and tasks setting were the following charcoal properties:

- low cost, as charcoal is currently produced from wood-processing waste [13, 14];
- high carbon content (up to 90.0 wt.%), which determines its electrical conductivity property [15, pp. 259–267].

## 2. Methods

In the way of the development the method for obtaining of charcoal-containing building materials the authors defined the optimal volumetric ratio in which it is necessary to mix powdered charcoal and building gypsum powder. The following steps were made to solve the indicated task.

Step 1. Preparing nine mixtures of the powdered charcoal and building gypsum powder with use of the laboratory powder mixer. Each of the prepared mixtures differed in the volumetric ratio of its constituent

powdered charcoal and dry building gypsum powder. The volumetric ratios of the indicated components were the following: 1:9, 1:4, 3:7, 2:3, 1:1, 3:2, 7:3, 4:1, 9:1.

Step 2. Adding water to every prepared mixture and mixing the first one with the second ones with use of laboratory liquid mixer. According to the research results, presented in the papers [16, 17], it was established, that the volume of the water added to the mixture must exceed 2 times the volume of the latter.

Step 3. Application of the mixtures, obtained on the step 2, on the cellulose substrates with use of spatula.

Step 4. Drying the mixtures, applied on the cellulose substrates, under the standard conditions [18].

Step 5. Visual control of the quality of the surfaces of the materials, obtained as a result of the steps 1–4 implementation. The used quality criterion – absence of cracks on the materials surfaces.

Step 6. Choosing the material, obtained as a result of the steps 1–4 implementation on the basis of the mixture, characterized by the optimal volumetric ratio of the powdered charcoal and building gypsum powder. The following criteria were used for choosing:

- there are no cracks on the material surface;
- the material is characterized by the biggest volumetric content of the powdered charcoal (the criterion was established due to the following two reasons: 1) there are no cracks on the several materials surfaces; 2) if the volumetric content of the powdered charcoal in the material is greater  $S_{21}$  value of the latter is less, due to the fact, that powdered charcoal is characterized by the electroconductivity property).

As a result of the described steps, it was established that the optimal volumetric ratio in which it is necessary to mix powdered charcoal and building gypsum powder when obtaining charcoal-containing building material is 2:3.

The authors determined that the following equipment and accessories needed to obtain of charcoal-containing building materials for electromagnetic radiation shielding: powder mixer, gypsum mixer, spatula, molds.

The developed by the authors method for obtaining of charcoal-containing building materials for electromagnetic radiation shielding includes the following steps.

Step 1. Mixing powdered charcoal and building gypsum powder in the established volumetric ratio (i. e. 2:3) with use of powder mixer.

Step 2. Adding 2 volume parts of the water in the mixture of powdered charcoal and building gypsum powder.

Step 3. Mechanical mixing of the water and the mixture of powdered charcoal and building gypsum powder with use of gypsum mixer.

Step 4. Application of the obtained material to the walls of the shielded room with use of spatula or filling the molds with the obtained material (in case, on the basis of this material, it is necessary to obtain plates for finishing of the shielded rooms walls).

The samples of charcoal-containing building materials were made according to the developed by the authors method. Table 1 presents the properties of these samples.

**Table 1. The properties of the samples.**

The sample name	Type of charcoal used for the sample making	The sample thickness, cm
1.1		0.3
1.2	Non-activated birch charcoal	0.5
1.3		1.0
2.1		0.3
2.2	Activated birch charcoal	0.5
2.3		1.0

The samples 1.1 and 2.1 were made by applying the mixture of the powdered charcoal, building gypsum powder and water (when the mixture was in the liquid phase) to cellulose substrates, the thickness of which was 3 mm. The indicated substrates are radiotransparency ones and due to this fact they do not impact on  $S_{11}$  and  $S_{21}$  values of the materials applied on them.

The samples 1.2, 1.3, 2.2 and 2.3 were manufactured by the following way:

1) filling full volume of the molds with the mixture of powdered charcoal, building gypsum powder and water (when the mixture was in the liquid phase); the molds length, width and thickness depend on the requirements to the corresponding parameters of the formed material; the used molds were made on the basis of flexible polymer radio-transparence material;

2) exsiccation of the mixture of powdered charcoal, building gypsum powder and water in the molds under the standard conditions [18];

3) extraction from the molds the obtained material.

$S_{11}$  and  $S_{21}$  values of the made samples were measured in the near zone in the frequency range 0.7–17.0 GHz with use of scalar network analyzer. The indicated frequency range was chosen for the measurements performing due to the fact that the spectrum density of the electromagnetic radiation, emitted by the modern electronic equipment, is characterized by the maximum values in this range or such equipment operates on the frequencies from this range (for example, radars or equipment, used for information transmission and receiving via the wireless channels) [6].

Fig. 1, 2 shows the measurement schemes of  $S_{11}$  and  $S_{21}$  values of the made samples.

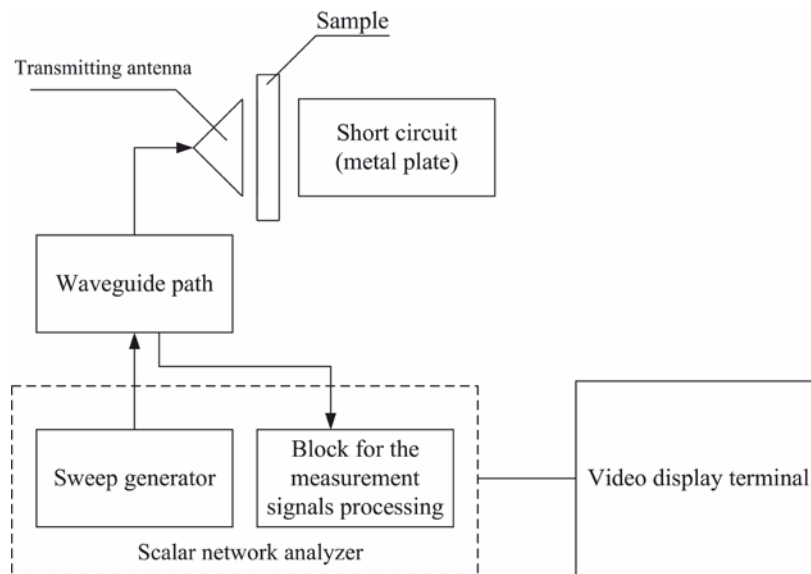


**Figure 1. The measurement schemes of  $S_{11}$  values of the made samples.**

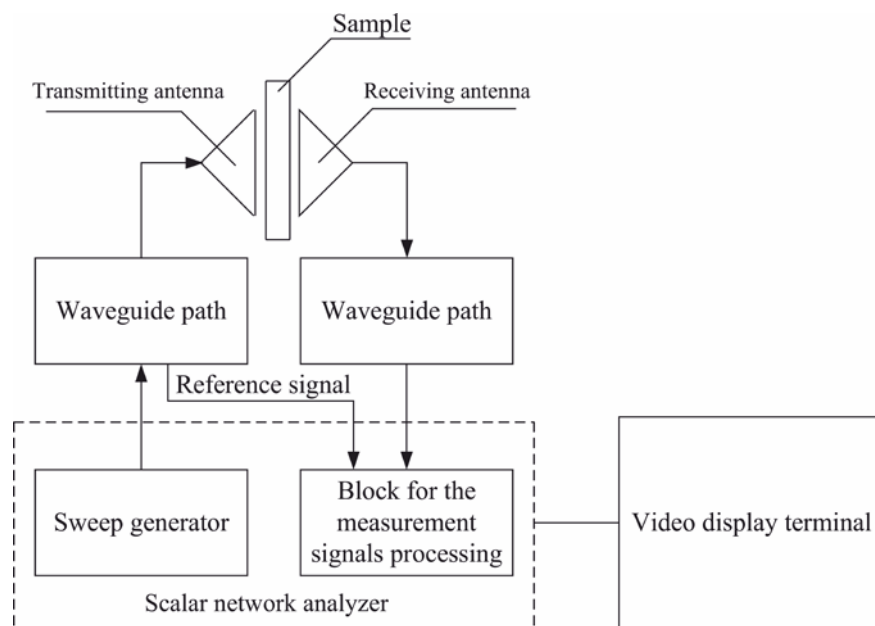


**Figure 2. The measurement schemes of  $S_{21}$  values of the made samples.**

### 3. Results and Discussion

Fig. 3–6 present  $S_{11}$  and  $S_{21}$  frequency dependences in the range 0.7...17.0 GHz of the made samples.

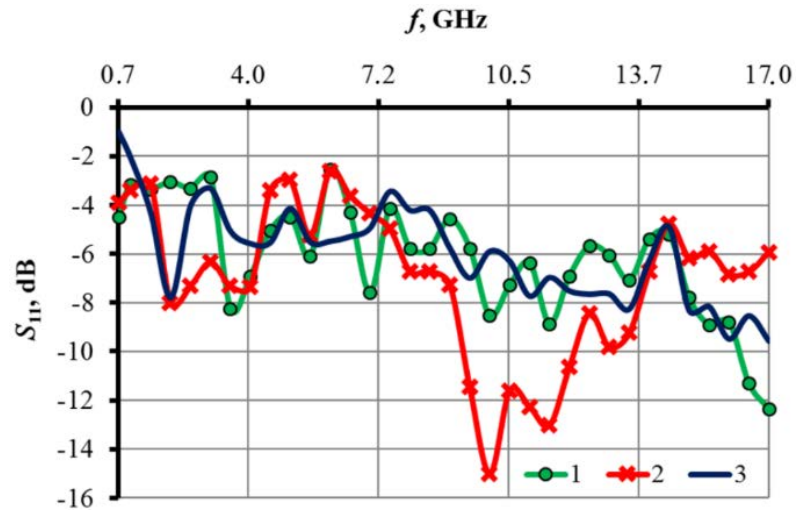


Figure 3.  $S_{11}$  frequency dependences in the range 0.7...17.0 GHz of the samples 1.1, 1.2 and 1.3 (curve 1, 2 and 3 respectively).

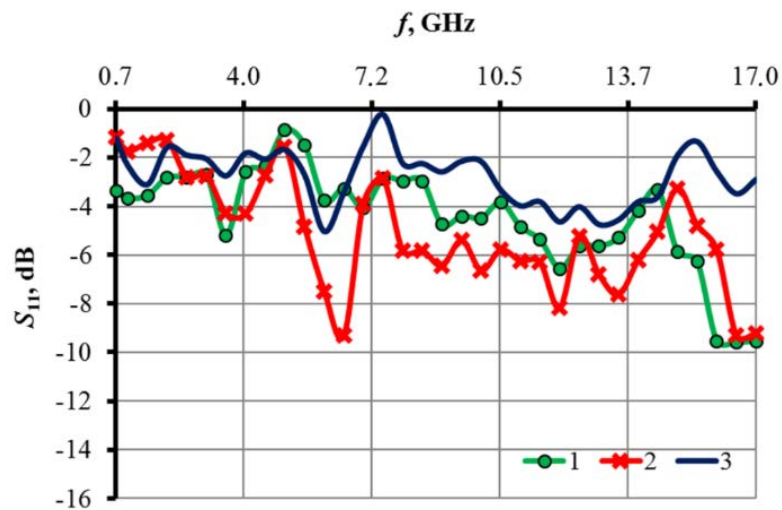


Figure 4.  $S_{11}$  frequency dependences in the range 0.7...17.0 GHz of the samples 2.1, 2.2 and 2.3 (curve 1, 2 and 3 respectively).

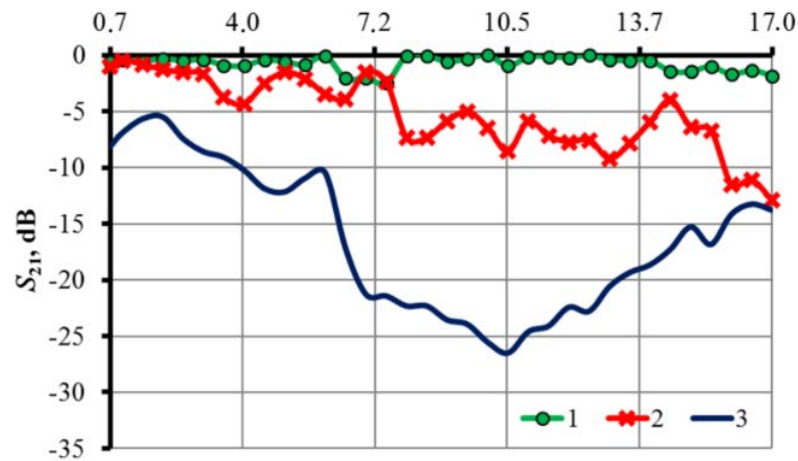
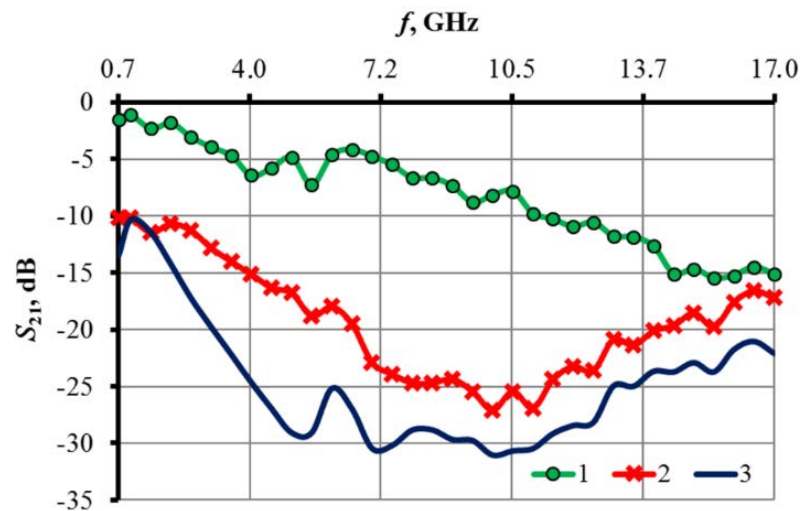


Figure 5.  $S_{21}$  frequency dependences in the range 0.7...17.0 GHz of the samples 1.1, 1.2 and 1.3 (curve 1, 2 and 3 respectively).



**Figure 6.  $S_{21}$  frequency dependences in the range 0.7...17.0 GHz of the samples 2.1, 2.2 and 2.3 (curve 1, 2 and 3 respectively).**

According to the results of comparative analysis of the frequency dependences presented in the Fig. 3 and 4 the following outcomes were obtained.

1. 0.3 material obtained according to the proposed method on the basis of non-activated birch charcoal is characterized by  $S_{11}$  values, changing from  $-3.0$  to  $-12.0$  dB. When such material thickness increases on 0.3 cm its  $S_{11}$  values increase on 1.0–7.0 dB. It's due to the fact that the phase difference of the electromagnetic waves reflected from the surfaces of 0.5 cm material and the short circuit (metal plate) is greater than the phase difference of the electromagnetic waves reflected from the surfaces of 0.3 cm material and short circuit (metal plate). When the considered material thickness increases to 1.0 cm its  $S_{11}$  values change no more than on 2.0 dB. It's due to the similarity of the phase difference of the electromagnetic waves reflected from the surfaces of 1.0 cm material and the short circuit (metal plate) and the phase difference of the electromagnetic waves reflected from the surfaces of 0.3 cm material and the short circuit (metal plate).

2.  $S_{11}$  values of the materials obtained according to the proposed method on the basis of activated birch charcoal is less by 2.0–5.0 dB compared to the materials obtained according to the proposed method on the basis of non-activated birch charcoal. It's due to the set of the following reasons:

- the materials obtained according to the proposed method on the basis of activated birch charcoal are characterized by the greater moisture content, compared to the materials obtained according to the proposed method on the basis of non-activated birch charcoal due to the fact that pore surface area of the activated charcoal is greater that pore surface area of the non-activated charcoal [19];
- material moisture containing increasing is the reason of its electrical conductivity increasing [20–22] and as a result the reason of increasing electromagnetic radiation reflection coefficient of this material [23–25].

According to the results of comparative analysis of the frequency dependences presented in Fig. 5 and 6 the following outcomes were obtained.

1. 0.3 cm material obtained according to the method of non-activated birch charcoal developed by the authors is characterized by  $S_{21}$  values, changing from  $-0.2$  to  $-3.0$  dB.  $S_{21}$  values of 0.5 cm and 1.0 cm materials obtained according to the developed method change correspondently from  $-1.0$  to  $-8.0$  dB and from  $-5.0$  to  $-27.0$  dB.

2.  $S_{21}$  values of the materials obtained according to the method of activated birch charcoal developed by the authors are greater on 2.0–15.0 dB compared to the materials obtained on the basis of non-activated birch charcoal. It's due to the set of the following reasons:

- the materials obtained according to the method of activated birch charcoal developed by the authors are characterized by the greater moisture content, compared to the materials obtained according to the proposed method of non-activated birch charcoal due to the fact that pore

surface area of the activated charcoal is greater than pore surface area of the non-activated charcoal [19];

- an increase in material moisture content is the reason of its electrical conductivity increasing [21] and a result of increasing electromagnetic radiation losses provided by this material [26, 27].

#### 4. Conclusion

The building materials obtained according to the method developed by the authors on the basis of non-activated birch charcoal are recommended for use in order to reduce the level of passive electromagnetic interference in rooms shielded with metals. At the same time, they should be applied in a layer 0.5 cm thick on the surface of metal sheets used for electromagnetic shielding of the rooms. This recommendation is due to the fact that  $S_{11}$  values of the developed materials, measured in short circuit mode, vary in the range from  $-3.0$  to  $-15.0$  dB (when these materials thickness equal to 0.5 cm), i.e., these materials at the specified thickness weaken the power of electromagnetic radiation reflected from by 2.0–32.0 times

The building materials obtained according the method developed by the authors on the basis of activated birch charcoal are recommended for use in electromagnetic shielding of the rooms housing interference sensitive electronic devices.

For this purpose, the developed materials should be used in one of the following forms:

- 1) in the form of plaster applied to the walls of the specified rooms (the optimal layer thickness of such plaster should be 1.0 cm);
- 2) in the form of plates with a thickness of 1.0 cm, intended for cladding of the walls of the specified rooms.

This recommendation is due to the fact that  $S_{21}$  values of the developed materials at their thickness of 1.0 cm vary from  $-10.0$  to  $-30.0$  dB, i.e., these materials provide an attenuation 10.0–1000.0 times the power of electromagnetic radiation interacting with them.

In general, on the basis of the achieved experimental results, it is possible to conclude, that the building materials obtained according to the method developed by the authors and their analogs presented in papers [7–11] are characterized by similar  $S_{21}$  values, due to the electrical conductivity property of powdered charcoal.  $S_{11}$  values of the building materials obtained according to the method developed by the authors are lower compared to the analogs. It's due to the following facts:

- the fractions size of the powdered charcoal is bigger compared to that of the powders, used for the analogs [7–11];
- if the powder fractions size is greater, the electromagnetic radiation energy dissipated by them is greater too [1].

Moreover, the building materials obtained according to the method developed by the authors are more cost-effective than their analogs, because they are produced from wood-processing waste, as it was indicated in the Introduction chapter of the paper.

Thus, the authors achieved the goal of the study.

#### References

1. Geetha, S., Satheesh Kumar, K.K., Rao, Chepuri R.K., Vijayan, M., Trivedi, D.C. EMI shielding: methods and materials – a review. *Journal of Applied Polymer Science*. 2009. 112(4). Pp. 2073–2086. DOI: 10.1002/app.29812
2. Batool, S., Bibi, A., Frezza, F., Mangini, F. Benefits and hazards of electromagnetic waves, telecommunication, physical and biomedical: a review. *European Review for Medical and Pharmacological Sciences*. 2019. 23. Pp. 3121–3128.
3. Kwon, J.H., Hyoung, C.H., Hwang, J.-H., Park, H.H. Impact of absorbers on the shielding effectiveness of metallic rooms with apertures. *Electronics*. 2021. 10(3). 237. DOI: 10.3390/electronics10030237
4. Sung, W., Kao, J., Chen, R. Medical building materials of structural properties and electromagnetic interference shielding in the quartz crystal plane coated Ni based thin film. *Applied Mechanics and Materials*. 2014. 599–601. Pp. 67–76. DOI: 10.4028/www.scientific.net/AMM.599-601.67
5. Singh, A.K., Shishkin, A., Koppel, T., Gupta, N. A review of porous lightweight composite materials for electromagnetic interference shielding. *Composites Part B: Engineering*. 2018. 149(15). Pp. 188–197. DOI: 10.1016/j.compositesb.2018.05.027
6. Shukla, V. Review of electromagnetic interference shielding materials fabricated by iron ingredients. *Nanoscale Advances*. 2019. 5. Pp. 1640–1671. DOI: 10.1039/c9na00108e
7. Zornoza, E., Catalá, G., Jiménez, F., Andión, L.G., Garcés, P. Electromagnetic interference shielding with Portland cement paste containing carbon materials and processed fly ash. *Materiales de Construcción*. 2010. 60(300). Pp. 21–32. DOI: 10.3989/mc.2010.51009

8. Samkova, A., Kulhavy, P., Tunakova, V., Petru, M. Improving electromagnetic shielding ability of plaster-based composites by addition of carbon fibers. *Advances in Materials Science and Engineering*. 2018. 3758364. DOI: 10.1155/2018/3758364
9. Guan, H., Liu, S., Duan, Y., Cheng, J. Cement based electromagnetic shielding and absorbing building materials. *Cement and Concrete Composites*. 2006. 28(5). Pp. 468–474. DOI: 10.1016/j.cemconcomp.2005.12.004
10. Chen, J., Zhao, D., Ge, H., Wang, J. Graphene oxide-deposited carbon fiber/cement composites for electromagnetic interference shielding application. *Construction and Building Materials*. 2015. 84. Pp. 66–72. DOI: 10.1016/j.conbuiltmat.2015.03.050
11. Wang, Z.J., Li, K.Z., Wang, C. Freezing–thawing effects on electromagnetic wave reflectivity of carbon fiber cement based composites. *Construction and Building Materials*. 2014. 64. Pp. 288–292. DOI: 10.1016/j.conbuiltmat.2014.04.091
12. Bantsis, G., Mavridou, S., Sikalidis, C., Betsiou, M., Oikonomou, N., Yioultis, T. Comparison of low cost shielding-absorbing cement paste building materials in X-band frequency range using a variety of wastes. *Ceramics International*. 2012. 38(5). Pp. 3683–3692. DOI: 10.1016/j.ceramint.2012.01.010
13. Anuszewicz, K.J., Kazimierski, P., Klein, M., Kardaś, D., Łuczak, J. Activated Carbon Produced by Pyrolysis of Waste Wood and Straw for Potential Wastewater Adsorption. *Materials*. 2020. 13. 2047. DOI: 10.3390/ma13092047
14. Kajina, W., Junpen, A., Garivait, S., Kamnoet, O., Keeratiisariyakul, P., Rousset, P. Charcoal production processes: an overview. *Journal of Sustainable Energy & Environment*. 2019. 10. Pp. 19–25.
15. Garche, J., Dyer, C., Moseley, P., Ogumi, Z., Rand, D., Scrosati, B. *Encyclopedia of Electrochemical Power Sources*. Netherlands, 2009. 4538 p.
16. Júnior, A.F.D., Pirola, L.P., Takeshita, S., Lana, A.Q., Brito, J.O., de Andrade, A.M. Hgscopcity of Charcoal Produced in Different Temperatures. *Cerne*. 2016. Vol. 22, 4, Pp. 423–430. DOI: 10.1590/01047760201622032175
17. Ahmed S.D. Al-Ridha, Ali A. Abbood, Hussein H. Hussein. Improvement of Gypsum Properties Using S.F. Additive. *International Journal of Science and Research*. 2017. Vol. 6, iss. 8. Pp. 504–509. DOI: 10.21275/ART20175774
18. McNaught, A.D., Wilkinson, A. *Compendium of Chemical Terminology*. Oxford, 2014. 1622 p.
19. Malekian, F., Ghafourian, H., Zare, K., Sharif, A.A., Zamani, Y. Surface Characteristics of Different Wood and Coal-Based Activated Carbons for Preparation of Carbon Molecular Sieve. *Journal of the Mexican Chemical Society*. 2019. 63 (2). Pp. 120–129. DOI: 10.29356/jmcs.v63i2.666
20. Fredriksson, M., Thybring, E.E., Zelinka, S.L. Artifacts in electrical measurements on wood caused by non-uniform moisture distributions. *Holzforschung*. 2021. 75 (6). Pp. 517–525. DOI: 10.1515/hf-2020-0138
21. Palanisamy, S., Tunakova, V., Miltky, J., Wiener, J. Effect of moisture content on the electromagnetic shielding ability of non-conductive textile structures. *Scientific Reports*. 2021. 11. 11032. DOI: 10.1038/s41598-021-90516-9
22. Suleiman, A.A., Muhamad, N.A., Bashir, N., Arief, Y.Z., Rahman, M.N.A., Phung, B.T. Moisture effect on conductivity of kraft paper immersed in power transformer vegetable-based insulation oils. *IET Generation, Transmission and Distribution*. 2017. 11(9). Pp. 2269–2274. DOI: 10.1049/iet-gtd.2016.1633
23. Guan, H., Chung, D.D.L. Radio-wave electrical conductivity and absorption-dominant interaction with radio wave of exfoliated-graphite-based flexible graphite, with relevance to electromagnetic shielding and antennas. *Carbon*. 2020. 157. Pp. 549–562. DOI: 10.1016/j.carbon.2019.10.071
24. Kim, H.-J., Kang, G.-H., Kim, S.-H., Park, S. Enhancement of electromagnetic wave shielding effectiveness of carbon fibers via chemical composition transformation using H<sub>2</sub> plasma treatment. *Nanomaterials*. 2020. 10 (8). 1611. DOI: 10.3390/nano10081611
25. Xia, X., Wang, Y., Zhong, Z., Weng, G.J. A theory of electrical conductivity, dielectric constant, and electromagnetic interference shielding for lightweight graphene composite foams. *Journal of Applied Physics*. 2016. 120. 085102. DOI: 10.1063/1.4961401
26. Mishra, R.R., Sharma, A.K. Microwave–material interaction phenomena: Heating mechanisms, challenges and opportunities in material processing. *Composites Part A: Applied Science and Manufacturing*. 2016. 81. Pp. 78–97. DOI: 10.1016/j.compositesa.2015.10.035
27. Kruželák, J., Kvasnicáková, A., Hložeková, K., Plavec, R., Dosoudil, R., Goralík, M., Vilčáková, J., Hudec, I. Mechanical, thermal, electrical characteristics and EMI absorption shielding effectiveness of rubber composites based on ferrite and carbon fillers. *Polymers*. 2021. 13. 2937. DOI: 10.3390/polym13172937

#### **Information about authors:**

**Olga Boiprav**, PhD in Technical Science

ORCID: <https://orcid.org/0000-0002-9987-8109>

E-mail: [smu@bsuir.by](mailto:smu@bsuir.by)

**Elena Belousova**, PhD in Technical Science

ORCID: <https://orcid.org/0000-0001-9834-6074>

E-mail: [belousova@bsuir.by](mailto:belousova@bsuir.by)

**Elena Ahmetdinova**,

E-mail: [tszi@bsuir.by](mailto:tszi@bsuir.by)

**Natalia Bogush**,

ORCID: <https://orcid.org/0000-0002-7832-8597>

E-mail: [nbogush@bsuir.by](mailto:nbogush@bsuir.by)

Received 28.01.2022. Approved after reviewing 06.09.2022. Accepted 04.10.2022.



Research article

UDC 624.139.2

DOI: 10.34910/MCE.117.10



## Energy efficiency of underground structures in harsh climatic conditions

V.A. Stetjukha 

Transbaikal State University, Chita, Russia

 [stetjukha\\_chita@mail.ru](mailto:stetjukha_chita@mail.ru)

**Keywords:** underground structure, temperature, thermal insulation, thermal conductivity, energy saving, finite element method, heat transfer

**Abstract.** The object of the study is an underground structure located in a region with a harsh climate. The placement of structures in the underground space solves the urgent problem of reducing the heating cost for buildings and structures in the northern regions. The paper proposes ways to improve the energy efficiency of underground structures through the choice of the structural characteristics of such structures by the criterion of minimum heat loss. The method for calculating heat energy losses through external enclosing structures is based on determining the temperature fields in the ground mass adjacent to the structure throughout the year. The temperature in the ground is determined by solving the non-stationary heat conduction problem. The results of the step-by-step solution of the heat transfer problem in the form of temperature fields are used further to calculate heat losses at specified time intervals. The results of determination of the influence of thermal insulation, the depth of the object relative to the ground surface and the temperature of the internal air on heat loss are presented. The analysis of the presented results makes it possible to make the correct choice of the design parameters of the designed underground facilities in various climatic conditions.

**Citation:** Stetjukha, V.A. Energy efficiency of underground structures in harsh climatic conditions. Magazine of Civil Engineering. 2023. 117(1). Article no. 11710. DOI: 10.34910/MCE.117.10

### 1. Introduction

Great attention is paid to topical problems of energy and energy efficiency of facilities in the world. One of the directions is the expansion of the use of alternative energy sources. Another effective way can be to reduce the amount of energy consumed for heating the premises or to maintain the required temperature regime in the premises. The enclosing structures of buildings and structures and the surface of the Earth are subject to the effects of cyclical changes in the air temperature. Huge resources are spent on elimination of such influences on indoor temperature. According to [1], about 40 % of the total heat produced is consumed only for heating residential buildings. Currently in the world there is an active development of natural resources in the northern regions with low air temperatures. Energy costs for buildings and structures heating in such regions of the Eurasian and American continents are especially high, and the delivery of energy carriers can be complicated.

At the same time, the average ground temperature at a certain depth is more stable and often exceeds the air temperature in the cold season. In such conditions, the reduction of heat energy losses by structures can be achieved by placing structures underground. At a certain depth, temperature fluctuations remain quite insignificant, and in some cases the ground temperature remains closer to the required indoor air temperature. The use of thermal energy of the near-surface layers of the ground during the warm season can contribute to an increase in the efficiency of underground objects.

The course of air and ground temperature in the regions of the Northern Hemisphere has been studied earlier and allows them to be used as initial data in the study of the problem posed. Areas where the

temperature of the near-surface ground layer reaches large negative values are described in [2–5]. Ground temperature and the pattern of its fluctuations at different depths throughout the year in some regions of the northern hemisphere are given in [6–9]. In one of the northern regions of Canada [6], the temperature at a depth of about 10 m remains practically constant and is about  $-3\text{ }^{\circ}\text{C}$ . At a depth of 4 m it can drop to  $-3.6\text{ }^{\circ}\text{C}$ , at a depth of 2 m it drops to  $-4.7\text{ }^{\circ}\text{C}$ , 1 m – up to  $-6.5\text{ }^{\circ}\text{C}$ . The grounds in the study area are represented by silty clay. On Olkhon Island (on Lake Baikal), a constant temperature of about  $0\text{ }^{\circ}\text{C}$  is maintained at a depth of 3.65 m [7]. At the same time, at a depth of 1.5 m, it decreases to  $-3.75\text{ }^{\circ}\text{C}$ , at a depth of 1 m, it decreases to  $-7.5\text{ }^{\circ}\text{C}$ . Here, the grounds on the site are represented by sandy loams. In the conditions of the alpine steppe in Tibet [8], a constant temperature of about  $0\text{ }^{\circ}\text{C}$  is maintained at a depth of about 10 m. The grounds here are represented by sand and gravel. At a depth of 3 m, in an alpine meadow, the ground temperature drops to  $-3\text{ }^{\circ}\text{C}$ . The results of the most ambitious studies in the Central Transbaikalia region are presented by N.A. Shpolyanskaya [9]. Here, for one of the wells, it is established that constant temperatures of about  $1.3\text{ }^{\circ}\text{C}$  are maintained at a depth of about 13 m. At a depth of 8 m, the temperature drops to  $0.8\text{ }^{\circ}\text{C}$ , at a depth of 4 m – to  $-0.8\text{ }^{\circ}\text{C}$ , at a depth of 2 m – up to  $-6\text{ }^{\circ}\text{C}$ . Here, sand with grit and sandy loam with grit occur in the near-surface layer. Ground temperature and its fluctuations at depth depend on the composition, moisture, ground structure, on the degree of surface shielding by natural and man-made factors.

Previous studies have shown that, under certain conditions, the costs of heating underground structures are significantly reduced in comparison with similar above-ground structures. For this reason, the interest in underground construction in the world is steadily growing. Prospects are being created for the rational use of underground structures in the northern regions. The energy efficiency of underground structures is confirmed by historical experience, experimental and theoretical studies of a number of authors and is analyzed in a number of works. The efficiency of the underground and semi-underground location of buildings is substantiated in [10]. Here, using the example of refrigerators built in the USA, it is noted that the operating costs of warehouses and refrigerators for underground versions are reduced tenfold. It also shows energy savings for underground industrial buildings in Sweden, Norway and Finland. There are extensive classifications of underground structures according to various characteristics and directions of its use [11, 12].

The history and examples of the use of underground space, the main directions and a systematic approach to planning this process, a discussion of efficiency criteria are presented in [12–14]. It is noted here that the main advantage of underground structures is provided by the thermal stability of grounds and their thermal insulation capacity. Passive heat supply from the accumulated thermal energy in the ground can occur even in the coldest periods of the year. The advantages and problems of underground construction, as well as the experience of foreign countries in the development of underground space are given in [15]. In the article of V.L. Belyaev [16] notes the presence of large complexes – underground cities – erected in Canada, Finland, Japan, Netherlands, China, Singapore. It also deals with the development of underground space in Moscow. The use of underground space in Helsinki is described in [17]. An example of using the thermal inertia of ground for storing food is given in [18]. Natural smoothing of extreme temperatures due to the thermal insulating properties of ground masses is also used in tunnels [19], underground rooms and shelters [20, 21]. Often, cultural and entertainment, sports objects, production and transport objects are being erected as objects of underground structures in the world. The expediency of using underground space for placing garages, warehouses, archives and other objects is noted.

Criteria and motives for the use of underground space can be associated with the preservation of the environment, with the lack of free space for building, with the smoothing of temperature fluctuations at the surface of the ground massifs, with the need for high sound insulation, the need to increase the energy efficiency of objects, the need to build metro and roads.

Permissible temperature values in rooms, including underground rooms, are established by regulatory documents. For example, according to the requirements of Russian Sanitary Rules and Regulations 2.2.4.548-96 (Industrial premises), the air temperature at production premises should not drop below  $16\text{ }^{\circ}\text{C}$ , and sometimes below  $13\text{ }^{\circ}\text{C}$ . According to the norms of Russian Construction Rules 113.13330.2012 (Parking of cars), the calculated air temperature in heated rooms is taken not lower than  $5\text{ }^{\circ}\text{C}$ .

Along with the general features and directions of the use of underground space, there are also significant differences in its use in the southern and northern regions. In the southern regions, when using underground structures, the problems of smoothing the maximum values of positive temperatures are mainly solved [21, 22]. In the North, an important role is played by smoothing out the impact of extreme values of negative outside air temperatures on structures or maintaining negative ground temperatures. Saving thermal energy in the northern regions during the construction of underground structures is considered in [23, 24], the prospects for the construction of such structures in the North are noted in [25]. The issues of cold accumulation are considered in paper [24], the preservation of permafrost in the foundations of buildings – in article [26].

The use of a large ground layer as a layer of thermal insulation above the structure will require significant costs for earthworks. Therefore, in underground construction, it is necessary to raise the question of the use of artificial effective thermal insulation, which will replace the ground layer around the structure and ensure even greater temperature stabilization at a certain depth and the conservation of thermal energy. Ways of using of thermal insulation in order to maximize the efficient conservation of thermal energy are considered in [27–30]. The influence of the thickness of the thermal insulation on the amount of heat loss for a partially recessed building in Poland is estimated in [27]. The effectiveness of thermal insulation for various climatic conditions of the three US states at three temperature options inside a completely buried and insulated along the entire contour of a warehouse facility is given in [28]. Experimental studies of the efficiency of tunnel insulation in China are presented in [29]. Analysis of the criteria for the effectiveness of thermal insulation of an underground facility using numerical modeling based on simplified techniques is carried out in [30]. In a harsh climate, the issues of using thermal insulation acquire special significance and are considered in [31, 32]. It also solves the actual problem of optimization of ground thermal insulation in the conditions of the Trans-Baikal region [32]. The above studies confirm that the use of thermal insulation reduces the depth at which significant fluctuations in the temperature of the environment occur, and makes it possible to reduce the size of the heat-insulating ground layer above the structure. In the latter case, the structure can be located closer to the surface, which reduces the cost of earthworks.

Various methods are used to calculate the heat loss of underground structures in the design. In most cases, to assess heat loss, separate formulas are used that take into account the difference in temperatures between the outside air and the air in rooms underground [24, 33, 34]. In [35] formulas for calculating heat losses in underground collectors are given, in [24, 33, 34] – formulas for determining heat losses in the buried part of buildings. The disadvantage of the above publications is the incomplete consideration of the influence of the ground massif temperature and the physical properties of the ground changing in different periods of the year.

Another approach to the determination of heat loss by underground objects includes the determination of temperature fields in the ground massif adjacent to the underground structure, taking into account the effect of temperature in room's underground [20, 36–38]. In [36], the temperature of the adjacent ground is determined by solving a linear problem in a polar coordinate system for an underground potash mine. The problems of heat transfer in the ground massif for slightly buried in the ground structures are solved in [20, 37–38]. This approach, taking into account the physical and mechanical properties of the ground massifs adjacent to the structures, increases the reliability of the results obtained. The results of experimental studies of heat transfer near underground structures, presented in [30, 39–41], confirm the high accuracy of solutions based on the latter approach to the problem. In this case, the calculation of the parameters of heat transfer of underground structures should be carried out on the basis of solving the non-stationary problem of heat transfer.

At the same time, the results of calculations, taking into account the thermal inertia of the ground, given in the publications presented above, assess the effectiveness of underground structures in the southern regions. The energy efficiency of underground construction in harsh climatic conditions, taking into account the choice of the necessary technical parameters of structures, has not been studied enough. This circumstance required an assessment in this article of the effectiveness and the feasibility of using underground structures in regions with severe climatic conditions.

The object of research is underground structures in the northern regions. The subject of research is the magnitude of the loss of thermal energy through the external enclosing structures of structures when they are underground. The purpose of the work is a numerical analysis of the loss of thermal energy and an increase in the energy efficiency of underground structures in harsh climatic conditions. To achieve the purpose, it is necessary to solve the following tasks: formation of a method for determining the heat loss of a structure, taking into account non-stationary heat transfer in the ground, temperature fields in the ground massif and heat loss at specified time intervals; determination of quantitative indicators that assess the advantages of the underground layout based on the clarification of the temperature and properties of the surrounding ground; assessment of the degree of influence on the energy efficiency of underground structures of such factors as the depth of the object from the day surface, the thickness of the thermal insulation layer, the temperature in the premises.

## 2. Methods

A ground massif subject to continuous temperature changes at each point associated with temperature changes on the day's surface during the year is considered. The nature of temperature changes over time is determined by the climatic parameters of the region. An underground structure is located at some depth from the earth's surface. A ground massif with structural elements of the structure and thermal insulation form the design model shown in Fig. 1. The structural elements of the structure's cross-section are

highlighted in blue, and the elements of thermal insulation are highlighted in orange. The variable parameters of the computational model are the distance from the structure to the day surface, the thickness of the thermal insulation, and the air temperature in the premises.

The problem is solved by the finite element method using the LIRA CAD software package. The design model of structures and ground is divided into finite elements. Finite elements of thermal conductivity and convective heat transfer are used. In the vertical direction, the ground massif, reinforced concrete structures and layers of thermal insulation are divided into finite elements with a step of 0.25 m, in the horizontal direction – with a step of 0.25 and 0.5 m. The temperature change in the ground massif and in structures is determined by a software package based on the theory of unsteady heat transfer. The phase transition under the influence of seasonal freezing and thawing of the soil is taken into account by stepwise adjustment of the parameters during the iterative process. The course of the outside air temperature and convective heat transfer are taken into account. The initial and boundary conditions on the contour of the ground massif model, on the day surface and in the ground massif are set on the basis of long-term observations. Numerous studies show that the obtained temperature fields at individual internal points of the computational model after repeated cyclic calculations do not depend on the initial temperature in the massif and are completely determined by the boundary conditions of the problem. The air temperature in the premises during the calculations is assumed to be constant. Energy costs for ventilation, water supply and sanitation depend on the purpose of the facilities. They are supposed to be taken into account when continuing research.

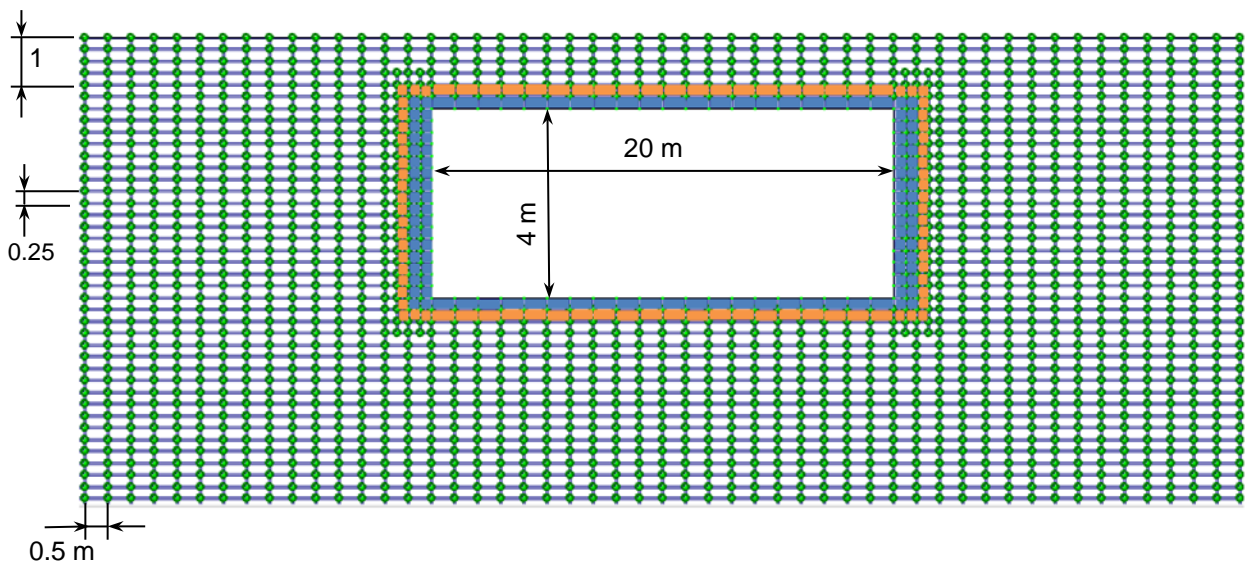


**Figure 1. Cross-section of an underground structure.**

As a result of the non-stationary problem of heat transfer solving, temperature fields are obtained in the ground and in structures. The loss of heat energy is determined by the solution of a quasi-stationary problem on specified time intervals of one month. Taking into account the temperature distribution in the ground massif, in the structures and in the premises, the heat flux from the structure through the ground massif is determined. The heat flux is calculated based on the average temperature fields for each month. Heat loss per year is obtained by summing heat fluxes for each month. Heat loss to the ground for a period equal to one month is [35]

$$Q = z \cdot F \cdot K \cdot (t_v - t_s), \quad (1)$$

where  $z$  is the heat transfer time, hour;  $F$  is area,  $m^2$ ;  $K$  is calculated heat transfer coefficient,  $(W / m^2 \cdot ^\circ C)$ ;  $t_v$  is internal air temperature,  $^\circ C$ ;  $t_s$  is the temperature of the adjacent ground,  $^\circ C$ .

Formula (1) defines the heat loss through a selected area with a given area. Redistribution of heat fluxes in the ground massif and its accumulation for discrete time intervals is determined at each step of solving the non-stationary heat transfer problem. The technique used differs by taking into account the change in the temperature fields in the ground adjacent to the structure.

### 3. Results and Discussion

A ground massif, which lies to a depth of 14 m from the day surface with an underground structure located in it, is considered. In the horizontal direction, the computational model includes a ground massif at

a distance of 20 m from the outer contour of the structure. Fig. 1 and the following figures show fragments of sections along the massif, which are necessary for an objective illustration of the studied parameters. The cross-section of the underground structure has dimensions of 20 and 4 m (see Fig. 1). The length of the structure is taken to be 100 m. The thickness of the bearing enclosing structures of the walls made of reinforced concrete is 0.5 m. The floor structures and covering constructions are 0.25 m thick. Structural elements inside the structure (columns and internal walls) are not shown in Fig. 1. The depth of the structure from the surface is taken equal to 1 and 2 m, the temperature in the rooms is 8 °C or 20 °C, the thickness of the thermal insulation layers of the enclosing structures along the outer contour for different options is 0.25 or 0.5 meters.

Boundary and initial conditions on the bottom and side faces of the ground massif correspond to the temperature values in the massif in natural conditions. The boundary conditions on the upper edge are determined by the course of the outside air temperature. The facility is located in one of the regions of the Trans-Baikal Territory. Average monthly and annual air temperature according to Russian Construction Rules 131.13330.2012 (Construction climatology) is given in Table 1.

**Table 1. Average monthly and average annual air temperature, °C.**

I	II	III	IV	V	VI	VII	VIII	IX	X	XI	XII	Year
-25.0	-20.2	-9.6	1	9.2	16.2	18.5	15.7	8.4	-0.8	-13.1	-22.6	-1.9

A homogeneous ground massif in the model is formed from loams with the following characteristics: dry ground density  $\gamma = 1.8 \text{ g/cm}^3$ , moisture content  $W = 20 \%$ , thermal conductivity coefficient of frozen and thawed ground  $\lambda_f = 2.0 \text{ W / (m} \cdot \text{°C)}$  and  $\lambda_{th} = 1.6 \text{ W/(m} \cdot \text{°C)}$ , heat capacity of frozen and thawed ground  $C_f = 2.41 \text{ J / (m}^3 \cdot \text{°C)}$   $10^{-6}$  and  $C_{th} = 3.17 \text{ J / (m}^3 \cdot \text{°C)}$   $10^{-6}$ , freezing start temperature  $T_{bf} = -0.2 \text{ °C}$ . Thermal conductivity and heat capacity of concrete  $\lambda = 1.69 \text{ W / (m} \cdot \text{°C)}$ ,  $c = 0.84 \text{ kJ / (kg} \cdot \text{°C)}$ , density of concrete –  $\gamma = 2.5 \text{ g / cm}^3$ . Thermal conductivity and heat capacity of a polystyrene foam heat insulator  $\lambda = 0.03 \text{ W / (m} \cdot \text{°C)}$ ,  $c = 1.34 \text{ kJ / (kg} \cdot \text{°C)}$ , density  $\gamma = 0.035 \text{ g / cm}^3$ .

To assess the energy efficiency of an underground object, the temperature fields in the massif and the loss of thermal energy through the enclosing structures are determined. Temperature values in the middle of each month in typical cross-sections for the considered basic ("basic") variant of the structure, buried by 1 m, when the temperature in the premises is taken equal to +8 °C, with a thermal insulation thickness of 0.25 m are given in Table 2. The distribution of temperature fields around the structure in mid-July and mid-February is shown in Fig. 2 and 3.

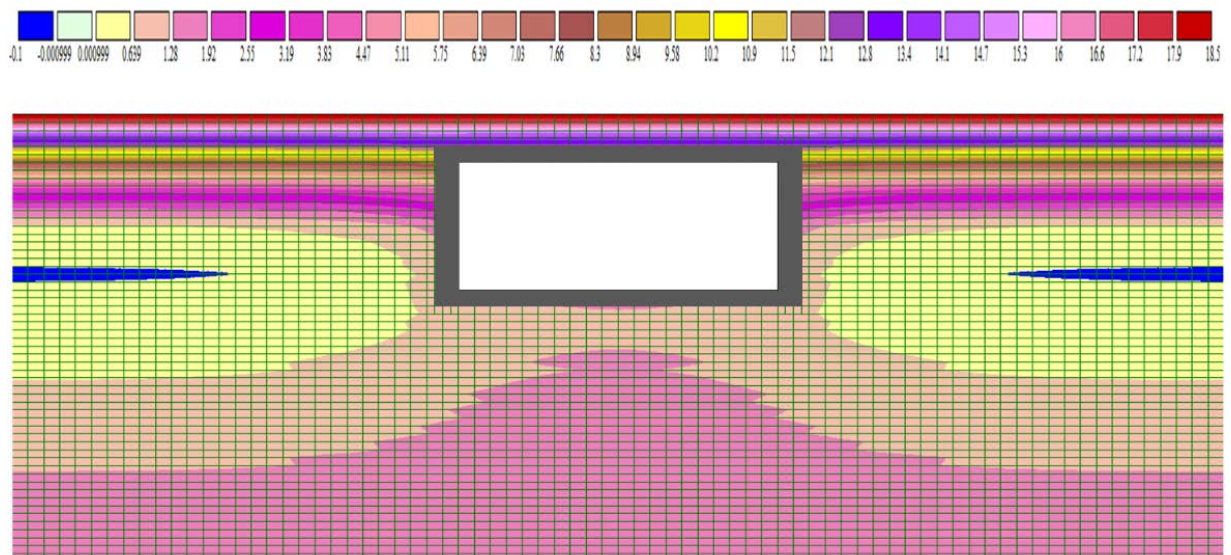


**Figure 2. Distribution of temperature in the massif in July (The numerical values on the color scale are given in °C).**

As can be seen from the presented results, the temperature of the ground near the surface of the covering structures during the year fluctuates in the range from 12.3 °C in July to -11.5 °C in February. The change in ground temperature above the covering structure with an increase and decrease in air temperature is more significant than a change in ground temperature in its natural state. This is due to the limitation of the heated zone with a layer of thermal insulation and the accumulation of thermal energy above the

covering constructions. The maximum ground temperature under the floor structure is 3.3 °C in February, the minimum is 0.9 °C in June. The ground temperature remains practically the same in the middle sections of the floor and the covering constructions and changes slightly as the corners are approached.

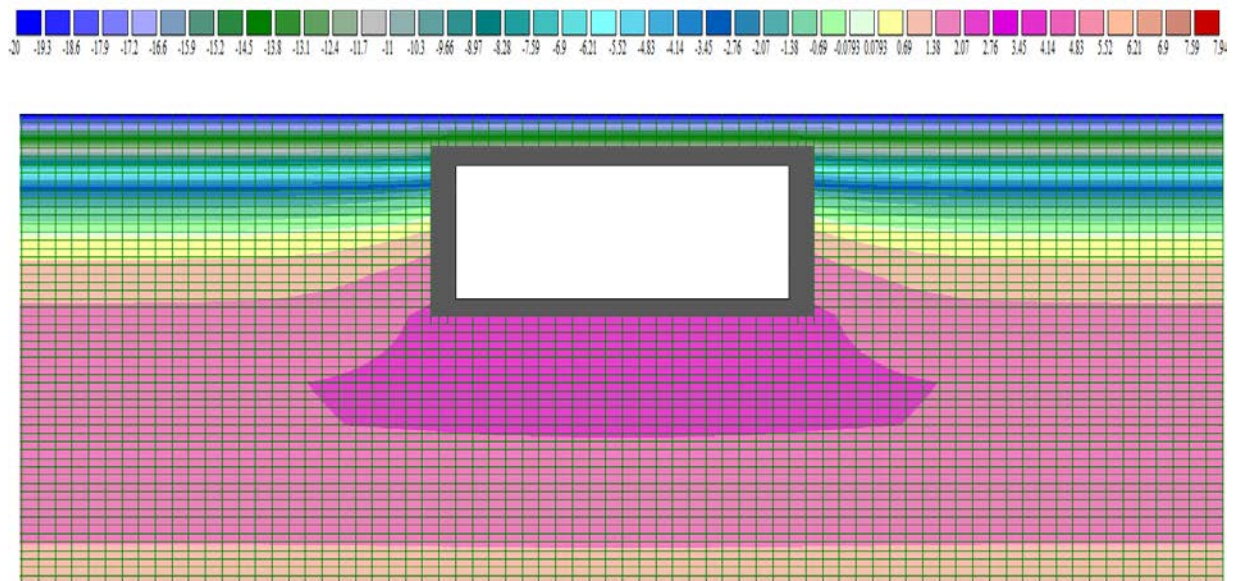


**Figure 3. Temperature distribution in the massif in February  
(The numerical values on the color scale are given in °C).**

**Table 2. Temperature values at different time periods.**

Time period	Temperature values at characteristic points of the outer surface of structures, °C						
	Covering construction points		Floor construction points		Wall construction points		
	Medial	Angled	Medial	Angled	Upper	Medial	Bottom
January	-8.4	-8.5	2.8	2.7	-3.4	1.6	2.4
February	-11.3	-11.5	2.5	2.4	-7.4	0.8	2.0
March	-2.7	-2.8	1.6	1.4	-2.7	-0.6	1.1
April	-1.1	-1.1	1.6	1.3	-1.5	-0.2	1.0
May	0.7	0.7	1.4	1.1	-0.1	0	0.7
June	9.3	9.3	1.2	0.9	5.5	0.5	0.7
July	12.2	12.3	1.3	1.0	8.5	1.4	0.8
August	11.4	11.5	1.9	1.6	9.5	4.2	1.5
September	8.3	8.3	3.2	2.9	8.3	5.5	3.1
October	4.1	4.0	3.3	3.2	5.4	5.4	3.5
November	0.8	0.8	3.1	2.9	1.9	3.3	2.6
December	-4.5	-4.6	3.0	2.8	-0.5	2.4	2.7

The nature of the change in ground temperature at the outer surface of the enclosing structures of the walls is more complex. At the top of the wall, temperature fluctuations are maximum. They vary in the range from -7.4 °C to 9.5 °C. The maximum and minimum ground temperatures at the base of the wall are 3.5 and 0.7 °C, respectively. The maximum and minimum temperatures at the middle of the wall and at the bottom of the wall are reached with a noticeable phase shift in relation to the extreme outside temperatures. It depends on changes in ground temperature at depth in natural conditions. Graphs of ground temperature changes at a depth of 3.5 and 6 meters in natural conditions are shown in Fig. 4. The upper part of the ground massif surrounding the structure, saturated with heat in summer, gives off thermal energy to the layers of ground located below. In the cold period of the year, the wave of a decrease in temperature spreads downward. The positive temperatures around the structure delays the penetration of extreme negative temperatures in depth for 2 months (until March) at a depth of 3.5 meters and for 5 months (until June) at a depth of 6 meters. The penetration into the depth of extreme positive temperatures occurs with a shift of 3 months (until October) at a depth of 3.5 and 6 meters. Such a phase shift distinguishes underground structures located in harsh climates from regions with high air temperatures [37], where there is a slight phase shift between ground and air temperatures. Wave-like changes in temperature in the ground massif adjacent to the structure affect the loss of thermal energy by the structure during the year. Thus, the inertia of the ground around the underground structure smooths out extreme fluctuations in the temperature of the

outside air. As a result, the influence of ground inertia is a positive factor for stabilizing the temperature of the grounds adjacent to the structure.

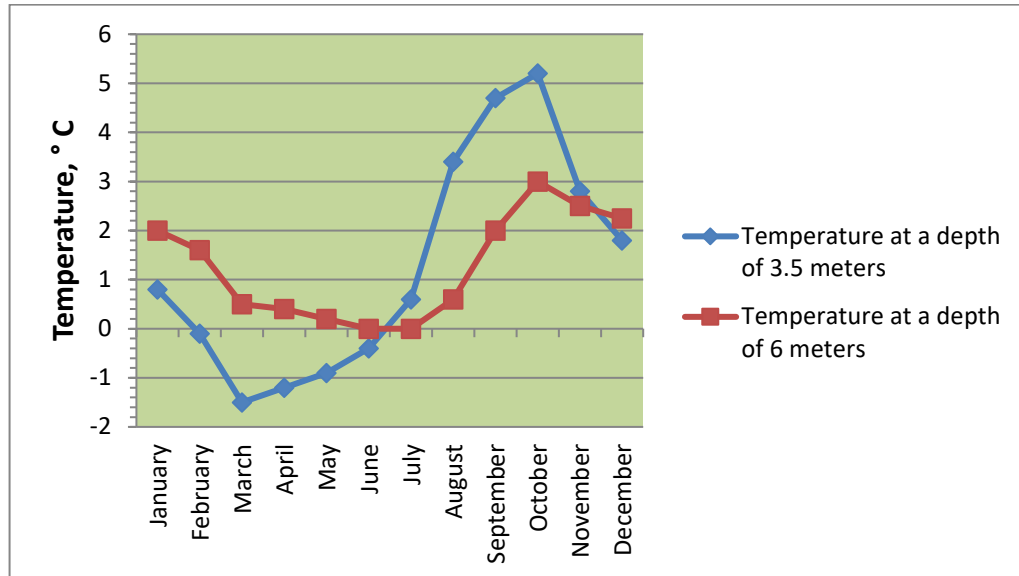


**Figure 4. Annual variation of ground temperature at a depth of 3.5 m and 6 m in natural conditions.**

In turn, the air temperature in the underground structure also affects the temperature of the adjacent ground massif. The influence of the structure under consideration on the ground temperature in the horizontal direction is about 8 meters. The zone of influence of a buried structure in the horizontal direction coincides with the result given in [37]. The effect on the ground temperature below the floor level is about 7.5 meters. This limited impact is due to the use of thermal insulation. The results of determining heat energy losses through the enclosing structures are presented in Table 3.

**Table 3. Loss of heat energy by the structure.**

Time period	Energy loss, kWh			Total
	Through covering construction	Through floor structures	Through wall structures	
January	2740	868	576	4184
February	3223	918	674	4815
March	1788	1068	685	3541
April	1520	1068	649	3237
May	1220	1102	622	2944
June	-218	1136	521	1439
July	-702	1120	410	828
August	-568	1018	268	718
September	-50	802	433	1185
October	652	786	236	1674
November	1202	902	410	2514
December	2088	836	473	3397
In just one year	12895	11624	5957	30476

The analysis of the heat losses presented in Table 3 indicates the highest total amount of losses through the ceiling (42.4 %) and floor (38.1 %) and less heat loss through the walls (19.5 %). This is due to the multiple difference in the areas of these surfaces, as well as year-round heat loss through a significant area of the floor surface. At the same time, in terms of the intensity of heat loss through a unit of area in the cold season, heat flow through the ceiling and walls prevails. As can be seen from Table 3, in the period from October to May there are significant losses of thermal energy through the ceiling, in the period from June to September, heat energy enters the ceiling (the energy values are marked in the table with a "-" sign). In regions with a warm climate the heat flux through the floor remains insignificant [20]. In our case the significant heat flux from the floor is due to the low positive ground temperatures under the floor structure throughout the year. At the same time, positive summer heat impulses do not have a significant effect on

ground temperature below floor level. The ground temperature here is significantly different from the indoor temperature.

When comparing the underground and aboveground options for structures, it was found that at the design temperature of the internal air +8 °C and the above design parameters, the heat loss for the underground structure was 1.5 times lower compared to a similar above-ground structure. A structure without thermal insulation is not considered, since this option will lead to freezing of structures and a decrease in the temperature of their inner surface below the dew point.

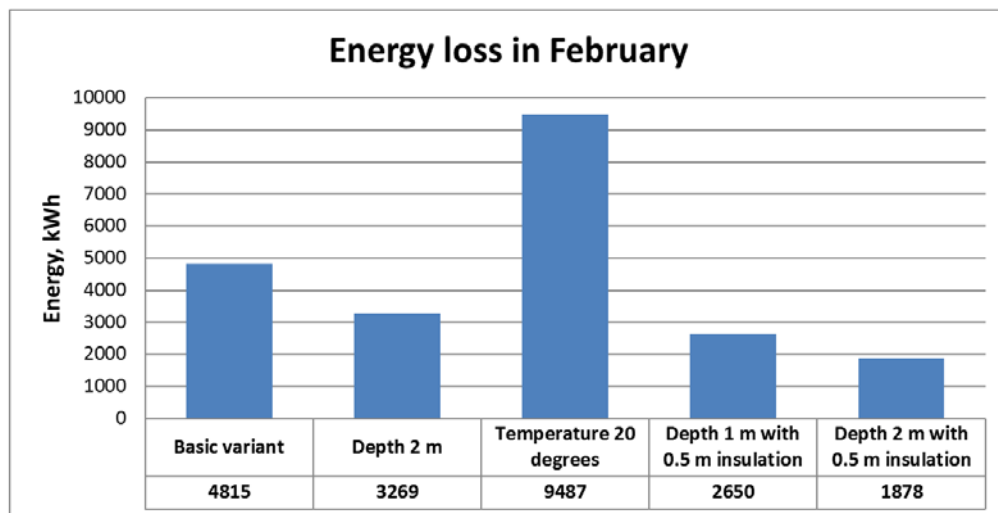
To assess the effectiveness of individual constructive measures, the temperature distribution on the contour of the structure and the corresponding heat energy losses in the most energy-intensive periods of the year (in January and February) are determined. The calculation results are presented in tables 4 and 5. Heat losses during this period fully reflect the influence of the investigated factors on the efficiency of underground structures. When the structure is deepened to 2 meters from the outer contour of the structure, the ground temperature near the outer contour of the covering construction in January and February becomes significantly higher due to the increase in the insulating function of the ground layer. At the same time, the temperature of the ground under the floor structure and in the zone of the lower part of the walls changes insignificantly due to its greater stability with increasing depth. An increase in the temperature of the internal air in the premises up to 20 °C have an insignificant effect on the temperature of the ground on the contour of the structure. The indicated increase in the air temperature leads to an increase in the temperature of the ground at the surface of the enclosing covering construction by 1.6–1.8 degrees. The ground temperature under the floor structure and at the bottom of the walls also increases in 2 winter months by 1.2–1.4 degrees. An increase in the size of the thermal insulation layer to 0.5 meters, regardless of the considered depth of the structure, limits the heating of the ground massifs adjacent to the structure and significantly reduces the temperature at the outer contour of the object (see Table 4).

**Table 4. Temperature values on the contour of the structure for different design features.**

Time period and technical features	Temperature values at characteristic points of the outer surface of structures, °C						
	Covering construction points		Floor construction points		Wall construction points		
	Medial	Angled	Medial	Angled	Upper	Medial	Bottom
January, basic version	-8.4	-8.5	2.8	2.7	-3.4	1.6	2.4
February, basic version	-11.3	-11.5	2.5	2.4	-7.4	0.8	2.0
January, depth 2 m	-0.6	-1.0	3.0	2.8	-0.1	2.4	2.8
February, depth 2 m	-3.1	-3.5	2.6	2.4	-1.3	1.6	2.3
January, indoor temperature is 20 °C	-7.8	-7.9	4.4	3.9	-2.6	2.8	3.5
February, indoor temperature is 20 °C	-10.7	-10.8	4.3	3.7	-6.4	2.2	3.2
February, insulation 0.5 m, deepening 1.25 m from the roof supporting structure	-13.7	-13.8	2.1	2.0	-7.7	0.4	1.7
February, insulation 0.5 m, deepening 2.25 m from the roof supporting structure	-5.2	-5.4	2.3	2.2	-1.6	1.2	2.0

**Table 5. Loss of thermal energy by the structure at different design features.**

Time period and technical features	Energy loss, kWh			Total
	Through covering construction	Through floor structures	Through wall structures	
January, basic version	2740	868	576	4184
February, basic version	3223	918	674	4815
January, indoor temperature is 20 °C	4640	2600	1354	8594
February, indoor temperature is 20 °C	5120	2620	1747	9487
January, depth 2 m	1440	840	442	2722
February, depth 2 m	1860	900	509	3269
February, insulation 0.5 m, deepening 1.25 m from the roof supporting structure	1840	500	310	2650
February, insulation 0.5 m, deepening 2.25 m from the roof supporting structure	1120	480	278	1878

**Figure 5. Energy losses of an underground structure in February.**

As follows from the results presented in Table 5, moving the structure to a depth of up to 2 meters from the surface of the outer contour of the structure reduces heat losses by a third in two months compared to the base case. An increase in the temperature of the indoor air in an underground room up to 20 °C doubles the heat loss in the two coldest months. An increase in the thickness of thermal insulation from 0.25 to 0.5 meters for a structure located at a depth of 1.25 meters from the supporting structure of the coating reduces heat loss by 1.82 times. For a structure located at a depth of 2.25 meters, heat losses are reduced by 1.74 times. Increasing the insulation layer turns out to be more effective than increasing the depth of the structure and less costly in terms of the amount of work. The effectiveness of constructive measures on the example of heat losses in February, characterized by the highest heat losses for the year, is clearly shown in Fig. 5.

#### 4. Conclusions

1. A method for determining heat losses in underground structures in a harsh climate, based on determining the temperature fields in the adjacent ground massifs by solving the non-stationary problem of heat conduction is presented. The technique is distinguished by taking into account the thermal inertia of the ground mass with significant fluctuations in the outside air temperature.

2. The degree of energy efficiency of underground construction objects in harsh climatic conditions was determined by the criterion of reducing the loss of thermal energy by the structure. Energy losses by an underground object in the considered climatic conditions and with the used design parameters are reduced by 1.5 times in comparison with a similar above-ground structure.

3. The effectiveness of individual design measures to reduce heat energy losses for underground structures has been established. Deepening a structure to 2 meters from the surface reduces heat energy losses by a third in the coldest months compared to a structure buried by 1 meter. The energy efficiency of

underground structures in the northern regions increases with the indoor temperature approaching the temperature of the ground in its natural state, as well as with the use of large layers of effective thermal insulation materials at the outer contour of the structures.

4. The problem to be solved is of great practical importance for assessing the feasibility of using underground construction facilities in harsh climatic conditions and for choosing the design parameters of underground facilities.

## References

1. Asaul, A.N., Kazakov, Yu.N., Pasyada, N.I., Denisova, I.V. *Teoriya i praktika maloetazhnogo zhilishchnogo stroitelstva v Rossii*. [Theory and practice of low-rise housing construction in Russia]. St. Petersburg: «Gumanistika», 2005. 563 p. (rus)
2. Obu, J., Westermann, S., Bartsch, A., Berdnikov, N., Christiansen, H., Dashtseren, A., Delaloye, R., Elberling, B., Etzelmuller, B., Kholodov, A., Khomutov, A., Kaab, A., Leibman, M., Lewkowicz, A., Panda, S., Romanovsky, V., Way, R., Westergaard-Nielsen, A., Wu, T., Yamkhin, J., Zou, D. Northern Hemisphere permafrost map based on TTOP modelling for 2000–2016 at 1 km<sup>2</sup> scale. *Earth-Science Reviews*. 2019. 193. Pp. 299–316. DOI: 10.1016/j.earscirev.2019.04.023
3. Magnin, F., Etzelmuller, B., Westermann, S., Isaksen, K., Hilger, P., Hermanns, R. Permafrost distribution in steep rock slopes in Norway: measurements, statistical modelling and implications for geomorphological processes. *Earth Surface Dynamics*. 2019. 7. Pp. 1019–1040. DOI: 10.5194/esurf-7-1019-2019
4. Luo, J., Yin, G., Niu, F., Lin, Z., Liu, M. High Spatial Resolution Modeling of Climate Change Impacts on Permafrost Thermal Conditions for the Beiluhe Basin, Qinghai-Tibet Plateau. *Remote Sensing*. 2019. 11 (11). 1294. DOI: 10.3390/rs11111294
5. Tao, J., Koster, R., Reichle, R., Forman, B., Xue, Y., Chen, R., Moghaddam, M. Permafrost variability over the Northern Hemisphere based on the MERRA-2 reanalysis. *The Cryosphere*. 2019. 13. Pp. 2087–2110. DOI: 10.5194/tc-13-2087-2019
6. Ground Temperature Data. Summary Report for the Mackenzie Gathering Pipelines, Mackenzie Valley Pipeline. Mackenzie Gas Project. Imperial Oil Resources Ventures Limited. July. 2006. 33 p. [Online]. URL: <https://apps.cer-rec.gs.ca> (reference date: 18.02.2022)
7. Khimenkov, A.N., Sergeev, D.O., Vlasov, A.N., Kozireva, E.A., Rybchenko, A.A., Svetlakov, A.A. Contemporary and paleo-cryogenic formations on Olkhon island. *Earth's Cryosphere*. 2015. 19(4). Pp. 48–57.
8. Li, A., Xia, C., Bao, C., Yin, G. Using MODIS Land Surface Temperatures for Permafrost Thermal Modeling in Beiluhe Basin on the Qinghai-Tibet Plateau. *Sensors*. 2019. 19. P. 4200. DOI: 10.3390/s19194200
9. Shpolyanskaya, N.A. *Vechnaya merzlota Zabaykalya*. [Permafrost of the Trans-Baikal region]. Moscow: Nauka, 1978. 132 p. (rus)
10. Tetior, A.N., Loginov, V.F. *Proyektirovaniye i stroitelstvo podzemnykh zdaniy i sooruzheniy*. [Design and construction of underground buildings and structures]. Kiev: Budivelnik, 1990. 168 p. (rus)
11. Konyukhov, D.S. Analiz slozhivshikhsya klassifikatsionnykh sistem podzemnykh sooruzheniy. [Analysis of the existing classification systems of underground structures]. *Vestnik MGSU*. 2010. 4. Pp. 48–55. (rus)
12. Varriale, R. "Underground Built Heritage": A Theoretical Approach for the Definition of an International Class. *Heritage*. 2021. 4. Pp. 1092–1118. DOI: 10.3390/heritage4030061
13. Tann, L., Sterling, R., Zhou, Y., Metjed, N. Systems approaches to urban underground space planning and management – A review. *Underground Space*. 2020. 5. Pp. 144–166. DOI: 10.1016/j.undsp.2019.03.003
14. Ariaratnam, S.T., Chammout, B. Underground space development resulting from increased urban migration. *Global Journal of Engineering and Technology Advances*. 2021. 08 (02). Pp. 046–055. DOI: 10.30574/gjeta.2021.8.2.0093
15. Lisikov, B.A., Kapluchin, A.A. *Ispolzovanie podzemnogo prostranstva* [Utilization of underground space]. Donetsk: Nord-Press, 2005. 390 p.
16. Belyayev, V.L. *Planirovaniye gradostroitel'nogo osvoyeniya podzemnogo prostranstva g. Moskvy*. [Planning of urban development of underground space in Moscow]. *Vestnik MGSU*. 2013. 1. Pp. 35–46. (rus)
17. Vahaaho, I. Underground space planning in Helsinki. *Journal of Rock Mechanics and Geotechnical Engineering*. 2014. 6. Pp. 387–398.
18. Mazarron, F. R., Cid-Falceto, J., Canas, I. Ground Thermal Inertia for Energy Efficient Building Design: A Case Study on Food Industry. *Energies*. 2012. 5. Pp. 227–242.
19. Zhang, J., Zhang, Y., Li, L., Liu, B., Mei, Z. Closed-Form Solution for the Analysis of Antifreeze Disease Fortification Length in a Permafrost Tunnel. *Advances in Civil Engineering*. 2020. Article ID 7367954. DOI: 10.1155/2020/7367954
20. Sakami, N., Boukhattem, L., Hamdi, H., Benhamou, B. Comparison of shallow basement thermal performance for different regions of Morocco using a three-dimensional heat transfer analysis. *Cogent Engineering*. 2019. 6 (1). 1602926. Pp. 1–22. DOI: 10.1080/23311916.2019.1602926
21. Guedouh, M.S., Naceur, K., Zemmouri, N., Assassi, A. Underground Building's Geothermal Potential: an Alternative Passive Sustainable Construction Facing Hot-Arid Climates. Case of historical NLA Hospital in Bitam. *Algerian Journal of Environmental Science and Technology*. 2021. 7(2). Pp. 1889–1896.
22. Alwetaishi, M., Benjeddou, O., Balabel, A., Alzaed, A. Can Underground Buildings Be Beneficial in Hot Regions? An Investigation of Field Measurements in On-Site Built Underground Construction. *Buildings*. 2021. 11. Pp. 1–16. DOI: 10.3390/buildings11080341
23. Galkin, A.F. *Teplovoy rezhim podzemnykh sooruzheniy Severa*. [Thermal regime of underground structures of the North]. Novosibirsk: Nauka. 2000. 304 p. (rus)
24. Gulyy, S.A. *Stroitelstvo podzemnykh zdaniy na Severe – odin iz putey ekonomii teplovoy energii*. [Construction of underground buildings in the North is one of the ways to save thermal energy]. *Vestnik YuUrGU. Seriya «Energetika»*. 2015. 15(4). Pp. 61–68. (rus)
25. Kuzmin, G.P. *Podzemnyye sooruzheniya v kriolitozone*. [Underground structures in permafrost]. Novosibirsk: Nauka. 2002. 176 p. (rus)

26. Rabinovich, M.V., Naberezhnyy, A.D. Formirovaniye temperaturnogo rezhima mnogoletnemerzlykh gruntov osnovaniy zdaniy na territorii mnogoetazhnoy zastroyki goroda Yakutsk. [Formation of the temperature regime of permafrost soils of building foundations on the territory of multi-storey buildings in the city of Yakutsk]. Promyshlennoye i grazhdanskoye stroitelstvo. 2019. 3. Pp. 70–76. DOI: 10.33622/0869-7019.2019.03.70-76. (rus)
27. Staniec, M., Nowak, H. Analysis of the earth-sheltered buildings' heating and cooling energy demand depending on type of soil. Archives of Civil and Mechanical Engineering. 2011. 11 (1) Pp. 221–235. DOI: 10.1016/S1644-9665(12)60185-X
28. Hanson, J., Kopp, K., Yesiller, N., Cooledge, C., Klee, E. The Use of Recycled Materials as Thermal Insulation in Underground Construction. American Society of Civil Engineering Geo-Chicago 2016. Chicago, Illinois. Pp. 94–103. DOI: 10.1061/9780784480137.010
29. Zhao, P., Chen, J., Luo, Y., Chen, L., Li, Y., Wang, C. Investigation of the Insulation Effect of Thermal Insulation Layer in the Seasonally Frozen Region Tunnel: A Case Study in the Zuomutai Tunnel. China Advances in Civil Engineering. Volume 2019. Article ID 4978359. 14 p. DOI: 10.1155/2019/4978359
30. Kim, B. S., Kim, K. Analyses on Thermal Insulation Performance of Earth-Covered Wall for Residential Underground Space by Using a Numerical Simulation Program. Journal of Asian Architecture and Building Engineering. 2004. 3 (2). Pp. 259–266.
31. Stetyukha, V.A., Rakhvalova, N.V. Otsenka effektivnosti teploizolyatsii mnogoletnemerzlykh gruntov. [Evaluation of the effectiveness of thermal insulation of permafrost soils]. Vestnik ZabGU. 10 (101). 2013. Pp. 82–88. (rus)
32. Stetyukha, V.A. Povysheniye energoeffektivnosti podzemnykh sooruzheniy na osnove optimizatsii teploizolyatsii. [Improving the energy efficiency of underground structures based on the optimization of thermal insulation]. Vestnik ZabGU. 2016. 12. Pp. 13–19. (rus)
33. Sotnikov, A.G. Teplofizicheskiy raschet teplopoter podzemnoy chasti zdaniy. [Thermophysical calculation of heat losses of the underground part of buildings]. Teploenergoeffektivnyye tekhnologii. 2010. 4. Pp. 23–28. (rus)
34. Belous, A.N., Overchenko, M.V. Teplopoteri zdaniya cherez neotaplivayemyye podvalnyye pomeshcheniya. [Heat loss of the building through unheated basements]. Stroitelstvo unikalnykh zdaniy i sooruzheniy. 2016. 4 (43). Pp. 7–17. (rus)
35. Rymarov, A.G., Titkov, D.G. Osobennosti poter teploty v massiv grunta podzemnogo kommunikatsionnogo kollektora. [Features of Heat Leakage into Soil Body of Underground Communication Collector]. Stroitelstvo: nauka i obrazovaniye. 2014. 4. Paper 2. [Online]. URL: <http://www.nso-journal.ru>. (reference date: 18.02.2022). (rus)
36. Bascompta, M., Castanon, A.M., Sanmiquel, L. and Oliva, J., Heat flow assessment in an underground mine: An approach to improve the environmental conditions. DYNA. 2016. 83(197). Pp. 175–180. DOI: 10.15446/dyna.v83n197.52182
37. Sakami, N., Boukhattem, L., Hamdi, H. Soil Inertia and Shallow Basement Envelope Impact on Cellar Internal Temperature. Journal of Renewable Energy and Sustainable Development. 2016. 2(1). Pp. 30–36. DOI: 10.21622/RESD.2016.02.1.030
38. Shi, L., Liu, J., Zhang, H. Optimization for energy efficiency of underground building envelope thermal performance in different climate zones of China. E3S Web of Conferences 22. 2017. 156. ASEE17 DOI: 10.1051/e3sconf/20172200156
39. Yua, W., Lua, Y., Hana, F., Liua, Y., Zhangb, X. Dynamic process of the thermal regime of a permafrost tunnel on Tibetan Plateau. Tunnelling and Underground Space Technology. 2018. 71. Pp. 159–165. DOI: 10.1016/j.tust.2017.08.021
40. Park, K-S., Nagai, H. Study on the Heat Load. Characteristics of Underground Structures Part 2. Computational Analysis of the Heat/Moisture Behavior and Heat Load of Underground Structures. Journal of Asian Architecture and Building Engineering. 2007. 6 (1). Pp. 189–196. DOI: 10.3130/jaabe.6.189
41. Park, K-S., Nagai, H., Iwata, T. Study on the Heat Load Characteristics of Underground Structures. Journal of Asian Architecture and Building Engineering. 2006. 5 (2). Pp. 421–428. DOI: 10.3130/jaabe.5.421

**Information about author:**

**Vladimir Stetjukha, Doctor of Technical Science**

E-mail: [stetjukha\\_chita@mail.ru](mailto:stetjukha_chita@mail.ru)

Received 22.02.2022. Approved after reviewing 06.09.2022. Accepted 09.09.2022.



Research article

UDC 691.3

DOI: 10.34910/MCE.117.11



## Peculiarities of hydration and frost resistance of cement with natural zeolite additive

A.L. Popov<sup>1,2</sup> , V.A. Yadrikhinsky<sup>1</sup> , A.E. Mestnikov<sup>1</sup> 

<sup>1</sup> North-Eastern Federal University, Yakutsk, Republic of Sakha (Yakutia), Russia

<sup>2</sup> Institute of Oil and Gas Problems of Siberian Branch of the Russian Academy of Sciences, Yakutsk, Republic of Sakha (Yakutia), Russia

✉ [surrukin@gmail.com](mailto:surrukin@gmail.com)

**Keywords:** frost resistance, freeze thawing, binders, hydration, cement, zeolite, compressive strength, concretes, nondestructive methods

**Abstract.** The work is directed to the researches of composite binders, especially their strength properties in conditions of negative temperatures. Since the slowing down of concrete hardening with the addition of pozzolanic additives limits the possibility of using composite binders in regions with a short period of positive temperatures, a whole area of scientific works fails to find its application. The article presents the results on the determination of strength properties and hydration processes in cement stone with pozzolanic additive from natural zeolite during freezing and thawing. In determining the strength of the cement stone we chose the method of ultrasonic penetration. Graduation dependence of strength on the time of ultrasound propagation was revealed for its correct application. It allowed us to obtain dependences of cement stone strength with different amounts of additives on cycles of alternate freezing and thawing. The obtained results made it possible to get information on frost resistance of different compositions of the binders. It was shown that the addition of 30 wt. % and more of ground natural zeolite into Portland cement slows down the destructive effect of freezing-thawing due to unfinished hydration processes, which leads to an increase in the critical number of freezing-thawing cycles and the Portland cement frost-resistance grade from F300 to F400, respectively.

**Citation:** Popov, A.L., Yadrikhinsky, V.A., Mestnikov, A.E. Peculiarities of hydration and frost resistance of cement with natural zeolite additive. Magazine of Civil Engineering. 2023. 117(1). Article no. 11711. DOI: 10.34910/MCE.117.11

### 1. Introduction

All over the world, there is a lot of experience in the use of composite binders, including cements with various mineral additives. However, their effective use in construction in cold climates is severely limited by temperature parameters, forcing to increase the cost of construction works by resorting to various additional technologies to control the curing conditions [1–3], while there are no attempts to increase the hydration capacity of binders in cyclic freezing and thawing. Thus, research is needed to improve the frost resistance of concrete binders and to expand the temperature conditions of their hardening.

It is a known fact that a low positive temperature slows down the process of setting and gaining strength of concrete, and then the negative temperature stops it completely. At negative temperatures, it is impossible to perform concrete work, because glaciated water at 0 °C is not able to bind with the cement. Thus, the hydration processes in concrete responsible for strength gain are stopped [4–7]. For example, at an ambient temperature of –15 °C, even taking into account the preheating of the concrete mixture to 60 °C,

in less than 60 hours the temperature of 200 mm thick concrete drops below zero throughout its entire thickness [8].

Because of this fact, the organization of construction work is carried out mainly in the period of positive temperatures, which, depending on the region of construction can be quite short. In this case, a well-known fact that Portland cement reaches natural strength within 28 days after mixing with water, which introduces its own limitations on the duration of concrete work, which should be carried out before the onset of sub-zero temperatures. In this regard, it becomes undesirable to use such new developments as mixed cements, which due to their pozzolanic properties slow down the process of setting the strength of concrete [9–12].

Thus, the retardation of hydration processes, typical for some composite binders, limits the possibility of their use in conditions of rapid onset of negative temperatures. Because of this fact in regions with a short period of positive temperatures the whole area of scientific developments dedicated to composite binders is not practically applied [13–20]. On this basis, studies that study the behavior of composite binders, namely their pozzolanic and hydration properties in conditions of negative temperatures are relevant.

The aim of the research is to establish the features of hardening processes and frost resistance of Portland cement with natural zeolite additive. As the first step to achieve this goal, the task of studying the process of changing the strength of cement stone during freezing-thawing cycles has been set. As a method of determining the strength is used ultrasonic screening method.

## 2. Materials and Methods

Portland cement of CEM I 32.5H grade produced by Yakutcement JSC (Mokhsogolokh, Russia) was used for the tests (Table 1). Ground natural zeolite produced by Suntarzeolite LLC (Suntar, Russia), an enterprise producing and enriching natural zeolite, was used as a pozzolanic additive. Properties of the additive are given in Table 2.

**Table 1. Properties of Portland cement CEM I 32.5H (JSC "Yakutcement").**

Indicator	Value
Normal density, %	25
Residue on sieve 008, %	7.0
Uniformity of volume change, mm	0.11
Timing of setting:	
– start, hr-min	2–35
– end, hour-minutes	3–55
Average activity of cement at the age of 28 days, MPa	40.95

**Table 2. Properties of pozzolanic additive – ground natural zeolite.**

Indicator	Value
ulk density, kg/m <sup>3</sup>	1420
True density, kg/m <sup>3</sup>	1780
Specific surface, m <sup>2</sup> /kg	3000
Activity towards CaO, mg/g	76.6
Quality factor as a component of the composite binder*	1.16

Samples of Portland cement with pozzolanic additive in the amount of 10, 30 and 50 % (instead of cement by mass) were made in the form of cubes 70×70×70 mm without using large and small aggregates according to interstate standard GOST 10180-2012 Concretes. Methods for strength determination using reference specimens. The number of samples in the series was 3 pieces. All samples in the series were made from the same sample of the cement mixture, with the same molding and hardening conditions. After the end of hardening, all samples are tested at the same age.

The molding and compaction of cement mixtures into molds was carried out manually using baying. Forms are filled with cement mix in 3 layers no more than 30 mm. Each layer is sealed by baying with a steel rod 16 mm in diameter with a rounded end.

Samples intended for hardening under normal conditions, after manufacturing before they are stripped, are stored in molds covered with a damp cloth, which excludes the evaporation of moisture from them, in a room with an air temperature of (20±5) °C. After stripping, the samples are placed in a chamber

with normal hardening conditions: temperature (20±2) °C and relative humidity (95±5) %. A schematic representation of the temperature regime of the medium of one cycle-freeze-thaw is shown in Fig. 1.

Before testing, the samples were kept for 4 hours at a temperature of (20±5) °C and a relative air humidity of at least 55 %.

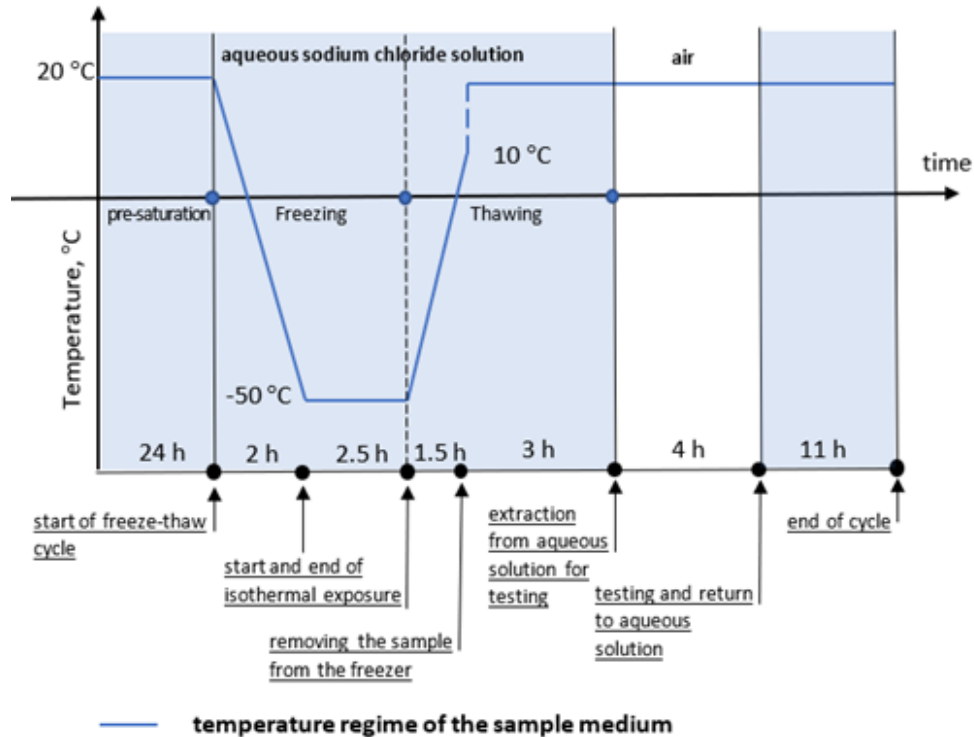


**Figure 1. Schematic representation of the temperature regime of the medium of one cycle-freeze-thaw.**

Ultrasonic measurement of the strength of the obtained cement stones were carried out with the device "Pulsar" according to the interstate standard GOST 17624-2012 Concrete. Ultrasonic method of strength determination.

Before testing specimens, calibration dependence "time of ultrasound spreading – strength" on the basis of specimen series of each binder composition was established. Graduation dependence was established according to formula 1 for specimens on day 28 of hardening.

$$R = a_1 \times t + a_0, \quad (1)$$

where,  $R$  is the strength of the sample according to the ultrasonic measurement, MPa;  $t$  is the time of ultrasound propagation according to the ultrasonic measurement,  $\mu\text{s}$ ;  $a_1$  and  $a_0$  is the calibration coefficients determined according to formulas 2 and 3.

$$a_1 = \frac{\sum_{j=1}^N (\bar{R}_f - R_{jf}) (\bar{t} - t_j)}{\sum_{j=1}^N (\bar{t} - t_j)^2}; \quad (2)$$

$$a_0 = \bar{R}_f - a_1 \times \bar{t}, \quad (3)$$

where,  $N$  is the number of samples in the series;  $\bar{R}_f$  is the average actual compressive strength of samples in  $N$  series of samples, MPa;  $\bar{t}$  is the average time of ultrasound propagation in  $N$  series of samples,  $\mu\text{s}$ ;  $R_{jf}$  and  $t_j$  is the single value of strength and ultrasound propagation time for  $j$  sample in the series.

Determination of frost resistance of cement stone samples was carried out in accordance with the interstate standard GOST 26134-2016 Concretes – Ultrasonic method of frost resistance determination.

The method for determining frost resistance is to determine the critical number of cycles of freezing and thawing ( $M$ ) using the breakpoint ( $K$ ) corresponding to a sharp increase in the spread of ultrasound after a certain number of cycles of freeze-thaw, determined on the logarithmic graph  $(N - N_m) - (t - t_m)$ , where  $t$  is the total value of ultrasound propagation time through 4 channels of one sample,  $t_m$  is the lowest value of the total ultrasound propagation time,  $N$ ,  $N_m$  is the corresponding freeze-thaw cycles. The breaking point is determined by the point of intersection of the linear dependence graphs of two groups of corresponding points – before and after a sharp increase in the ultrasonic propagation time. In this case, the very definition of the breaking point is carried out through a system of equations and substitution of one equation into another. Thus, critical number of freezing and thawing cycles will be determined according to formula (4).

$$M = N_m + K. \quad (4)$$

One cycle of freezing-thawing of samples corresponded to freezing in closed containers filled with 5 % aqueous sodium chloride solution at  $-50\text{ }^\circ\text{C}$  for 2.5 hours and subsequent thawing for 2.5 hours at  $+20\text{ }^\circ\text{C}$ , after which the ultrasound propagation time was measured.

### 3. Results and Discussion

Tests were carried out to determine physical and mechanical characteristics of cement stone samples based on Portland cement with pozzolanic additive in the amount of 10, 30 and 50 % (instead of cement by mass) in the form of  $70 \times 70 \times 70$  mm cubes (Table 3). The dosages were chosen based on the results of earlier studies on the rational content of mineral components in concretes and a review of the scientific literature [21–23]. Increase in addition of ground natural zeolite leads to reduction of average density of samples and water absorption index. Also, a decrease in the specific amount of Portland cement in the samples leads to a decrease in the strength of the samples at 28 days, which may be due to the fact that natural zeolite minerals show their pozzolanic activity in the late stages of hardening. This fact was also shown in the works of researchers from the Bulgarian Academy of Sciences, who found a decrease in the specific pore volume between samples with the addition of natural zeolite aged 28 days and 180 days, due to new formations that have arisen as a result of pozzolanic reactions [24]. In addition, Turkish researchers found, using EDX analysis, unreacted zeolite minerals in their mixed samples on the 28<sup>th</sup> day of hardening, and it is also said that a significant contribution of the pozzolanic effect to the strength of cement stones is achieved with large dosages of additives from natural zeolite [25].

**Table 3. Physical and mechanical characteristics of cement stone samples of different compositions.**

Binder composition	Average mass, kg	Average density, $\text{kg/m}^3$	Natural humidity, %	Water absorption, %	Average compressive strength at 28 days of age, MPa
Pure Portland cement	0.718	2093	2.7	4.4	29.1
Portland cement with the addition of 10% ground natural zeolite	0.692	2017	2.9	5.8	21.1
Portland cement with the addition of 30% ground natural zeolite	0.646	1883	3.6	7.7	26.8
Portland cement with the addition of 50% ground natural zeolite	0.643	1875	3.6	8.1	24.1

To establish the calibration dependence "ultrasound propagation time – strength" the average values of actual compressive strength and ultrasound propagation time of a preliminary series of samples from each composition were determined. Then calibration coefficients  $a_1$  and  $a_0$  were determined according to formulas 2 and 3. Because of small sample quantity and its description by linear dependence the value of approximation reliability is not high and makes 0.87.

**Table 4. Establishment of the graduation dependence "time of ultrasound propagation – strength".**

Binder composition	$R_{jf}$ , MPa	$t_j$ , $\mu$ s	$\bar{R}_f$ , MPa	$\bar{t}$ , $\mu$ s	$a_1$	$a_0$
Pure Portland cement	32.30	19.85	25.29	21.31	-2.99066109	89.01907188
	25.95	20.96				
Portland cement with the addition of 10% ground natural zeolite	21.99	22.32				
	26.27	22.10				
Portland cement with the addition of 30% ground natural zeolite	31.18	19.53				
	22.37	19.99				
Portland cement with the addition of 50% ground natural zeolite	21.49	22.67				
	20.79	23.04				

After the graduation dependence has been established, 13 cycles of freezing and thawing of samples of each composition have been performed, after each of which the mean values of parallel tests of ultrasound propagation time have been determined (Table 5, Fig. 2) and strength characteristics have been calculated by formula 1 (Table 6, Fig. 3). In spite of the low reliability of the certain dependence approximation, the strength of the cured pure Portland cement stone before freezing is quite consistent with the declared strength of CEM I 32.5H. Also, immediately after the first cycle of freezing-thawing the strength of Portland cement without the addition of ground natural zeolite begins to decrease, indicating that the images have reached their maximum strength and undergo destruction in the process of freezing-thawing. When ground natural zeolite is added to Portland cement the strength of obtained cement stone keeps growing during freeze-thaw cycles. Thus, after addition of 10 % of ground natural zeolite after the 1<sup>st</sup> cycle the strength of obtained cement stone increases by 4 %, and after the 3<sup>rd</sup> cycle it decreases by 1 % after every 2<sup>nd</sup> cycle of freezing-thawing. When ground natural zeolite is added 30 % and 50 % to Portland cement, the peak strength of cement stone samples is achieved after the 3<sup>rd</sup> cycle of freeze-thawing and amounts to 113 % of 28 day strength, and the decrease of strength after the 5<sup>th</sup> cycle occurs more intensively – about 4 % every 2 cycles. Thus, delayed strength growth of binders with the addition of natural zeolite makes it possible to increase the strength of cement stone damaged by freezing and thawing cycles. Not the last role in the continuation of the strength gain of the samples is assigned to the conditions of freezing-thawing of the samples. Freezing and thawing does not occur instantly in containers with an aqueous solution of sodium chloride, and during positive temperatures of the set mode (Fig. 1), incomplete pozzolanic reactions continue, provided that ground natural zeolite is added. Based on the above, the conclusions of the work of the authors from Southeast University [26] are supplemented, on the possibility of standard curing of concretes damaged by freeze-thaw cycles at an early age, in our case, standard curing continues in the later stages of hardening, provided that the cement contains a pozzolanic additive.

**Table 5. Time of ultrasound propagation through cement stone of different composition depending on freezing and thawing cycles.**

Number of freeze-thaw cycles	0	1	3	5	7	9	11	13
Pure Portland cement	18.82	18.96	19.04	19.05	19.21	19.31	19.43	19.53
Portland cement with the addition of 10% ground natural zeolite	19.75	19.34	19.43	19.51	19.82	19.91	20.10	20.19
Portland cement with the addition of 30% ground natural zeolite	21.66	21.31	20.57	21.15	21.36	21.69	21.85	22.32
Portland cement with the addition of 50% ground natural zeolite	21.93	21.07	20.83	21.33	21.52	21.76	21.91	22.26

**Table 6. Strength of cement stone of different compositions as a function of freezing and thawing cycles.**

Number of freeze-thaw cycles	0	1	3	5	7	9	11	13
Pure Portland cement	32.74	32.32	32.08	32.04	31.57	31.27	30.90	30.60
Portland cement with the addition of 10% ground natural zeolite	29.94	31.18	30.90	30.66	29.74	29.48	28.91	28.64
Portland cement with the addition of 30% ground natural zeolite	24.23	25.28	27.49	25.78	25.13	24.15	23.67	22.27
Portland cement with the addition of 50% ground natural zeolite	23.44	26.00	26.71	25.23	24.66	23.95	23.50	22.45

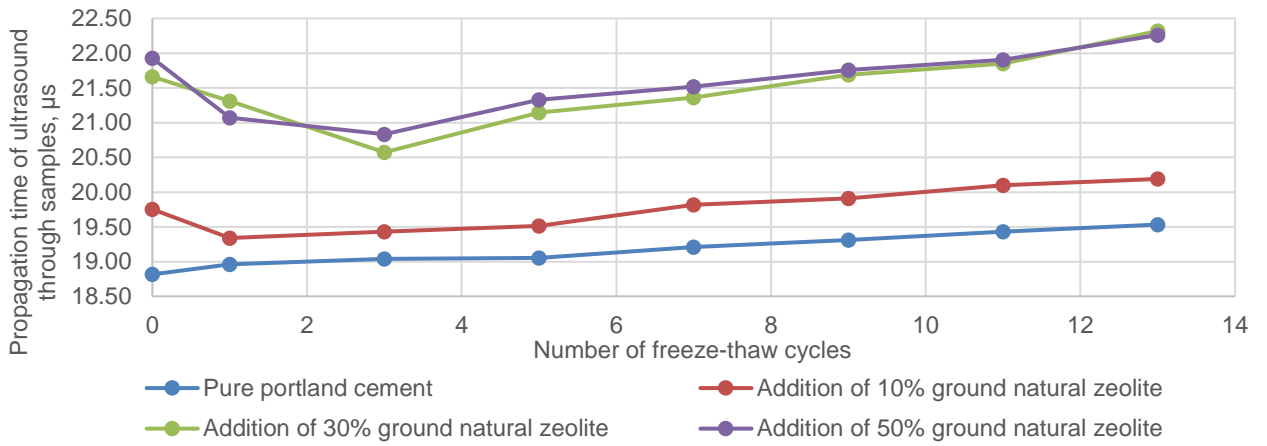


**Figure 2. Time of ultrasound propagation through cement stone of different compositions as a function of freezing and thawing cycles.**

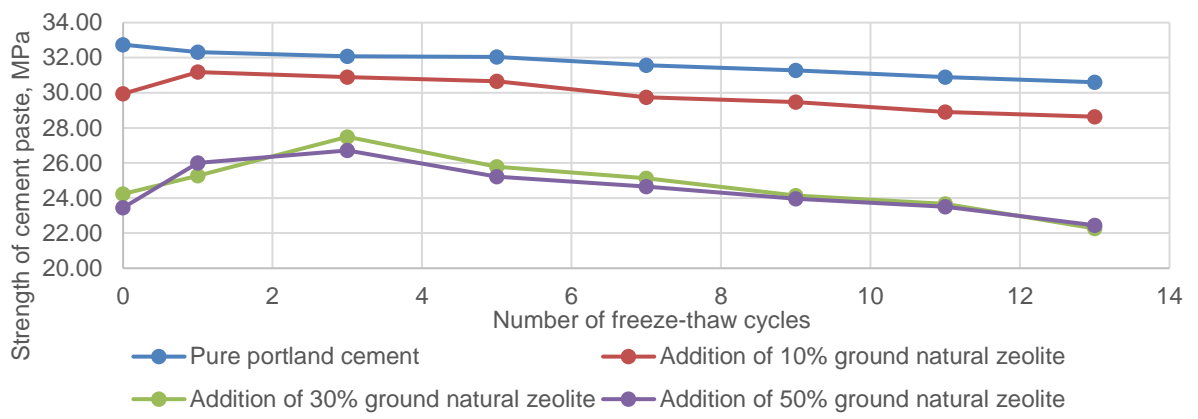


**Figure 3: Strength of cement stone of different compositions as a function of freezing and thawing cycles.**

In order to determine frost resistance of cement stone samples of each binder composition according to the interstate standard GOST 26134-2016, on logarithmic diagrams  $(N - N_m) - (t - t_m)$  the changes of average total values of ultrasound spreading time through 4 channels of samples sounding have been plotted versus the minimum fixed value taken as  $t_m$  and corresponding to it freeze-thaw cycles value –  $N_m$  (Fig. 4–7). The obtained points are divided into two groups of corresponding points – before and after sharp increase of ultrasound propagation time, linear dependences for each group of points are found by regression method.

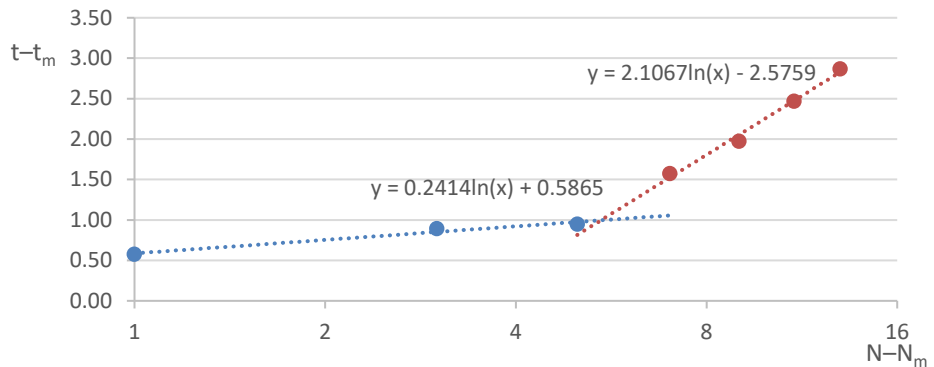


**Figure 4: Graph of ultrasonic measurements of pure Portland cement.**

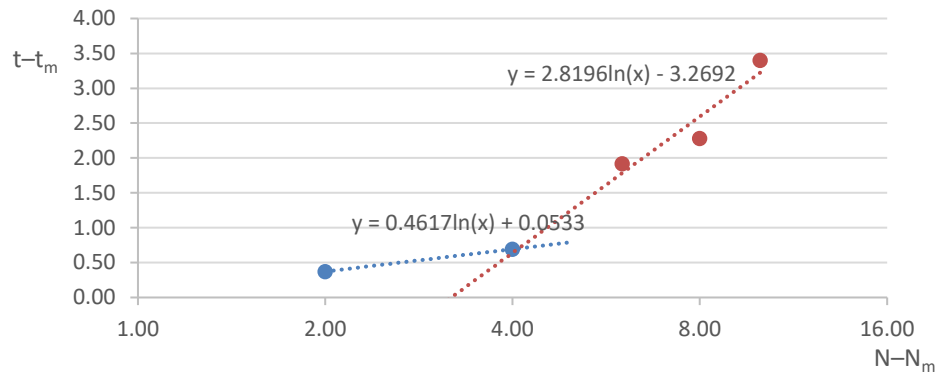


**Figure 5. Graph of ultrasonic measurements of Portland cement with the addition of 10 % ground natural zeolite.**

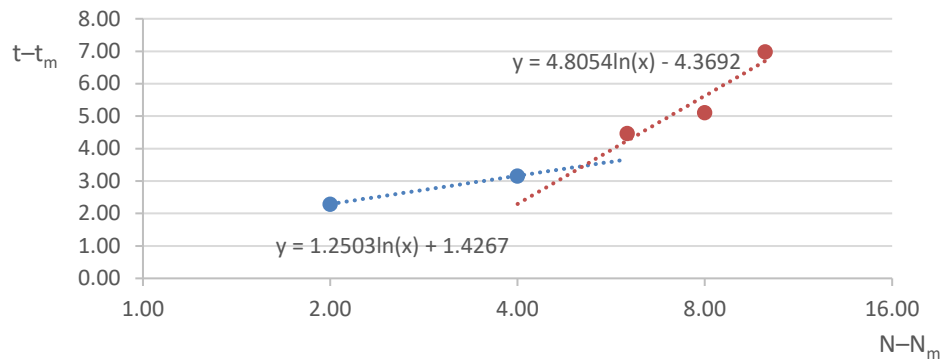


**Figure 6: Graph of ultrasonic measurements of Portland cement with the addition of 30 % ground natural zeolite.**

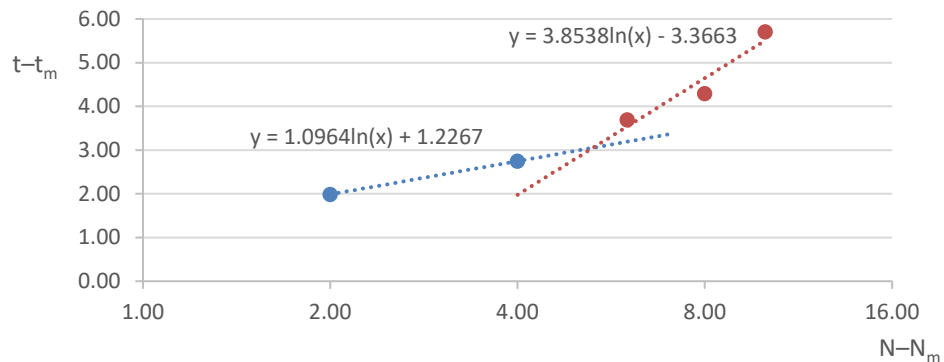


**Figure 7. Graph of ultrasonic measurements of Portland cement with the addition of 30 % ground natural zeolite.**

The given equations are used for determining breaking points ( $K$ ), values of critical number of freezing-thawing cycles ( $M$ ), after which there is a sharp increase of ultrasound spreading time in the sample and corresponding index of frost-resistance grade according to GOST 26134-2016 for each binder composition (Table 7). The addition of 30 % or more of ground natural zeolite into Portland cement results in increase of critical number of freeze-thaw cycles, due to which freeze-thaw resistance grade of cement increases from F<sub>1</sub>300 to F<sub>1</sub>400. Adding a smaller amount of additive does not change the critical number of freeze-thaw cycles. Thus, the introduction of pozzolanic additive in the form of natural zeolite can increase the long-term strength of the cement stone, which leads to an increase in frost resistance. Thus, the introduction of a pozzolanic additive in the form of natural zeolite makes it possible to increase the long-term strength of the cement stone, which leads to an increase in frost resistance, which is consistent with the studies of Chinese scientists, who also noted that frost resistance may not depend on the degree of concrete strength [27].

**Table 7. Data on the frost resistance of cement stone of different compositions.**

Number of freeze-thaw cycles	$t_m$	$N_m$	$K$	$M$	Mark frost resistance
Pure Portland cement	75.27	0	5.45	5	F <sub>1300</sub>
Portland cement with the addition of 10% ground natural zeolite	77.36	1	4.09	5	F <sub>1300</sub>
Portland cement with the addition of 30% ground natural zeolite	82.29	3	5.11	8	F <sub>1400</sub>
Portland cement with the addition of 50% ground natural zeolite	83.33	3	5.28	8	F <sub>1400</sub>

#### 4. Conclusion

Thus, the process of changing the strength of cement stone during freeze-thaw cycles has been studied on the basis of which the following was established:

1. Graduation dependence "time of ultrasound spreading - strength" with reliability of approximation 0.87 has been revealed. This allowed us to obtain dependences of cement-stone samples durability with different amount of additives on cycles of alternate freezing and thawing.

2. A delayed growth of the strength of binders with natural zeolite addition allows you to continue to gain strength of cement stonedamaged by cycles of freezing and thawing. Thus, if pure cement is characterized by strength reduction after the first cycle, then in case of addition of ground natural zeolite the strength keeps growing in spite of being exposed to freezing-thawing cycles. The addition of 10 % of ground natural zeolite causes strength to decrease after the 3<sup>rd</sup> cycle, and 30 % and 50 % after the 5<sup>th</sup> cycle.

3. The increase of long term strength of cement stone by adding natural zeolite, results in increase of frost resistance. The addition of 30 % or more of ground natural zeolite into Portland cement results in increase of critical number of freeze-thaw cycles, due to which increase of cement stone frost-resistance grade from F<sub>1300</sub> to F<sub>1400</sub> is possible. Adding a smaller amount of additive does not change the critical number of freeze-thaw cycles. This fact is associated with longer processes of pozzolanic reactions that go beyond the generally accepted cement hydration rate of 28 days. Moreover, a larger amount of natural zeolite makes it possible to maintain the strength growth of the damaged cement stone with a large number of freeze-thaw cycles.

#### References

1. Imaykin, D.G., Ibragimov, R.A., Evstigneeva, Y.V. Perfecting Technology of Winter Concreting of Cast-in-Situ Columns. IOP Conference Series: Materials Science and Engineering. 2019. 687. 044013.
2. Yudina, A., Oganyan, R. Technology Of Winter Concreting Of Monolithic Constructions With Application Of Heating Cable. Architecture and Engineering. 2017. 2. Pp. 43–48.
3. Tzarenko, A., Yurgaytis, A. Possibilities for Intensifying Construction Work's Dynamic on Objects of the Annual Production Program by Winter Concreting Technology. IOP Conference Series: Materials Science and Engineering. 2020. 753. 032072.
4. Mazur, B., Kotwa, A. Influence of Low Temperature on Concrete Properties. IOP Conference Series: Materials Science and Engineering. 2019. 471. 032026.
5. Rubene, S., Vilnitis, M. Impact of Low Temperatures on Compressive Strength of Concrete. International Journal of Theoretical and Applied Mechanics. 2017. 2. Pp. 97–101
6. Hafiz, M.A., Skibsted, J., Denarié, E. Influence of Low Curing Temperatures on the Tensile Response of Low Clinker Strain Hardening UHPFRC under Full Restraint. Cement and Concrete Research. 2020. 128. 105940.
7. Alzaza, A., Ohenoja, K., Langås, I., Arntsen, B., Poikelispää, M., Ilikainen, M. Low-Temperature (–10 °C) Curing of Portland Cement Paste – Synergetic Effects of Chloride-Free Antifreeze Admixture, C–S–H Seeds, and Room-Temperature Pre-Curing. Cement and Concrete Composites. 2022. 125. 104319.
8. Ju Shelehov, I., Dorofeeva, N.L., Shelehov, M.I., Dorofeev, I.A. Optimization of Concrete Works Technological Process in the Winter Period. IOP Conference Series: Earth and Environmental Science 2021. 751. 012080.
9. Zhao, J., Li, D., Liao, S., Wang, D., Wang, H., Yan, P. Influence of Mechanical Grinding on Pozzolanic Characteristics of Circulating Fluidized Bed Fly Ash (CFA) and Resulting Consequences on Hydration and Hardening Properties of Blended Cement. Journal of Thermal Analysis and Calorimetry. 2018. 132. Pp. 1459–1470.
10. Cizer, O., van Balen, K., van Gemert, D., Elsen, J. Hardening of Mortars Made from Cement, Rice Husk Ash and Lime. Proceedings of the Institution of Civil Engineers – Construction Materials. 2009. 162 (1). Pp.19–27.
11. Uppalapati, S., Vandewalle, L., Cizer, Ö. Monitoring the Setting Process of Alkali-Activated Slag-Fly Ash Cements with Ultrasonic P-Wave Velocity. Construction and Building Materials. 2020. 271. 121592.
12. Zhang, D., Zhao, J., Wang, D., Wang, Y., Ma, X. Influence of Pozzolanic Materials on the Properties of Natural Hydraulic Lime Based Mortars. Construction and Building Materials. 2020. 244. 118360.
13. Vasileva, D., Protodiakonov, E., Egorova, A., Antsupova, S. Modifying Admixtures to Cement Compositions Produced from Local Raw Materials. MATEC Web of Conferences. 2018. 143. 02006.

14. Fediuk, R., Lesovik, V., Liseitsev, Y., Timokhin, R., Bituyev, A., Zaiakhanov, M., Mochalov, A. Composite Binders for Concretes with Improved Shock Resistance. *Magazine of Civil Engineering*. 2019. 85. Pp. 28–38.
15. Nelubova, V.V., Hou, P., Strokova, V.V., Singh, L.P., Netsvet, D.D., Bondarenko, D.O. Complex Study of Modified Binder Properties. *Proceedings of the International Conference "Actual Issues of Mechanical Engineering" 2017 (AIME 2017)*. Tomsk, 2017. Pp. 543–548.
16. Alfimova, N.I., Gridchin, A.M., Glagolev, E.S., Lesovik, R.V., Levchenko, O.V., Pirieva, S.I. Effective Composite Binders. *Proceedings of the International Conference "Actual Issues of Mechanical Engineering" 2017 (AIME 2017)*. Tomsk, 2017. Pp. 42–47.
17. Lesovik, V., Voronov, V., Glagolev, E., Fediuk, R., Alaskhanov, A., Amran, Y.H.M., Murali, G., Baranov, A. Improving the Behaviors of Foam Concrete through the Use of Composite Binder. *Journal of Building Engineering*. 2020. 31. 101414.
18. Liu, S., Wang, L., Li, Q., Song, J. Hydration Properties of Portland Cement-Copper Tailing Powder Composite Binder. *Construction and Building Materials*. 2020. 251. 118882.
19. Han, F., Zhang, Z., Wang, D., Yan, P. Hydration Kinetics of Composite Binder Containing Slag at Different Temperatures. *Journal of Thermal Analysis and Calorimetry*. 2015. 121. Pp. 815–827.
20. Han, F., Zhang, Z., Liu, J., Yan, P. Effect of Water-to-Binder Ratio on the Hydration Kinetics of Composite Binder Containing Slag or Fly Ash. *Journal of Thermal Analysis and Calorimetry*. 2017. 128. Pp. 855–865.
21. Popov, A.L., Strokova, V.V., Mestnikov, A.E. Analysis of the quality of quartz-feldspar sand as a component of a composite binder. *Key Engineering Materials*. 2021. 887. Pp. 516–520.
22. Akgün, Y., Yılmaz, T. Thermal performance of mortars/concretes containing analcime. *Journal of Thermal Analysis and Calorimetry*. 2021. 146 (1). Pp. 47–60.
23. Nagrockiene, D., Girskas, G., Skripkiunas, G. Cement freezing-thawing resistance of hardened cement paste with synthetic zeolite. *Construction and Building Materials*. 2014. 66. Pp. 45–52.
24. Lilkov, V., Rostovsky, I., Petrov, O. Physical and Mechanical Characteristics of Cement Mortars and Concretes with Addition of Clinoptilolite from Beli Plast Deposit (Bulgaria), Silica Fume and Fly Ash. *Clay Minerals*. 2011. 46. Pp. 213–223.
25. Uzal, B., Turanlı, L. Blended Cements Containing High Volume of Natural Zeolites: Properties, Hydration and Paste Microstructure. *Cement and Concrete Composites*. 2012. 34. Pp. 101–109.
26. Liu, D., Tu, Y., Sas, G., Elfgrén, L. Freeze-Thaw Damage Evaluation and Model Creation for Concrete Exposed to Freeze–Thaw Cycles at Early-Age. *Construction and Building Materials*. 2021. 312. 125352.
27. Peng, G.F., Ma, Q., Hu, H.M., Gao, R., Yao, Q.F., Liu, Y.F. The Effects of Air Entrainment and Pozzolans on Frost Resistance of 50-60 MPa Grade Concrete. *Construction and Building Materials*. 2007. 21. Pp. 1034–1039.

**Information about authors:**

**Aleksandr Popov**, PhD in Technical Science

ORCID: <https://orcid.org/0000-0002-7829-6839>

E-mail: [surrukin@gmail.com](mailto:surrukin@gmail.com)

**Vasily Yadrikhinsky**,

ORCID: <https://orcid.org/0000-0002-3516-1440>

E-mail: [vasilyyad@gmail.com](mailto:vasilyyad@gmail.com)

**Alexey Mestnikov**, Doctor of Technical Science

ORCID: <https://orcid.org/0000-0003-4522-0296>

E-mail: [mestnikovae@mail.ru](mailto:mestnikovae@mail.ru)

Received 11.03.2022. Approved after reviewing 02.08.2022. Accepted 05.08.2022.



Research article

UDC 625.856

DOI: 10.34910/MCE.117.12



## Stone mastic asphalt modified with stabilizing additives of multifunctional action

A.Yu. Fomin<sup>1</sup> , E.R. Hafizov<sup>1</sup>  , E.A. Vdovin<sup>1</sup> , F.R. Fafanov<sup>2</sup> 

<sup>1</sup> Kazan State University of Architecture and Engineering, Kazan, Russia

<sup>2</sup> OOO Rettenmeier RUS, Moscow, Russia

 [edward\\_76@bk.ru](mailto:edward_76@bk.ru)

**Keywords:** stone mastic asphalt, stabilizing additive, asphalt mixtures, strength, mechanical properties

**Abstract.** The paper presents the results of studies of the physicomaterial properties of stone mastic asphalt (SMA) with the use of stabilizing additives of multifunctional action aimed at increasing the strength characteristics of SMA, resistance to plastic deformations, increase in shear stability of asphalt concrete, as well as reduction of the negative impact of technological temperatures on oil bitumen contributing to its oxidation and premature aging in the production of asphalt mixes. The structure of bitumen modified with composite thermoplastic elastomer was studied by nuclear magnetic resonance. For experimental verification of the effectiveness of additives in the composition of SMA, standard methods used for all types of asphalt concrete were applied and the following indicators of physical and mechanical properties were studied: compressive strength, water saturation, shear resistance, abrasion, resistance to plastic deformation. The results of studies of physical and mechanical properties of SMA grades 10 and 15 containing additives of the Viatop Plus CT40 and Viatop Plus FEP series showed that the values of compressive strength at 20 and 50 °C exceed similar indicators of properties of SMAs with the use of a stabilizing additive Viatop 66 considered as control compositions.

**Citation:** Fomin, A.Yu., Hafizov, E.R., Vdovin, E.A., Fafanov, F.R. Stone mastic asphalt modified with stabilizing additives of multifunctional action. Magazine of Civil Engineering. 2023. 117(1). Article no. 11712. DOI: 10.34910/MCE.117.12

### 1. Introduction

During the last 17 years, stone mastic asphalt have been widely used in Russia when arranging pavements with high load-bearing stresses, considering their high transport and operational performance (roughness), and resistance to external influences (water resistance, shear resistance) [1, 2]. The experience of using stone mastic asphalt in the Republic of Tatarstan in Russia is more than 15 years. Fig. 1 shows the kinetic dependence of the output volumes of the main types of asphalt concrete mixtures in the Republic of Tatarstan: SMA, type B grade II, produced in accordance with Russian State Standard 9128, as well as other types of asphalt concrete.

An analysis of the above dependence shows that SMA production is relatively high and averages 90.5 thousand tons per year.

Currently, road manufacturing enterprises are developing the release of SMA according to new standards. So, in 2017, the Volgadorstroy LLC asphalt concrete plant organized the production of SMA-19 asphalt concrete designed in accordance with PNST (preliminary national standard) 127-2016. When developing the composition of SMA-19, they use bituminous binders that take into account the temperature range of operation of the road surface and the characteristics of traffic loads for each particular construction project or repair. SMA-19 was used in the repair of the transport interchange of the M-7 Volga highway in

Zelenodolsky district of the Republic of Tatarstan, as well as in the repair of the roadway section of Kulakhmetov Street in Kazan, Russian Federation. Also on the main streets in the cities of the Republic of Tatarstan and the supporting network of regional roads carried out repair work with the application in the top coat of asphalt mix SMA-20 on polymer-bitumen binder, which improves their durability.

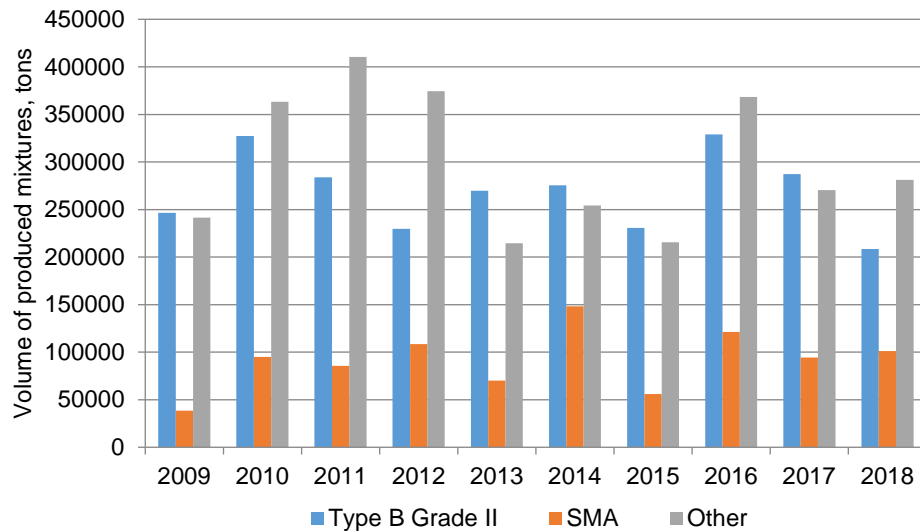


**Figure 1. Kinetic dependence of the output of asphalt mixtures.**

SMA was developed in Germany in 1966, and since 1970 it has been widely used in the upper layers of road surfaces with high traffic density and is an independent type of asphalt concrete [3–6].

SMA is characterized by an increased content of gravel and bitumen (up to 80 % and 7.5 % by weight, respectively) and residual porosity of up to 1%. Studies show that the coefficient of internal friction  $t_g$  largely depends on the grain composition of the mixture. When designing the composition of SMA, it should be borne in mind that a greater effect in the fight against rutting is provided by a stable gravel frame rather than the increased viscosity of the bitumen used [7]. To keep free bitumen on the gravel surface, at the stage of road construction, it is necessary to introduce fibrous stabilizing additives into the mixture [8]. So, in the SMA production practice, additives of the brands Viatop, TOPCEL and others, which are granular material containing cellulose fiber and organic components, have most widely proven themselves [9–12]. The stabilizing additives based on fibrous industrial waste have been widely studied as well [13–16].

The results of research [17] showed that the introduction of 20 mm long fibers in the amount of 0.2 % of the mass of bitumen increases the cracking resistance of the bitumen, increases its structural strength and fatigue life.

In [18], the influence of various additives from the class of mineral fibers, cellulose fiber, styrene-butadiene-styrene (SBS) on the properties of SMA was studied, including an increase in the service life of asphalt concrete coatings, as well as a possible reduction in the thickness of coating layers. It was found that the service life of the modified mixture coating is 1.07, 1.081 and 1.243 times longer than that of the unmodified mixture, respectively.

In [19], it was shown that the introduction of nanoscale  $\text{SiO}_2$  and nano  $\text{TiO}_2$  particles in the amount of 1.2 % and 0.9 % of the bitumen mass, respectively, into the SMA mixture increases the strength of the SMA and fatigue life.

In [20] it was found that the introduction of polyethylene terephthalate (PET) as an additive in asphalt, in the amount of 4 %, 6 %, 8 % and 10 % by weight of the content of bitumen, increases the resistance of the latter to aging.

The influence of various types of aggregates (large and small basalt, large and small limestone, large basalt and small limestone) on the low-temperature characteristics and resistance to cracking of the lime is studied [21].

It was found [22] that the introduction of polyvinyl chloride waste and electric arc furnace dust into the SMA reduces the sensitivity of the SMA to moisture and increases the resistance to aging of asphalt binders, improves their tensile strength, water permeability and resistance to destruction of asphalt concrete mixtures.

A comparative analysis in [23] showed that the use of polymer-bitumen binder in the composition of SMA as well as fibers of natural origin (banana fibers) has a positive effect on the properties of the binder and asphalt concrete. Thus, the introduction of natural fibers increases the binder's resistance to aging and water and the fatigue strength SMA. At the same time, the mixtures modified with polymer additives require less energy for their compaction in comparison with the natural fiber SMA. Also, the effectiveness of using leather industry waste [24] and plastic bottles [25] as stabilizing additives in the composition of SMA has been established.

The purpose of this work was to study the indicators of physical and mechanical and operational and technical properties of stone mastic asphalt grade SMA-10 and 15, containing stabilizing additives multifunctional action brand Viatop series Plus, as well as the establishment of optimal technological factors for the preparation of new SMA.

To achieve this goal, the following tasks were adopted:

1. To make the comparative analysis of indicators of properties of SMA-10 and 15 containing additives Viatop Plus FEP and Viatop 66 defining their resistance to formation of plastic and shear deformations;
2. To make the comparative analysis of indicators of properties of SMA-10 and 15 containing the Viatop Plus CT40 additive and prepared at different temperature conditions (140 and 170 °C) and similar asphalt concretes containing the Viatop 66 additive.

## 2. Methods

Samples of gravel and mastic asphalt concrete were investigated in accordance with current regulatory documents. Conclusions on their quality are made in accordance with the requirements of current standards, as well as on the basis of construction codes.

For a comparative assessment of the physicomechanical properties of SMA grades 10 and 15 containing additives of the Viatop Plus CT40 and Viatop Plus FEP series, we used SMA of similar grades containing the Viatop 66 additive as control compositions.

The preparation of asphalt mixtures was carried out at various temperature conditions. So, mixtures with the addition of Viatop Plus FEP were prepared at a traditional temperature of 160–170 °C. Mixtures with the Viatop Plus CT40 additive were prepared both at a temperature of 160–170 °C and at 140 °C (by the warm method) in order to establish the effectiveness of the components included in the Viatop Plus CT40 additive and to obtain SMA-15 samples with the properties corresponding to the regulatory requirements.

Technical characteristics used to evaluate the quality of asphalt concrete were determined according to Russian State Standard 12801-98, Russian State Standard 31015-2002, PNST 181-2016, PNST 180-2016 test methods. To determine the physical and mechanical properties of SMA we used the necessary complex of standard equipment. The tests were carried out in the laboratory for testing road-building materials of the Test road scientific-production center of the Institute of Transport Constructions of Kazan State University of Architecture and Civil Engineering.

To determine the strength of the gravel mineral grains, we used: a hydraulic press P-50 according to Russian State Standard 9753-88 with a maximum load of 500 kN, with a force meter providing an error of not more than 2 % of the measured load, steel cylinders with a removable bottom and a plunger with an inner diameter of 75 and 150 mm, laboratory balance with measuring limits of 0.5 and 1 kg of the 4<sup>th</sup> accuracy class, a set of standard sieves with a diameter of 1.25; 2.5; 5.0; 10; 20 and 40 mm.

To determine the grain composition of mineral materials, we used: laboratory scales with measuring limits of 0.5 and 1 kg of the 4<sup>th</sup> accuracy class, a set of standard sieves with diameters from 0.14 to 40 mm.

To determine the bulk density of mineral materials we used laboratory scales according to Russian State Standard 24104, 4<sup>th</sup> accuracy class and vessels with a capacity of 3.0, 5.0 and 10.0 liters.

For the manufacture of SMA cylinder samples in accordance with Russian State Standard 12801-98, we used: a drying cabinet (SHSS – 80P), with a heating temperature of up to +200 °C, a vibrating platform, a hydraulic press P-50 according to Russian State Standard 9753-88 with an ultimate load of up to 500 kN with a force meter providing an error of not more than 2 % of the measured load, a press-out device for extracting asphalt concrete samples from cylindrical forms and other auxiliary equipment.

To determine the compressive strength of SMA samples, we used: an MGM 100 A test electronic machine with a measurement limit of up to 100 kN with a force meter providing an error of not more than 2 % of the measured load, mercury thermometers and vessels with a capacity of 3.0 to 10.0 liters, thermostat (TVB –18).

To determine the average density of SMA samples, laboratory scales were used according to Russian State Standard 24104 of the 3<sup>rd</sup> accuracy class with a device for hydrostatic weighing (BP 3100S).

To determine the water saturation and average density of SMA samples, we used: a vacuum unit (SHSV 45K), laboratory balance in accordance with Russian State Standard 24104, 3<sup>rd</sup> accuracy class with a device for hydrostatic weighing (BP 3100S), chemical mercury thermometers with a division value of 10 °C according to Russian State Standard 400, vessels with a capacity of 3.0; 5.0 and 10.0 liters.

To determine the abrasion of asphalt concrete samples, we used the VTI's Prall installation – a system that imitates wear of asphalt concrete pavement with studded tires. During testing, the abrasive effect on a cylindrical SMA specimen is reproduced by 40 steel spheres within 15 minutes.

To determine the resistance of asphalt concrete to plastic deformation, we used the Lintel L KNK-20 installation, which provides for the simultaneous testing of two samples and simulates the process of pavement deformation under the influence of multiple vehicle loads.

The material composition of the Viatop Plus FEP additive includes a polymer additive from the class of elastomers, therefore, the study of the structural and dynamic changes of bitumen in the presence of a polymer was of scientific interest. For comparative analysis, as an additive in this experiment, we used mixed thermoplastic elastomer (TEP) – a material from the class of elastomers that includes polymers: polyethylene, ethylene-propylene rubber and isoprene rubber. The dosage of the TEP additive in bitumen was 2.5–4 %. To study the structure of bitumen modified by TEP, the pulsed method of nuclear magnetic resonance (NMR) was used. The transverse relaxation times were measured by spin-spin relaxation methods on laboratory nuclear magnetic resonance spectrometers. The proton resonance frequency was 20.0 and 19.5 MHz. The duration of the  $\pi/2$  radio frequency pulse was 3  $\mu$ s. The settings were controlled by a computer; during measurements, digital signal accumulation was used.

### 3. Results and Discussion

The introduction of stabilizing additives into the bitumen leads to significant changes in the slope of the free induction decay (FID) and the value of spin-spin relaxation, as well as to changes in the populations of fast and slow relaxing components. The tangent of the tilt angle of the fast and slow relaxing components of the FID differ by about 5 times. Qualitatively, we can conclude that the slowly relaxing component is determined by the mobility of low – molecular components of the system, and the rapidly relaxing component is determined by the mobility of high-molecular components.

Based on the analysis of FID, the values of spin – spin relaxation times and population of the two decay components were estimated (Figs. 2, 3).

It was found that the introduction of the TEP additive leads to a shortening of the relaxation time of the slowly relaxing T2A component (Fig. 2). This effect is especially noticeable at high temperatures, when the mobility and time of spin-spin relaxation should increase. The introduction of TEP in bitumen inhibits the development of molecular mobility of low molecular weight components. In the temperature range of 50–60 °C, a break in the temperature dependences is observed. The location of this fracture, which characterizes the defrosting of molecular mobility, turns out to be significantly higher than the similar fracture for the initial bitumen at 44 °C. This means that the introduction of the TEP additive leads to an increase in the softening temperature of the material (thawing of the translational motion modes) and, accordingly, the heat resistance of asphalt concrete.

In Fig. 3 shows the dependence characterizing the relaxation of macromolecular components in the system. From the figure, it follows that additives of the TEP series also affect high molecular weight components in bitumen.

Thus, the data obtained by the NMR method made it possible to directly confirm that the addition of mixed TEP substantially inhibits the molecular mobility of bitumen, providing a potential increase in the heat resistance of asphalt concrete. The results suggest that the polymer additive that is part of the Viatop Plus FEP additive likewise has a positive effect on bitumen and on asphalt concrete modified with this additive, in the form of an increase in its heat resistance and strength. The latter was reflected in the study of physical and mechanical properties SMAs.

Analysis of the dependences of the physical and mechanical properties of SMA-10 showed that the introduction of additives of the Viatop Plus CT40 and Viatop Plus FEP series in the composition of the mixture improves the compressive strength of SMA at 20 °C (R20) by 12–26 %. The strength index at 50 °C (R50) is increased by 5 and 55 % for mixtures containing the additive Viatop Plus FEP and Viatop Plus CT40, respectively (Fig. 4). The increase in strength characteristics at positive temperatures is consistent with the studies of bitumen with additives of stabilizing additives of the Viatop Plus CT40 and Viatop Plus FEP series by NMR.

Thus, an increase in strength characteristics with positive ones is consistent with the results of studies of bitumen with a polymer additive by NMR.

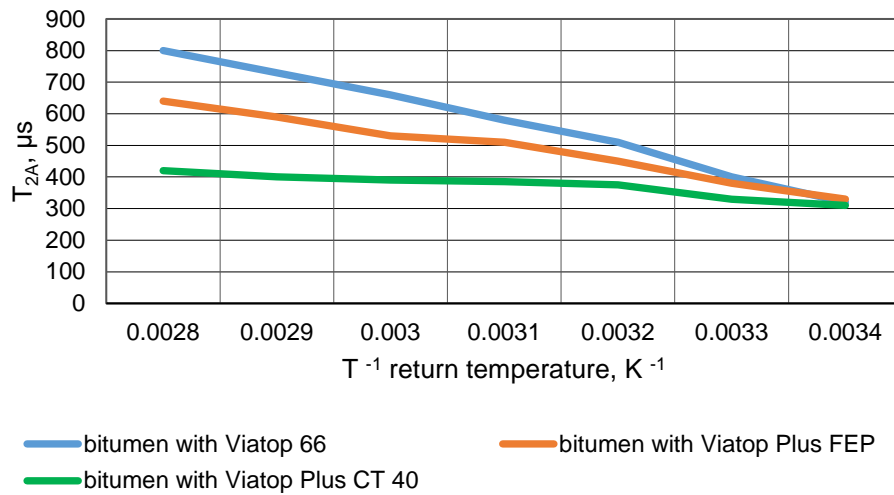


**Figure 2. Dependence of the spin-spin relaxation time of the slowly relaxing  $T_{2A}$  component on temperature.**

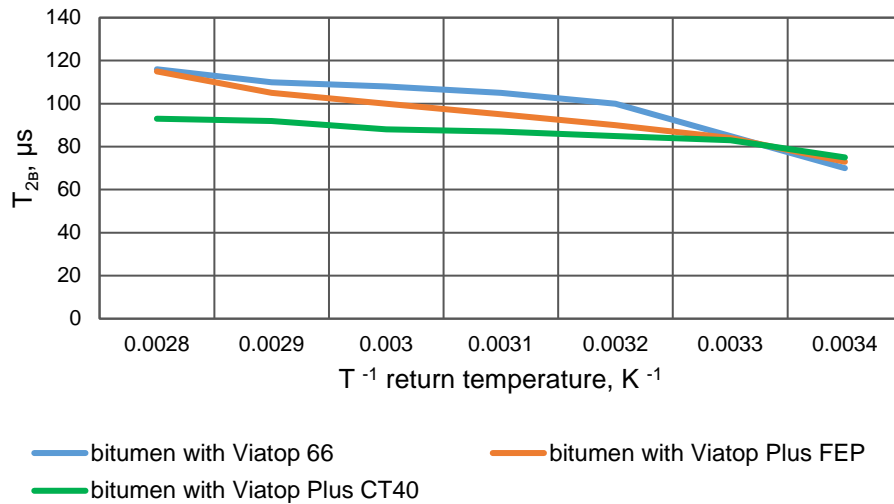


**Figure 3. Dependence of the spin-spin relaxation time of the rapidly relaxing component of  $T_{2B}$  on temperature.**

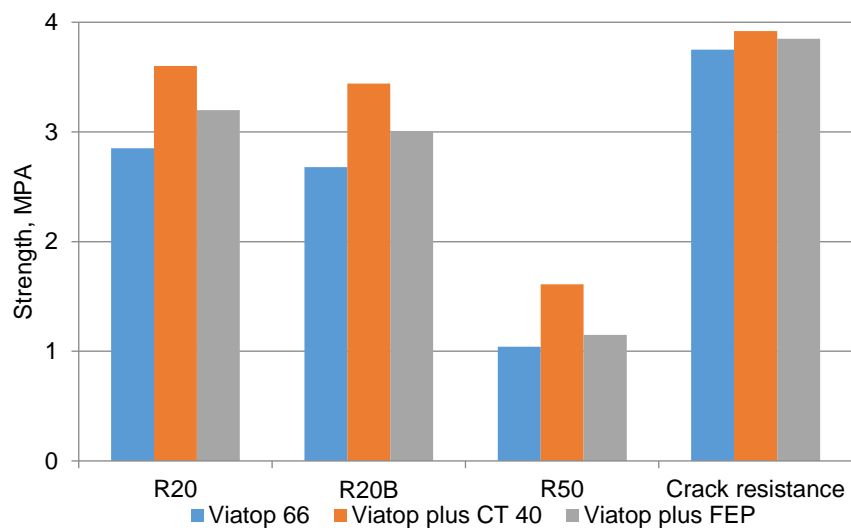


**Figure 4. Physical and mechanical properties of SMA-10.**

The water saturation rate of SMA-10 asphalt concrete containing the Viatop Plus CT40 additive is increased by 6 % compared with the control sample. A similar SMA with Viatop Plus FEP, on the contrary, is reduced by 5 %, which is probably due to the higher adhesive properties of the bitumen binder, which is modified by the polymer component that is part of the Viatop Plus FEP additive during the preparation of the asphalt mix.

The water resistance coefficient ( $K_v$ ) of SMA-10 with the addition of Viatop Plus CT40 and Viatop Plus FEP increases slightly (by 1 %) in comparison with the control composition of SMA containing Viatop 66.

The main shear stability indicators of asphalt concrete affecting the gauge depth include the coefficient of internal friction and the coefficient of asphalt concrete adhesion during shear.

With the introduction of the additives Viatop Plus CT40 and Viatop Plus FEP in the SMA-10, the rate of shear resistance increases. The coefficient of internal friction practically remains unchanged, and the coefficient of adhesion during shear at 50 °C increases by 73 % for the mixture with the addition of Viatop plus CT40 and by 10 % for the mixture with the addition of Viatop Plus FEP. The results of SMA-10 physical and mechanical properties research are given in Table 1.

The addition of Viatop Plus CT40 and Viatop Plus FEP additives to the mixture improves the split strength. So, for example, for SMA-10 with the addition of Viatop Plus CT40, this indicator increases on average by 5 %, and for a mixture with the addition of Viatop Plus FEP by 3 % compared with the control composition on Viatop 66.

The rate of runoff of the binder in comparison with the control composition of the mixture is reduced by 0.01–0.02 %, which increases the resistance to SMA segregation during storage, transportation, loading and unloading.

**Table 1. Physical-mechanical properties of SMA-10.**

Mix type	Compressive strength [MPa]			Water resistance coefficient	Shear resistance		Crack resistance [MPa]	Average track depth (RD) mm	Abrasion of SMA [cm <sup>3</sup> ]
	R20	R20B	R50		Internal friction coefficient [MPa]	Adhesion during shear at 50 °C [MPa]			
Mixture 1 (Viatop 66)	2.85	2.68	1.04	0.94	0.95	0.19	3.75	0.16	21.11
Mixture 2 (Viatop Plus CT40)	3.60	3.44	1.61	0.95	0.96	0.33	3.92	0.14	20.95
Mixture 3 (Viatop Plus FEP)	3.20	3.01	1.15	0.95	0.95	0.21	3.85	0.15	21.18

Along with studies of the basic physical and mechanical characteristics of SMA, regulated in Russian State Standard 31015, we carried out additional experimental studies of the resistance of asphalt concrete to rutting and to abrasive loads.

As a result of the tests, we found that the introduction of the additives Viatop Plus CT40 and Viatop Plus FEP into the SMA-10 formulations does not significantly affect the rate of their abrasability, as well as the rate of gauge after 10,000 cycles of applied load. So, the values of the obtained indicators are almost comparable with the test results of SMA-10 on Viatop 66, the values are presented in Table 1.

The following are the test results of the physicomechanical properties of the investigated SMA-15 formulations, the values are presented in Table 2.

The analysis of the dependences of the physical and mechanical properties of SMA-15 showed that the introduction of additives of the Viatop Plus CT40 and Viatop Plus FEP series leads to an increase in compressive strength at 20 °C (R20) of asphalt concrete by 6–34 %; the strength at 50 °C (R50) for SMA-15 with the addition of Viatop Plus CT40 is 11 % higher in comparison with the control composition, and for

SMA with the addition of Viatop Plus FEP the value of the same indicator remains practically unchanged (Fig. 5).

The water saturation index SMA-15 with the addition of Viatop Plus CT40 and Viatop Plus FEP increases by an average of 18 %.

The water resistance coefficient of SMA-15 with Viatop Plus CT40 and Viatop Plus FEP additives remains high in the water saturation mode under vacuum and increases slightly (by 1 %) compared to the initial mixture with Viatop 66 additive.

With the introduction of the additives Viatop Plus CT40 and Viatop Plus FEP, the shear resistance of SMA-15 practically does not change.

The crack resistance of asphalt concrete is increased by 11 % with the introduction of Viatop Plus CT40, and by 4 % with the introduction of Viatop Plus FEP. The binder runoff rate for SMA-15 formulations does not change.

**Table 2. Physical-mechanical properties of SMA-15.**

Mix type	Compressive strength [MPa]			Water resistance coefficient	Shear resistance		Crack resistance [MPa]	Average track depth (RD) mm	Abrasion of SMA [cm <sup>3</sup> ]
	R20	R20B	R50		Internal friction coefficient [MPa]	Adhesion during shear at 50 °C [MPa]			
Mixture 1 (Viatop 66)	2.62	2.47	1.06	0.94	0.95	0.19	3.45	2.2	19.25
Mixture 2 (Viatop Plus CT40)	3.51	3.35	1.18	0.95	0.94	0.22	3.84	1.9	18.96
Mixture 3 (Viatop Plus FEP)	2.78	2.65	1.08	0.95	0.94	0.20	3.30	2.0	19.21

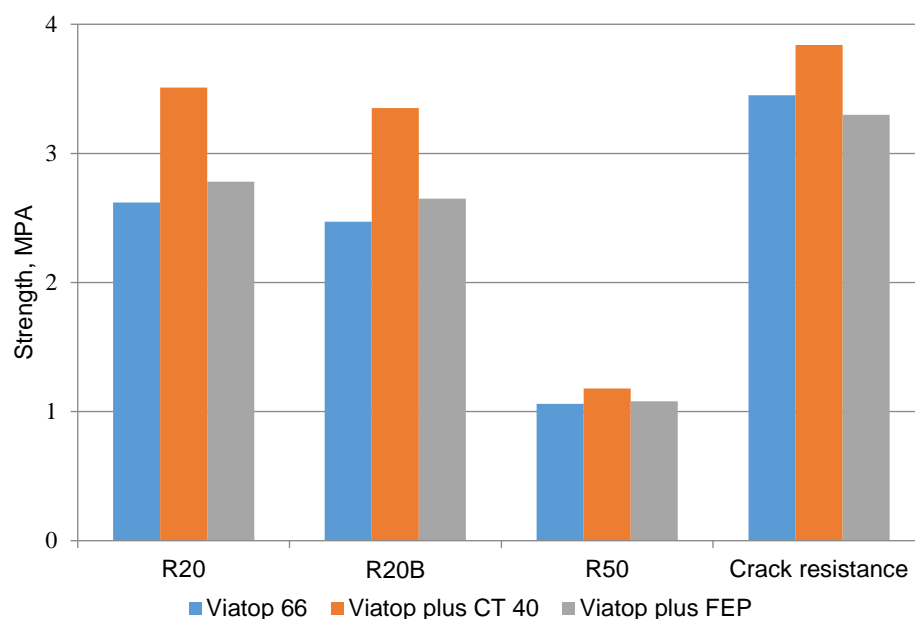


**Figure 5. Indicators of physical and mechanical properties of SMA-15.**

As a result of abrasion tests, we found that with the introduction of Viatop Plus CT40 and Viatop Plus FEP additives in SMA-15, this indicator slightly increases by 1–1.5 %, i.e. additives have virtually no effect on this indicator. As a result of SMA-15 tests for determining the track depth after 10,000 load cycles, we

also revealed that there is a slight improvement of this indicator by 0.2–0.3 mm, the values are presented in Table 2.

#### 4. 4. Conclusions

1. An analysis of the results allows us to conclude that the introduction of Viatop Plus CT40 and Viatop Plus FEP additives in the composition of SMA asphalt concrete grades 10 and 15 positively affects the change in the final physical and mechanical properties of the materials. Thus, the compressive strength at 20 °C of the samples under study is 26–34 % higher than the values for control samples supplemented with Viatop 66.

2. The compressive strength at 50 °C of SMA-10 containing Viatop Plus FEP is 55 % higher than that of the control sample, which characterizes its high resistance to plastic deformation.

3. The molecular mobility of bitumen with the addition of mixed TEP by the NMR method was studied. It was found that the introduction of the additive significantly inhibits the molecular mobility of bitumen, providing an increase in heat resistance and strength of crushed stone-mastic asphalt concrete.

4. We found that the physical and mechanical properties of SMA-10 and 15 asphalt concrete containing Viatop Plus CT40 and prepared by the warm method meet the requirements of GOST 31015, while the compressive strength of SMA-15 at 20 °C is 20 % higher compared to the control composition, which confirms the possibility and efficiency of the production of stone mastic asphalt mixtures at a lower temperature (140 °C) in comparison with the traditional mode of preparation (160–170 °C).

5. It was found that the addition of Viatop Plus CT40 and Viatop Plus FEP additives to the composition of SMA-15 promotes some improvement in the gauge depth index by 0.2–0.3 mm, in comparison with the control samples with the Viatop 66 additive.

#### References

1. Yadykina, V., Tobolenko, S., Trautvain, A., Zhukova, A. The influence of stabilizing additives on physical and mechanical properties of stone mastic asphalt concrete. *Procedia Engineering*. 2015. 117(1). Pp. 376–381. DOI: 10.1016/j.proeng.2015.08.181.
2. Yastremsky, D.A., Abaidullina, T.N., Chepur, P. V. Determination of Stone-Mastic Asphalt Concrete Durability. *Journal of Physics: Conference Series*. 2018. 1015 (3). Pp. 032150. DOI: 10.1088/1742-6596/1015/3/032150.
3. McGhee, K.K., Associate Principal Scientist, P., Clark, T.M., Director, P., Rorrer, T.M., Author, C., ii, R. Stone Matrix Asphalt in Virginia: a Ten-Year Performance Review. *Trb*. 2012.
4. Karakuş, A. Investigating on possible use of Diyarbakir basalt waste in Stone Mastic Asphalt. *Construction and Building Materials*. 2011. 25(8). Pp. 3502–3507. DOI: 10.1016/j.conbuildmat.2011.03.043
5. Hainin, R., Reshi, W.F., Niroumand, H. The importance of stone mastic asphalt in construction. *Electronic Journal of Geotechnical Engineering*. 2012. 17(49). Pp. 56–74.
6. Prowell, B.D., Hurley, G.C. Evaluation of Stone Matrix Asphalt (Sma) for Airfield Pavements. *FAA Worldwide Airport Technology Transfer Conference*. 2010.
7. Qiu, Y.F., Lum, K.M. Design and performance of stone mastic asphalt. *Journal of Transportation Engineering*. 2006. 132(12). DOI: 10.1061/(ASCE)0733-947X(2006)132:12(956)
8. Woodside, A.R., Woodward, W.D., Akbulut, H. Stone mastic asphalt: Assessing the effect of cellulose fibre additives. *Proceedings of the Institution of Civil Engineers: Municipal Engineer*. 1998. 127(3). Pp. 103-108. DOI: 10.1680/imuen.1998.30985
9. Martinho, F., Picado-Santos, L., Capitão, S., Neves, J. Avaliação Do Desempenho De Misturas Betuminosas Temperadas Contendo MBR. *7o Congresso Rodoviário Português*, At Lisboa. 2013.
10. Barazi Jomoor, N., Fakhri, M., Keymanesh, M.R. Determining the optimum amount of recycled asphalt pavement (RAP) in warm stone matrix asphalt using dynamic creep test. *Construction and Building Materials*. 2019. 127(3). Pp. 103–108. DOI: 10.1016/j.conbuildmat.2019.116736
11. Tóth, C., Soós, Z. The effect of VIATOP plus FEP on the stiffness and low temperature behaviour of hot mix asphalts. *Epitoanyag - Journal of Silicate Based and Composite Materials*. 2015. 67(4). Pp. 126–131. DOI: 10.14382/epitoanyag-jsbcm.2015.20
12. Hafeez, I., Kamal, M.A., Mirza, M.W. Assessing rutting potential of stone mastic asphalt using wheel tracker and dynamic modulus testing. *Baltic Journal of Road and Bridge Engineering*. 2014. 9(4). Pp. 325–332. DOI: 10.3846/bjrbe.2014.39
13. Yastremsky, D., Chepur, P., Abaidullina, T. Microstructure of the pulp and paper additives for stone-mastic asphalt concrete. *AIP Conference Proceedings*. 2017. 1800(1). 020002. DOI: 10.1063/1.4973018.
14. Venkatesh, U.M. V., Prasad, S.G.S. A Review on Stone Matrix Asphalt by Using Stabilizing Additives. *International Journal of Technical Innovation in Modern Engineering & Science*. 2018.
15. Chelovian, A., Shafabakhsh, G. Laboratory evaluation of Nano Al<sub>2</sub>O<sub>3</sub> effect on dynamic performance of stone mastic asphalt. *International Journal of Pavement Research and Technology*. 2017. 10(2). Pp. 131–138. DOI: 10.1016/j.ijprt.2016.11.004
16. Lyons, K.R., Putman, B.J. Laboratory evaluation of stabilizing methods for porous asphalt mixtures. *Construction and Building Materials*. 2013. 49. Pp. 772–780. DOI: 10.1016/j.conbuildmat.2013.08.076
17. Mahrez, A., Karim, M.R. Fatigue characteristics of stone mastic asphalt mix reinforced with fiber glass. *International Journal of Physical Sciences*. 2010. 5(12). Pp. 1840–1847.
18. Mokhtari, A., Moghadas Nejad, F. Mechanistic approach for fiber and polymer modified SMA mixtures. *Construction and Building Materials*. 2012. 36. Pp. 381-390. DOI: 10.1016/j.conbuildmat.2012.05.032

19. Bindu, C.S., Beena, K.S. Waste plastic as a stabilizing additive in stone mastic asphalt. *International Journal of Engineering and Technology*. 2010. 2 (6). Pp. 388–391.
20. Ahmadiania, E., Zargar, M., Karim, M.R., Abdelaziz, M., Ahmadiania, E. Performance evaluation of utilization of waste Polyethylene Terephthalate (PET) in stone mastic asphalt. *Construction and Building Materials*. 2012. 36. Pp. 984–989. DOI: 10.1016/j.conbuildmat.2012.06.015
21. Cao, W., Liu, S., Feng, Z. Comparison of performance of stone matrix asphalt mixtures using basalt and limestone aggregates. *Construction and Building Materials*. 2013. 41. Pp. 474–479. DOI: 10.1016/j.conbuildmat.2012.12.021
22. Ziari, H., Nasiri, E., Amini, A., Ferdosian, O. The effect of EAF dust and waste PVC on moisture sensitivity, rutting resistance, and fatigue performance of asphalt binders and mixtures. *Construction and Building Materials*. 2019. 203. Pp. 188–200. DOI: 10.1016/j.conbuildmat.2019.01.101
23. Shiva Kumar, G., Shankar, A.U.R., Ravi Teja, B.V.S. Laboratory Evaluation of SMA Mixtures Made with Polymer-Modified Bitumen and Stabilizing Additives. *Journal of Materials in Civil Engineering*. 2019. 31(4). DOI: 10.1061/(ASCE)MT.1943-5533.0002652
24. Babu, E.S.D., Lakshmi, S., Banupriya, K. Design of SMA using leather waste. *International Journal of Civil Engineering and Technology*. 2017. 8(5). Pp. 832–841. DOI:
25. Ahmadiania, E., Zargar, M., Karim, M.R., Abdelaziz, M., Shafigh, P. Using waste plastic bottles as additive for stone mastic asphalt. *Materials and Design*. 2011. 32(1). Pp. 4844–4849. DOI: 10.1016/j.matdes.2011.06.016

**Information about authors:**

**Aleksei Fomin**, PhD in Technical Science

ORCID: <https://orcid.org/0000-0002-4795-1212>

E-mail: [fomin-al.78@mail.ru](mailto:fomin-al.78@mail.ru)

**Eduard Hafizov**, PhD in Technical Science

ORCID: <https://orcid.org/0000-0003-4227-1733>

E-mail: [edward\\_76@bk.ru](mailto:edward_76@bk.ru)

**Evgenii Vdovin**, PhD in Technical Science

ORCID: <https://orcid.org/0000-0002-0649-4342>

E-mail: [vdovin007@mail.ru](mailto:vdovin007@mail.ru)

**Roman Fafanov**,

ORCID: <https://orcid.org/0000-0003-0833-1771>

E-mail: [roman.fafanov@rettenmaier.ru](mailto:roman.fafanov@rettenmaier.ru)

Received 26.12.2019. Approved after reviewing 08.11.2021. Accepted 23.05.2022.



Research article

UDC 531

DOI: 10.34910/MCE.117.13



## Elliptical underground concrete block bridge with minimal weight

**Yu.Ya. Tyukalov**    
Vyatka State University

 [yutvgu@mail.ru](mailto:yutvgu@mail.ru)

**Keywords:** arch bridge, finite element method, concrete blocks, optimal parameters, possible displacements principle

**Abstract.** An algorithm for determining the optimal parameters of an elliptical road bridge made of concrete blocks is proposed. The arch section heights are determined from the condition that the height of the concrete compressed zone should not be less than half the section height at any position of the automobile load. To solve the problem by the finite element method in physically nonlinear formulation, the principle of possible stress states is used. The nodes equilibrium equations of the arch are compiled using the possible displacements principle. The arch internal forces by a finite element length are approximated with linear functions, the concrete deformation diagram is represented in a piecewise-broken curve. Also, to determine the bearing capacity reserve of the optimal arch, the arch calculations were performed with a gradual increase in the automobile load up to destruction. Three options for the vehicle load location were considered. The optimal parameters of an arched road bridge with a span of 12 meters and its bearing capacity have been determined. It is shown that the arch destruction occurs with an increase in the load from the car by about 1.6 times.

**Citation:** Tyukalov, Yu.Ya. Elliptical underground concrete block bridge with minimal weight. Magazine of Civil Engineering. 2023. 117(1). Article no. 11713. DOI: 10.34910/MCE.117.13

### 1. Introduction

Arched concrete and reinforced concrete structures with soil backfill are widely used for bridge crossings and overpasses. Such constructs are easy to manufacture and economical. The article [1] proposes an analytical method for determining the internal forces of arched lintels. Elastoplastic work of the arch material is considered. Three differential equations of equilibrium are solved analytically, and an example of calculating an arch for a concentrated force action is given. In [2], a model of cracking and plastic deformation of reinforced concrete arches is considered. The solution was obtained based on the additional energy functional and the generalized criterion for the propagation of the Griffith's crack. Comparison of numerical solutions with an experimental data is carried out. In articles [3], [4] numerical and experimental studies of brick arches are given. In [3], an arch is represented by a rigid blocks system connected by three links. The study used combinatorial analysis to determine the hinges position at small supports displacements. The article [5] investigates the mechanisms of a stone vaults destruction under the concentrated forces action. There is noted the importance of considering the of occurrence displacements possibility between rigid blocks.

Several articles are devoted to the optimization of the arches shape [6, 7]. The article [6] optimizes the shape of an underground concrete arch to reduce bending stresses. The arch is calculated using a nonlinear finite element model. The arch center line approximated by the Bezier curve with three freedom degrees. The optimal parameters are determined using a genetic algorithm. The mechanisms of stone arches destruction and concrete blocks arches are very similar. The articles [8–11] are devoted to the masonry arched bridges. The article [12] provides an overview of studies on the methods of reinforcing

brick arches with composite materials. In particular, the use of fiber cement matrix (FRCM) materials for reinforcing brick arches is investigated in [13]. The article presents numerical and experimental studies of arches reinforced with such materials. Arches are modeled using a set of rigid blocks. In a few works, volumetric finite elements are used for calculating stone and concrete structures [11, 14, 15]. In [11], the application of the combined finite discrete element method (FDEM) for the analysis of three-dimensional stone structures from dry stone is presented. The article [16] presents the results of experimental and numerical studies of the response of a multi-span arched masonry bridge by vertical static loads. In [17], a two-phase strategy for the numerical simulation of the stone destruction process of arched bridges is presented. The stone blocks are represented by solid elements, and the solution is described by special finite elements. Three modes of destruction (compression, tension, shear) of masonry materials are considered. Article [18] is devoted to the numerical analysis of masonry, based on experimental data. When calculating arched bridges, it is important to consider shear deformations. The theory of shear deformations accounting of the circular arches was proposed in [20]. This article presents an analytical solution for calculating circular arches, based on the use of logarithmic functions. Consideration of shear deformations based on stress approximations is presented in [19, 20]. In [21], an algorithm for determining the optimal dimensions of swept arches from concrete blocks is presented. To solve a physically nonlinear problem, the functional of additional energy is used in combination with the possible displacement principle [22, 23]. Internal forces along the length of a finite element are approximated by piecewise constant functions. The discrete element method has been successfully used to calculate stone arches considering nonlinearity [24-27]. Considerable attention is paid to considering the influence of such factors as rain, displacement of supports, shock loads on the strength and stability of arched structures [28-30].

The purpose of this work is to build an algorithm for finding the optimal dimensions of an arched elliptical bridge made of concrete blocks. With a given bridge span and a given minimum section height, it is required to determine the arch height and the section height change along the arch length, ensuring the minimum arch weight under the design loads action.

The solution of a physically nonlinear problem is based on the principles of possible stress states and possible displacements. Internal forces are approximated by linear functions, a concrete deformation diagram is represented in a piecewise-broken curve.

## 2. Methods

The arch concrete blocks are deformed together, and the nodes remain rigid, due to the joints compression by the longitudinal forces that arise in the arch systems, and due to the friction forces, that act at the junction between the blocks (Fig. 1). The absence of shear translation between the blocks is ensured by the friction forces of concrete against concrete in the compressed zone. Therefore, the required arch section height will be determined from the condition of concrete strength, as well as from the condition of ensuring the compressed zone height is not less than half of the section. In calculation process, the section shear strength will be tested against the transverse force action that occurs in the section (30). Therefore, in the finite element scheme, the nodes are assumed to be rigid.

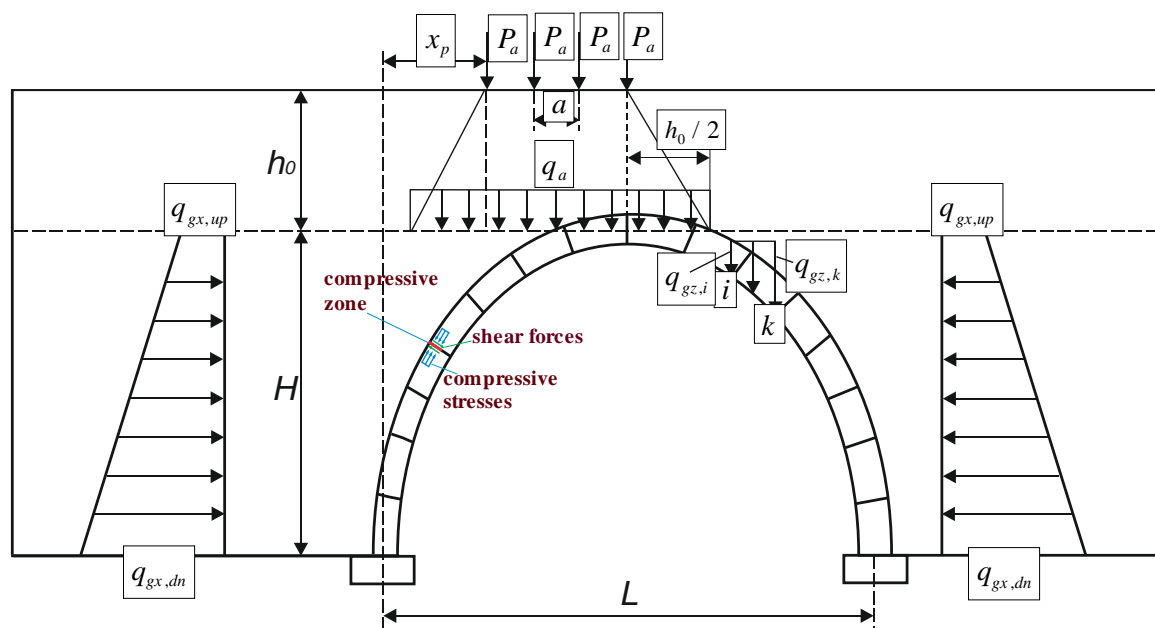
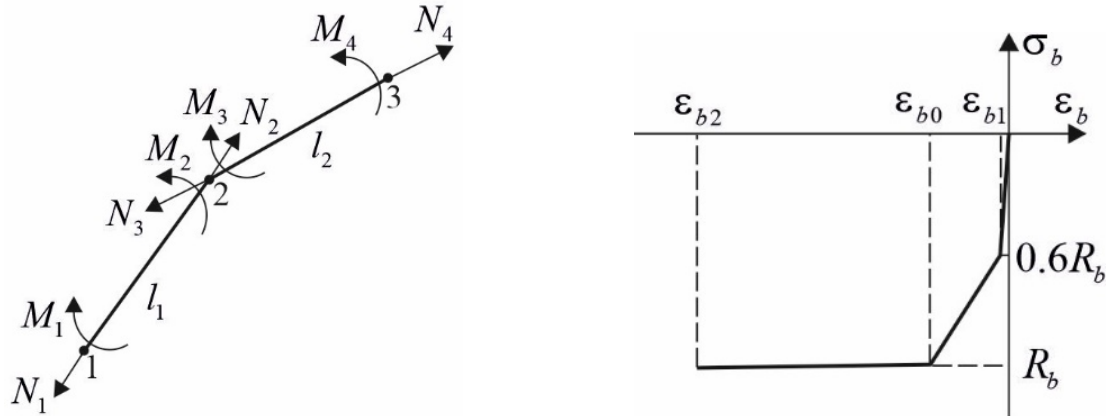


Figure 1. Loads acting on the arch.

The arch is divided lengthwise into finite elements. Bending moments and longitudinal forces are approximated along the length of each finite element by linear functions independently (Fig. 2). In Fig. 2 the unknowns numbering for the first two finite elements are shown. Due to the node equilibrium equations, under the action of a possible displacement in a rotation angle form, the equality of the moments in the nodes will be ensured.

The concrete stress-strain diagram of the arch is presented in the piecewise-broken curve form, which does not consider the tensile concrete stresses (Fig. 3). Such a diagram is used because tensile stresses cannot arise in the concrete blocks joints sections. In the sections between the joints, for the safety margin, the tensile concrete stresses will also be neglected. With this approach, the arch calculation will not depend on the length of the concrete blocks and the number of joints.



**Figure 2. Numbering of the unknown nodal forces. Figure 3. Diagram of a concrete deformation.**

To solve the problem with a physically nonlinear formulation, we will use the possible stress states principle. For an arbitrary step of an increasing load, variation of the additional deformation energy increment  $\delta(\Delta\Pi_i)$  is zero (1).

$$\delta(\Delta\Pi_i) = \int_V (\epsilon_i + \delta(\Delta\epsilon_i)) \delta(\Delta\sigma_i) dV = 0. \quad (1)$$

$\epsilon_i, \Delta\epsilon_i$  are the current deformations and deformations increments at a loading step  $i$ ;  $\Delta\sigma_i$  is the stresses increments, which must satisfy the equilibrium equations at loading step  $i$ ;  $V$  is subject area. The deformations and stresses increment at each step are interconnected by the deformation tangent modulus  $E_i^t(\epsilon_i)$ :

$$\Delta\sigma_i = E_i^t(\epsilon_i) \Delta\epsilon_i. \quad (2)$$

Substituting (2) into (1), we get:

$$\delta(\Delta\Pi_i) = \int_V E_i^t(\epsilon_i) (\epsilon_i + \delta(\Delta\epsilon_i)) \delta(\Delta\epsilon_i) dV = 0. \quad (3)$$

From expression (3) it follows that the additional strain energy increment will have the following form:

$$\Delta\Pi_i = \int_V \left( E_i^t(\epsilon_i) \epsilon_i \Delta\epsilon_i + \frac{1}{2} E_i^t(\epsilon_i) \Delta\epsilon_i^2 \right) dV. \quad (4)$$

Let us calculate the additional energy deformations increment of a rod finite element. The strains increments are determined according to the straight normal hypothesis:

$$\Delta\epsilon_i = \Delta\epsilon_{0i} - z\Delta\chi_i. \quad (5)$$

$\Delta\epsilon_{0i}$  is the increment of midline deformation;  $\Delta\chi_i$  is axis curvature increment. Substituting (5) into (4), we get:

$$\Delta\Pi_{i,k} = \int_0^{l_k} \int_{-h/2}^{h/2} b(\varepsilon_{0i} - z\chi_i)\Delta\sigma_i dz dx + \frac{1}{2} \int_0^{l_k} \int_{-h/2}^{h/2} bE_i^t(\varepsilon_i) \left( \Delta\varepsilon_{0i}^2 - 2z\Delta\varepsilon_{0i}\Delta\chi_i + \Delta\chi_i^2 \right) dz dx. \quad (6)$$

Let us introduce notation for the following integrals:

$$EA^t = \int_{-h/2}^{h/2} bE_i^t(\varepsilon_i) dz, \quad ES^t = \int_{-h/2}^{h/2} bE_i^t(\varepsilon_i) z dz, \quad EI^t = \int_{-h/2}^{h/2} bE_i^t(\varepsilon_i) z^2 dz. \quad (7)$$

Integrals (7) are calculated numerically using the concrete stress-strain diagram (Fig. 3) by the trapezia method. Considering (7), the internal forces increment in the section are determined by the following formulas:

$$\Delta N_i = \int_{-h/2}^{h/2} b\Delta\sigma_i dz = \int_{-h/2}^{h/2} bE_i^t(\varepsilon_i) (\Delta\varepsilon_{0i} - z\Delta\chi_i) dz = \Delta\varepsilon_{0i}EA^t - \Delta\chi_{ii}ES^t, \quad (8)$$

$$\Delta M_i = - \int_{-h/2}^{h/2} b\Delta\sigma_i z dz = - \int_{-h/2}^{h/2} bE_i^t(\varepsilon_i) (z\Delta\varepsilon_{0i} - z^2\Delta\chi_i) dz = -\Delta\varepsilon_{0i}ES^t + \Delta\chi_{ii}EI^t. \quad (9)$$

From expressions (8), (9) we obtain

$$\Delta\varepsilon_{0i} = \frac{\Delta N_i EI^t + \Delta M_i ES^t}{EA^t EI^t - ES^{t2}}, \quad \Delta\chi_i = \frac{\Delta N_i ES^t + \Delta M_i EA^t}{EA^t EI^t - ES^{t2}}. \quad (10)$$

Substituting (10) into (6), we get

$$\Delta\Pi_{i,k} = \int_0^{l_k} (\varepsilon_{0i}\Delta N_i + \chi_i\Delta M_i) dx + \frac{1}{2} \int_0^{l_k} \left( \frac{EI^t \Delta N_i^2}{EI^t EA^t - ES^{t2}} + \frac{EA^t \Delta M_i^2}{EI^t EA^t - ES^{t2}} + \frac{2ES^t \Delta M_i \Delta N_i}{EI^t EA^t - ES^{t2}} \right) dx. \quad (11)$$

Let us introduce the vectors of unknown nodal forces and its increments for a finite element  $k$ :

$$\mathbf{S}_{i,k} = \begin{Bmatrix} N_{i,2k-1} \\ M_{i,2k-1} \\ N_{i,2k} \\ M_{i,2k} \end{Bmatrix}, \quad \Delta\mathbf{S}_{i,k} = \begin{Bmatrix} \Delta N_{i,2k-1} \\ \Delta M_{i,2k-1} \\ \Delta N_{i,2k} \\ \Delta M_{i,2k} \end{Bmatrix}. \quad (12)$$

To approximate the forces and moments along the finite element length, we will use linear functions. The approximations are independent for each finite element. In this case, the global flexibility matrix has a block-diagonal shape and be easily reversible. The expression (11) can be written in matrix form:

$$\Delta\Pi_{i,k} = \frac{1}{2} \Delta\mathbf{S}_{i,k}^T \mathbf{D}_{i,k}^t \Delta\mathbf{S}_{i,k} + \Delta\mathbf{L}_{i,k}^T \Delta\mathbf{S}_{i,k}, \quad (13)$$

The second integral in (11), which determines the tangent matrix elements, is calculated numerically using the trapezia formula. Divide the finite element into  $n$  equal segments  $\Delta l_k = l_k / n$ . Let us denote the shear stiffness generalized parameters of the section at an arbitrary point  $j$  of a finite element  $k$ :

$$EA_{k,j}^t = \int_{-h_j/2}^{h_j/2} b_j E_{k,i}^t(\varepsilon_{k,j}) dz, \quad ES_{k,j}^t = \int_{-h_j/2}^{h_j/2} b_j E_{k,i}^t(\varepsilon_{k,j}) z dz, \quad EI_{k,j}^t = \int_{-h_j/2}^{h_j/2} b_j E_{k,i}^t(\varepsilon_{k,j}) z^2 dz, \quad (14)$$

$$ER_{k,j}^t = EI_{k,j}^t EA_{k,j}^t - ES_{k,j}^{t2}.$$

$b_j, h_j$  are the section dimensions at point  $j$ .  $\varepsilon_{k,j}(z)$  is the deformation at point  $j$ :

$$\varepsilon_{k,j} = \left( \varepsilon_{i,2k-1} - z\chi_{i,2k-1} \right) \left( \frac{l_k - x_j}{l_k} \right) + \left( \varepsilon_{i,2k} - z\chi_{i,2k} \right) \left( \frac{x_j}{l_k} \right). \quad (15)$$

$\varepsilon_{i,2k-1}, \chi_{i,2k-1}, \varepsilon_{i,2k}, \chi_{i,2k}$  are deformations and curvatures of axis at the beginning and end a finite element  $k$ ;  $x_j$  is a local coordinate of point  $j$ . Let us introduce the tangent matrix  $\mathbf{D}_{i,k}^t$  elements notation:

$$\begin{aligned} d_{1,1} &= \sum_{j=2}^n \frac{EI_{k,j}^t \left(1 - \frac{x_j}{l_k}\right)^2}{ER_{k,j}^t} + \frac{EI_{k,1}^t}{2ER_{k,1}^t}, d_{1,2} = \sum_{j=2}^n \frac{ES_{k,j}^t \left(1 - \frac{x_j}{l_k}\right)^2}{ER_{k,j}^t} + \frac{ES_{k,1}^t}{2ER_{k,1}^t}, d_{1,3} = \sum_{j=2}^n \frac{EI_{k,j}^t \left(1 - \frac{x_j}{l_k}\right) \frac{x_j}{l_k}}{ER_{k,j}^t}, \\ d_{1,4} &= \sum_{j=2}^n \frac{ES_{k,j}^t \left(1 - \frac{x_j}{l_k}\right) \frac{x_j}{l_k}}{ER_{k,j}^t}, d_{2,2} = \sum_{j=2}^n \frac{EA_{k,j}^t \left(1 - \frac{x_j}{l_k}\right)^2}{ER_{k,j}^t} + \frac{EA_{k,1}^t}{2ER_{k,1}^t}, d_{2,3} = d_{1,4}, d_{2,4} = \sum_{j=2}^n \frac{EA_{k,j}^t \left(1 - \frac{x_j}{l_k}\right) \frac{x_j}{l_k}}{ER_{k,j}^t}, \\ d_{3,3} &= \sum_{j=2}^n \frac{EI_{k,j}^t \left(\frac{x_j}{l_k}\right)^2}{ER_{k,j}^t} + \frac{EI_{k,n+1}^t}{2ER_{k,n+1}^t}, d_{3,4} = \sum_{j=2}^n \frac{ES_{k,j}^t \left(\frac{x_j}{l_k}\right)^2}{ER_{k,j}^t} + \frac{ES_{k,n+1}^t}{2ER_{k,n+1}^t}, d_{4,4} = \sum_{j=2}^n \frac{EA_{k,j}^t \left(\frac{x_j}{l_k}\right)^2}{ER_{k,j}^t} + \frac{EA_{k,n+1}^t}{2ER_{k,n+1}^t}. \end{aligned} \quad (16)$$

The final matrix  $\mathbf{D}_{i,k}^t$  expression is as follows:

$$\mathbf{D}_{i,k}^t = \Delta l_k \begin{bmatrix} d_{1,1} & d_{1,2} & d_{1,3} & d_{1,4} \\ d_{1,2} & d_{2,2} & d_{2,3} & d_{2,4} \\ d_{1,3} & d_{2,3} & d_{3,3} & d_{3,4} \\ d_{1,4} & d_{2,4} & d_{3,4} & d_{4,4} \end{bmatrix}. \quad (17)$$

From the matrices  $\mathbf{D}_{i,k}^t$  of finite elements we form the global matrix:

$$\mathbf{D}_i^t = \begin{bmatrix} \mathbf{D}_{i,1}^t & & & \\ & \mathbf{D}_{i,2}^t & & \\ & & \ddots & \\ & & & \mathbf{D}_{i,n}^t \end{bmatrix}. \quad (18)$$

Consider the linear nature of the change in forces and moments along the finite element, we obtain the expression for the vector  $\Delta_{i,k}$ :

$$\Delta_{i,k} = l_k \begin{Bmatrix} \frac{\varepsilon_{i,2k-1}}{3} + \frac{\varepsilon_{i,2k}}{6} \\ \frac{\chi_{i,2k-1}}{3} + \frac{\chi_{i,2k}}{6} \\ \frac{\varepsilon_{i,2k-1}}{6} + \frac{\varepsilon_{i,2k}}{3} \\ \frac{\chi_{i,2k-1}}{6} + \frac{\chi_{i,2k}}{3} \end{Bmatrix}. \quad (19)$$

Then, for the whole system, we obtain the following expression for the increment of additional energy of the deformations:

$$\Delta \Pi_i = \frac{1}{2} \Delta \mathbf{S}_i^T \mathbf{D}_i^t \Delta \mathbf{S}_i + \Delta_{i,k}^T \Delta \mathbf{S}_i. \quad (20)$$

In accordance with the possible stress states principle, the forces and moments increments must satisfy the equilibrium equations. Such equations for nodes can be obtained using the possible

displacements principle [23]. The vertical, horizontal displacements and angles rotations of nodes are taken as possible displacements. As a result, we obtain equations for the equilibrium of forces and moments for each unsecured arch node. For the whole system, the equilibrium equations can be written in the following matrix form:

$$\mathbf{L}\Delta\mathbf{S}_i + \Delta\mathbf{P}_i = 0. \quad (21)$$

The equilibrium global matrix  $\mathbf{L}$  is formed from equilibrium matrices  $\mathbf{L}_k$  of finite elements.

$$\mathbf{L}_k = \begin{bmatrix} \frac{-\cos \alpha_k}{2} & \frac{\sin \alpha_k}{l_k} & \frac{-\cos \alpha_k}{2} & \frac{-\sin \alpha_k}{l_k} \\ \frac{-\sin \alpha_k}{2} & \frac{-\cos \alpha_k}{2} & \frac{-\sin \alpha_k}{2} & \frac{\cos \alpha_k}{2} \\ 0 & 1 & 0 & 0 \\ \frac{\cos \alpha_k}{2} & \frac{-\sin \alpha_k}{l_k} & \frac{\cos \alpha_k}{2} & \frac{\sin \alpha_k}{l_k} \\ \frac{\sin \alpha_k}{2} & \frac{\cos \alpha_k}{l_k} & \frac{\sin \alpha_k}{2} & \frac{-\cos \alpha_k}{l_k} \\ 0 & 0 & 0 & -1 \end{bmatrix}, \cos \alpha_k = \frac{x_{2k} - x_{2k-1}}{l_k}, \sin \alpha_k = \frac{y_{2k} - y_{2k-1}}{l_k}. \quad (22)$$

Note that the matrix  $\mathbf{L}$  is geometric and does not depend on a load. The load vector  $\Delta\mathbf{P}_i$  is formed from the forces concentrated in the nodes and the loads distributed over the finite element. For that we must calculate the load work at possible displacements of the nodes.

Using the Lagrange multiplier method, we add the nodes equilibrium equations (21) with the functional (20). We get the following advanced functional:

$$\Delta\Pi_i = \frac{1}{2}\Delta\mathbf{S}_i^T \mathbf{D}_i^t \Delta\mathbf{S}_i + \Delta_i^T \Delta\mathbf{S}_i + \mathbf{w}_i^T (\mathbf{L}\Delta\mathbf{S}_i + \Delta\mathbf{P}_i). \quad (23)$$

The Lagrange multipliers vector consists of nodal displacements and rotation angles values:

$$\mathbf{w}_i^T = (u_1 \quad w_1 \quad \varphi_1 \quad u_2 \quad w_2 \quad \varphi_2 \quad \cdots \quad \cdots \quad u_n \quad w_n \quad \varphi_n). \quad (24)$$

Equating the functional derivatives with respect to vectors  $\Delta\mathbf{S}_i^T$  and  $\mathbf{w}_i^T$ , we obtain the linear algebraic equations system:

$$\begin{aligned} \mathbf{D}_i^t \Delta\mathbf{S}_i + \Delta_i + \mathbf{L}^T \mathbf{w}_i &= 0, \\ \mathbf{L}\Delta\mathbf{S}_i + \Delta\mathbf{P}_i &= 0. \end{aligned} \quad (25)$$

Let us express from the first equation the forces increment vector

$$\Delta\mathbf{S}_i = -\mathbf{D}_i^{t-1} \Delta_i - \mathbf{D}_i^{t-1} \mathbf{L}^T \mathbf{w}_i. \quad (26)$$

The matrix  $\mathbf{D}_i^t$  is block-diagonal and easily inverted. Let us introduce notation of the matrix product:

$$\mathbf{K}_i = \mathbf{L}\mathbf{D}_i^{t-1} \mathbf{L}^T. \quad (27)$$

From the second equation (25) we obtain the resolving system of nonlinear algebraic equations

$$\mathbf{K}_i \mathbf{w}_i = \Delta\mathbf{P}_i - \mathbf{L}\mathbf{D}_i^{t-1} \Delta_i. \quad (28)$$

For solving (28), we will perform iterative refinement according to the Newton - Raphson scheme. We will use the following calculation algorithm with given automobile position:

1. Calculate matrix  $\mathbf{L}$  and vector  $\mathbf{P}$ ;  $\mathbf{S}_0 = 0$ ; for each node  $k$ :  $\varepsilon_{0,k} = 0$ ,  $\chi_{0,k} = 0$ .

2. Accept  $\Delta \mathbf{P}_i = \mathbf{P}$ ,  $i=0$ .
3. Begin cycle of iterative refinement; accept  $i = i + 1$ .
4. Calculate matrices  $\mathbf{D}_i^t$ ,  $\mathbf{D}_i^{t-1}$ ,  $\mathbf{K}$ ,  $\Delta_i$ .
5. Calculating equations system (28), we get  $\mathbf{w}_i$ .
6. Using (26), we calculate  $\Delta \mathbf{S}_i$ .
7. Using (10), we calculate for all nodes:  $\Delta \varepsilon_{i,k}$ ,  $\Delta \chi_{i,k}$ ;
8. Calculate for all nodes  $\varepsilon_{i,k} = \varepsilon_{i-1,k} + \Delta \varepsilon_{i,k}$ ,  $\chi_{i,k} = \chi_{i-1,k} + \Delta \chi_{i,k}$ .
9. Using in (8) and (9) the secant modulus of deformations we calculate  $\bar{\mathbf{S}}_i$ .
10. Calculate  $\Delta \bar{\mathbf{S}}_i = \mathbf{S}_{i-1} - \bar{\mathbf{S}}_i$ .
11. Calculate  $\Delta \bar{\mathbf{P}}_i = \mathbf{L} \Delta \bar{\mathbf{S}}_i$  and accuracy  $Ex(\Delta \mathbf{P}_i) = 100 \frac{\sqrt{\sum_{j=1}^{n_d} (P_{i,j} - \Delta \bar{P}_{i,j})^2}}{\sqrt{\sum_{j=1}^{n_d} P_{i,j}^2}}$ .
12. If  $Ex(\Delta \mathbf{P}_i) > [Ex]$ , then we calculate  $\Delta \mathbf{P}_i = \mathbf{P}_i - \mathbf{L} \Delta \bar{\mathbf{S}}_i$ ;  $\mathbf{S}_i = \bar{\mathbf{S}}_i$  and go to 3.
13. If  $Ex(\Delta \mathbf{P}_i) \leq [Ex]$ , then we have end of iterative refinement.

The resulting bending moments are used to calculate the shear forces in finite elements:

$$Q_k = \frac{M_{2k} - M_{2k-1}}{l_k}. \quad (29)$$

Next, a check is carried out for a possible displacement of the sections at the joints of concrete blocks:

$$|Q_k| \leq k_{fr} |N_{2k-1}|, \quad |Q_k| \leq k_{fr} |N_{2k}|. \quad (30)$$

$k_{fr}$  is the friction coefficient of concrete on concrete;  $N_{2k-1}, M_{2k-1}, N_{2k}, M_{2k}$  are the internal forces at the finite element beginning and end. If conditions (30) are not done, then a shift of concrete blocks relative to each other is possible and it is necessary to change a design scheme.

At each node of the arch, the eccentricity modulus of the longitudinal force and the required section height are calculated, which provides the compressed zone will be equal to half the section height (with a linear stress diagram in the compressed zone):

$$e_i = \left| \frac{M_i}{N_i} \right|, \quad h_i^s = 3 \cdot e_i. \quad (31)$$

Calculations have shown that the maximum compressive stresses are far from the limiting value; therefore, the stress diagram in the compressed zone is practically linear. Nonlinearity of deformations is associated with the exclusion of the stretched concrete zone from the work.

The required heights of the arch cross sections will be determined using the following iterative algorithm:

1. For each arch node  $i$ , we set the initial value of the section height  $h_i = h_{\min}$ .
2. Begin cycle of  $h_i$  finding.
3. Set  $h_i^{iter} = h_i$ .

4. Begin cycle on  $x_p$  (Fig.1) from 0 to  $\left(\frac{L}{2} - \frac{a_x}{2}\right)$  with step 0.1 m.
5. We perform the arch calculation according to the algorithm given above.
6. For each arch node, we calculate  $h_i^s$  (31).
7. If  $h_i^s > h_i^{iter}$ , then  $h_i^{iter} = h_i^s$ .
8. End cycle on  $x_p$ .
9. For each arch node  $i$ , we calculate  $h_i = \left(\frac{10000 \cdot h_i^{iter} + h_i}{10000}\right) \geq h_{\min}$ .
10. Rounding  $h_i$  to 5 cm.
11. Go to 3.

The calculations have shown that the process of refining the cross-section heights converges in no more than 15 iterations. As a result of the calculation, for each node, the maximum eccentricities of the longitudinal force and the required section height are determined. These heights will ensure the compressed zone value at least half of the cross section at any automobile load position.

### 3. Results and Discussion

Consider the problem of determining the optimal parameters of an elliptical arch bridge. The arch is subject to loads from the weight of the backfill soil and a load from the moving vehicle (Fig. 1). In this case, the compressed zone minimum height should be at least half the arch section height. When searching for the optimal parameters, we will assume that the arch span  $L$  is given, and the optimal arch height  $H$  must be selected. The optimal height is determined by sequential calculation of the arches with it gradual increasing. The all data for the calculation are given in Table 1. The arch was divided along the length into 16 finite elements.

**Table 1. Arch calculation data.**

Denotation	Dimension	Value	Parameter
$h_0$	m	2.0	Backfill height from the arch top
$\varphi_{gr}$	degree	35	Angle of internal soil friction
$\gamma_{gr}$	kN/m <sup>3</sup>	17.7	Soil volume weight
$a$	m	1.2	Distance between vehicle axles
$P_a$	kN	250	Vehicle axle load
$a_x$	m	3.6	Load length from vehicle
$a_y$	m	2.7	Load width from vehicle
$L$	m	12	Arch span
$B$	m	0.5	Arch width is a bridge strip width on which the load is collected
$h_{\min}$	m	Need to assign	The minimum height of the arch cross section
$H$	m	Need to define	Arch height

Vertical and horizontal loads from the vehicle and the ground (Fig. 1) are determined by the following formulas:

$$q_a = \frac{1.2 \cdot B \cdot P_a}{(h_0 + a_x)(h_0 + a_y)}, q_{gz,i} = 1.1 \cdot \gamma_{gr} (H + h_0 - z_i) \cdot B. \quad (32)$$

$$q_{qx,up} = 1.1 \cdot \gamma_{gr} h_0 \cdot tg^2 \left( 45 - \frac{\varphi_{gr}}{2} \right) B, q_{qx,dn} = 1.1 \cdot \gamma_{gr} (H + h_0) \cdot tg^2 \left( 45 - \frac{\varphi_{gr}}{2} \right) B. \quad (33)$$

To these loads is added the load from the arch own weight.

The parameters of the compressed concrete deformation diagram were taken as follows:  $\varepsilon_{b1} = -0.000314$ ,  $\varepsilon_{b0} = -0.002$ ,  $\varepsilon_{b2} = -0.0035$ ,  $R_b = 17000 \text{ kN} / \text{m}^2$  (Fig. 2).

Fig. 4 shows the most optimal arch minimum weight ( $h_{\min} = 0.4 \text{ m}$ ).

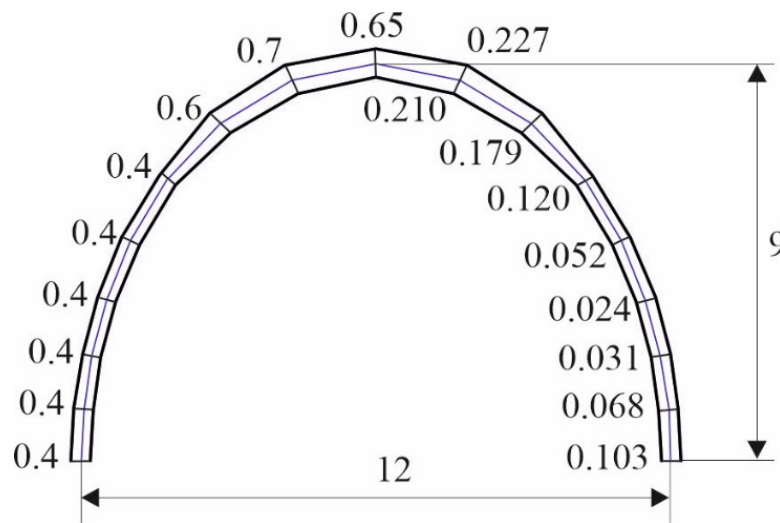


**Figure 4. Arch with minimum weight of 15.409 tons: on the left side the blocks section heights are indicated; on the right side the maximum eccentricities of the longitudinal force (in meters) are indicated.**

The arch division into finite elements was carried out automatically. Arch nodes were defined as the point of intersection of a straight line drawn from the span middle and an elliptical arc. Straight lines were drawn with an angular step of 11.25 degrees. The angles were measured from the horizontal line. The first five finite elements of half-arch have a minimum cross-section height. Further, an increase of the section height is required to 0.6–0.7 meters.

**Table 2. Arch weight (tons) depending on geometric parameters.**

$H$ [m]	$h_{\min}$ [m]		
	0.4	0.5	0.6
8.8	-	17.471	<b>18.534</b>
8.9	15.498	<b>16.690</b>	18.668
9.0	<b>15.409</b>	16.816	18.802
9.1	15.761	17.175	18.936
9.2	16.001	17.536	19.308

Table 2 shows optimal weights of arches, depending on an arch height and a specified minimum section height. Note that the arch optimal weight is more influenced by a value of minimum section height, which is specified. Setting a minimum arch height is necessary to meet possible construction requirements. Also note that the greater a minimum section height, the lower an optimal arch height.

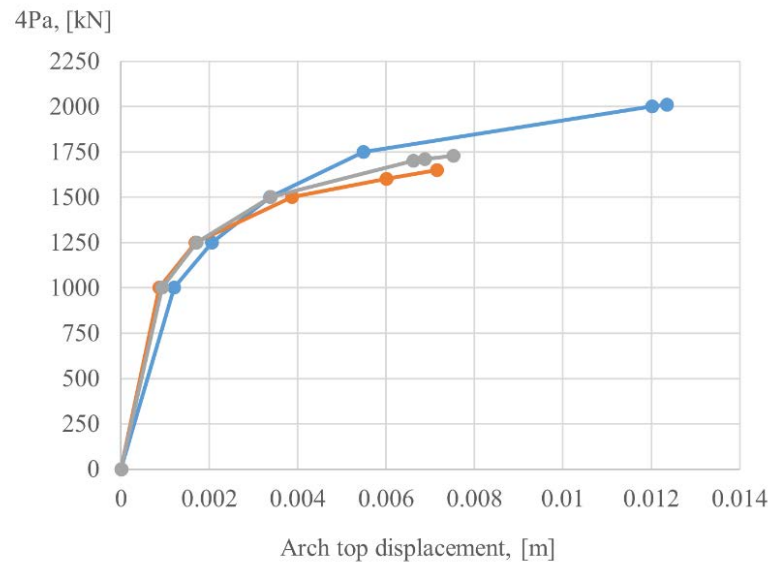


**Figure 5. The arch top displacements depending on the Vehicle axle load value. Blue line – the load is located symmetrically from the center; gray line – the load is displaced on 1.2 meters from the center; red line – the load is displaced on 2.4 meters from the center.**

Also, to determine the bearing capacity reserve of the optimal arch, the arch calculations were performed with a gradual increase in the automobile load up to destruction. Three options for the vehicle load location were considered (Fig. 5). The most dangerous is the load location with an offset of 2.4 meters from the top of the arch (red line in Fig. 5). In this case, the ultimate automobile load is approximately 1.6 times higher than the calculated one. This value shows the safety margin of the arch. The danger of an asymmetrical arrangement of the load for arches made of stone blocks is also noted in [1, 4]. If the vehicle load is located symmetrically with respect to the arch top, then the breaking load value is twice the calculated one. If it is necessary to provide a greater safety margin for the arch, then we must take the minimum height of the compressed zone more than half the section height. The arch, which is optimal in terms of weight, has a cross section that is variable in length, so concrete blocks must be manufactured individually. Also, the blocks must have the required slope of the faces to ensure the compressive forces transmission. For the manufacture of such blocks, it is necessary to have a steel mold with three moving faces, which is quite technically feasible and will not lead to a significant blocks cost increase. At the same time, by reducing the concrete arch volume, the building materials cost is can reduced significant. If necessary, you can determine the arch optimal height with a constant section size, but such an arch will not have a minimum weight. For example, the arch in Fig. 4 with the constant maximum required section height of 0.7 meters will have a weight of approximately 22 tons, which is 1.5 times more than the optimal one.

#### 4. Conclusions

1. An algorithm for determining the optimal parameters of an elliptical arched road bridge made of concrete blocks is proposed. With a given bridge span and a given minimum section height, the arch height and the section height change along the length are determined, providing the minimum arch weight under the design loads action.

2. The solution of a physically nonlinear problem is based on the principles of possible stress states and possible displacements. Internal forces are approximated by linear functions, the concrete deformation diagram is represented as a piecewise broken curve.

3. The optimal parameters of an arched road bridge with a span of 12 meters and its bearing capacity have been determined. It is shown that the arch destruction occurs with an increase in the automobile load by about 1.6 times, what shows the safety margin of the arch. This arch with the constant maximum required section height of 0.7 meters will have a weight of approximately 22 tons, which is 1.5 times more than the optimal one.

#### References

1. AudioNet, A., Fanning, P., Sobczak, L., Peremans, H. 2-D analysis of arch bridges using an elasto-plastic material model. *Engineering Structures*. 2008. 30(3). Pp. 845–855. DOI:10.1016/j.engstruct.2007.05.018.
2. Amorim, D.L.N.D.F., Proença, S.P.B., Flórez-López, J. A model of fracture in reinforced concrete arches based on lumped damage mechanics. *International Journal of Solids and Structures*. 2013. 50(24). Pp. 4070–4079. DOI:10.1016/j.ijsolstr.2013.08.012.

3. Galassi, S., Misseri, G., Rovero, L., Tempesta, G. Failure modes prediction of masonry voussoir arches on moving supports. *Engineering Structures*. 2018. 173. Pp. 706–717. DOI:10.1016/j.engstruct.2018.07.015.
4. Gattesco, N., Boem, I., Andretta, V. Experimental behaviour of non-structural masonry vaults reinforced through fibre-reinforced mortar coating and subjected to cyclic horizontal loads. *Engineering Structures*. 2018. 172. Pp. 419–431. DOI:10.1016/j.engstruct.2018.06.044.
5. Beatini, V., Royer-Carfagni, G., Tasora, A. Modeling the shear failure of segmental arches. *International Journal of Solids and Structures*. 2019. 158. Pp. 21–39. DOI:10.1016/j.ijsolstr.2018.08.023.
6. Houšť, V., Eliáš, J., Miča, L. Shape optimization of concrete buried arches. *Engineering Structures*. 2013. 48. Pp. 716–726. DOI:10.1016/j.engstruct.2012.11.037.
7. Kimura, T., Ohsaki, M., Fujita, S., Michiels, T., Adriaenssens, S. Shape optimization of no-tension arches subjected to in-plane loading. *Structures*. 2020. 28. Pp. 158–169. DOI:10.1016/j.istruc.2020.08.053.
8. Misseri, G., Justin, M., Rovero, L. Experimental and numerical investigation of the collapse of pointed masonry arches under quasi-static horizontal loading. *Engineering Structures*. 2018. 173. Pp. 180–190. DOI:10.1016/j.engstruct.2018.06.009.
9. Pulatsu, B., Erdogmus, E., Lourenço, P.B. Comparison of in-plane and out-of-plane failure modes of masonry arch bridges using discontinuum analysis. *Engineering Structures*. 2019. 178. Pp. 24–36. DOI:10.1016/j.engstruct.2018.10.016.
10. Scozzese, F., Ragni, L., Tubaldi, E., Gara, F. Modal properties variation and collapse assessment of masonry arch bridges under scour action. *Engineering Structures*. 2019. 199. Pp. 109665. DOI:10.1016/j.engstruct.2019.109665.
11. Smoljanović, H., Živaljić, N., Nikolić, Ž., Munjiza, A. Numerical analysis of 3D dry-stone masonry structures by combined finite-discrete element method. *International Journal of Solids and Structures*. 2018. 136–137. Pp. 150–167. DOI:10.1016/j.ijsolstr.2017.12.012.
12. Zampieri, P., Simoncello, N., Tetougueni, C.D., Pellegrino, C. Review article A review of methods for strengthening of masonry arches with composite materials. *Engineering Structures*. 2018. 171. Pp. 154–169. DOI:10.1016/j.engstruct.2018.05.070.
13. Zampieri, P., Simoncello, N., Gonzalez-libreros, J., Pellegrino, C. Evaluation of the vertical load capacity of masonry arch bridges strengthened with FRCM or SFRM by limit analysis. *Engineering Structures*. 2020. 225. 111135. DOI:10.1016/j.engstruct.2020.111135.
14. Dmitriev, A., Lalin, V., Novozhilov, Y., Mikhalyuk, D. Simulation of Concrete Plate Perforation by Coupled Structures. 2020. 92(9207). DOI:10.18720/CUBS.92.7.
15. Ribeiro, F., Sena-Cruz, J., Branco, F.G., Júlio, E. 3D finite element model for hybrid FRP-confined concrete in compression using modified CDPM. *Engineering Structures*. 2019. 190. Pp. 459–479. DOI:10.1016/j.engstruct.2019.04.027.
16. Zani, G., Martinelli, P., Galli, A., di Prisco, M. Three-dimensional modelling of a multi-span masonry arch bridge: Influence of soil compressibility on the structural response under vertical static loads. *Engineering Structures*. 2020. 221. 110998. DOI:10.1016/j.engstruct.2020.110998.
17. Zhao, C., Xiong, Y., Zhong, X., Shi, Z., Yang, S. A two-phase modeling strategy for analyzing the failure process of masonry arches. *Engineering Structures*. 2020. 212. Pp. 110525. DOI:10.1016/j.engstruct.2020.110525.
18. Mohireva, A., Proskurovskis, A., Belousov, N., Nazinyan, A., Glebova, E. Strength and deformability of compressed-bent masonry structures during and after fire. *Construction of Unique Buildings and Structures*. 2020. 92(9203). Pp. 2–6. DOI:10.18720/CUBS.92.3.
19. Thai, S., Thai, H.T., Vo, T.P., Patel, V.I. A simple shear deformation theory for nonlocal beams. *Composite Structures*. 2016. 183(1). Pp. 262–270. DOI:10.1016/j.compstruct.2017.03.022.
20. Pydah, A., Batra, R.C. Shear deformation theory using logarithmic function for thick circular beams and analytical solution for bi-directional functionally graded circular beams. *Composite Structures*. 2017. 172. Pp. 45–60. DOI:10.1016/j.compstruct.2017.03.072.
21. Tyukalov, Y.Y. Optimal Shape of Arch Concrete Block Bridge. *Construction of Unique Buildings and Structures*. 2020. 93. 9307. DOI: 10.18720/CUBS.93.7
22. Tyukalov, Y.Y. Calculation of circular plates with assuming shear deformations. *IOP Conference Series: Materials Science and Engineering*. 2019. 687(3). DOI: 10.1088/1757-899X/687/3/033004.
23. Tyukalov, Y.Y. Calculation of bending plates by finite element method in stresses. *IOP Conference Series: Materials Science and Engineering*. 2018. 451(1). DOI: 10.1088/1757-899X/451/1/012046.
24. Cannizzaro, F., Pantò, B., Caddemi, S., Calì, I. A Discrete Macro-Element Method (DMEM) for the nonlinear structural assessment of masonry arches. *Engineering Structures*. 2018. 168. Pp. 243–256. DOI: 10.1016/j.engstruct.2018.04.006.
25. Mahmoudi Moazam, A., Hasani, N., Yazdani, M. Incremental dynamic analysis of small to medium spans plain concrete arch bridges. *Engineering Failure Analysis*, 2018. 91. Pp. 12–27. DOI: 10.1016/j.engfailanal.2018.04.027.
26. Pulatsu, B., Erdogmus, E., Bretas, E. M. Parametric Study on Masonry Arches Using 2D Discrete-Element Modeling. *Journal of Architectural Engineering*. 2018. 24(2). 04018005. DOI:10.1061/(asce)ae.1943-5568.0000305.
27. Zhang, Y., Tubaldi, E., Macorini, L., Izzuddin, B. A. Mesoscale partitioned modelling of masonry bridges allowing for arch-backfill interaction. *Construction and Building Materials*. 2018. 173. Pp. 820–842. DOI: 10.1016/j.conbuildmat.2018.03.272.
28. Fusade, L., Orr, S. A., Wood, C., O'Dowd, M., Viles, H. (2019). Drying response of lime-mortar joints in granite masonry after an intense rainfall and after repointing. *Heritage Science*. 2019. 7(1). DOI: 10.1186/s40494-019-0277-7.
29. Leontari, A., Apostolou, M. Stability and rocking response of non-uniform masonry arches: The 'part-elliptical' profile. *Engineering Structures*. 2021. 228. DOI:10.1016/j.engstruct.2020.111519.
30. Grosman, S., Bilbao, A. B., Macorini, L., Izzuddin, B. A. Numerical modelling of three-dimensional masonry arch bridge structures. *Proceedings of the Institution of Civil Engineers - Engineering and Computational Mechanics*. 2021. 174(2). Pp. 96–113. DOI:10.1680/jenm.20.00028.

### **Information about authors:**

**Yury Tyukalov, Doctor of Technical Science**

ORCID: <https://orcid.org/0000-0001-6184-2365>

E-mail: [yutvgu@mail.ru](mailto:yutvgu@mail.ru)

*Received 25.05.2021. Approved after reviewing 03.11.2023. Accepted 03.11.2022.*

